New Technologies for Control and Measurement of Polyatomic Molecules

Thesis by
Ashay Naren Patel

In Partial Fulfillment of the Requirements for the
Degree of
Doctor of Philosophy

CALIFORNIA INSTITUTE OF TECHNOLOGY
Pasadena, California

2025
Defended May 16, 2025

To Śrī Ādi Parāśakti,
She who soars in the sky of the Heart,
Who illuminates and dances in each particle of the cosmos.

> *"By the power of her own will…She unfolds the universe upon her own screen."*
>
> ---
>
> *Pratyabhijñahṛdayam*, Kṣemarāja, translated by Jaideva Singh

> *"Receive the waves in your body: what splendour is in the region of the sea!"*
>
> ---
>
> *Songs of Kabîr*, Sant Kabir, translated by Rabindranath Tagore

Acknowledgements

Building this thesis has been the most enriching and challenging experience of my life. So many people have been an integral part of me and my work, and I am eternally grateful to you all, and for the opportunity I have here to recognize your contributions.

Above all, my advisor Nick Hutzler has been the most caring, compassionate, patient, and wise intellectual mentor I could have asked for. I came to Caltech to join Nick's group, and I never looked back. From crisis to crisis, you have been a constant source of support, and your guidance is the reason I completed this milestone. You allowed me to attend the 2018 YbOH summit with our collaborators several months prior to my joining the group officially, and I knew from that point onward that I was welcome and valued as part of this team.

Nick has fostered an inclusive and welcoming lab culture, for which I am very grateful. Throughout the challenges I faced in completing this work, my labmates have been a major factor in keeping me on track.

Arian Jadbabaie has been a vital mentor to me, as well as a dear friend, comrade, and housemate. I treasure our friendship, conversations, and spiritual connection, and I am grateful that I met such a gem of a human being in the lab. Our late night physics and gaming chats, our drives to and from the office (thank you!), our hangouts during the early part of my time at Caltech, and, of course, your introducing me to your friends—who are now my friends—are memories that I will cherish for a lifetime. Nick Pilgram was the first member of the lab I met when I visited Caltech, and he is a major reason why I ultimately came to Caltech. You mentored me through particularly difficult moments during my PhD, especially when vacuum, cryogenics, and plumbing were involved. I appreciated getting to know you and am grateful you invited me to attend your lovely wedding. Yi Zeng was the other labmate in my graduate cohort, and he was a major help in building our cryogenic beam source and showing me the ropes

of the data acquisition system, while always taking time to talk video games with me. Phelan Yu not only provided tremendous help with the vacuum, cryogenic, and laser systems in the lab, but he has been a wonderful friend, and collegial coworker. Your careful perspective and thoughtfulness is something I will always appreciate, along with our numerous Chipotle dinners. I am particularly fond of the time we worked together on healthcare advocacy. Chi Zhang has been a great postdoc to work with and to get to know. Joining the group under chaotic circumstances and pandemic-related delays, you are a great mentor and conversation partner, a font of incredible ideas, and a great proponent of sustainable workplace culture.

Chandler Conn, I have always enjoyed your sense of humor, your care for lab culture, commiseration over magnets and magnet-related textbooks, and your movie takes. Madison Howard—I am so glad that we could work together at the tail end of my PhD, and I really appreciate your attention to detail and the care you show towards other people inside and outside of the lab. Yuiki Takahashi—I met you when you were a visiting student, and I was very happy when you joined our group. You have done, and will continue to do, great things. Yuxi Yang—I had a great time sharing the experiment with you in my last few months at Caltech and experiencing DAMOP in Fort Worth.

I would also like to acknowledge members of our lab who are now in different groups—Daniel Grass and Harish Ramachandran—for being a part of my time at Caltech. I had the fortune working with a number of undergrad students in our lab, and I'd like to thank them for being part of my journey. I'd especially like to shout out Alicia Tirone, Jacquie Ho, and Adele Basturk with whom I shared many great conversations, and Victoria Su, who was a great undergraduate advisee.

Our day-to-day work would not be possible without the support of the administrative assistants in our group. Cherie Capri, Nancy Roth-Rappard, Tracy Mikuriya, and most recently Stephanie Malin—you all made sure we were organized and taken care of, and I will always appreciate your diligent presence in our group.

My work was completed as part of the PolyEDM collaboration, and I would like to extend my deepest gratitude to John Doyle, Tim Steimle, and Amar Vutha for your scientific expertise, mentorship, and collegiality. I am also grateful for the support of the Doyle group, and in particular Ben Augenbraun, Zack Lasner, Loïc Anderegg, Louis Baum, Alex Frenett, Hiro Sawaoka, Abdullah Nasir, Annika Lunstad, Paige Robichaud, Nathaniel Vilas, and Christian Hallas, some whom I knew well from my time at Williams College and the rest whom I had the pleasure of knowing in more recent years. In particular, I thank the Doyle group for lending us two of their TA

Pro laser systems, which we used in studying Zeeman-Sisyphus deceleration, and for sharing various pieces of atomic and molecule structure code throughout the years.

I would like to thank my thesis committee for their support and guidance—Brad Filippone who chaired it, along with Yanbei Chen and Ryan Patterson. I particularly enjoyed taking Ryan's introductory particle physics course as a G1, and auditing Brad's nuclear physics course in my sixth year.

I could not have accomplished this work without the mentors who took me under their wing while I was a student at Williams. Charlie Doret advised my undergraduate thesis and made me into a scientist. Thank you so much for continuing to believe in me, when I had trouble doing so myself, and for the continual guidance and mentorship. Kevin Jones was another important mentor to me from the moment I stepped into his mechanics course at Williams, and he introduced me to Paul Lett, who advised me on research during the summer I spent at UMD JQI as well as on my graduate school applications. I would also like to thank my postdoc mentors at JQI—Donald Fahey, Brie Anderson, and Bonnie Marlow.

Jefferson Strait let me join his optics lab immediately after my first year of college, setting me on this journey. Tiku Majumder embodies what it means to do precision measurement and AMO physics at a small liberal arts college, and I am one of many people who have benefited from the legacy he has created at Williams. Frederick Strauch and Swati Singh let me get my hands dirty simulating quantum jumps in Python and Matlab, a particularly fun project.

Several of my other professors at Williams were key parts of my intellectual and personal development, and I want to thank you all—Mihai Stoiciu (math and senior colloquium advisor), Catherine Kealhofer (physics), William Wootters (physics), Susan Loepp (math), Julie Blackwood (math), Thomas Garrity (math), the late Stephen Fix (English), Christopher Pye (comparative literature), Anjuli Raza Kolb (comparative literature), Daniel Aalberts (physics), David Tucker-Smith (physics), Devesh Chandra (tabla instructor), and Aparna Kapadia (history).

I want to now thank my dear friends, family, and comrades who in no small part made me the human I am today.

Mom and Dadu—thank you for loving and nurturing me, taking care of me through extremely challenging times, protecting me, for giving me your values while giving me the space and freedom to develop my own, and for supporting me at every step of this very tumultuous process. Eshaan—you are the best little brother one could ask for, and while I am sad I didn't get to spend much time with you over these past seven years, I am very excited to make up for that lost time in the years to come. Much love also to Trusha, Raadhay, Hitesh Fua, Varsha Foi, Arvind Dada, Hansa Baa, Raju Mama, Pinky Ben, Shilpa Didi, Tanvi Didi, Neil Kaka, Jyotsana Masi, and everyone else in my enormous and loving family. I especially remember those who are no longer here, but who are a deep part of me—Mota Dada, Dahi Baa, Megha, Kamla Baa, Suraj Baa, Narmada Masi, Kaka, and Arvind Mama. My godparents, Atul and Pratibha Gosalia, have also played a large role in my academic life, and I owe so much to you for your support since I was a small child. I thank my ancestors whose blessings continue to bear fruit.

I extend my love to my dear friends who I met before I came to Caltech, and especially those who have endeavored to stay in touch with me—Sean, Darla, Sam, Anna, Jamie, Jonathan, Madina, Aaron, Josh, Youngsoo, Abdullah, Leah, Ryan, Emily, Bingyi, Ellery, Felix, Christine, Kevin, Hannah, Daniel, Will, Nathaniel, Nate, Matt, Jeff, Aidan, Noah, Claudia, Thi, Tarun, Justin, Sarah, and many others. Thank you all for being in my life through its ups and downs.

To my lovely friends at Caltech—Jane, Brigitte, Richard, Alex, Arian, Charles, Aeryn, Bobbi, Sean, Sarah, Dawna, Ollie, Kat, Vasilije, Kate, Abdullah, Sam, Ryan, Kriti, Zoya, Christian, Ali, Luka, Gabe, James, Fayth, Nathaniel, Lori, Jae, Erica, Román, Xuan, Lauren, and Francesca—thank you for being in my life, for organizing with me, for the support, for our collective study, and for being the best friends I could ask for.

I especially want to thank my housemates—Jane, B, Arian, Charles, Bobbi, and Aeryn–for welcoming me into the house and for becoming my family here. In particular, Jane and B—you have consistently provided me support in our moments of crisis, and I treasured all our adventures, movie nights, and chill times. I'm also very grateful for the many, many times you drove me somewhere, and for being both present and deeply considerate. I also shout-out my Dungeons and Dragons group—Christian, Ali, Xuan, Lauren, B, Jane (our forever DM), and James (who sheltered me and three cats during the 2025 LA fires). I would also like to sincerely thank Sarah and Farnoush for letting me stay in their home in Culver City for three weeks while displaced by the LA fires. Without their support, this thesis would not have come together in its present form.

The animals in my life have emotionally supported me throughout this entire process and I thank them here–the adorable Snuggles, lovable gremlin John Brown, scrunkly Artemis, wormy Sandwich, big baby Mordy–as well as sleepy Sparky and ever playful Sassy both of whom are no longer with us.

An enormous part of my life in Pasadena was involved in organizing around social and political causes as a part of SoC, Caltech for Affordable Healthcare, Pasadena Tenants Union, Pasadena 4 Rent Control, and Caltech Grad Students and Postdocs United. Through our collective sweat we won so many sweet victories, like a new and improved healthcare plan for grad students, a historic rent control charter amendment in Pasadena (perhaps one of the strongest measures in the entire country), and the first labor union at Caltech. So I conclude by thanking some of my loving PTU comrades—Ryan, Liberty, Deb, Rebecca, the late Ira West, and Bin and Dan (who kindly helped me evacuate from the 2025 LA fires), as well as my union siblings that won important battles and negotiated a historic contract for grad students and postdocs to come. Together, may we build a world where science and technology are used for human betterment instead of as raw materials for exploitation, occupation, extraction, and war.

On this point, I recognize that the work described here was accomplished on the ancestral homeland of the Gabrielino Tongva people, who continue to reside in the Los Angeles area in resistance to settler colonialism and ethnic cleansing. I am in solidarity with them and all peoples struggling for sovereignty and dignity.

Finally, I conclude my acknowledgments by thanking enlightened beings who illuminate our communities with knowledge, just as the sun illuminates our planet. May this work be a humble offering.

Oṃ bhūr bhuvaḥ svaḥ
Tat savitur vareṇyaṃ
Bhargo devasya dhīmahi
Dhiyo yo naḥ pracodayāt.
Ṛgveda 03.062.10

Rendered in English by Sarvepalli Radhakrishnan as:
“We meditate on the adorable glory of the radiant sun; may She inspire our intelligence.”

Abstract

The Standard Model of particle physics has tremendous explanatory power, and while cosmological evidence assures us that it is incomplete, we have never observed a convincing signature of its violation in a laboratory setting. Extensions of the Standard Model proposed to solve one or more of the theory's open questions generically allow for violation of fundamental, discrete symmetries such as CP symmetry, and cosmological processes such as baryogenesis point to CP violation as a fundamental ingredient of our cosmos. Searches for a permanent electric dipole moment (EDM) of the electron inside polar molecules are sensitive probes of new CP violating physics, and these experiments have constrained new CP violating physics to beyond energy scales that are directly accessed at the Large Hadron Collider. EDM experiments with polar molecules are typically limited in sensitivity by either molecule number or coherence time. An electron EDM experiment in ultracold, trapped polyatomic molecules promises to extend the new physics reach by many orders of magnitude, but there are a number of major technical challenges with these experiments, including molecular beam deceleration and high-resolution spectroscopy of cold, free radicals. This thesis reports the development of new technologies and methods for control and measurement of polyatomic molecules in support of next-generation EDM measurements.

Published Content and Contributions

[1] A. N. Patel, M. I. Howard, T. C. Steimle, and N. R. Hutzler, *Rapid, broadband, optical spectroscopy of cold radicals*, (May 6, 2025) `10.48550/arXiv.2505.03650`, `http://arxiv.org/abs/2505.03650`,
A.N.P. led the system integration of the spectrometer and supercontinuum laser with the cryogenic molecular source and data acquisition system, measured all of the spectral data shown in the manuscript, and performed initial analysis and fits of the data in PGOPHER to validate its performance. A.N.P. also prototyped the system using atomic titanium, lanthanum, dysprosium, and thulium, at both room temperature and at cryogenic temperatures (not included in the manuscript), made the necessary modifications to the cryogenic apparatus, and participated in the writing of the manuscript.

[2] Y. Zeng, A. Jadbabaie, A. N. Patel, P. Yu, T. C. Steimle, and N. R. Hutzler, "Optical cycling in polyatomic molecules with complex hyperfine structure," Physical Review A **108**, 012813 (2023) `10.1103/PhysRevA.108.012813`,
A.N.P. led the assembly of the cryogenic molecular beam source used in this manuscript, which details the first new molecular measurements generated by this apparatus.

CONTENTS

LIST OF FIGURES

LIST OF TABLES

Chapter 1 Introduction

"The tradition of all dead generations weighs like a nightmare on the brains of the living."

Karl Marx, *The Eighteenth Brumaire of Louis Bonaparte*

In his 1894 dedication of the Ryerson Physical Laboratory at The University of Chicago, Albert A. Michelson remarked [1]:

> *While it is never safe to affirm that the future of Physical Science has no marvels in store even more astonishing than those of the past, it seems probable that most of the grand underlying principles have been firmly established and that further advances are to be sought chiefly in the rigorous application of these principles to all the phenomena which come under our notice. It is here that the science of measurement shows its importance—where quantitative work is more to be desired than qualitative work. An eminent physicist remarked that the future truths of physical science are to be looked for in the sixth place of decimals.*

Michelson's assertion proved prescient for several reasons. First, and with some irony, it is certainly the case that there have been a number of tremendously "astonishing" discoveries and observations since he made these remarks. The development of the special and general theories of relativity and quantum mechanics is foundational to our understanding of the universe at the largest and smallest scales. A person witnessing the advent of this new science would likely find it far more than a perturbation of the principles that were "firmly established" prior.

In the intervening century between Michelson and ourselves, the Standard Model has become the most precisely tested theory of the natural world, with corroborative measurements in both tabletop and collider settings. For example, the magnetic moment of the electron has been measured to part per 10^{13} precision, confirming Standard Model calculations [2]. No departure from the Standard Model has ever been demonstrated *convincingly* on our planet, though tensions between theory and experiment exist in a preliminary way. Perhaps we find ourselves in Michelson's position, where the "underlying principles" have been determined and all that remains is to confirm the quantitative details to ever greater precision. Unfortunately, or fortunately as it may be, the Michelson's distinction between quantitative and qualitative is a complicated one when it comes to the Standard Model.

Cosmological observations tell us that the Standard Model is not complete. Galactic rotation and the angular power spectrum of the Cosmic Microwave Background (CMB) tell us that 26.8% of the mass-energy in the universe is comprised of "dark matter," which gravitates but interacts only weakly with the matter we observe directly [3]. Furthermore, the accelerating expansion of spacetime could imply that 68.3% of the mass-energy is made of "dark energy," which contributes to spacetime properties in distinct ways from matter and radiation [3]. The measly, remaining 4.9% is the ordinary matter we have measured and characterized with stunning precision.

There are major outstanding problems in the ordinary matter sector we know so well. The quantum field theory calculations that miraculously predict the electron's magnetic moment are fiendishly difficult when applied to bound systems of quarks—protons, neutrons, and the nuclei they comprise. A panoply of nuclear models and calculational methods exist to generate predictions of behavior for even the simplest of nuclei [4]; it is therefore safe to say that the quantum chromodynamics (QCD) that governs the nuclear sector of ordinary matter is not understood at the level of quantum electrodynamics (QED), and predicted QCD properties generally have larger error bars than those of QED.

Furthermore, beyond the interpretation of the Standard Model as we have it, there are issues with the structure itself. For example, one asks why there are three generations of each Standard Model fermion? Other mysteries include the mass ordering of neutrinos, the extremely low value of θ_{QCD} perhaps hinting at an underlying symmetry, the reasons for and consequences of the value of the Higgs mass, and the apparent fine-tuning of Standard Model constants. These are not issues with the Standard Model per se, but they may be pointing to viable model extensions that provide more satisfying "answers."

Physicists are thus in a situation where more correct models may be developed that differ in significant qualitative ways from the Standard Model as we know it. One approach is to directly produce new particles and interactions in high energy colliders in order to uncover their properties. Another approach is to appeal to Michelson's "science of measurement," and search for clues in the sixth decimal place and, in fact, far beyond. This "precision measurement" approach is not limited to uncovering the truth of our own models to greater depths, although this is valuable. When experimental measurements access higher precision, they are indirectly probing physics due to higher energy particles and interactions. The hope is that we may one day demonstrate an unambiguous violation of Standard Model predictions in a system that is well-understood and precisely measured on or just outside our home planet. We have the best possible chance to do this by building experiments that can probe new physics beyond the Standard Model (BSM) at the highest and most inaccessible energy scales.

This thesis details contributions to experiments searching for BSM physics that violates CP symmetry. In the rest of this chapter, we discuss fundamental discrete symmetries and their violation and motivate why CP violation is a promising avenue to search for new physics. Then we survey recent experiments measure CP violation in the electron and nuclei in polar molecules. Finally, we introduce efforts to build an experiment to measure the CP-violating electric dipole moment (EDM) of the electron in trapped, polyatomic molecules.

1.1 Fundamental symmetries and their violation

We begin our study of physics in the world of mechanics. We first write down the forces on a set of particles and integrate the differential equations that describe their behavior. Then, we recast these vector differential equations into simpler scalar equations for energy that vastly simplify the calculation. When we proceed to electromagnetic theory, we write down the equations for the force between charges, using the laws of mechanics to solve for their motion. Through abstracted notions of electric field and electric potential, we are able to simplify problems using Gauss' law and by appealing to symmetries in the problem. This story—using symmetry to simplify complex physical problems—plays out again and again in physics.

The first example given is a description of Noether's theorem, where continuous symmetries imply conserved quantities. In the case of mechanics, time, translation, or rotational invariance lead to conservation of energy, momentum, and angular momentum, respectively. In the second example, we find that geometric symmetries can greatly simplify complicated integrals. In this case, the symmetries need not be continuous. For example, the integral of an odd function that exhibits reflection symmetry about the y axis over a symmetric interval $[-a, a]$ is zero. In this case, the oddness or evenness of a function is a discrete symmetry.

In quantum mechanics, the Hamiltonian operator governs the time evolution of a system, and its symmetries determine the symmetries of the resulting wavefunctions. Observables are written as expectation values of a particular operator for these wavefunctions. These observables amount to integrals of products of wavefunctions and operators, and the integrals can be simplified through the symmetry of the integrand. For example, the spherical symmetry of an atomic Hamiltonian implies that the angular parts of the wavefunctions are spherical harmonics, whose integrals are easily written down in a coordinate-free manner (see Chap. 5 of [5]).

Many of the laws of physics conserve so-called fundamental discrete symmetries like charge (C), parity (P), and time (T). The C, P, and T operations invert matter into antimatter, coordinates ($\vec{r} \to -\vec{r}$), and dynamics ($t \to -t$), respectively. It is apparent that Maxwell's equations and the Newton's law of gravitation are symmetric with respect to C, P, and T. It was only when weak interaction decays were studied that P-violating physics was discovered, leading to the distinction between right-handed and left-handed particles [6, 7]. Since P violation was first discovered, C, T, CP, CT, and PT violation have also been observed, either directly or indirectly assuming that CPT is an exact symmetry of nature.[1]

The Standard Model contains a certain amount of discrete symmetry violation, but its extensions generically posit greater violation of some of the symmetries listed above, such as CP. Precision experimental tests of symmetry violation both constrain (symmetry-violating) BSM theories and may shed light on the incongruities between experimental tests of the Standard Model and cosmological evidence that the model is incomplete. In the following section, we look at one cosmological mystery that hints at further CP violation than what is provided in the Standard Model.

---

[1] CPT symmetry is intimately related to Lorentz invariance [8]. Some exotic BSM theories posit CPT violation [9].

1.2 Baryon asymmetry of the universe (BAU) and CP violation

One major problem with the Standard Model that was not already mentioned is the baryon asymmetry of the universe (BAU). Restated, the 4.9% of our universe that is made of matter contains no free antimatter. If there were portions of our cosmos that contained regions of antimatter, we would expect to observe gamma rays from the annihilation between matter and antimatter regions, which are not observed in gamma ray spectra [10].

There are two commonly cited, independent pieces of evidence for the observed asymmetry between baryons and antibaryons η, where

$$\eta = \frac{n_B}{n_\gamma} - \frac{n_{\bar{B}}}{n_\gamma} \approx 6 \times 10^{-10}, \tag{1.1}$$

and where n_B, $n_{\bar{B}}$, and n_γ are the number densities of baryons, antibaryons, and photons, respectively. The first observation is the observed primordial abundance of ^{3}He, ^{4}He, D, ^{6}Li, and ^{7}Li from Big Bang nucleosynthesis (BBN) [11]. The second is the anisotropy in the CMB angular power spectrum, which is caused by energy density perturbations due to the coupling between baryons and photons [12]. Both observations point to $\eta \approx 6 \times 10^{-10}$.

Sakharov posited three conditions that would allow for baryogenesis with a baryon asymmetry, which are [13]:

1. Baryon number (B) violation
2. C violation and CP violation
3. Departure from thermal equilibrium.

The first condition of B violation requires that a process produces more baryons than antibaryons. The third condition ensures that baryons and antibaryons have enough time to annihilate before rapid spacetime expansion freezes out collisions. The second condition requires C violation, ensuring that baryon excess-producing reaction rates are larger than antibaryon excess-producing reaction rates. In order to see why CP violation is required, we consider a process that violates C but not CP.

Consider a particle X that decays into two right-handed quarks q_R. If we have C violation, then we could have that

$$\Gamma\left(X \rightarrow q_R q_R\right) \neq \Gamma\left(\bar{X} \rightarrow \bar{q}_R \bar{q}_R\right), \tag{1.2}$$

where Γ denotes the reaction rate for the process. However, if CP is an exact symmetry we must also have

$$\Gamma\left(X \to q_R q_R\right) + \Gamma\left(X \to q_L q_L\right) = CP\Big(\Gamma\left(X \to q_R q_R\right) + \Gamma\left(X \to q_L q_L\right)\Big) \tag{1.3}$$

$$= \Gamma(\bar{X} \to \bar{q}_R \bar{q}_R) + \Gamma(\bar{X} \to \bar{q}_L \bar{q}_L). \tag{1.4}$$

Taking the chirality of the quarks into account, CP symmetry does not produce the BAU. While Standard Model and BSM baryogenesis scenarios have been described elsewhere and are beyond the scope of this thesis, we suspect that CP violation is an essential ingredient in generating the BAU [14].[2].

The Standard Model contains CP violation in the quark sector. The CabibboKobayashi-Maskawa (CKM) matrix, which describes the relationship between mass eigenstates and weak eigenstates of the three generations of quarks, contains a single complex phase typically denoted by $e^{i\delta_{13}}$ that causes CP violation. Specifically, CP violation can occur in the quark sector in Feynman diagrams where all three generations of quarks are involved. However, because the off-diagonal terms in the CKM matrix are much less than 1, diagrams that involve all three quarks are suppressed, and the corresponding observables can be difficult to measure.

Interpretation of the CP violation within the Standard Model and its consequences for baryogenesis is an active area of research. For this thesis, it is sufficient to note that BSM theories generically permit larger amounts of CP violation than is afforded by the Standard Model, which has a direct bearing on open questions of cosmology and particle physics such as baryogenesis. A precision search for CP violation is a fruitful strategy for constraining the wide array of BSM theories that are proposed, including supersymmetric models [16].

1.3 Measuring CP violation in low-energy polar molecules

Fraunhofer's work measuring the spectral lines of atoms was a prelude to today's marvelously precise characterization of atomic systems, particularly enabled by the invention of the laser. Precision measurement in atoms and molecules can be used to measure and set stringent bounds on new particles and forces, such as the CP violating objects that are predicted in numerous BSM extensions. Though atoms and molecules

---

[2] There are also exotic models that predict that CP symmetry was spontaneously broken and CP symmetry is only violated at the Standard Model level today [15]

are low-energy systems, CP violating particles and interactions at high energy scales can couple to them, generating CP violating electromagnetic moments at atomic energy scales. Theorists use chiral effective field theory to connect high-energy physics to their low-energy consequences, described through a set of effective parameters [17].

The CP violating moment of particular interest for the work described in this thesis, and for which tremendous progress has been made in the last decade, is the (permanent) electric dipole moment (EDM) of the electron, denoted by d_e. Before proceeding, we first show that the electric dipole moment of the electron violates P and T symmetry. For a dipole moment $\vec{d}$ in an electric field $\vec{\mathcal{E}}$, the electric dipole interaction is given by

$$\begin{aligned} \hat{H}_{\mathrm{EDM}} &= -\vec{d}\cdot\vec{\mathcal{E}} && (1.5) \\ &\propto -d_e\,\vec{S}\cdot\vec{\mathcal{E}}, && (1.6) \end{aligned}$$

where $\vec{S}$ is the electron spin angular momentum operator. There are several reasons typically given for why $\vec{d}$ must lie parallel to $\vec{S}$. For the thesis author, the most convincing argument relies on the Wigner-Eckart theorem, which when applied to the electron posits that all observables its are proportional to the electron's angular momentum. In the case of the bare electron, this angular momentum refers to the spin $\vec{S}$. If this statement were not true, then the electron would possess another quantum number associated with the orientation of $\vec{d}$, which would have widespread (and unobserved) ramifications for spin statistics and orbital occupation in atoms.

Applying the parity operation P to the above expression, we find that $\vec{S} \to \vec{S}$, as it is an angular momentum operator (parity even). On the other hand, $\vec{\mathcal{E}} \to -\vec{\mathcal{E}}$ under P because electric fields are generated by charge distributions through Gauss' law. Therefore, $\hat{H}_{\mathrm{EDM}}$ has odd parity. We repeat this procedure for T and find that T takes $\vec{\mathcal{E}} \to \vec{\mathcal{E}}$ and $\vec{S} \to -\vec{S}$. Thus $\hat{H}_{\mathrm{EDM}}$ is also T odd. By appealing to the CPT theorem, we conclude that $\hat{H}_{\mathrm{EDM}}$ is also CP odd. A measurement of a nonzero value for the electron EDM (eEDM) would imply CP violating physics. [3]

A recent calculation demonstrates that the Standard Model actually predicts an effective value of $d_e \sim 10^{-35}\ e\ \mathrm{cm}$ [18]. When the work in this thesis began, calculations had previously neglected a semileptonic interaction that ultimately increased the estimate by three orders of magnitude. Nevertheless, as discussed later in this section, the Standard Model limit is five orders of magnitude lower than constraints set by experiments.

---

[3] If the electron were not a fundamental (point) particle, and its EDM were proportional to a charge distribution in physical space, one would erroneously conclude that $\vec{d}$ is P odd and that $\hat{H}_{\mathrm{EDM}}$ is P even, unlike the case when $\vec{d}$ is proportional to $\vec{S}$.

EDM searches are then a generic way to probe for new CP violating physics in a (largely) model independent and virtually background-free manner, with clear pathways to continue approaching the Standard Model background.

In analogy to measurements of the electron magnetic moment $\vec{\mu}$, one of the most precisely measured quantities in physics, one can determine $\vec{d}_e$ by observing the spin precession rate of the electron in an electric field $\vec{\mathcal{E}}$. For a "small" value of d_e, the best measurements will make use of the largest values of $\vec{\mathcal{E}}$ that are attainable. Unfortunately, a bare electron in an electric field would simply accelerate away. Furthermore, steady-state electric fields generated in a laboratory are limited to $\sim$ 100 kV/cm before field ionization of materials is engaged. Neutral atomic and molecular systems, on the other hand, do not experience net forces in electric fields, and the electric fields between electrons and protons in atoms are $\sim$ 1 GV/cm scale—a four to five order-of magnitude enhancement. In particular, the electric field experienced by an electron with wavefunction overlapping a heavy nucleus is enhanced by a factor of between $Z^2 - Z^3$ due to relativistic length contraction and finite nuclear size effects [19].

In summary, the ideal atomic system is comprised of a heavy nucleus to maximize the effective electric field on the electron, a nonzero electron spin, and a S orbital electron with maximal overlap with the nucleus.[4] The first-order energy shift due to H_{EDM} for an atomic eigenfunction $|\psi\rangle$ is given by

$$\Delta E = \langle\psi|\hat{H}_{\mathrm{EDM}}|\psi\rangle. \tag{1.7}$$

Because $|\psi\rangle$ is an eigenfunction of the field-free atomic Hamiltonian, which is parity symmetric, $|\psi\rangle$ is either parity even or odd, or in other words,

$$P|\psi\rangle = \pm|\psi\rangle. \tag{1.8}$$

---

[4] Closed-shell atoms and molecules with no unpaired valence electrons are not sensitive to the eEDM, but can be used to measure the (unscreened) EDM of the nucleus, known as the nuclear Schiff moment (NSM). Open shell systems with nuclear spin $I > 1$ can be used for measurements of the CP violating nuclear magnetic quadrupole moment (NMQM). Our lab is building an experiment to measure the NMQM for ^{173}YbOH with $I = 5/2$. Hadronic CP violation is equally interesting to new physics in the leptonic sector, if not more so, but the Hutzler Lab NMQM experiment is beyond the scope of this thesis.

Remembering that $\hat{H}_{\mathrm{EDM}}$ is P odd,

$$\begin{aligned}
\Delta E &= \langle\psi|\hat{H}_{\mathrm{EDM}}|\psi\rangle && (1.9)\\
&= \langle\psi|P^{-1}P\hat{H}_{\mathrm{EDM}}P^{-1}P|\psi\rangle && (1.10)\\
&= \langle\psi|P^{\dagger}P\hat{H}_{\mathrm{EDM}}P^{\dagger}P|\psi\rangle && (1.11)\\
&= \langle\psi|\pm P\hat{H}_{\mathrm{EDM}}P^{\dagger}\pm|\psi\rangle && (1.12)\\
&= \langle\psi|P\hat{H}_{\mathrm{EDM}}P^{\dagger}|\psi\rangle && (1.13)\\
&= \langle\psi|-\hat{H}_{\mathrm{EDM}}|\psi\rangle && (1.14)\\
&= -\langle\psi|\hat{H}_{\mathrm{EDM}}|\psi\rangle && (1.15)\\
\implies \Delta E &= 0, && (1.16)
\end{aligned}$$

where we appealed to the unitarity of the parity operator in line three and that parity anticommutes with $\hat{H}_{\mathrm{EDM}}$ in line six. There are therefore no observable consequences of the eEDM on field-free atomic eigenfunctions. This situation is rectifiable by applying an external electric field to polarize the atomic wavefunctions, breaking the parity symmetry of the Hamiltonian and the resulting wavefunctions. An external electric field has the effect of mixing states of opposite parity and inducing an electric dipole moment in the atom, a process called polarization. To summarize, a polarized atom with an induced electric dipole moment allows for a nonzero observable energy shift due to the electron's permanent electric dipole moment.

For small applied fields, the degree of polarization is inversely proportional to the energy difference between nearby opposite parity states. In typical atomic systems, the closest states of opposite parity are electronic levels like S and P states in hydrogen, with $\sim$ 100 THz frequency spacing. Therefore, the maximum polarization achievable in an atomic system under even large laboratory electric fields is a mere $\sim 10^{-3}$. Polar molecules containing heavy nuclei with electron orbital overlap provide eEDM sensitivity for the same reasons as for atoms, but they generically contain much closer states of opposite parity opposite parity states that are much closer in energy. In general, the first two rotational levels (see Chap. 2) in heteronuclear diatomic molecules like YbF are split by $\sim$ 10 GHz, allowing appreciable polarization in lab fields of $\sim 100\ \mathrm{kV/cm}$. Other molecules, like ThO experience rotational perturbations that split a single rotational line into closely-spaced states of opposite parity called parity doublets. The Ω-doublets in ThO are spaced by a mere $\sim$ 360 kHz for the $J'' = 1$ state, allowing full polarization in fields less than $10\ \mathrm{V/cm}$ [20, 21].

The basic measurement scheme is shown in Fig. 1.1. First, an atom or a molecule is placed in a magnetic field $\vec{\mathcal{B}}_{\mathrm{lab}}$ to split the magnetic sublevels $|\pm M\rangle$ (which are

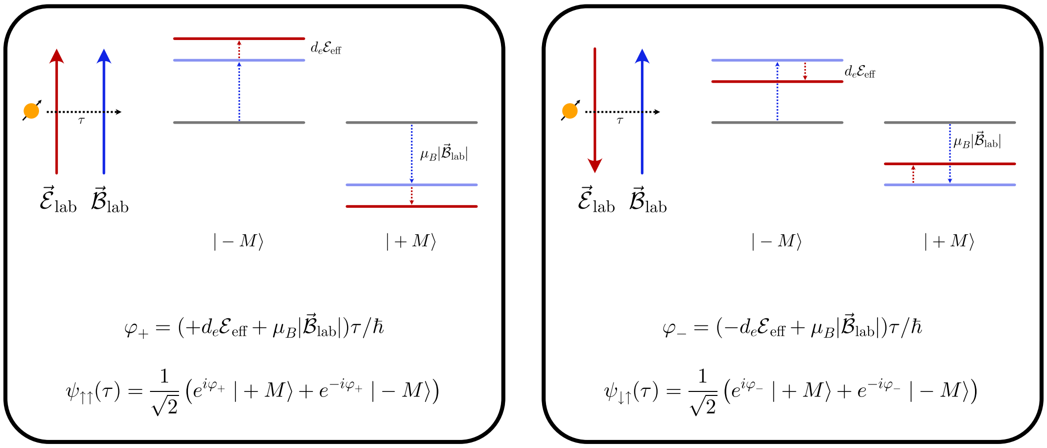

$$d_e = \frac{\hbar(\varphi_+ - \varphi_-)}{2\tau\mathcal{E}_{\text{eff}}}$$

Figure 1.1: Basic EDM measurement scheme. The spin precession phase between T-reversed states is measured when $\vec{\mathcal{E}}_{\text{lab}}$ is aligned and anti-aligned with $\vec{\mathcal{E}}_{\text{lab}}$. The red colored states have both Stark and Zeeman shifts applied. The difference in phases φ_+ and φ_- is proportional to d_e.

connected by the T operation). Then one applies an external electric field $\vec{\mathcal{E}}_{\text{lab}}$ either parallel or antiparallel to $\vec{\mathcal{B}}_{\text{lab}}$. Then, one prepares an equal superposition of $|\pm M\rangle$, which is allowed to precess in $\vec{\mathcal{E}}_{\text{lab}}$. Because $\vec{\mathcal{E}}_{\text{lab}}$ is applied, the electron is able to access and precess under the large internal electric field within the atom for a time τ. One can show that the difference of the total precession phase for $\vec{\mathcal{E}}_{\text{lab}}$ parallel and antiparallel to $\vec{\mathcal{B}}_{\text{lab}}$ leaves a total phase proportional only to d_e. The effect of $\vec{\mathcal{B}}_{\text{lab}}$ cancels and allows for a sensitive, differential measurement of a very small quantity d_e. The quantum projection noise-limited sensitivity of this protocol for N precessing atoms is given by

$$\delta d_e = \frac{\hbar}{2|P|\mathcal{E}\tau\sqrt{N}}, \tag{1.17}$$

where $|P|$ is the degree of polarization, $\mathcal{E}$ is the magnitude of the *internal* electric field, and τ is the spin precession time. Molecules with closely-spaced opposite parity states are chosen to allow $|P| \sim 1$, and molecules with large valence electron overlap with a heavy nucleus are chosen to maximize $\mathcal{E}$. Molecules with parity doublets like ThO provide an additional advantage because the atoms can be prepared spectroscopically in states with opposite orientation without reversing $\vec{\mathcal{E}}_{\text{lab}}$. Imperfect reversal of $\vec{\mathcal{E}}_{\text{lab}}$ can lead to systematic errors when combined with non-reversing $\vec{\mathcal{B}}_{\text{lab}}$ or elliptical AC Stark shifts arising from, for example, optical substrate birefringence [21].

State-of-the-art eEDM experiments with large N and low $\tau \sim 1$ ms have been conducted in cryogenic molecular beams of both ThO (ACME Collaboration) and YbF (Imperial College EDM) [22, 23]. At the same time, a recent eEDM experiment using trapped HfF^+ ions, where $\tau \sim 1$ s and much smaller N, set the most current best limit of $|d_e| < 4.1 \times 10^{-30}$, surpassing the previous limit of $|d_e| < 1.1 \times 10^{-29}$ set by ACME II [24].[5]

Trapped molecule experiments also occur in relatively small region in space, which is much easier to shield from stray magnetic fields than several-m long beamlines. Over the last decade, EDM experiments in molecules have improved the limit on d_e by an astounding order of magnitude, constraining new CP violating particle masses at one loop to over 40 TeV [24, 26]. The reach of eEDM experiments is therefore probing CP violating physics at energies an order of magnitude beyond what is directly accessible in the Large Hadron Collider.

There is then currently a tradeoff between the long interaction times afforded by molecular ion traps and the large numbers of neutral molecules generated in beam experiments. Diatomic molecules like YbF are laser coolable using techniques adapted from atomic laser cooling, but lack the parity doublet structure of ThO [27]. Similarly, diatomic molecules like ThO with states of nonzero orbital angular momentum in the ground state do not permit laser cooling. Polyatomic molecules—the motivating system of this thesis—combine the high yields when produced in cryogenic beams, systematic error rejection from parity doublets, and the use of laser cooling and trapping techniques.

1.4 Towards EDM experiments in trapped polyatomic molecules

In this section, we briefly overview the opportunities and challenges afforded by polyatomic molecules for a next-generation eEDM measurement. While we defer discussion of the origins of the relevant molecular structure to Chap. 2, there are a number of features in some classes of polyatomic molecules that make them attractive for EDM experiments.

While diatomic molecules possess a single vibrational mode (stretching), polyatomic molecules generically have additional vibrational modes associated with stretching and bending. For example, SrOH has stretching modes for the $\mathrm{Sr-O}$ and $\mathrm{O-H}$

---

[5] The eEDM sensitivity for N trapped molecules is a more complicated expression than 1.17. See Eq. 7.31 in [25].

bonds, as well as a mode corresponding to the O atom bending motion. When this bending mode is coupled to the rotation of the molecule, an orbital angular momentum corresponding to rotations of the bending atom, labeled by the quantum number ℓ, is formed. There are two degenerate bending modes (in-plane and out-of-plane) that are split by the rotation by ~ 10 MHz into states of opposite parity. In paramagnetic molecules, these bending modes have both sensitivity to the eEDM as well as parity doublet structure for systematic error rejection, with very small splittings that enable full polarization in extremely modest $\sim 10 - 100$ V/cm lab fields [28]. Unlike in ThO, where the EDM science state is the $H^3\Delta_1$ excited state with a 4.2 ms lifetime, the bending modes in polyatomic molecules occur in the ground electronic state and can have lifetimes on the order of ~ 1 s [28, 29]. Even if ThO could be trapped, the lifetime in the science state is too short to be able to make use of the longer integration times; this limitation is generically untrue for EDM sensitive polyatomic molecules.

As discussed further in Chap. 2), molecules composed of a heavy atom with s^2 valence structure ionically bonded to a single-electron accepting ligand like F, OH, or OCH_3 permit laser cooling. These molecules leave a single electron remaining on the heavy nucleus in an $^2\Sigma$ orbital (analogous to S orbitals in atoms), which enable laser cooling schemes using suitably modified methods from atomic laser cooling. Polyatomic molecules with this structure combine the coolability with generic, EDM sensitive bending mode parity doublets.

Because the $^2\Sigma$ ground state has an unpaired electron spin and no orbital angular momentum, it is sensitive to magnetic fields to first order, in contrast to the $H^3\Delta_1$ state in ThO with zero first-order Zeeman shift. The additional structure of polyatomic systems, however, provide avenues for rejection of electromagnetic noise despite first-order sensitivity. In particular, $\vec{\mathcal{E}}_{\text{lab}}$ can generically be chosen to tune the science state g-factor to near-zero while maintaining EDM sensitivity and polarization. In collaborators' 2023 measurement, the EDM spin precession protocol was demonstrated in an optical dipole trap of ultracold CaOH, where this zero g-factor method was used to increase the coherence time from 0.5 ms to 30 ms [30]. This experiment was not conducted with any magnetic shielding, and with magnetic shielding coherence times closer to 1 s should be possible. Additional work in our group has posited that the same magnetic tuning can be used to eliminate magnetic field sensitivity for transitions as well as states, with demonstrations currently underway in ^{174}YbOH [31].

Since beginning this thesis work, and as illustrated by the aforementioned CaOH result, many of the steps to conduct an eEDM experiment in trapped polyatomic molecules have been demonstrated by the PolyEDM collaboration, consisting of the groups of Nick Hutzler (Caltech), John Doyle (Harvard), Amar Vutha (University of Toronto), and Tim Steimle (Caltech and Arizona State University). The molecule CaOH is not particularly useful for setting an EDM limit because of the light mass of Ca that does not provide intrinsic EDM sensitivity. In 2018, the collaboration began working in earnest to study, laser cool, and trap YbOH towards a next-generation eEDM measurement with PeV energy reach [28]. However, unforeseen low-lying perturbed states in YbOH due to inner f shell excitations of the Yb atom prevented laser cooling without several years of a challenging spectroscopy effort. Such an effort is underway in YbF, which suffers from essentially the same issue [32–34]. Furthermore, laser slowing of YbOH proved difficult and lossy, requiring further research and development. Therefore, the collaboration switched to SrOH (see Sec. 6.4) as a nearer-term eEDM measurement platform, which had been laser cooled and has since been trapped in a magneto-optical trap (MOT) [35].

While rules of thumb hint that particular molecules are likely viable for a next-generation eEDM experiment, years of spectroscopy have been required historically in order to be able to address viability in a definitive manner. Furthermore, laser deceleration of molecules produced in cryogenic beams has been a challenging and inefficient prerequisite for laser cooling and trapping. This thesis describes our efforts to develop new technologies in support of next-generation precision measurements with trapped molecules, particularly to overcome the severe hurdles of laser deceleration and survey spectroscopy. Chap. 2 provides a brief overview of the atomic and molecular structure referenced in this thesis. Chap. 3 details the construction and operation of a $1\ \mathrm{K}$ cryogenic beam source for atoms and molecules along with typical experimental and simulation methods used to study molecular beams. Chap. 4 discusses possibilities for efficient deceleration of molecular beams, simulations of these methods, and apparatus construction to test Zeeman-Sisyphus deceleration in particular. Chap. 5 surveys a experimental testing with a prototype, permanent magnet Zeeman-Sisyphus decelerator in beams of cold $^{23}\mathrm{Na}$ and $^{39}\mathrm{K}$. Chap. 6 describes spectroscopic efforts for the SrOH eEDM experiment and a novel technology for simultaneous, broadband, high-resolution spectroscopy of cold, free radicals. Finally, Chap. 7 provides brief concluding remarks and an outlook for the work described in this thesis.

Chapter 2

Review of Atomic and Molecular Structure

"There is a great rock which is full of tenderness and affection, which is obvious and ever clearly perceived, which is soft, which is omnipresent and eternal. Within it countless lotuses blossom. Their petals sometimes touch one another, sometimes not, sometimes they are exposed and sometimes they are hidden from view. Some face downwards, some face upwards and some have their roots intertwined. Some have no roots at all. All things exist within it though they do not."

Vasistha's Yoga, translation of the *Yoga Vasiṣtham* by Swami Venkatesananda

In this chapter, we briefly survey some principles of atomic and molecular structure that are relevant to the work described in this thesis. The discussion here is a digest of important facts and physical arguments. For a more thorough understanding of (linear) polyatomic molecular structure, especially their vibronic structure as it relates to precision measurements, the reader should consult previous theses in the Hutzler Lab [36, 37]. For an overview of molecular structure as a whole, the reader can consult textbooks such as [5, 38, 39].

This thesis describes experimental work using ^{23}Na, ^{39}K, ^{40}CaF, ^{174}YbOH, and ^{88}SrOH, and these species will be used as exemplar atoms and molecules to illustrate particular principles. In this thesis, we adopt the common convention where a double-primed symbol corresponds to ground states $|\psi''\rangle$ and a single-primed symbol corresponds to excited states (e.g., $|\psi'\rangle$).

2.1 Overview of alkali atomic structure

Atoms are bound and charge-neutral systems of nuclei and electrons, held together through Coulombic attraction. Consider an atom composed of Z protons. The Hamiltonian for this general atom is given by

$$\hat{H}_{\text{atom}} = \frac{\hbar^2}{2m_e}\sum_i \nabla_i^2 - \sum_i \frac{Ze^2}{4\pi\epsilon_0 r_i} + \sum_{i\neq j} \frac{e^2}{4\pi\epsilon_0 |r_i - r_j|}, \tag{2.1}$$

where i, j label each electron, r_i is the radial distance of electron i from the center of the nucleus, and m_e and e are the electron mass and charge, respectively. The first term is the kinetic energy of all the electrons, the second term is the energy due to electrostatic attraction between each electron and the nucleus, and the last term is the energy due to electrostatic repulsion between individual electrons. Finding the analytical eigenstates and energies for this Hamiltonian is intractable, but we write it here to indicate an important fact with deep consequences.

In particular, $\hat{H}_{\text{atom}}$ is spherically symmetric, which implies that the angular parts of the wavefunctions are given by spherical harmonics, or by spherical tensors in a coordinate-free representation (see Chap. 5 of [5]). Because important operators such as $\vec{d} = -e\vec{r}$ and $\vec{S}$ can also be written as spherical tensors, an algebraic procedure can be followed, using for example the Wigner-Eckart theorem, to write down the expectation value of an observable up to a so-called reduced matrix element, which contains the remaining electronic structure "content" of the observable. These reduced matrix elements are ultimately determined by experiment. While the spherical tensor algebra can be cumbersome, it is a powerful and exact tool enabled through the study of symmetry.

Of course, for a multi-electron system, there is an additional complication that electrons are fermions and therefore subject to anti-symmetrization rules, which lead to increasingly complex descriptions of the electronic wavefunction with increasing electron number. One important approximation in atoms is to assume that filled shells act essentially to screen the full nuclear charge of the proton. One can see this by applying Gauss' law to determine the potential of a spherical nucleus with uniform charge $+Ze$ surrounded by a uniformly charged sphere with charge $-(Z-k)e$. Due to spherical symmetry of the Hamiltonian, filled electron orbitals are spherically symmetric as well. The consequence is that the properties of atomic states are largely determined by the valence electrons.

Single atomic electrons are described by the quantum numbers n, l, m_l, and m_s, corresponding to the energy level, total orbital angular momentum, orbital angular momentum projection, and spin orientation (up or down). For multi-electron systems, the way these angular momenta couple is nontrivial and depends strongly on the size of the nucleus. A common coupling scheme is LS coupling, where all the values of $\vec{l}$ and $\vec{s}$ for each electron are added to form $\vec{L}$ and $\vec{S}$, the total orbital angular momentum and total spin angular momentum operators. This distinction is immaterial for single-electron systems.

An array of perturbations to $\hat{H}_{\text{atom}}$ cause shifting and splitting of degeneracies in atoms. This thesis will not endeavor to enumerate them, but will instead group them by energy scale. The fine structure perturbations in atoms arise from a relativistic coupling between $\vec{L}$ and $\vec{S}$, and the fine-structure splitting can be parametrized by an additional term in the Hamiltonian $a\ \vec{L} \cdot \vec{S}$. The quantum numbers L and S are no longer "good," but instead the quantum number J corresponding to $\vec{J} = \vec{L} + \vec{S}$ describes the eigenstates (following the usual angular momentum addition rules). This gives rise to an atomic term symbol ${}^{2S+1}L_J$, where $L = 0, 1, 2, 3$ is written as $S, P, D, F, ...$ and $J = L + S$.

Another set of perturbations, classified under hyperfine structure, are caused by the interaction of the electron's combined spin and orbital angular momentum $\vec{J}$ with the nuclear spin $\vec{I}$. Similarly, the interaction can be written as $\vec{I} \cdot \vec{J}$, and the total angular momentum operator $\vec{F}$ is formed, with associated quantum number F. Each level given by J is split into levels with different values of F for each allowed relative orientations of J and I, as with the fine structure. A pictorial representation of the effect of perturbations on alkali atoms is shown in Fig. 2.1.

Transitions and couplings between states of different S, L, J, I, and F are determined through "selection rules" that arise from the same angular momentum algebra applied to different spherical tensor operators. For example, allowed electric dipole transitions between ground state $|\psi''\rangle$ and excited state $|\psi'\rangle$ are determined by the matrix element $-e\langle\psi''|\vec{r}|\psi'\rangle$. Similarly, the Stark and Zeeman effects for an atom can be determined by evaluating matrix elements for $-e\ \vec{r} \cdot \vec{\mathcal{E}}$ and $-\ \vec{\mu} \cdot \vec{\mathcal{B}}$, respectively. A basis is chosen for the atomic eigenstates, a Hamiltonian is constructed using matrix elements computed through spherical tensor algebra, and the Hamiltonian is then diagonalized

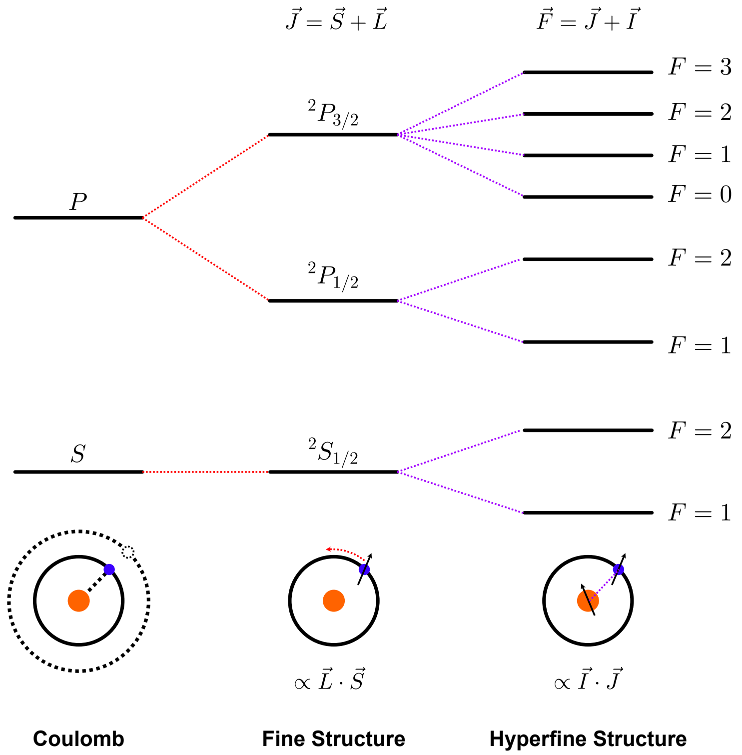

Figure 2.1: Perturbations in atoms that cause splittings. The Coulomb interaction, fine structure splitting, and hyperfine structure splitting are represented from left to right for an alkali atom with $I = 3/2$. The perturbations that cause overall energy shifts, such as the Darwin and Thomas precession terms, are not represented here.

to determine the eigenstates exactly. One subtlety here is the use of an "effective Hamiltonian" approach, whereby Hamiltonians are calculated and diagonalized for the ground and excited states separately and perturbations are modeled using effective interaction terms such as $\vec{L} \cdot \vec{S}$. In reality, atoms have many excited states and a full Hamiltonian considering all states would be cumbersome for calculation and provide limited physical insight. Moreover, the fine structure contains contributions from many different physical sources, but all of them are grouped together under the effective interaction $\vec{L} \cdot \vec{S}$. The portions of the fine structure that lead to overall energy level shifts (as opposed to splittings) are included as part of the unperturbed Hamiltonian because energy levels for many states $^{2S+1}L_J$ in atoms have been measured experimentally. The effective Hamiltonian approach is particularly powerful for the molecular setting, where there are a tremendous number of states within even a single ground state, and where often two sets of states do not even follow the same angular momentum coupling scheme.

We now consider the highly simplified setting of alkali atoms, where there is only a single valence electron. The ground state is described by the term symbol $^2S_{1/2}$. The first excited states are given by $^2P_{1/2}$ and $^2P_{3/2}$, where they are split by fine structure due to their different values of J. The fine structure splitting in the P states of $^{23}\mathrm{Na}$ and $^{39}\mathrm{K}$ are both ~ 1 THz, although this quantity scales approximately quadratically with the atomic charge. The $^2S - {}^2P$ gap is of the order $\sim 100 - 1000$ THz depending on the particular atom in question, which is typically bridged by light in the visible, near-infrared, or near-ultraviolet frequency regions. Each state is further split by hyperfine structure, where the number of states is determined by the nuclear spin I, which is a nucleus dependent quantity. Both $^{23}\mathrm{Na}$ and $^{39}\mathrm{K}$ have $I = 3/2$, which means that, for example, the $^2S_{1/2}$ ground state is split into $F'' = 1$ and $F'' = 2$ state, separated by $\sim 1 - 10$ GHz depending on the species. The alkali properties webpage of Daniel Steck is a great resource to learn more about the properties of alkali atoms [40, 41].

2.2 Molecular energy levels

Every aspect of molecules, which are bound systems of multiple atoms, is more complex than that of atoms. The simplest molecule is H_2^+, whose structure can be solved analytically after making some approximations (see App. 6.1 of [5]). Even in this simplest possible case, it is apparent that the spherical symmetry of an atom has given way to a reduced cylindrical symmetry in the diatomic molecule. The loss of spherical symmetry has tremendous consequences for molecular structure. In particular, the strong electrostatic field along the internuclear axis $\hat{n}$ connecting each atom has the effect of "pinning" angular momenta we defined in atoms, such as S, L, and J, to lie along it. The corresponding angular momenta about $\hat{n}$ are given by $\Sigma = \langle \hat{n} \cdot \vec{S} \rangle$, $\Lambda = \langle \hat{n} \cdot \vec{L} \rangle$, and $\Omega = \langle \hat{n} \cdot \vec{J} \rangle$. In analogy to atoms, we describe molecular states through molecular term symbols $^{2S+1}\Lambda_\Omega$, where $\Lambda = \Sigma, \Pi, \Delta, \ldots$.

While atoms have electronic structure, fine structure, and hyperfine structure, molecules have a much more involved hierarchy of energies (Fig. 2.2). In additional to the electronic structure from the electrostatic interaction between the atoms and surrounding electrons, there is vibrational structure due to electrostatic coupling between nuclei, and rotational structure from the (approximately) rigid rotation of the nuclei. There are also a number of perturbations—the usual fine structure spin-orbit coupling for the electronic states, anharmonic modifications to the vibrational energies, spin-rotation splitting, parity-doubling, and the hyperfine structure from both atoms. In linear triatomic molecules, the other case we will discuss here, there is also a splitting called ℓ-doubling from the coupling of bending vibration and molecular rotation.

There is one subtlety about symmetry we have elided here. The reduction from spherical symmetry to cylindrical symmetry is one that is present in the molecule-fixed axis, or in other words, in the molecule's rotating frame. The molecular Hamiltonian is also parity symmetric because the electrostatic forces involved all respect parity. The physical wavefunctions then also have definite parity, which are equal mixtures of states with $\pm\Lambda$. Unfortunately, the need to distinguish between the lab reference and the rotating molecule's reference frame arises constantly; angular momenta pinned to $\hat{n}$ are defined in the rotating frame, while total angular momenta, such as J and F are defined in the lab frame, for example. When computing matrix elements described by angular momenta in both frames, Wigner rotation matrices must be used to move from one frame to another. In fact, the situation is quite complex because angular momenta defined in the rotating frame have anomalous commutation relations compared to angular momenta in the lab frame. For more details, see Sec. 2.3 of [21] and Sec. 5.5.6 of [5].

As a brief illustration of the importance of proper accounting of reference frames, one often learns in chemistry that polar molecules, such as water, have electric dipole moments that indicate the polarity of the charge distribution. One might think that this electric dipole moment violates CP symmetry and might point to new physics. This is, of course, impossible because the underlying laws of electromagnetism do not violate CP. The solution to this apparent paradox is that the molecules electric dipole moment is being defined in its rotating frame. In the the lab frame where the molecule rotates, this electric dipole moment is averaged over states with spherical symmetry and is therefore zero in all cases.

For the rest of the chapter, we primarily consider *linear*, polar molecules in which a metal atom with s^2 valence (e.g., Ca, Sr, Yb,...) is bonded ionically to a ligand such as F or OH, because, as alluded to in Chap. 1, this structure is favorable for laser cooling. Diatomic molecules and linear triatomic molecules differ in the presence of bending vibration and associated perturbations that occur only in the latter, as well as hyperfine structure from the additional atom. Otherwise, their structure is largely identical.

2.2.1 Electronic structure

The electronic structure of molecules is complex. For the case of diatomic and linear polyatomic molecules with a metal-ligand ionic bond, ligand field theory provides an intuitive and accurate description of the electronic states. For this discussion, we ignore the vibration and rotation of the molecules.

In an ionic bond, the metal donates a number of electrons to the ligand. Ligands like F and OH tend to accept a single electron, leaving a singly ionized metal and ligand (e.g., Ca^+ and F^-, which is now closed-shell). The electrostatic field from the ionized, closed-shell ligand then perturbs the states of the metal ion, which has one valence electron remaining. The presence of an electric field will shift the energy levels of the metal due to the Stark effect. It will then split states of different Λ, forming the familiar molecular orbitals out of atomic orbitals. For example, the atomic d state will form a molecular d state split into three projections called $d\sigma$, $d\pi$, and $d\delta$. Finally, the nearby states with the same projection mix and form the molecular states described by the molecular term symbol. For example, $p\sigma$ and $d\sigma$ projections can mix to form a ${}^2\Sigma$ molecular state [42].

In CaF, CaOH, etc. the ground electronic state is ${}^2\Sigma$, and the first excited state are ${}^2\Pi_{1/2}$ and ${}^2\Pi_{3/2}$ which arise from spin-orbit coupling. The next excited state which is sometimes used in experiments is also a ${}^2\Sigma$ state. Traditionally, ground electronic states are labeled by X, and then subsequent states are labeled as $A, B, ...$ in order of increasing energy, though for some legacy cases states are labeled in the order they were discovered. For our exemplar molecules the first Π excited states are labeled with A and the next excited state is labeled by B. In polyatomic molecules, including linear ones, the labels have a tilde on them, such as $\tilde{X}$. This tilde used with linear polyatomics is inherited from notation used for general polyatomics with non-cylindrical symmetry, in order to prevent confusion with symmetry labels that denote the symmetry group representation for the state.

As with atoms, electronic states have energies at $100 - 1000$ THz, with spin-orbit splittings that are ~ 1 THz. As with atoms, this splitting can become quite large with molecules containing heavy metals. In the much heavier ^{174}YbOH molecule, for example, the $A^2\Pi$ spin-orbit splitting is ~ 40 THz [43].

2.2.2 Vibrational structure

The description of the electronic structure in the previous section assumes that the electrons are interacting in a fixed electrostatic potential created by stationary nuclei. In reality, there is an electrostatic repulsion between the nuclei, which leads to an approximately harmonic confinement of the nuclei in the molecule. The vibrating nuclei then perturb the electrostatic potential felt by the electrons.

There are two relevant approximations that allow for a sensible and practical description of vibrating (and rotating) molecules. The adiabatic approximation considers the nuclear vibrational motion as slow compared to the electron motion. This can be understood as due to the dramatic ~ 2000-fold mass difference between the electron and proton. The consequence of this approximation is that electrons are treated as adiabatically following the electrostatic potentials as they slowly change with nuclear vibration [44]. As a result, the electronic equation of motion can be solved at each value of the nuclear separation, R, giving eigenenergies for every electronic state that are smoothly connected into functions of R. Each energy $E_i(R)$, where i labels the electronic state, is called a potential energy curve, or in the case of multiple vibrations, a potential energy surface. For example, a triatomic molecule like SrOH has a multidimensional potential energy surface due to the two stretch modes and one bending mode coordinate. Bound molecular states have potential energy curves with minima, and in many cases, the curve is very close to harmonic for low-lying states sufficiently near the potential minimum. The position of this minima for a particular electronic state gives the equilibrium separation, R_{eq}, which is ultimately the molecule's equilibrium bond length in that state.

For each electronic state these harmonic potentials support a number of (approximately) harmonic oscillator wavefunctions (Fig. 2.2). These wavefunctions are the vibrational wavefunctions, labeled by the electronic state and the quantum number v, which numbers the harmonic oscillator excitation. For molecules like SrOH, with three vibrational degrees of freedom, vibrational states in a given excited state are given by $(v_1\ v_2^{|\ell|}\ v_3)$, where each v represents the different vibrations from largest to smallest energy. The middle label v_2, representing the bending mode, has a label $|\ell|$ to indicate the ℓ-doubling component, where $|\ell| = v_2, v_2 - 2, ...$; ℓ-doubling is discussed in more detail later in Sec. 2.2.3.

The second simplification is the Born-Oppenheimer approximation, which argues that the electronic and nuclear motions can be separated into product wavefunctions, because

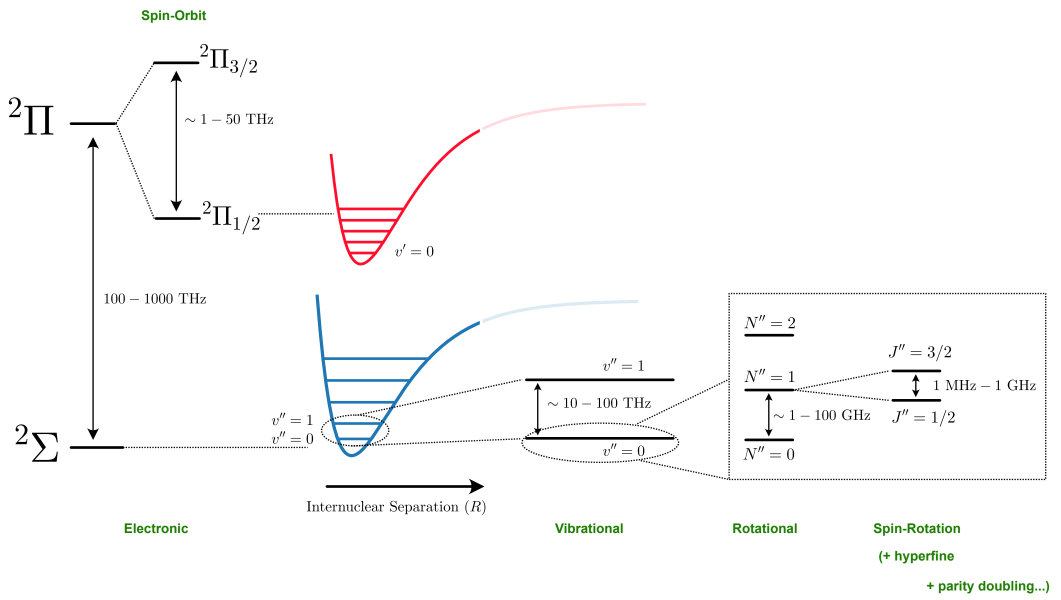

Figure 2.2: The hierarchy of energy scales and interactions for a simple diatomic molecule that obeys the adiabatic and Born-Oppenheimer approximations. The vibrational branching ratios are determined by the vibrational wavefunctions supported by the ground and excited state vibrational potentials, in blue and red, respectively. More complex molecules with less symmetry contain more interactions due to hyperfine couplings, additional rotational degrees of freedom, and bending angular momenta.

these motions occur at radically different timescales. Indeed, while electronic states are separated by $100-1000$ THz, the vibrational gaps in a single electronic manifold are $\sim 10-100$ THz, an order of magnitude smaller. The same separation of energy scales applies for rotational motion, which we now consider.

2.2.3 Rotational structure and other perturbations

For the same reasons that the rotational portion of the atomic wavefunction is simple to describe and calculate, the rotational component of the molecular wavefunction is also considerably “simpler.” This is due to the rigid structure imposed by angular momentum conservation and the algebraic formalism we use to calculate with it. In particular, the diatomic molecule wavefunctions are rigid rotor wavefunctions. This is also true for polyatomic, linear molecules, in which the rotation along $\hat{n}$ does not contribute any angular momentum. Only end-over-end rotation of the molecule, described by operator $\vec{R}$, where $R=0,1,2,...$. The rotational Hamiltonian is given by

$$\hat{H}_{\text{rot}} = B\vec{R}^2, \tag{2.2}$$

where $\vec{J}$ is the total electron angular momentum, and B is the rotational constant given by

$$B = \frac{\hbar^2}{2I}, \tag{2.3}$$

where I is the moment of inertia about $\hat{n}$. The energy scale of rotation can be easily estimated using a typical value for an equilibrium bond length and the masses of nuclei. Rotational splittings are typically $\sim 1 - 100$ GHz.

The complexity of the rotational structure enters via the plethora of different angular momentum coupling schemes that can be used to form $\vec{J}$ for a given molecule. These coupling schemes arise due to the relative strength of the various interactions that occur in molecules. Different states in molecules can have very different coupling schemes, and basis conversions must be used when working with states defined in a particular coupling scheme. A good coupling scheme is one in which the resulting Hamiltonian will be nearly diagonal, and where the remaining off-diagonal terms can be treated as small perturbations. The main two Hund's cases we consider here are case (a) and case (b).

We start with Hund's case (a), in which the electrostatic interaction is the strongest and where the spin-orbit coupling is also much stronger than the rotational energy. In this case, $\vec{L}$ is fixed to the internuclear axis, giving the quantum number Λ. Due to strong spin-orbit coupling, the spin is also fixed to the same axis, giving quantum number Σ. Then Σ and Λ are combined to form quantum number Ω corresponding to an operator $\vec{\Omega}$ that lies along the internuclear axis. We form $\vec{J} = \vec{\Omega} + \vec{R}$, and rotational states are labeled by $J = \Omega, \Omega + 1, ...$. The $A^2\Pi$ states in our exemplar molecules are well-described by case (a) basis functions $|\eta\Lambda\Sigma J\Omega IFM_F\rangle$, where η represents all other quantum numbers.

In Hund's case (b), the electrostatic interaction is the strongest, but the rotational interaction is much stronger than the spin-orbit interaction. It is straightforward to find case (b) states by default by considering Σ states, where $\Lambda = 0$, since the spin-orbit interaction is exactly zero. The ground and second excited states in our exemplar molecules are all described by case (b) basis functions $|\eta NSJIFM_F\rangle$. With no spin-orbit coupling, $\vec{S}$ is not pinned to $\hat{n}$, unlike in case (a), and S is a good quantum number. In this coupling scheme, we define the rotational quantum number to be $\vec{N} = \vec{\Lambda} + \vec{R}$. Then, $\vec{J} = \vec{N} + \vec{S}$. In this case, the rotational levels are described by $N = \Lambda, \Lambda + 1, ...$. Hund's cases are discussed in detail and shown pictorially in Sec. 6.7 of [5].

One important rotational perturbation is the spin-rotation interaction, written as a constant proportional to $\vec{N} \cdot \vec{S}$. One can intuitively think of the spin-rotation interaction as arising from the magnetic moment created by the rotating electron generating a magnetic field that interacts with the electron spin. This causes the rotational levels to be split between states where $\vec{N}$ and $\vec{S}$ are aligned and states where they are anti-aligned. The spin-rotation splitting can vary from 1 MHz $-$ 1 GHz depending on the state and moments of inertia.

There are a number of other perturbations that occur due to anharmonicities in the vibrational potentials, the coupling of rotation and vibration (especially pronounced for high J rotational states) that is ignored in the Born-Oppenheimer approximation, parity doubling, and ℓ-doubling. We briefly discuss parity doubling and ℓ-doubling here because they are relevant for EDM experiments in polar diatomic and polyatomic molecules, respectively. Parity doubling can intuitively be thought to arise from the fact that orbital angular momentum states with $\pm\Lambda$ about $\hat{n}$ must form superpositions of good parity in the lab frame. The positive and negative parity states have $\cos(\Lambda\phi)$ and $\sin(\Lambda\phi)$ amplitudes, which lead to different electron cloud density relative to the axis of rotation. This electron density difference leads to a small splitting between opposite parity states in rotating molecules (see A.4 of [45]). In this case where the Λ degeneracy is lifted, the parity doubling is called Λ-doubling.

Finally, ℓ-doubling is the source of EDM sensitive parity doublets in linear polyatomic molecules. A bending linear molecule has two degenerate bending motions, into and out of the plane, respectively. A rotating bending molecule resembles a bent molecule rotating about the prior internuclear axis, and there is an angular momentum and projection associated with this bending-rotation. For a linear, non-bending molecule, the rotation about $\hat{n}$ does not contribute energy, but this is no longer true for a bending molecule. The degeneracy between the in-plane and out-of-plane bending rotations is broken due to the usual end-over-end rotation of the molecule, and a small parity splitting develops between the states for the same intuitive geometric reason as in Λ-doubling. In the case of bending vibrations, this phenomenon is called ℓ-doubling, and it gives rise to the science states usable for EDM experiments.

2.3 Laser cooling molecules

We now briefly consider requirements for laser cooling molecules and discuss why our exemplar molecules in this chapter are in principle and in practice laser coolable. As in the case of ultracold atoms, laser cooling requires momentum transfer due to repeated scattering of photons. The ability to continuously scatter photons from an atom or molecule is called photon cycling. Photon cycling requires that population from the ground state that gets driven into an excited state decays back into the same ground state. If instead population leaks into other ground states, additional lasers are needed to "repump" population into an excited state that decays preferentially to the ground state. In atomic systems, due to their relative simplicity, only a handful of repump lasers are required, with acousto-optic modulators (AOMs) and electro-optic modulators (EOMs) used to bridge hyperfine splittings. Atomic selection rules, dictated by angular momentum algebra, ensure that population does not leak into more than a handful of loss channels.

In molecules, on the other hand, the presence of electronic, vibrational, and rotational structure greatly complicates the question of laser cooling. Electronic structure is fairly straightforward in that one can select a species where there is no intermediate state between the ground and first excited state to leak into, and there are electronic selection rules for dipole transitions, as with atoms. Vibrational closure, on the other hand, is the primary obstacle for laser cooling molecules. Population excited to a particular excited vibrational state can in principle decay to all ground vibrational levels. In the worst case scenario, one would have to deploy a large number of repump lasers, given the 10 THz-scale spacing between vibrational levels that cannot be bridged through modulation.

There are no selection rules governing vibrational decays. Instead, vibrational decay is governed through the Franck-Condon principle, which states that to first order, vibrational branching ratios are determined by overlap integral of the ground and excited vibrational wavefunctions, called a Franck-Condon factor (FCF). One can understand this principle intuitively by recognizing that the optical excitation and decay of the electron to the excited state occurs instantaneously compared to the vibrational motion. Therefore the electron's excited vibrational state is projected onto the ground state vibrational basis, an example of the sudden approximation. A molecule is said to be "diagonal" if its FCFs obey $\mathrm{FCF}(v'' = i, v' = j) = \delta_{i,j}$, or in other words, only transitions between states with the same vibrational quantum number are allowed. This can only be true exactly if the ground and excited state vibrational potentials were identical, leading to an identical, orthogonal set of basis functions. In practice, real molecules are only approximately diagonal to varying degrees, and 1% and smaller losses are possible to a limited set of other vibrational states. In this case, however, the number of repump lasers can be ~ 10, which is far more doable than 100.[1] This discussion becomes more complicated for polyatomic molecules, because the potential energy surfaces are multidimensional, but methods exist to evaluate FCFs for polyatomics as well.

The molecules composed of an metal with s^2 valence bonded to a ligand are all generally diagonal due to the fact that the metal-centered electron that is optically active does not participate in the bond, leading to an excited state potential that is very similar to the ground state potential. Ligand field theory considerations from before show that the electric field from the ligand ion mixes the $s\sigma$ and $p\sigma$ states, causing sp hybridization of the orbital, pushing the remaining valence electron away from the bonding region. This electron retains overlap with the metal nucleus, enabling simultaneously sensitivity to CP violation and laser cooling. In polyatomics, the bending vibrations add parity doublets, giving us all three of our criteria for a trapped EDM experiment. Determining a workable repumping scheme requires an often lengthy measurement process to determine vibrational branching ratios as in as in [47]. See Sec. 6.3.6 for a discussion of a method that could enable more rapid measurements of vibrational branching ratios.

We should not neglect to mention that rotational closure is also an important factor in laser cooling. Fortunately, rotational transitions are also governed by selection rules, and following the procedure in [48], where $J'' = 1 \rightarrow J' = 0$ transitions are driven largely prevents rotational leakage. Spin-rotation splittings can be bridged with standard modulation, and microwaves can be used to couple population between rotational states if needed. Because a laser cooling scheme in which the ground state has higher angular momentum than the excited state is required for rotational closure, a MOT operated using these transitions will eventually drive population to dark states. This is a general feature of so-called Type II MOTs, in which $J'' > J'$, but dark states have been remixed using resonant RF radiation to couple dark and bright states (RF MOT) or by rapidly switching the MOT laser polarizations in conjunction with the magnetic field orientation.

Here we have omitted discussion of radiative slowing, which also requires the ability to cycle photons. Deceleration is considered in greater detail in Chap. 4. The combination of laser slowing and cooling for a general molecule requires $\sim 10^4 - 10^5$ photon scatters

---

[1] There are practical limitations to the quantity of repump lasers that can be implemented in a laser cooling experiment. In particular, the laser cooling transition scattering rate is reduced as more and more ground states are coupled to the same excited state via a laser (see Eq. 2 in [46]). To see the intuition for this fact, note that the two-level system, on-resonance scattering rate is proportional to $s_0/(1+s_0)$, where s_0 is the saturation parameter. Because $s_0 \propto g_e/g_g$, where g_e and g_g are the excited and ground state degeneracy factors, the scattering rate decreases as the number of ground states increases.

before losing population to dark states. Ultimately, the ultracold molecules in a MOT can be transferred into a conservative optical dipole trap (ODT) for use in precision measurement. During the years in which this thesis was written, CaF was trapped in optical tweezers [49], CaOH was trapped in a MOT, ODT, and optical tweezers [50–52], SrOH was trapped in a MOT [35], and deceleration and 2D cooling of YbOH was demonstrated [53, 54]. Our group and our collaborators at Harvard are working together to produce and study radium-containing molecules such as RaF and RaOH, which are predicted to be both extremely diagonal and provide 10^3 fold enhancement to nuclear CP violation due to the octupole deformation in the radium nucleus.

Trapped polyatomic molecules are an important frontier for both ultracold molecule and precision measurement research. While these additional degrees of freedom generate a complexity that must be understood deeply and tamed, this complexity enables novel schemes for quantum state preparation, control, and measurement.

Chapter 3

Molecular Beam Methods for Precision Measurement

"And blood-black nothingness began to spin... A system of cells interlinked within cells interlinked within cells interlinked within one stem... And dreadfully distinct against the dark, a tall white fountain played."

Blade Runner 2049

Tabletop, precision measurement proposals present candidate atoms or molecules, describing the features of those species that make them sensitive to new physics and well suited for the measurement. There has been a tendency in recent decades to shift towards greater system complexity in order to leverage the additional quantum states for enhanced sensitivity. For example, the use of polar molecules have improved the electron EDM limit by about two orders of magnitude compared to limits set by atomic experiments [24, 26]. These molecules tend to have two or more atoms and unpaired electrons in the case of electron EDM experiments, and in general producing sufficient quantities of cold molecules is more difficult than creating atomic beams.

One method for producing cold molecules is via assembly, where trapped, ultracold atoms are photoassociated or magnetoassociated into trapped, ultracold molecules. At the end of this process, the system entropy is low, and no additional laser cooling is required in order to perform a measurement. Nonetheless, the atomic constituents must themselves be laser coolable for ultracold assembly to be applicable, and many of the resulting molecules are not amenable for electron EDM or nuclear MQM experiments.[1]

---

[1] There is a proposal for a Schiff moment measurement, which are performed in closed-shell systems, using trapped FrAg molecules produced via ultracold assembly [55].

Another common approach is to produce beams of cold molecules through chemical reactions that take place through laser ablation of solid "targets" that contain the atomic constituents of a molecule (possibly in the presence of other gaseous reagents). The reaction products could include many different atoms, molecules, and atomic/molecular ions, including the particular molecule of interest. In general, many orders of magnitude more molecules can be produced through laser ablation compared to using ultracold assembly, but they are relatively hot and have high internal entropy, populating many rotational states. Non-reactive gases at cryogenic temperatures can be used to thermalize the translational and rotational states in molecules and entrain the molecules into cold, bright beams. This approach–cryogenic buffer gas cooling–is the primary technique by which arbitrary molecules, including free radicals, can be produced at cold temperatures. Molecules produced in this way must be further cooled to "ultracold" temperatures in order to load them into magneto-optical traps. Due to the difficulties in decelerating heavy molecules (see Chapter 4), there is an advantage in producing molecular beams that are as slow (and cold) as possible from their inception. Therefore, we built a 1 K cryogenic buffer gas beam (CBGB) source, which we was used to investigate particular molecules and develop methods applicable to polar molecules generally. This cryogenic beam source was the primary site of all of the experimental work described in this thesis.

This chapter provides a summary of relevant details about our CBGB source design, construction, and performance as well as a brief overview of the most common methods performing measurements on cold atomic and molecular beams. The construction of the beam apparatus was completed over two years, and was accomplished primarily by myself, Yi Zeng, and Phelan Yu, and the reader is referred to other doctoral theses in the Hutzler Lab for details on particular aspects of this beam source, where appropriate [36, 37, 56]. Later chapters focusing on particular experimental work describe the particular modifications made to the beam source and simulations that are specific and relevant to those projects. Additionally, a Monte Carlo simulation framework for studying atomic and molecular beams is described. The simulation framework was developed over two years by the thesis author.

3.1 Cryogenic buffer gas beam sources

Cryogenic buffer gas beam sources are commonly used in molecular beam experiments because they achieve lower temperatures than effusive beams and lower beam velocities than supersonic beam sources [57]. In many cases, buffer gas sources can also generate more intense beams than supersonic sources with molecular pulses of a factor of 10 or higher duration. Experiments that seek to slow, cool, and trap molecules benefit from working with beams that are as bright, cold, and slow as possible. Here we describe the basic principle of operation of a CBGB source. Quantitative details in terms of cell parameters are available in the review of buffer gas beams by Hutzler et al. [57].

3.1.1 Principles of operation

A cryogenic buffer gas beam source relies on collisions between molecules produced in the gas phase at temperatures as high as ~ 10000 K and buffer gas atoms at cryogenic temperatures. Noble gases, such as neon or helium, are commonly used as buffer gases due to their negligible chemical reactivity.[2]. By maintaining buffer gas densities in a cryogenic cell to a range of $n = 10^{14} - 10^{17}\ \mathrm{cm}^{-3}$, a sufficient number of collisions can take place to thermalize translational and rotational degrees of freedom of the molecule before molecules diffuse out to the edge of the cell.

By adding a few-mm aperture to the cell, molecules can exit the cell. For a buffer gas flow rate in a typically intermediate Reynolds number regime, the molecules experience "hydrodynamic enhancement" and become entrained into a molecular beam. Furthermore, the angular spread of the beam is reduced in cases where the mass of the buffer gas atom is less than the mass of the molecule, increasing the brightness along the beam axis [57]. Because the buffer gas is itself inert, this method can be used to produce cold beams of both non-reactive molecules as well as free radicals that are commonly used for EDM experiments, with typically $10^{10} - 10^{13}$ molecules produced per ablation shot, depending on the species, ablation target, and reaction kinetics.

The two most important timescales that must be understood for creating a buffer gas beam source are the diffusion time τ_{diff}, the time required for a molecule to diffuse out to the cell walls, and the pumpout time τ_{pump}, the time molecules spend in the cell before being extracted through the aperture. Both of these times tend to be between 1-10 ms. A ratio of these two timescales can be defined as

$$\gamma_{\mathrm{cell}} \equiv \frac{\tau_{\mathrm{diff}}}{\tau_{\mathrm{pump}}}, \tag{3.1}$$

---

[2] At vacuum pressures, helium does not freeze at any temperature, allowing helium buffer gases to be operated at lower temperatures (typically 4 K or lower) compared to neon. Neon buffer gases do not contribute extra pressure in molecular beam experiments because neon is efficiently cryopumped by 10 K cryogenic surfaces. Helium can also form liquid thin films at low temperatures, which can complicate ablation dynamics. Optimal choice of a buffer gas is therefore system dependent.

in order to parameterize the cell extraction. In the "hydrodynamic enhancement" regime, where $\gamma_{\text{cell}} \gtrsim 1$, molecules exit the cell into the beam efficiently prior to diffusing and sticking to the cell walls. The actual relationship between the extraction efficiency and buffer gas flow rate depends strongly on the cell geometry and method for introducing the particular species, but efficiencies for typical molecules are $\sim 10\%$, with $> 40\%$ efficiencies observed in some species [57]. For CBGB operation, thermalization with buffer gas atoms should proceed at timescales shorter than both τ_{diff} and τ_{pump}. Buffer gas sources usually operate in the effusive or intermediate Reynolds number regime, with particular cell and aperture designs to create slower beams, greater extraction efficiency, etc. [58, 59].

For the goal of slowing, cooling, and trapping molecules, the beam forward velocity is a critical parameter. In the intermediate flow regime, the beam velocity is determined by collisions with buffer gas atoms near the cell aperture, where these collisions lead to boosting of the molecule forward velocity relative to their thermal velocity. The forward velocity increases from the effusive velocity limit linearly with Reynolds number, then increases sub-linearly until it asymptotes to the velocity for molecules in the supersonic limit [57].

As discussed in detail in Chapter 4, laser cooling and trapping molecules requires efficient deceleration. To further reduce the beam forward velocity, a slowing cell can be employed. A slowing cell is an additional square cross-sectional region attached to the first cell. The first cell is constructed with the typical geometries described above to achieve large extraction efficiency. The second cell contains several vents (with e.g., copper meshes) for buffer gas to escape so as to reduce the buffer gas density. The lower density reduces the number of collisions between molecules and buffer gas that occur in the second-stage, and these collisions reduce the forward velocity of the molecules without heating them. Thus, a slowing stage allows for generating a cold, effusive beam that leverages the high extraction of the first stage. However, the second stage reduces the extraction by a factor of $10 - 100$, which must be taken into account in determining the overall enhancement in slower velocity classes from using a slowing cell.

3.1.2 Building a 1K cryogenic buffer gas beam source

The cryogenic beam source consists of two basic subsystems: (1) a vacuum chamber containing a cryocooler, thermal radiation shields, buffer gas lines, and cryogenic cell where molecules are produced, and (2) a room temperature beamline where the molecular beam can be manipulated and measured. When the work in this thesis began, closed-cycle 1K pulse tube cryocoolers had recently become commercially available. The technology we employed was new and the vacuum system was littered with critical engineering flaws. Rectifying these issues, along with personnel limitations and supply chain disruptions caused by the Covid-19 pandemic, greatly delayed the construction and operation of this cryocooler. The modifications that were made to the cryogenic system were devised by our collaborators, Louis Baum, Ben Augenbraun, Zack Lasner, and John Doyle, and several of these designs were further adapted for our system by Phelan Yu (Appendix C of [60]). These modifications are briefly described in this thesis where appropriate.

Cryogenic vacuum chamber

Cryogenic temperatures are achieved using a Cryomech PT415 pulse tube refrigerator with a 1K liquid helium pot, housed in a Precision Cryogenic Systems, Inc. aluminum vacuum chamber. The PT415 cryocooler, pictured in Fig. 3.1(a) has three cold heads. The first two are held at just below 50 K and 4 K, respectively, through the operation of the pulse tube. The third cold head is cooled to 1.4 K through evaporation of liquid helium, and adiabatic expansion of the gas through a Joule-Thompson valve. The helium then reliquefies into a pot anchored to the cold head. A copper thermal switch connecting the 1K and 4K cold heads (Fig. 3.1(b)) can be deployed for initial cooldown of the 1K cold head to 4 K, promoting helium condensation in the pot. The thermal switch provided with the system did not supply reliable thermal contact and in practice had to be toggled repeatedly to ensure good performance, but the switch was not ultimately necessary to achieve 1K operation.

The majority of modifications made to our system revolved around issues with the manufacturer's initial engineering of this closed-cycle helium loop used to reach 1.4 K. One class of issues revolve around contamination and obstruction of the helium loop, which obstructs liquid helium condensation and evaporation and prevents 1 K operation. The adsorber installed as part of this loop contained a dirty, cotton-like material that led to frequent contamination of the line. Moreover, the supplied scroll pump that creates a pressure differential across the loop contains a elastic tip seal that slowly releases molecules that can also freeze in this line. In order to ensure contamination-free operation, this adsorber was bypassed and sent through a liquid nitrogen cold trap from Oxford Instruments (H6-103 cold trap) attached via a custom adapter plate (H9-HND0057) to a 38 L dewar (IC-38RX-CTI 38 li), with 0.5 μm inline VCR filters. This

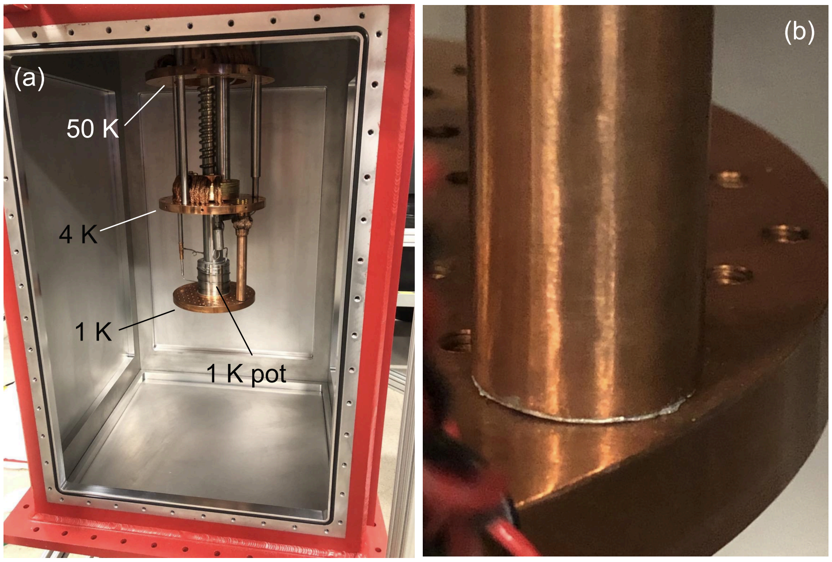

Figure 3.1: The Cryomech PT415 cryocooler. (a) The cryocooler mounted inside an aluminum vacuum chamber with the 50K, 4K, and 1K cold heads labeled. (b) A closeup of the thermal switch connection between the 4K and 1K stages. In practice, this switch needed to be toggled repeatedly before adequate thermal contact between the 4K and 1K stages was established, though the switch is ultimately not needed for 1K operation when other heat loads are mitigated.

system, shown in Fig. 3.2(b) was designed and assembled by Phelan Yu. The addition of the cold trap means that the 1K recirculation system is no longer truly closed-loop, but the large dewar volume allows operation for 7 to even 21 days before needing to refill with nitrogen, which is both manageable and convenient. A large volume of nitrogen is depleted on initial cool-down of the cold trap, and therefore periodically filling it with a single small dewar every 2-3 days allows for largely interruption-free operation. The adsorbers in the cold trap can become full over an approximate period of six months to two years, depending on how continuously the cryostat is in operation. The cold trap would then need to be baked out at 100°C. Over the course of this thesis work, the cold trap was baked out no more than twice.

Another major issue with the cryostat as we received it was the lack of internal volume in the 1K loop for helium that evaporates out of the pot. In particular, as the system cools down, the amount of liquid helium that accumulates in the pot is minimal, and much of the helium stays in the system in gaseous form until liquefaction begins. The 5 psig blowoff valves included in the system easily overpressure given the amount of helium that has to be loaded into the pot for cooldown and the minimal volume in the line. There were six blowoffs like these present, and each of them had a 30%

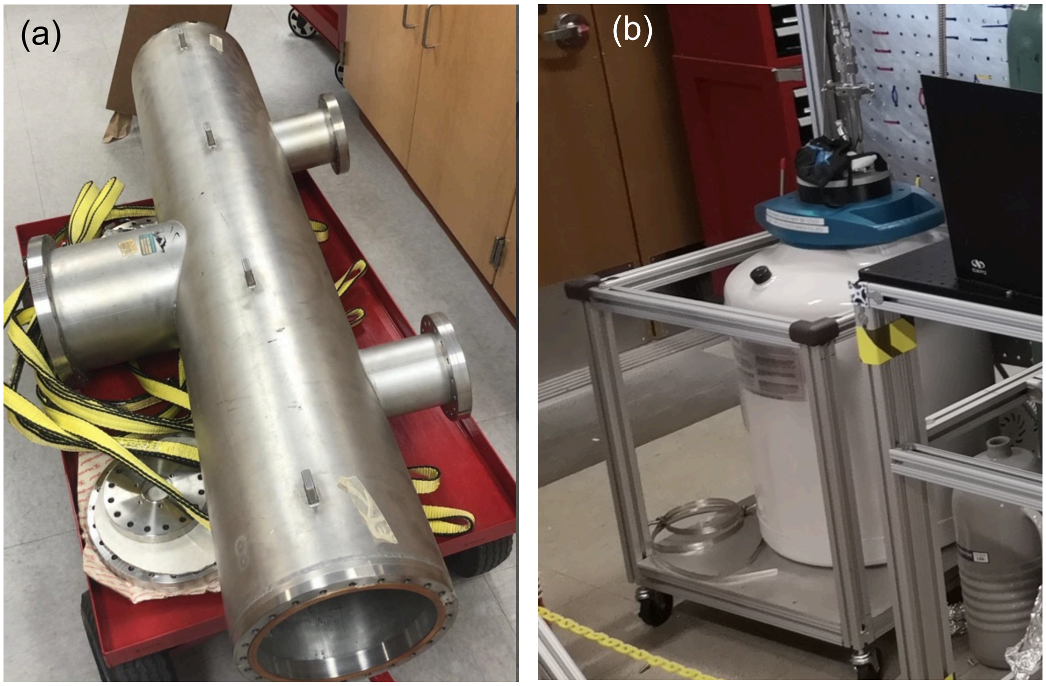

Figure 3.2: Volumes added to the 1K line of the cryogenic system. (a) An old CF vacuum chamber used as a dump volume for gaseous helium in the 1K line. (b) A liquid nitrogen cold trap used to prevent contamination and clogging of the 1K line.

probability of resealing, which meant that there was a large likelihood of contaminants being introduced and frozen inside the 1K loop through at least one of the blowoffs that failed to seal. Therefore, the blowoffs were replaced with more reliable and replaceable Swagelok SS-4C-5 5 psig valves.

This replacement does not address the fundamental overpressuring issue, so we additionally installed a large "dump" volume vacuum chamber in the 1K loop that would ensure that the system pressure never exceeds 1 atm at any point during helium loading and 1K pot operation (Fig. 3.2(a)). Given the volume of the pot, we can use a mass-flow controller (Alicat MCR-100SLPM-D-20X63-.25VCRM/5M) and pressure gauges to send in the required number of Helium atoms to fill approximately half the pot with liquid helium, with assurance that this amount of atoms would not ovepressure the system. Another minor concern was leaky flexible aeroquip hoses included in the reliquefier system, so these were replaced with flexible KF hoses that were checked for leaks. The combination of new blowoffs, replacement of leaky components, addition of a dump volume, and liquid nitrogen cold trapping ensured reliable, stable, and continuous 1K operation for several months at a time. Additionally, upon warming up, the system valves can be configured to use the 1K pot itself as a cold trap for helium that is pumped back into the dump volume, ensuring that the helium loaded from the volume is clean. After a loading and boil-off cycle, more than 80% of the helium is recycled for the next run.

The remainder of the cryogenic apparatus was designed by Yi Zeng and closely follows the 4 K cryostat design in Nick Pilgram's thesis (Chap. 3 of [37]), with changes to accommodate our much larger vacuum chamber and an additional 1K cold head. Radiation shields are connected to the 50K and 4K cold heads, respectively, through flexible copper 101 braids. The 50 K shields are made of polished aluminum and hang from the top of the vacuum chamber from threaded rods. The 4K shields are made of polished copper 101 and hang from the 50K shield with threaded rods. Each of these radiation shields has uncoated NBK7 windows for optical access. Titanium helicoils in combination with brass screws and stainless steel Belleville washers are used throughout the entire system to ensure reliability of fasteners under thermal expansion or contraction. There are no 1K radiation shields because the blackbody heat load from 4K surfaces onto 1K surfaces is negligible. Each of the four side plates and the bottom plate for the radiation shields are covered by 16-layers of aluminized mylar superinsulation. The superinsulation layers are packed into a "curtain" with cutouts for windows and grommet fasteners to facilitate removal and fastening onto radiation shields. Because a significant amount of the cooling power of the 4K cold head is spent cooling helium in the 1K loop, these curtains are essential to managing the heat loads, especially when flowing buffer gas and performing laser ablation.

The vacuum chamber was initially pumped down to $\sim 500\ \mathrm{mTorr}$ pressures with an Agilent IDP-10 dry scroll pump. The scroll pump then backs a Agilent TwisTorr 304 FS turbomolecular ("turbo") pump, connected to the vacuum chamber, which brings the source pressure down to $< 10\ \mathrm{mTorr}$ as read by a convectron gauge at room temperature. Over five years of operating with scroll pumps, the need for frequent, time-consuming tip-seal changes and the contamination of source from tip seal fragments pushed us to switch to dry roots pumps (Leybold ECODRY 35 Plus) in second half of 2024, when the work described in Chapter 6 was done. For temperature monitoring, a set of Lakeshore diode (DT-670) and Rox temperature sensors (ROX-102A) are fastened to cold heads, radiation shields, and the buffer gas cell, and a trio of cartridge heaters are also placed on the 50K, 4K, and 1K cold heads to allow for rapid warm-up of the system.

Helium at 1K is used as the buffer gas in this apparatus. Because helium collisions outside the buffer gas cell can collide with the molecular beam and degrade its brightness,

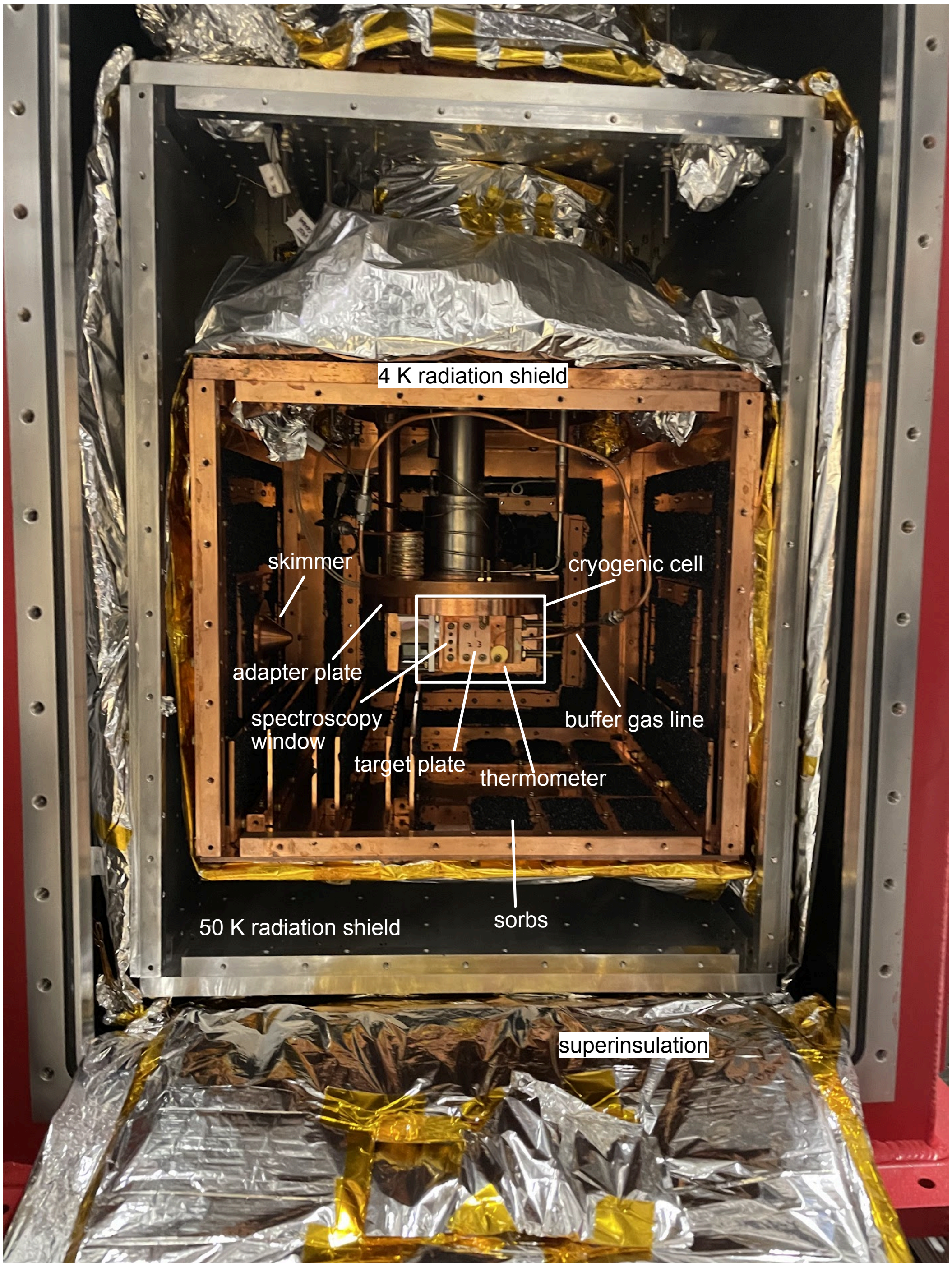

Figure 3.3: Inside of the cryogenic vacuum chamber. The cryogenic cell is mounted to the 1K cold head via an adapter plate. The image shows the side of the chamber behind the target plate.

helium pressures outside the cell must be minimized. Unlike neon, helium does not freeze to 4K surfaces, and therefore "cryo-pumping" is employed to mitigate helium pressure buildup [61]. Towards this end, large portions of the inside of the 4K radiation shields are covered with activated coconut charcoal adsorbers ("sorbs"), epoxied with Stycast 2850 FT Black with catalyst 24 LV, and a number of additional vertical "fin" sorb plates fastened to the bottom of the radiation shield. Activated coconut charcoal has been demonstrated to adsorb helium at cryogenic temperatures with nearly unit probability upon collision. Depending on flow rates, the sorbs can become full after several days of continuous operation. Therefore, we regenerate the sorbs at the end of each day of datataking by running current the heaters until the source temperatures increase above ~ 35 K [61].

Charcoal sorbs can be contaminated with water if the vacuum chamber is erroneously vented below the dew point of water, which occurred once in our system. The result of this was elevated source pressures ($6 - 10$ mTorr on a convectron gauge fastened to the top of the vacuum chamber) and reduced helium cryopumping capacity. To rectify this problem, the sorbs were removed from the chamber and baked out at 70°C overnight in a vacuum oven pumped on by a scroll pump. Upon re-installation, the source pressures dropped to 2.1 mTorr, which seemed to indicate the success of this procedure.

Helium buffer gas is introduced into the cryogenic cell via a gas cylinder connected to an Alicat MC-20SCCM-D-.25VCRM-PCA10/5M mass flow controller that is attached to an $1/8$ in stainless steel VCR line (outside the vacuum chamber).[3] The in-vacuum portion of this line is an $1/8$ in copper tube that is braised to three heat exchangers attached to the 50K, 4K, and 1K stages, respectively, which successively cool the helium buffer gas introduced into the system. Ultimately the 1K portion of the helium fill line is attached to the cell via a braised VCR fitting. [4]

Due to both corrosion on the threaded holes on 1K cold head and the $21°$ angle of the hole pattern relative to the beam propagation direction, Yi Zeng built an adapter plate to attach and align the buffer gas cell [56]. The buffer gas cell is a 2 in cube made of copper 101. The cell body has a 1.5 in diameter bore, and at one end of this bore is helium buffer gas line. The other end of the cell bore has an $1/8$ in thick

---

[3] For convenience, the same helium cylinder is used to load the 1K pot and the buffer gas and helium recirculation lines are separated via VCR tees and valves.

[4] There is a second fill line outside of the vacuum system that can be used to introduce methanol reagent into the cell through a heated fill line, but the heated fill line, built by Yi Zeng, has not been installed in the system (Chap. 3 of [56]).

aperture plate with 7 mm diameter bore for molecules to exit. Transverse to the cell bore axis is a 1/8 in thick copper target plate, to which various ablation targets can be attached. The opening directly across from the target plate contains a snorkel plate and window. There are also a pair of windows and an optical path parallel to the snorkel plate and target plate, near the cell aperture plate to allow for an in-cell absorption probe. These optical surfaces tend to become coated with ablation detritus over time, requiring the periodic replacement of cell windows. Empirical evidence from Caltech and Harvard suggest that cell leaks can be problematic if sufficiently large, even when the cell aperture is itself a "large leak." To reduce helium leakage and promote molecule thermalization, every cell installed in the 1K source is sealed using indium wire.

Room temperature beam extension

Molecules that exit the buffer gas cell travel ~ 7 in in before reaching a conical skimmer attached to the 4K radiation shields with a 0.25 in diameter collimating hole. The skimmer prevents background gas particles from colliding with the molecular beam output, and it additionally collimates the beam, reducing the transverse velocity spread. There is also a second collimator in the 50K shield. After traveling a total of ~ 10.75 in to the edge of the vacuum chamber, there is a KF-50 flange leading to the room temperature beam extension, where molecular beam measurements take place (Fig. 3.4). A KF-50 gate valve separates the cryogenic vacuum chamber from the room temperature beam extension.

The beam extension region is pumped out by an independent combination of Agilent TwisTorr 74 FS turbo pump backed by a scroll pump. The scroll pump forelines for the beam extension and cryogenic chamber are connected via a valve, but this valve is typically left closed in order to keep these systems isolated. For much of this thesis, the beam extension turbo pump was backed by an Edwards nXDS15i scroll pump, but this pump does not have a inlet isolation valve in case of power loss. Therefore, this pump was eventually replaced with a Agilent IDP-10 scroll pump, which does not have this issue. When measurements are performed on the beamline, the gate valve is opened and the two subsystems are connected. Exposed to the cryogenic source, the beam extension pressure as read by a Granville-Philips 392 Micro-Ion Plus gauge falls to $\sim 10^{-7}$ mTorr levels. Components of the beam extension are cleaned extensively and baked-out in a vacuum oven to the extent possible prior to installation to prevent outgassing from the beam extension from freezing to the inside of the cryogenic system.

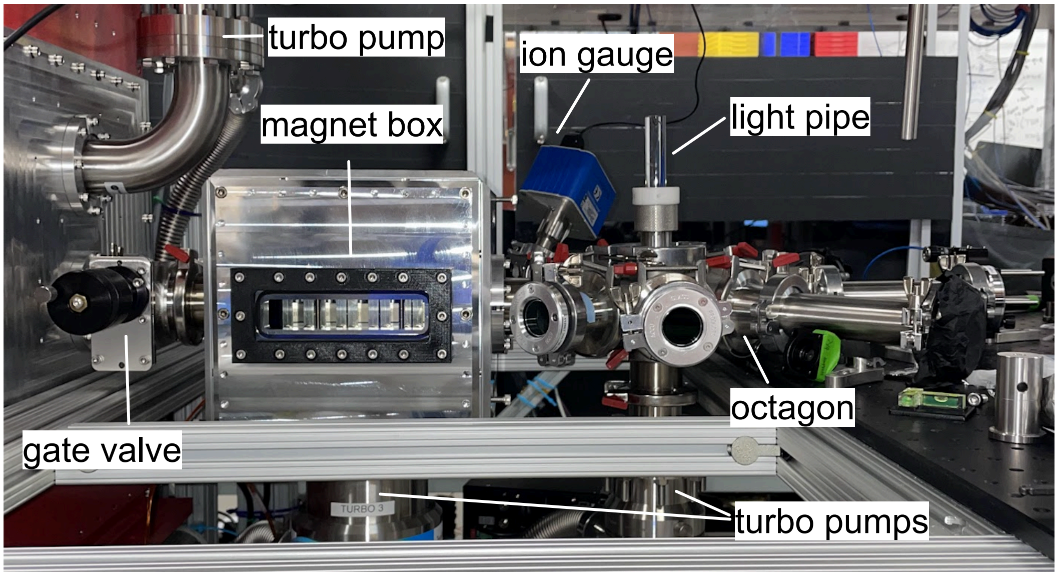

Figure 3.4: Room temperature beam extension for molecule measurements. The magnet box shown is used for some work described in Chapter 5. The gate valve and octagonal vacuum chamber are a permanent portion of the beam extension.

The primary component of the beam extension present in the various iterations described in this thesis is an octagonal, custom KF-50 vacuum chamber from ANCORP. There are eight available ports in the plane of the molecular beam, with an additional pair of ports directly above and below the center of the chamber. The bottom port is mounted to the scroll pump, while the top port contains light collection optics for fluorescence measurements. The fluorescence collection port is most commonly used for mounting a light pipe that leads to a photomultiplier tube (PMT), with a series of colored-glass and interference filters present in the intermediate region. A 2 in lens tube and blackened foil surrounds the atmosphere-side light collection optics to prevent noise from stray room lights. One of the ports in the molecular beam plane is attached to the gate valve and an additional port is used to mount the micro-ion gauge. This leaves six ports for mounting windows for optical access and other components. The two ports transverse to the the beam propagation axis are practically always used to mount (coated) windows for transverse fluorescence measurements, and in many cases an additional pair of windows at a 45° angle to the beam are used for velocity measurements. The beam extension region has been modified to suit each measurement described in this thesis, and the specific modifications are detailed in the corresponding chapters.

Atom and molecule production

Molecules are produced via laser ablation of targets on the target plate with 15-50 mJ, 6 ns pulses generated from a 532 nm, Q-switched Nd:YAG laser (Quantel/Big Sky from Anderson Lasers, Inc.). The molecules are initially produced in a hot plasma, where chemical reactions take place, and they rapidly thermalize with cryogenic helium atoms. Collisions with these atoms cools the translational and rotational degrees of freedom for molecules (but not the vibrational modes). The laser ablation and helium gas flow introduce additional heat loads to the cell at 1K, and the YAG repetition rate, pulse energy, and gas flow rate must be monitored. A typical figure of merit for selecting these parameters is the size of the molecule fluorescence signal in the beam extension. Note that while increasing the helium flow rate can improve thermalization, the beamline pressure can also increase, degrading the downstream molecule signals. Improved cryo-pumping and higher capacity vacuum pumps reduce the impact of increased buffer gas flow on the beam brightness, though the beam forward velocity will still increase.

For the experiments described in this thesis, all ablation targets have been solid targets containing all of the constituents of the molecule. In general, powders are mixed together in some proportion (usually in a stoichiometric ratio, but not always), and then 4%-by-mass polyethylene glycol (PEG) binder is added. In general, powders are crushed in a mortar and pestle, or in more recent years, a ball mill, prior to filtering them through a 200-mesh sieve. Only after ensuring sufficiently small grain size are powders mixed together. The mixture is then pressed at 10 MPa for 15 minutes in a hydraulic press using an 8 mm die. The resulting pellet is epoxied to a target plate attached to the cryogenic cell. It has been empirically observed that targets with greater density produce molecules more consistently from shot to shot, and therefore it has become a standard practice in our group to add 200-mesh Yb metal powder, generally in equal proportion by mass to one of the other powders in the mixture. This Yb "doping" both increases the density of the resulting target while also darkening the end result, possibly increasing absorption of 532 nm light. The presence of Yb atoms in ablation also provides a convenient diagnostic of cell and beamline properties for troubleshooting. So far, we have not observed an obvious disadvantage to including Yb in the standard pressed powder target recipes.

Pressed powder ablation targets suffer from greater variability in production compared to molecules produced via heated fill lines with flowing reagent. One may ablate a location on the target between 10 and 100 times before signals degrade and the location must be moved. Yb-doping improves the production stability in a noticeable way, but nonetheless the ablation spot must be moved periodically. Electronic mirrors can be used to raster the ablation spot automatically, but this has not been set up on the experiments described in this thesis. Instead, the ablation spot is manually adjusted when necessary.

Optically exciting reagents to excited states has been shown to increase the yield of molecules produced by adding energy to the system to overcome the reaction barrier. For example, exciting Yb to the $^3P_1$ state increases the amount of YbOH produced through ablation, with even greater yields observed when used with OH-containing reagents introduced via heated fill line [62]. This process is commonly referred to as "optical enhancement" of the in-cell chemistry. This approach also allows enhancement of particular isotopologues through selective excitation of transitions in a particular isotope. For example, optical enhancement was used in our apparatus to map out the rotational cycling transitions in $^{173}\mathrm{YbOH}$, a molecule with complex hyperfine structure [63]. This rotational cycling result was the first published molecular data generated from our apparatus. The work described in this thesis did not make use of optical enhancement due to laser availability constraints.

The searchable parameter space for optimizing molecule production is large. One can vary the ablation energy, wavelength, and repetition rate. One can also experiment with multiple ablation pulses with a fixed time delay. One can exploit liquid helium thin films that develop inside the cell to improve molecule thermalization, as well as introduce different gaseous reagent molecules. Another approach seeks to increase target density as much as possible, and ablation targets can be "sintered" at high temperatures to form dense ceramics. Because OH-containing targets tend to release water at temperatures much lower than those typically used in sintering, "cold" sintering techniques have been developed to increase the density of typical YbOH targets, as detailed in Arian Jadbabaie's thesis (Sec. 3.2.3.2 of [36]). Many of these ideas to improve production are currently being explored in the Hutzler Lab. In the case of radioactive molecules, such as RaOH, optimizing production is essential, but for the simpler, non-radioactive species in this thesis, the general observation has been that all ablation targets and schemes perform equally well within an order of magnitude. Therefore, any further discussion of attempts to optimize production are not discussed here.

3.2 Laser systems and data acquisition

Here, we briefly overview some of the common laser systems used in experiments as well as a description of the data acquisition system, developed by Yi Zeng and Arian Jadbabaie (Appendix A of [56]). Specific lasers will be discussed in the relevant chapters where particular experiments are described.

External cavity diode lasers (ECDLs) are prevalent in AMO physics experiments due to their simplicity and cost. Our lab has several ECDLs manufactured by MogLabs, as well as several Littrow-configuration lasers assembled in the lab using commercially available holographic diffraction following the Kang-Kuen Ni design, modified by Yi Zeng (Sec. A.3 of [56]). In particular, we built a 405 nm ECDL was used to study ^{39}K via a metastable excited state (see Chapter **5**). Madison Howard additionally built a 688 nm ECDL for monitoring production of SrOH (see Chapter 6). These ECDLs are typically simple to operate at single frequencies, but are limited in output power and tunability, and in practice suffer from mode-hopping which must be managed by a human. These lasers are locked to a reading on a HighFinesse WS7-30 wavemeter through PID feedback on the piezoelectric transducer (PZT) that are fastened on the diffraction grating mount.

ECDLs are commonly used as seeds for other complex laser systems. The aforementioned work in ^{39}K was primarily accomplished using a pair of 770 nm Toptica TA Pro lasers, borrowed from Harvard university collaborators, which are ECDL seeds amplified via a tapered amplifier chip. Additionally, a number of the MogLabs IR ECDLs are frequency-doubled in NKT waveguide doubling cavities and using MPB Raman Fiber Amplifiers (RFA) to generate intense laser light. A 595 nm RFA was briefly tested for suitability for optical pumping into the fundamental bending vibration of SrOH (see Chapter 6 for details). Both doubling cavity and RFA systems are locked to the same wavemeter, with feedback applied to the ECDL PZT.

Solid-state pumped ring cavity systems were also used extensively in this thesis. In particular, the Coherent MBR-110 Ti:Sapph laser with short-wavelength optics and the Coherent 699 dye laser both are pumped by 532 nm light from a solid state Coherent Verdi (V10 for the MBR and V5 for the dye laser). In the former, a Ti:Sapph crystal is pumped and in the latter, a jet of fluorescent, organic dye dissolved in an organic solvent like methanol. Both these systems are capable of outputting several hundred mW of power with sub-MHz linewidth over a large wavelength range. Both systems include an internal etalon for stabilization and linewidth narrowing. Ultimately, the laser frequency is locked externally to a wavemeter. The MBR was used to probe ^{39}K (see Chapter 5) and the dye laser was used to study SrOH (see Chapter 6).

A Ti:Sapph laser can be used in combination with an intense fiber laser in a sum-frequency generation (SFG) system to produce light in the visible range with high output power. The Sirah MixTrain, consisting of a Sirah Mattise Ti:Sapph, pumped by a Millennia solid state laser, and NKT ADJUSTIK+BOOSTIK fiber laser, is a workhorse laser used commonly with YbOH. During the work discussed in this thesis, the MixTrain was used to generate the 589 nm light used to study ^{23}Na (see Chapter 5). The MixTrain has an internal mechanism for frequency stabilization and can also be stabilized in conjunction with an external wavemeter.

The final laser system used extensively in this thesis is an NKT pulsed, supercontinuum laser that generates light over the visible and NIR at high power. This laser, described in detail in Chapter 5, is an essential part of an integrated spectrometer design for rapid spectroscopic characterization of molecules. By imaging the supercontinuum light on a high-resolution spectrometer, the absorption spectrum of an entire band in a molecule can be mapped out in a single-shot. Because what is ultimately measured is absorption of the broadband laser output, stabilization to a single-frequency is irrelevant.

The data acquisition (DAQ) system uses National Instruments (NI) LabView software, in conjunction with NI hardware (PXIe-1073 chassis and multifunction PXIe-6361 card) for executing experimental control sequences and recording analog signals from devices such as PMTs and photodiodes. An additional NI PXIe-6738 card is used to send analog output signals to various lasers to provide the feedback for frequency stabilization. TTL pulses produced by an arbitrary function generator provides the master timing for the entire system. At a high level, the DAQ uses command files—arrays of 1s and 0s to send triggers to various pieces of hardware (laser shutters, pre-amps, etc.)—as well as recording signals at regular intervals. A particular command sequence can be repeated a number of times before moving onto the the next command sequence, and an entire cycles of command sequences can be repeated a number of times before scanning a laser frequency by one step. The wavemeter is connected to an eight-channel Leoni eol 1x8 8-channel fiber switch, allowing eight laser frequencies to be read out using a LabView program. The same program can apply PID feedback to stabilize the corresponding lasers. Other experimental equipment, such as the YAG ablation laser, are controlled through independent LabView programs.

Time stamps and data from run of the experiment are saved as a .txt file with metadata written to the first several lines of the file. The data is then read out and analyzed through

Jupyter Notebooks and scripts developed by members of the Hutzler Lab for their personal work. The metadata includes essential information such as the experimental configuration (e.g., of the shutters) and both the laser setpoint and measured frequency.

3.3 Measurements on atomic and molecular beams

The most common measurements on molecular beams in our beam sources are DC absorption and in-beam fluorescence. There are a number of other detection methods that are also used in particular instances that are described in Chapter 6, but these generally fall under the category of absorption and fluorescence. Both types of measurements offer advantages for determining particular properties of the molecular beam.

3.3.1 Absorption measurements

For absorption measurements, laser light of a particular frequency is sent through a molecular cloud and the resonant attenuation of the laser intensity is measured on a photodetector using filters to reject light from the ablation laser. This approach involves observing a signal against a nonzero background. We briefly turn to a microscopic model of the absorption process. The gas of absorbing molecules is assumed to have uniform density n_g. A laser of angular frequency ω propagates along the x-axis and its intensity is attenuated by the gas of molecules. Then the change in intensity as the laser propagates through the absorbers is given

$$dI = -n_g \sigma_{ge}(\omega) I(x) \mathrm{d}x, \tag{3.2}$$

where $\sigma_{ge}(\omega)$ is the molecule-light absorption cross section. This quantity is determined by the transition dipole moment, linewidth, and frequency, and branching ratio with additional factors due to state degeneracies and laser polarization. The Beer-Lambert law describes the attenuation due to propagation of a laser over distance L through the molecular gas

$$I(L) = I_0 e^{-n_g \sigma_{ge} L} \equiv I_0 e^{-OD}, \tag{3.3}$$

where

$$OD \equiv -n_g \sigma_{ge} L. \tag{3.4}$$

Importantly, OD is directly proportional to the number density. Solving for the optical depth, we find that

$$OD = \ln\left(\frac{I_0}{I}\right). \tag{3.5}$$

In the limit of small absorption, and $I_0 = I + \delta I$, for small δI, then we have that

$$OD = \ln\left(1 - \frac{-\delta I}{I}\right) \approx \frac{\delta I}{I} \tag{3.6}$$

$$= \frac{I_0 - I}{I}. \tag{3.7}$$

For larger absorptions, the approximation for the OD is no longer valid and the logarithm must be computed in order to preserve proportionality to the molecule number density. When the sample is either a very strong absorber or sufficiently dense so as to completely absorb the probe light, the absorber is described as "optically thick." Practically, this is observed when the probe signal on a detector is reduced to zero, and in this case, the absorption cannot be used to extract the optical depth and molecule number density. Note that photodetector voltage signals can be used to compute the optical depth because they are proportional to the laser intensity.

Practically, absorption of laser light sent through the spectroscopy window of the buffer gas cell is used to confirm and quantify production of a given species in a particular state, as well as confirm sufficient thermalization of the molecules with the buffer gas. A poorly thermalized molecular pulse will appear as a very narrow signal in absorption, whereas typical absorption signals for well-thermalized molecules are observed for 1-2 ms or more. The density of molecules is maximized in the buffer gas cell, and for typical ablation sources the absorption on E1-allowed transitions is observable, and laser light can be multipassed using intensity-buildup cavities to increase the signal size [64]. Absorption features in the buffer gas cell are Doppler-broadened, which makes single-frequency DC absorption non-ideal for measuring molecular spectra. Chapter 6 details our work using broadband light sources to measure entire molecular spectra simultaneously with DC absorption and a sensitive, high-resolution spectrometer. Absorption of light in front of the buffer gas cell is also performed to provide information about the extraction of the buffer gas cell. Commonly, in-cell or front-of-cell absorption measurements are used to normalize other signals downstream, such as molecule fluorescence, against fluctuations in production due to their proportionality to molecule number in certain cases. Example absorption signals for an atom and a molecule are shown in Fig.3.5.

In our data analysis routines for real signals, photodetector voltage signals are pre-processed before computing the optical depth. First, the zero-signal photodiode offset is subtracted from the raw signal. Then this new signal is smoothed with a cubic Savitzky-Golay filter. The region of the smoothed signal where there is no absorption is fit to a degree-2 polynomial, and the quadratic and linear terms are subtracted off to

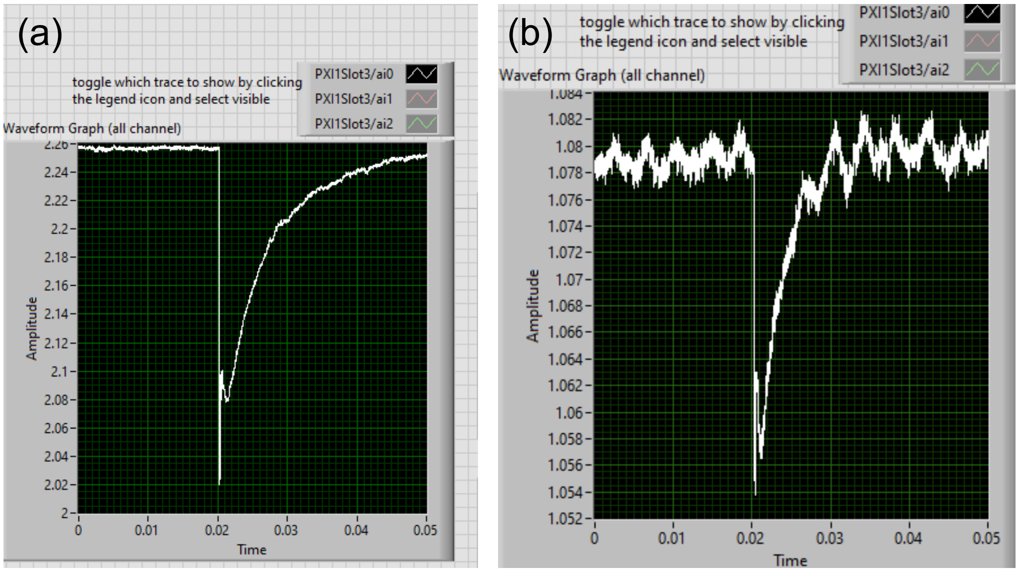

Figure 3.5: Example atomic and molecular in-cell absorption signals as measured on an amplified photodiode. (a) Absorption of $24720.1538\ \mathrm{cm}^{-1}$ light through ^{39}K atoms at 1.4 K. (b) Absorption of $14542.8775\ \mathrm{cm}^{-1}$ light through SrOH molecules at 5.1 K.

give the corrected signal $V(t)$. The constant term is used to determine the background level V_0. Then, the optical depth is determined by

$$OD(t) = \ln\left(\frac{V_0}{V(t)}\right). \tag{3.8}$$

Note that the voltages are directly proportional to the light intensity when the photodiode is in a linear regime. Then, the integrated optical depth is computed through $\Sigma_t\ dt\ OD(t)$ for the experimental time step dt (typically $dt = 10\ \mu$s). This quantity is what is ultimately used to normalize other molecular beam measurements further downstream from the buffer gas cell.

3.3.2 Fluorescence measurements

Typically, molecular fluorescence is collected for spectroscopy and state-selective readout necessary for EDM measurements. In this approach, a laser resonant with a transition in the molecule is used to drive population to an excited state and the photons emitted in spontaneous emission are all collected on a PMT or camera via a light collection system. In our source, these measurements occur in the beam extension region at room temperature. With perfect spatial filtering (e.g., using light blocking panels, apertures, and black-painted vacuum components), the detector only collects photons when the laser is resonant with a particular transition, which distinguishes fluorescence-based measurements as zero-background, aside from noise introduced by the detector itself.

In practice, backgrounds from scattered laser light leak into the detector and contribute to noise. To mitigate scattered light in molecules, we can leverage fluorescence decay to a different vibrational ground state from the initial state in conjunction with bandpass filters to separate the signal photons from the background photons. This approach is referred to as "off-diagonal" detection. Because the molecular beam encounters collimators between the cell and the detection region, the transverse velocity spread is smaller than it would be inside the buffer gas cell, greatly reducing the Doppler broadening of spectral features. Signals can be further increased by increasing the probe power (e.g., using multipass cavities) until saturation is reached and by enhancing ground state population through optical pumping. Potentially large SNR and negligible Doppler broadening make fluorescence measurements ideal for spectroscopy, at the cost of decreased molecular density compared to inside the buffer gas cell.

The most common type of fluorescence measurement uses a probe transverse to the molecular beam. Because the transverse velocity of the molecular beam is reduced through the use of apertures, the transverse fluorescence spectrum is not limited by Doppler broadening. The fluorescence vs. time then gives a measure of the state population for all forward velocity classes. This configuration can be used to study a particular transition, or for measuring optical pumping into or depletion out of a particular state.

Another common configuration is so-called "diagonal fluorescence," in which the fluorescence probe laser propagates at a $\sim 45°$ angle relative to the molecular beam. In this case, $\vec{k}$ for the probe laser has a nonzero projection along the beam propagation axis, which means that the observed transition is Doppler shifted for the different molecule forward velocity classes. Measuring the fluorescence while detuning the probe laser then gives a measure of the relative proportions of different velocity classes, and these data can be used to extract the molecular beam forward beam velocity distribution.

Assume $\vec{k}_{\text{laser}}$ makes an angle θ with the beam propagation axis $\hat{z}$, and consider a particle in the molecular beam with velocity $\vec{v} \approx (0, 0, v_z)$. This is approximation is valid for molecular beams where $v_x, v_y \ll v_z$ due to beam collimation. Additionally, assume that the laser frequency is resonant with the Doppler-shifted transition f for the velocity class v_z. Then we can write simply

$$\vec{k}_{\text{laser}} = \vec{k}, \tag{3.9}$$

where

$$f = \frac{ck}{2\pi}. \tag{3.10}$$

We now derive the relationship between v_z its corresponding resonance f. The Doppler shifted frequency of a transition at frequency f_0 in the molecule rest frame is given by

$$\begin{aligned} f &= f_0 + \frac{\vec{k} \cdot \vec{v}}{2\pi} & (3.11) \\ &= f_0 + \frac{k v_z \cos(\theta)}{2\pi} & (3.12) \\ &= f_0 + \frac{v_z \cos(\theta)}{\lambda} & (3.13) \\ &= f_0 + f \frac{v_z}{c} \cos(\theta). & (3.14) \end{aligned}$$

Rearranging and solving for v_z, we find that

$$v_z = \frac{c}{\cos(\theta)} \left(1 - \frac{f_0}{f}\right). \tag{3.15}$$

If we scan the fluorescence probe frequency f, and obtain a diagonal fluorescence signal $S(t)$ vs f, the above expression allows us to relate each $S(t)$ to a particular velocity class v_z, to which it corresponds. Integrating $S(t)$ for each v_z, allows us to extract the forward velocity distribution of the beam $N(v_z)$. In the most typical cases $\theta = \pi/4$ (co-propagating with the beam) or $\theta = 3\pi/4$ (counter-propagating), which affects correspondence between red or blue detuning the probe laser with larger or smaller velocity classes. Fig. 3.6 shows examples of a 1D transverse fluorescence plot and 2D fluorescence plot for an atomic beam of ^{39}K in our beam source.

3.4 Monte Carlo simulation of atomic and molecular Beams

Along with measurement methods described above, Monte Carlo simulation methods were also heavily used in studying molecular beams during this thesis. In particular, it was necessary for the work described in Chapters 4 and 5 to simulate the behavior of the molecular beam when exposed to lasers and other electromagnetic field gradients. The semiclassical simulation framework, developed in Python was used, for example, to model deceleration of molecular beams and the behavior of magnetic guides, with

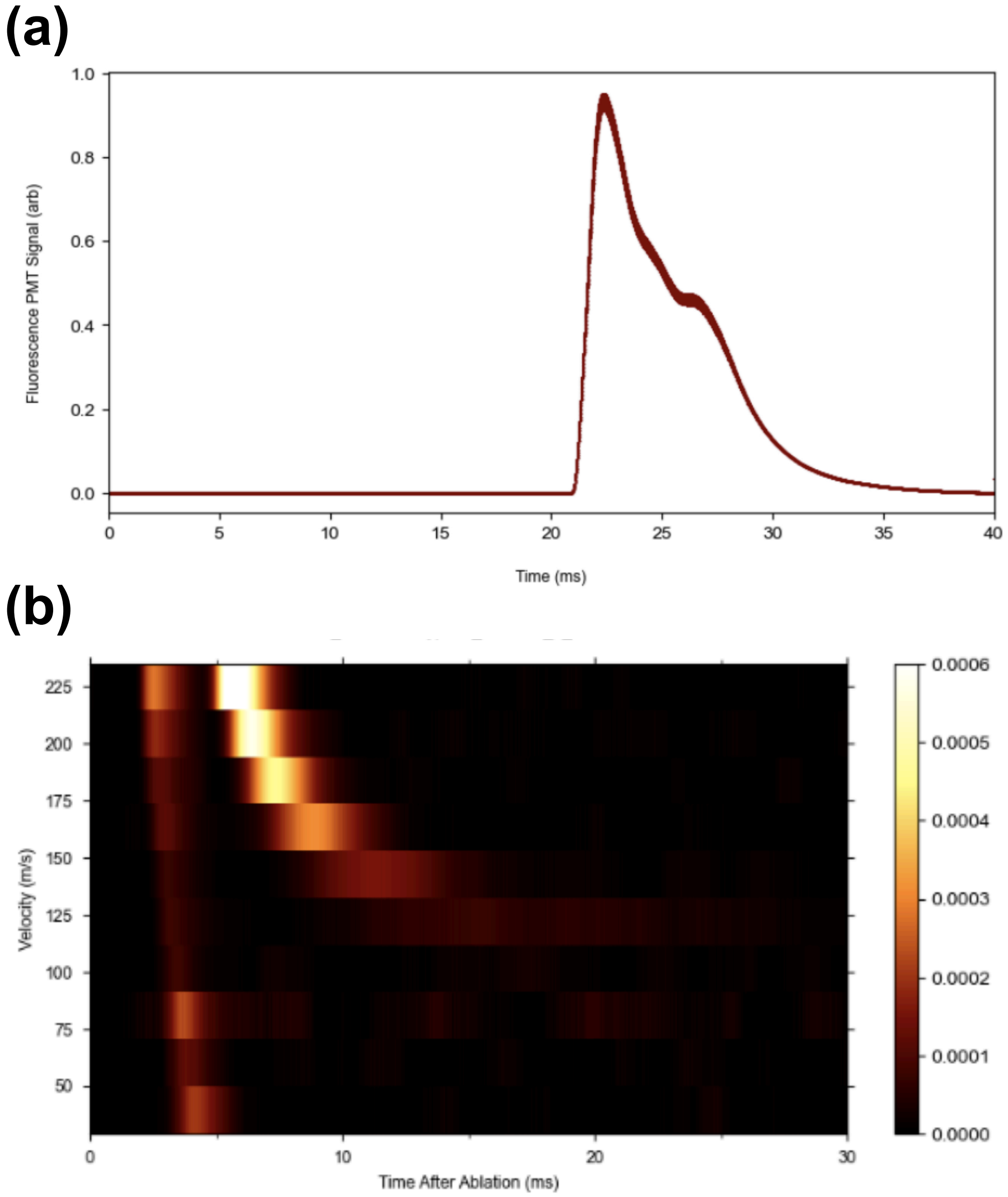

Figure 3.6: Atomic beamline fluorescence signals measured on a PMT. (a) PMT transverse fluorescence signal from Yb atoms in the beamline. (b) 2D diagonal fluorescence signal from ^{39}K in the beamline. The feature on the left is due to a nearby transition that has been Doppler shifted into resonance for large v_z velocity classes. The 1D forward velocity distribution can be determined by integrating the signal against time for each velocity class.

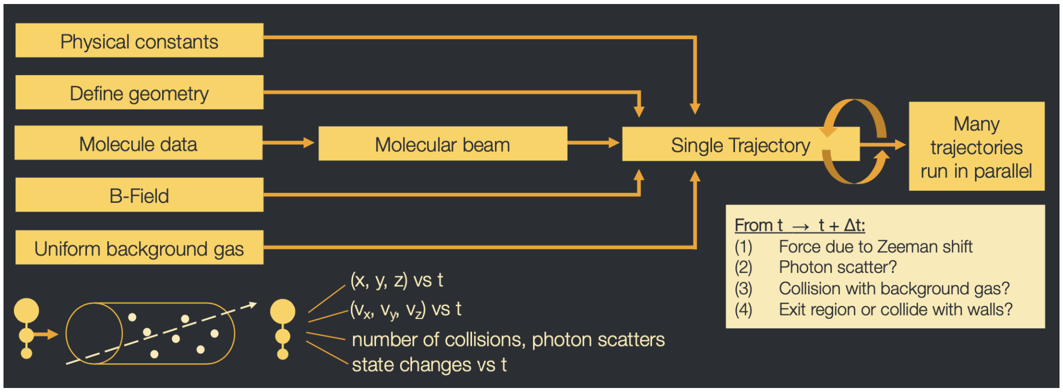

Figure 3.7: Block diagram of a Python-based molecule trajectory simulation code for particles with initial velocity distribution moving through a 3D region with arbitrary uniform-density background gas, B-fields, and laser fields. Branching ratios, transition moments, and Zeeman shifts are used to implement a semiclassical treatment of molecular excitation and spontaneous emission.

opportunities to extend its functionality. Here we describe the basic structure of the simulation software in order to contextualize specific simulation results described in Chapter 4.

The simulation code was developed using an object-oriented approach, which while requiring non-negligible development overhead, allowed the code to be easily extended from its initial purpose (studying deceleration) to handle other scenarios (e.g., both analytical and empirical magnetic fields, collisions with static background gas). The version of the program described here is the most up-to-date, though it was developed in stages from a 1D to 3D model, from simple to arbitrary magnetic fields, etc. The simulation is initialized in the `zeemanSisyphus_init.py` file using several custom Python objects. The simulation framework is shown pictorially in Fig. 3.7.

The `coordinates3D` object defines a grid in Cartesian coordinates with a maximum and minimum value and grid spacing, along with the total amount of time for the simulation (in μs) and the time step. The time step must be small enough for the particle to experience mm-scale features in the magnetic field profile for typical particle velocities. Note that the z-axis denotes the propagation direction of the magnetic field. The `MagneticField` object generates functions that return the value of $|\vec{B}(\vec{r})|$ and $\vec{\nabla}|\vec{B}(\vec{r})|$, in units of T and T/mm, respectively. Additionally the object includes information about the number of "stages" in the case the magnetic field magnitude is periodic as well as a list of "checkpoints," which are values of z that the program will flag and report the particle position and velocity. Using class methods in Python, the `MagneticField` object can handle analytical magnetic fields and lookup tables of field values and gradients, from which the program will create fixed-grid interpolating functions.

The `twoLevelMolecule` object defines a molecule with a particular mass and a single ground state and excited state, each of which can have a nontrivial degeneracy, separated by a frequency in MHz with a given linewidth in MHz. Additionally, this object includes a 2D array of branching ratios and transition dipole moments between the different states. The transition dipole moment array can be modified to account for different drive laser polarizations. The current iteration of the code uses a single 2D array for branching ratios/transition dipole moments even though the eigenstates generically change in nonzero electromagnetic fields. This single array is chosen to apply to the eigenstates for field values where transitions are highly likely to happen, and that the state mixtures are approximately identical for these locations is verified. The Zeeman shift for each state ($U_i(|\vec{B}(\vec{r})|)$ for state i) are also included, either by specifying g-factors for each state (as a factor of μ_B in MHz) or by importing a table of Zeeman shifts for the ground and excited states that is interpolated. The derivative $\frac{\mathrm{d}U_i}{\mathrm{d}|\vec{B}|}$ is also computed because it can be used to determine the force from the magnetic field on the molecule. Using the chain rule, the force on a molecule in state i at position $\vec{r}$ is given by

$$\vec{F}_i(\vec{r}) \equiv -\vec{\nabla}U_i(\vec{r}) = -\frac{\mathrm{d}U_i}{\mathrm{d}|\vec{B}|}\vec{\nabla}|\vec{B}(\vec{r})|. \tag{3.16}$$

In the current iteration, the simulation initializes all molecules in the same initial state, which is also specified when constructing the object.

The `moleculebeam` object takes the molecule defined above as an input and determines the initial position and velocity distributions. In simulations performed thus far, molecules uniformly fill a rectangular or circular aperture. Likewise, both the forward and transverse velocities are sampled uniformly between 0 and a maximum velocity (in $\frac{\mathrm{mm}}{\mu\mathrm{s}}$), with the azimuthal and polar angles of the velocity vector with the z-axis sampled uniformly as well.[5]

The background gas environment is defined using the `backgroundgas` object. Currently, a helium or neon background gas with uniform number density, fixed temperature, and fixed flow velocity assumed to lie along the z-direction has been implemented because these are two of common buffer gas species. Collisions are modeled using

---

[5] The angles are not sampled from an actual uniform distribution, but rather the distribution that leads to uniform coverage of the hemisphere oriented towards the z-axis.

direct simulation Monte Carlo methods described in more detail in Chapter 4, where a collision partner with a particular velocity is selected and its effect modeled following the formalism described in [65]. The velocity and impact angle of the atom in the molecule's rest frame is sampled using a Maxwell-Boltzmann distribution modified to account for the shift in reference frame. Then this velocity vector is converted back into the lab frame. These modified distributions and frame conversions were calculated by David Shlivko and Yuiki Takahashi [59].

The laser fields are defined back in the initialization file. By default, two independent laser frequencies are present and assumed by default to be present over the entire simulation region, with intensities defined as a saturation parameters.[6] Every iteration of the simulates computes the trajectory of a single molecule. At every time step, the molecule propagates under the influence of $\vec{F}$. Then, whether the molecule collides elastically with a background gas atom is determined and the molecule momentum is modified accordingly. A semiclassical model is used to determine the average number of photons scattered $\bar{n}$. By default, the scattering rate between ground states i and excited state j, $R_{i,j}(s, \delta)$ is calculated using saturation parameter s and detuning δ_{ij} with

$$R_{ij}(s, \delta) = \frac{\Gamma s}{2\left(1 + s + 4\frac{\delta_{ij}^2}{\Gamma^2}\right)}. \tag{3.17}$$

Multiplying the scattering rate by the time step yields $\bar{n}$. By default, the probability of photon scattering is determined by selecting the largest of the values for average photon number and comparing against a uniformly sampled random variable in the interval $[0, 1]$. The excited state for the transition and ground state after spontaneous decay are determined probabilistically from the branching ratios and transition dipole moments. This approach for computing the probability of photon scattering is valid only when $dt \ll \frac{1}{R_{i,j}T_{ij}}$, where T_{ij} is the transition intensity between i and j [66]. A typical, small $dt \sim 1 - 10$ ns can lead to unreasonably long simulation times, and an alternative method has been implemented for cases where $\bar{n}$ is allowed to be greater than 1. In this case, the photon is certain to scatter. An excitation to an excited state and decay to a ground state is determined probabilistically for each photon until the final ground state is different from the initial ground state. At this point, the photon scatter ceases. While the momentum transfer from the photon scattering is small, its effect is also included when computing the molecules final velocity in this time step.

---

[6] In order to model the laser fields along particular positions in space, for example, in the case of lasers that propagate transverse to the z-axis, the intensities can be defined as functions of space.

The final positions and velocities are compared to the previous values and the simulation continues to integrate the molecule motion until the molecule exits the simulation region or it satisfies a number of "failure conditions." For simplicity of analyzing simulation results, every run of the simulation uses a fixed number of time steps. The failure conditions then account for the molecule colliding with the edge of the simulation region, its forward velocity v_z becoming negative, the molecule propagating backward, or the molecule failing to reach the exit in the number of time steps allotted.

For every trajectory the simulation records the positions, velocities, total number of photon scatters, total number of background gas collisions, ground state occupation and excited state occupation (in the event of a photon scatter) as a function of time, along with the total time elapsed and specific positions and velocities at the aforementioned magnetic field z-axis "checkpoints." Because each trajectory is independent, the simulations are performed in parallel, with a fixed number of trajectories saved in batches prior to computing subsequent batches. In order to conserve storage space, only a fixed fraction of the full trajectories are saved, but position and velocity information at checkpoints and the exit status is recorded for all trajectories. Summary statistics, such as the fraction of particles with particular initial and final velocities that exit the simulation, can be computed solely using the abbreviated data from a large number of trajectories.

This semiclassical model does not take into account coherent quantum effects or quantum superposition, but the model is sufficient to study the effect of classical fields on molecules beam propagation. Uniform sampling distributions, e.g., for the initial positions, are common in the simulation, but the use of statistical weighting allows one to infer the results for arbitrary initial distributions from the uniform sampling results. In its most current form, the simulation is particularly slow when interpolating large magnetic field lookup tables generated by realistic magnets, such as those generated by COMSOL software. The use of high-performance computing clusters, then, offers a natural speed-up for these computations.

Acknowledgments

This work was supported by the Gordon and Betty Moore Foundation and the Alfred P. Sloan Foundation.

Chapter 4

Methods for Efficient Deceleration of Molecular Beams

> *"Your mind fizzes. A thousand new shoots break through the soil. They entwine with you, embrace you. Some part of you decays while something else feeds from that decay. The spores of your new thoughts float away in shifting clouds and settle in new soil. Then you see Gardener out there, still planting. And they stop, like an old man resting in the fields, and they turn to face you. And you join the chorus. And together you sing the song of growing things."*
>
> *Citizen Sleeper*

As in atomic systems, magneto-optical trapping of molecules requires the repeated excitation and emission of photons (photon cycling), which carry the forces responsible for cooling and trapping. Unlike in atoms, however, the amount of photon cycling in a molecular system is limited by decays to vibrational and rotational dark states. As discussed in Sec. 2.3, electron hybridization in alkaline-earth metal halides and hydroxides (SrF, SrOH, etc.) causes these species to have diagonal Franck-Condon factors between the ground and first excited state, allowing for approximate vibrational closure [47, 67, 68]. Furthermore, rotational selection rules enforce rotational closure in these species when driving $J'' = 1 \rightarrow J' = 0$ transitions. When quasi-diagonal Franck-Condon factors and rotational closure is taken into account, the species discussed here can cycle about $10^4 - 10^5$ photons before population is lost to dark states. The number of photons scattered before loss to dark states is often called the "photon budget."

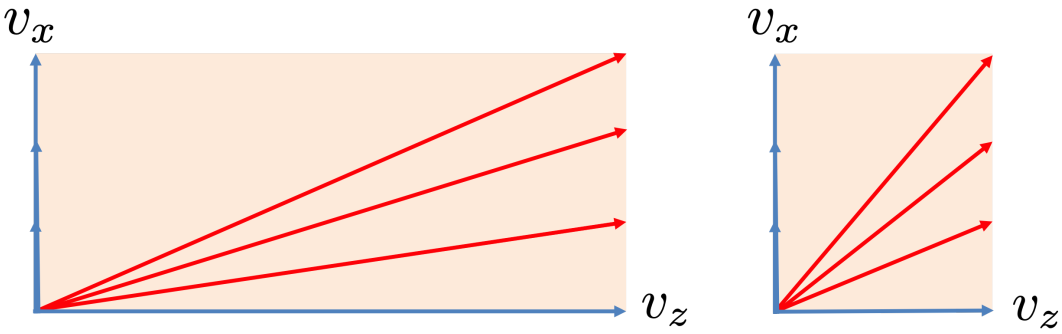

Figure 4.1: Beam divergence occurs when the forward velocity is reduced without keeping the transverse velocity confined. The increased divergence angle relative to the propagation axis causes additional losses due to deceleration.

Cryogenic beam sources produce molecular beams with typical forward velocities of 10^2 $\mathrm{m/s}$, about one order-of-magnitude larger than typical molecular MOT capture velocities. While shifting the peak of the forward velocity distribution by an order of magnitude or more is ideal, it is often easier (and acceptable) to increase the proportion of molecules in the slow tail of the velocity distribution, effectively increasing the number of molecules in the MOT capture window. Sufficient deceleration of molecular beams in order to load enough molecules into a MOT is often difficult and inefficient. Molecules that are most sensitive to BSM physics tend to be heavy (e.g., $^{174}\mathrm{YbOH}$ is 191 $\mathrm{a.m.u.}$), and radiative slowing schemes that leverage the momentum transfer from photon cycling are both lossy and deplete a large fraction of the photon budget ($\sim\ 10^4$ photons), though schemes have been proposed to improve the efficiency of laser slowing [69, 70]. Furthermore, in any deceleration scheme, reduction in the forward velocity of the molecular beam increases the angle of the velocity vector relative to the propagation axis—an effect called transverse pluming—that leads to loss of molecules due to beam divergence. These losses can be significant in radiative slowing methods that involve long slowing distances (Fig. 4.1).

Several "non-radiative" deceleration methods that do not rely on photon cycling have been proposed and demonstrated to address the inefficiencies of the radiative methods, but several of these schemes are "pulsed" in nature, such as Stark deceleration and optical Stark deceleration [71–73]. Typical cryogenic buffer gas sources produce few-ms wide pulses of molecules through laser ablation with $\sim 1 - 10$ Hz repetition rates. Synchronizing the molecular pulses with the time-dependence of the slowing scheme thus presents an additional complication, as many of the time-dependent schemes can slow only short segments of the wide pulses produced in buffer gas sources.

Therefore, the development of time-independent, non-radiative deceleration methods is of intrinsic interest for trapping heavy molecules for BSM physics searches. In this thesis we investigated a two such methods proposed over the course of building the PolyEDM experiment. The first–deceleration of molecules through collisions with a counterpropagating gas–was explored theoretically and numerically as discussed in Sec. 4.1. The second is Zeeman-Sisyphus (ZS) deceleration, first proposed by Fitch and Tarbutt [66] in 2016 and was demonstrated experimentally in CaOH and YbOH molecules using superconducting magnets in 2021 and 2023, respectively [53, 74]. Sec. 4.2 introduces the ZS scheme and overviews the recent experimental demonstration using superconducting magnets by our collaborators in the Doyle Group at Harvard University. In this section, we also discuss the motivation behind building and testing a permanent magnet ZS decelerator. Sec. 4.3 discusses our design and testing of optimized *permanent* magnet arrays for building a ZS slower. Finally, Sec. 4.4 reviews our work simulating ZS deceleration in our Monte Carlo particle tracing simulator. Experimental prototyping of a permanent magnet ZS slower is discussed in detail in Chap. 5.

4.1 Deceleration via collisions with counter-propagating gas in a magnetic guide

Cryogenic buffer gas beam sources use collisions with background gas to thermalize molecules produced in laser ablation and the gas flow entrains these molecules into a beam. An idea that has repeatedly been proposed in the PolyEDM collaboration is to use a gas counter-propagating with the molecular beam to reduce the beam forward velocity. In addition to lowering the forward velocity, collisions with counter-propagating gas would naturally transfer kinetic energy into transverse motion of the molecules. If the molecules' transverse velocity components grow too large, they will exit the beam and be lost. Furthermore, state changing collisions to unconfined states can also cause loss. Therefore, another feature is proposed in addition to counter-propagating gas—a transverse magnetic guide. Note that this restricts the species of interest to those with a nonzero magnetic moment.

The precise statement of the idea is thus as follows: buffer gas at some cryogenic temperature counterpropagates against the molecular beam in a magnetic guide. The background gas is in equilibrium and can be described by a uniform density and constant flow velocity. Is there a temperature, flow, and density regime that allows molecules to be slowed to within the MOT capture velocity? Which velocity classes are slowed sufficiently? Are the collisional losses out of the magnetic guide manageable?

We explored this idea using particle tracing simulations. In summary, simulations and theoretical work show that this method is *not* a promising means of decelerating molecular beams.

4.1.1 Collisions in a magnetic guide – Simulations

Using the simulation framework discussed in Sec. 3.4, deceleration using a counterflow buffer gas was explored. The molecule used in the simulation was $^{174}\mathrm{YbOH}$, which was treated as having two ground states corresponding to the valence electron spin orientation (and a single excited state that is irrelevant for this simulation since there are no laser fields present). Each ground state was given a magnetic moment of $\pm\mu_B$ parallel to the direction of the magnetic field, with the corresponding energy shift being given by $\mp\mu_B|\vec{B}|$, for a magnetic field with magnitude $|\vec{B}|$. The magnetic field $\vec{B}(x, y, z)$ is given by the analytical function

$$|\vec{B}(x, y, z)| = B_0\left(\frac{x^2 + y^2}{w_0^2}\right), \tag{4.1}$$

where $B_0 = 1\ \mathrm{T}$ and $w = 5\ \mathrm{mm}$. The entire guide and beamline is a $100\ \mathrm{mm}$ long cylinder with a diameter of $10\ \mathrm{mm}$. Thus, the guide attains a field magnitude of $1\ \mathrm{T}$ at the edge. Given the magnetic moment of the weak-field seeking state, the guide is able to confine molecules that originate in the center with initial transverse velocity between $0 - 7.6\ \mathrm{m/s}$ (transverse velocity acceptance). Molecules are initialized in a $10\ \mathrm{mm}$ diameter circular aperture at $z = 0\ \mathrm{mm}$.

The background gas parameters include the background gas species, number density, temperature, and (lab frame) forward flow velocity. The species tested include Ne and He, and temperatures between $0.5\ \mathrm{K}$ and $4\ \mathrm{K}$ were tested. The background gas density was varied between $0 - 9 \times 10^{12}\ \mathrm{cm}^{-3}$, and in some older simulations used for testing, the number of collisions experienced by YbOH molecules was held fixed. Finally, the counterflow velocity was varied between $0 - 100\ \mathrm{m/s}$ (with a direction opposing the initial forward velocity of the YbOH). Several simulations were conducted, but here we share one representative simulation that illustrates the common observed behavior for this proposed deceleration method.

The following discussion is for a simulation of 50000 trajectories through a $0.5\ \mathrm{K}$ He buffer gas with $n = 0,\ 3 \times 10^{12}\ \mathrm{cm}^{-3},\ 9 \times 10^{12}\ \mathrm{cm}^{-3}$ and counterflow velocity

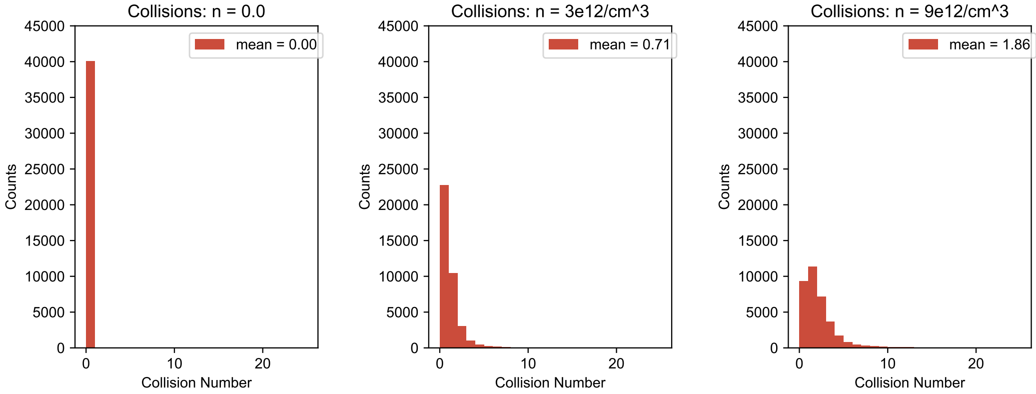

Figure 4.2: Number of collisions between 50000 simulated YbOH molecules and a static He background gas at various number densities, for particles that exit the beamline.

$v_{\text{counter}} = 0, -30, -60, -100$ m/s. The YbOH molecules are initialized with forward velocities uniformly sampled between $0 - 100$ m/s, and transverse velocities up to the guide's transverse velocity acceptance. Note that in the following comparisons, the same simulation results were used for all other parameters where $n = 0$, since the behavior is independent of v_{counter} in this case. The simulation keeps track of the number of collisions that occur for each trajectory. Fig. 4.2 shows histograms of the number of collisions for $v_{\text{counter}} = 0$ m/s. As expected, no collisions occur when there are no background gas atoms, and the average number of collisions increases with increasing n. Similar histograms were observed for the other values of v_{counter}.

In processing the results, each trajectory was distributed into 1 m/s-wide initial forward velocity classes. In each bin, the trajectories corresponding to particles that (1) exited the beamline successfully (see Sec. 3.4 for the "success" conditions) and (2) had a final forward velocity less than 10 m/s were identified. Finally, the fraction of particles of particles in the velocity class that meet both these conditions was computed. Fig. 4.3 shows a plot of this quantity for simulations where $v_{\text{counter}} = -30$ m/s.[1] Increasing the background gas density indeed causes slowing of faster velocity classes, but increased collisions also lead to more losses of particles from the guide altogether.

---

[1] A few features of this plot may seem peculiar. Only 80% of the particles in slow velocity classes exit with the same velocity for $n = 0$ where no slowing is expected. This is because some fraction do not originate on the beam axis and may have transverse velocities that cause them to collide with the walls of the guide. Furthermore, a very small fraction of the slowest velocity class exits the guide. This is an artifact of the simulation whereby particles that do not exit the guide after a large, fixed number of time steps are considered lost.

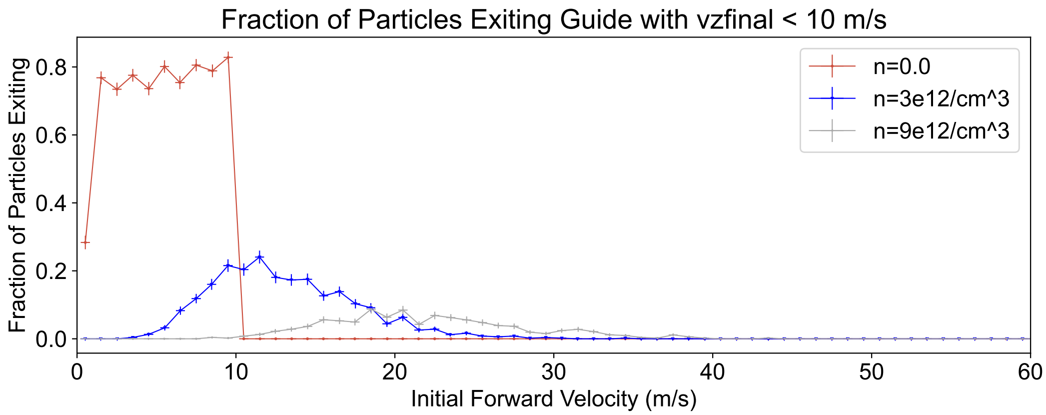

Figure 4.3: Fraction of simulated YbOH in each velocity class exiting magnetic guide with $v_{z,f} < 10\ \mathrm{m/s}$ as a function of He background gas density for $v_{\text{counter}} = -30\ \mathrm{m/s}$. The shown error bars are computed using Bernoulli statistics, where the probability of success is given by the exit fraction and the number of trials is given by the total number of particles in the velocity class.

These plots are the result of analyzing the uniform initial forward velocity distribution that was input into the simulation, but through a (relatively) straightforward mathematical procedure, these results can be re-analyzed for an arbitrary initial distribution. In this case, it is particularly informative to re-cast these results for an effusive distribution described by a most-probable velocity v_p, given by

$$f(v, v_p) = N \times \left(\frac{v}{v_p}\right)^2 \exp\left(-\left(\frac{v}{v_p}\right)^2\right), \tag{4.2}$$

$$v_p = \sqrt{\frac{2k_\mathrm{B}T}{m_{\mathrm{YbOH}}}} \tag{4.3}$$

where N is a normalization constant (Fig. 5 of [75]). A series of effusive distributions with $v_p = 0 - 50\ \mathrm{m/s}$ are now considered in $1\ \mathrm{m/s}$ bins. A distribution is then computed for each value of v_p, discretized over $0.1\ \mathrm{m/s}$ bins between $0 - 120\ \mathrm{m/s}$). Within each distribution $f(v, v_p)$, the cumulative distribution function (cdf) is computed for each bin edge (v_i and $v_{i+1} = v_i + 0.1$) using the built-in `erf` function in Python. The difference of these cdfs yields what we will call the *probability weight* in that bin. Computed for each bin within a single distribution $f(v, v_p)$, the result is essentially a plot of probability weights for the effusive distribution. These weights are then compared with the weights given by the cdf of the uniform distribution over the same bins. The appropriate ratio of these weights allows us to convert the histogram of final velocities for the uniform distribution to that of $f(v, v_p)$, which can be used to extract the fraction of exiting particles with final velocities slower than $10\ \mathrm{m/s}$.

We then repeat this procedure for all $f(v, v_p)$ for $v_p = 0 - 50\ \mathrm{m/s}$. This gives us plot similar to that in Fig. 4.3, but where each point now represents an entire velocity distribution. We show these slow exit fraction plots in Fig. 4.4 for each counterflow velocity and for all simulated densities. Typical forward velocities for a slow YbOH beam in a $1\ \mathrm{K}$ source range from $30 - 60\ \mathrm{m/s}$, with the slowest velocities achievable using slowing cells and a complex $^3\mathrm{He}$ pot (Chap 3. of [76]). Over all configurations tested, there was no major increase in the fraction of exiting slow molecules over the configuration without background gas, for any reasonable slow YbOH beam.

Other simulations were also conducted with different background gas temperatures and using a Ne background gas at higher temperatures, but none of these suggested the efficacy of this proposed slowing scheme. Instead, what was observed were large losses of already slow molecules with limited increase due to slowing. These simulations suggest that the ratio of transverse kinetic energy transfer compared to forward energy transfer is unfavorable, leading to loss out of the magnetic guide, which is especially pronounced for initially slow particles.

4.2 Zeeman-Sisyphus (ZS) deceleration

Zeeman-Sisyphus deceleration is another time-independent, non-radiative deceleration technique leverages the ground state Zeeman shift in large magnetic fields. Consider a molecule with $^2\Sigma_{1/2}$ ground state, such as the alkaline-earth(-like) hydroxides, in a magnetic field $\vec{B}$ with periodic magnitude along the coordinate z. In regions where $|\vec{B}(z)| \neq 0$, ground states with spin-orientation aligned with $\vec{B}$ will decrease in energy, while those states anti-aligned with $\vec{B}$ will increase in energy. The former states are called strong-field-seeking (SFS) states, while the latter are called weak-field-seeking (WFS) states. The periodic magnetic field causes a corresponding periodic Zeeman shift in the WFS and SFS states, with the WFS and SFS experiencing shifts with opposite sign and magnitude corresponding to the effective g-factor of the state.

A molecule in a WFS state traveling through a region of increasing magnetic field magnitude will lose kinetic energy equal to the increase in its internal energy from the Zeeman shift. As the magnetic field decreases in magnitude, the molecule will regain this kinetic energy. However, if the molecule were optically pumped into a SFS state before entering a region where $|\vec{B}|$ is decreasing, the molecule would once again lose kinetic energy in this decreasing region. Through optical pumping, a molecule in a periodic magnetic field can be made to lose kinetic energy. This scheme is illustrated

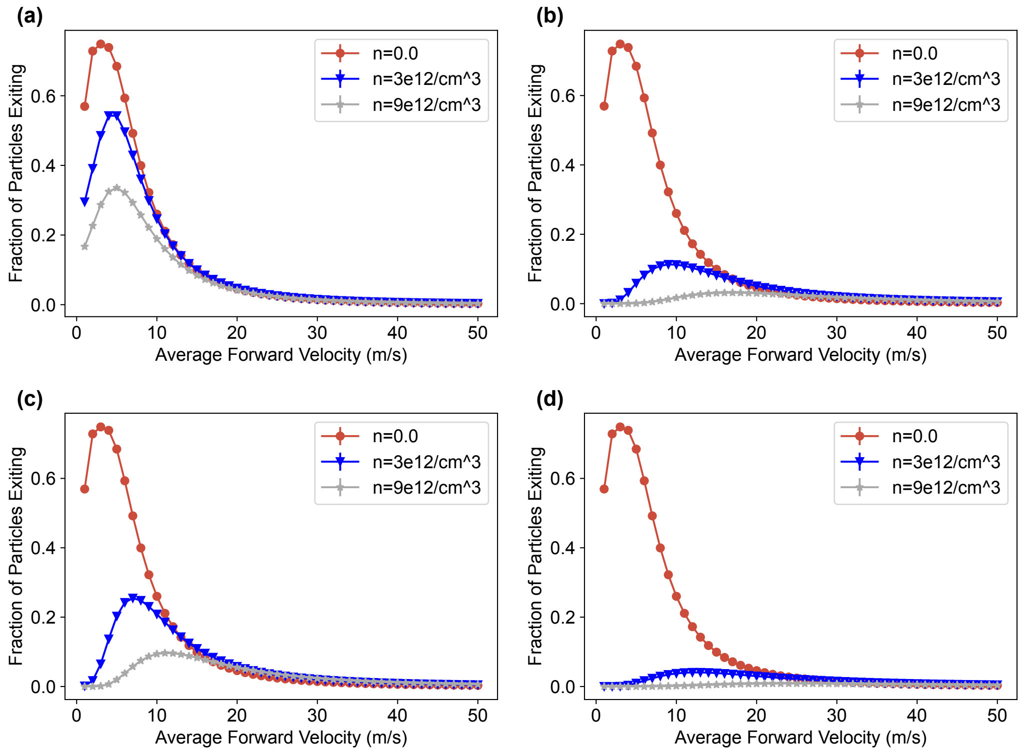

Figure 4.4: Fraction of simulated YbOH with an effusive velocity distribution given by the x-axis exiting magnetic guide with $v_{z,f} < 10$ m/s as a function of He background gas density for (a) $v_{\text{counter}} = 0$ m/s, (b) $v_{\text{counter}} = -30$ m/s, (c) $v_{\text{counter}} = -60$ m/s, and (d) $v_{\text{counter}} = -100$ m/s. The shown error bars are computed using Bernoulli statistics, as in Fig. 4.3.

in Fig 4.5. Note that a second optical pumping step is required to transfer the SFS molecules back into a WFS state before it traverses the second magnetic field period. In this scheme, photons are scattered sparingly, used only to transfer population between WFS and SFS states, and with all of the deceleration deriving from the Zeeman effect. As is typical of a Sisyphus mechanism, the molecules are made to repeatedly climb potential energy hills, prevented from “rolling down.” From this point forward, we will refer to each hill or period as a *stage*.

Note that SFS pump is slightly blue-detuned from the zero-field resonance in order to avoid accidental optical pumping of WFS particles in low-field regions. Furthermore, in order to ensure that all sublevels of the WFS ground states are pumped, the WFS pump should be red-detuned slightly away from the value corresponding to the magnetic field maximum. This detuning reduces the amount of energy removed, but is necessary for the scheme to work in practice.

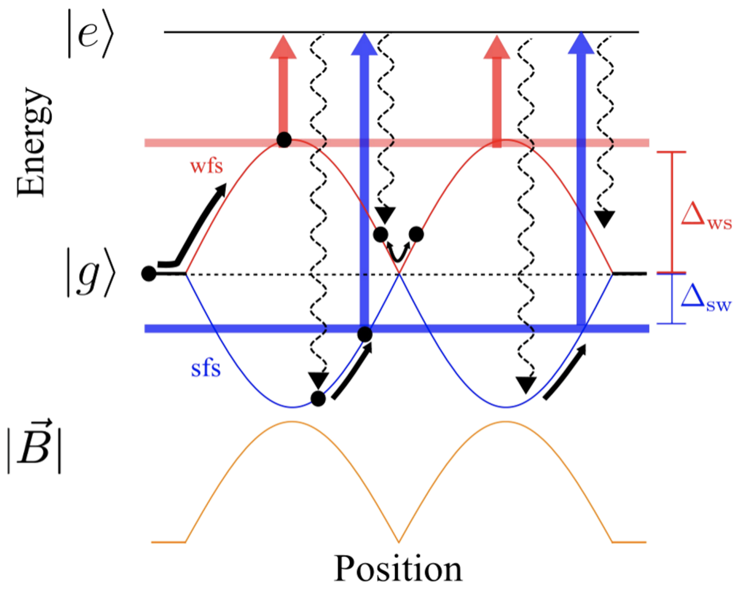

Figure 4.5: Basic Zeeman-Sisyphus deceleration scheme. Adapted from [66]. Lasers optically pump population between strong-field seeking (SFS) and weak-field seeking (WFS) states as particles are decelerated climbing up potential hills created by a periodic magnetic field.

4.2.1 Efficiency comparison between Zeeman-Sisyphus and radiative slowing

In radiative slowing approaches, momentum is removed from an atom or molecule through absorption of light from a counter-propagating laser. Because spontaneous emission occurs with equal likelihood in all directions, on-average momentum is removed from the species along the laser propagation axis, in accordance with conservation of momentum. Because each individual momentum kick is small compared to the atom's momentum, many photons must be scattered before the atom can be slowed to a stop. A ^{174}YbOH molecule moving at $150\ \mathrm{m/s}$ has the equivalent momentum of ~ 40000 $577\ \mathrm{nm}$ photons.

In contrast, Zeeman-Sisyphus deceleration relies on conservative forces from a magnetic field on a magnetic dipole. In this scheme, photons are only used to transfer population between states that experience deceleration, and deceleration arises from kinetic energy removal in contrast to momentum transfer. We can directly compare the efficiency of the two approaches with a simple calculation.

Consider a periodic magnetic field with a maximum magnitude of $1\ \mathrm{T}$. A molecule with ground state magnetic moment $\mu = \mu_B$, after traversing a single magnetic field period, will lose approximately $1.35\ \mathrm{K}$ of kinetic energy (using $E \sim k_B T$). A ^{174}YbOH molecule with forward velocity of $60\ \mathrm{m/s}$ would exit the field with $59.02\ \mathrm{m/s}$. In the best case scenario, this deceleration would require scattering two photons to optically pump from $\mathrm{WFS} \rightarrow \mathrm{SFS}$ and $\mathrm{SFS} \rightarrow \mathrm{WFS}$. We can compare the amount of deceleration to the momentum transfer from two $577\ \mathrm{nm}$ photons on YbOH in a radiative deceleration scheme. The final velocity after the momentum transfer from two photon scatters is $59.993\ \mathrm{m/s}$. In other words, in best-case scenario with efficient optical pumping, the two photons used in the ZS scheme offer a 270-fold increase in the deceleration compared to the photon momentum transfer alone. Therefore, ZS schemes have potential to slow molecules with few photon scatters. In the case described above, a $60\ \mathrm{m/s}$ molecule could be slowed to below $10\ \mathrm{m/s}$ after 30 stages, and under 100 photons.

The change in velocity $dv = v_f - v_i$ for a particle of mass M and initial velocity v_i from a photon of wavelength λ is given by momentum conservation to be

$$dv = -\frac{h}{\lambda M}, \tag{4.4}$$

which is entirely independent of the initial velocity v_i. This is rather unlike the case of energy removal, in which a fixed amount of kinetic energy removed from the system leads to a greater magnitude of dv for slower velocities. To see this consider a much slower YbOH molecule, traveling at $30\ \mathrm{m/s}$. In this case, a single ZS stage brings the velocity to $28.0\ \mathrm{m/s}$, which is about twice the deceleration experienced by a $60\ \mathrm{m/s}$ molecule. Relying on momentum transfer alone, the final velocity would be $29.993\ \mathrm{m/s}$, which is the result of the same total deceleration as experienced by a $60\ \mathrm{m/s}$ molecule.

4.2.2 Non-adiabatic transitions in Zeeman-Sisyphus deceleration

The discussion of ZS at this point has glossed over a number of subtleties and challenges present in a practical realization of the scheme. One major subtlety is the possibility of non-adiabatic transitions. The information here came out of very useful conversations with PolyEDM collaborators, and in particular with Amar Vutha.

First, note that in Fig. 4.5, there is an assumption that a particle that is in a WFS state in the first stage will remain in a WFS state in the second stage even as the magnetic field magnitude appears to reach zero between the two stages. The assumption in this scheme is that the magnetic field is strongly pointing along a particular direction and slowly varying with distance across the beamline such that the quantization axis it sets moves adiabatically along the entire slower. This assumption must be reconsidered when dealing with near-zero magnetic fields. These near-zero fields are possible when adjacent magnet stages have opposite magnetization, though perfect cancellation is unlikely in any real system. If the residual field between magnet stages is low enough, non-adiabatic transitions between WFS and SFS through the zero-crossing are possible.

Using the Landau-Zener formalism, one can show that the probability of this WFS → SFS transition is given by

$$P_{\mathrm{non-adiabatic}} = \exp\left(-(\mu_B/h)(B_x)^2/\left(v_z\,\frac{\mathrm{d}B_z}{\mathrm{d}z}\right)\right), \tag{4.5}$$

where B_x is the residual transverse field in the near-zero crossing region, v_z is the forward velocity, and $\frac{\mathrm{d}B_z}{\mathrm{d}z}$ is the slope of the dominant magnetic field direction with the longitudinal displacement. With $B_x = 15$ G and $\frac{\mathrm{d}B_z}{\mathrm{d}z} = 1$ T/cm, a 100 m/s particle has a 4% chance of making the non-adiabatic transition. For 20 G, this probability is just 0.4%. Therefore, a transverse bias field of 20 G should all but guarantee that these undesired transitions would not occur, though we have not implemented this in our experimental implementations because strong permanent magnets often have fields of this size in the transverse direction.

This problem can be avoided if magnet stages pointing in the same direction are employed because near-zero field regions will never occur in this case. However, these magnets will repel each other and mounting strong repulsive magnets in close proximity poses unique design challenges. Other complications, and in particular those surrounding optical pumping in real systems, are discussed in Chap. 5.

4.2.3 Overview of Zeeman-Sisyphus deceleration using superconducting magnets

Zeeman-Sisyphus slowing was demonstrated first in CaOH in 2021, and then subsequently in the heavier and more complex ^{174}YbOH molecule in 2023, both at Harvard University in the group of PolyEDM collaborator John M. Doyle [53, 74]. Unlike in the initial proposal, which modeled an array of permanent magnets with longitudinal optical pumping beams, both experimental realizations used used a pair of superconducting solenoid stages to generate ~ 2.5 T fields in each stage; furthermore, these solenoids were designed for transverse optical pumping beams, allowing one to limit the optical pumping to single locations along the beamline as opposed to the entire set of locations that satisfy the resonance condition with a longitudinal pump laser. Each of the pair of magnets were also aligned with the same orientation, unlike in the initial proposal, where subsequent magnet stages had opposing magnetization directions. The two superconducting coils were about 30 cm in length. A magnetic guide was inserted at the end of the decelerator in order to increase the fluorescence detection efficiency of slowed molecules in the WFS state, and optical pumping lasers (and the solenoid current) could be shut on and off to confirm the deceleration effect.

In both CaOH and YbOH implementations, a 2 K cryogenic buffer gas source was used to produce the molecules. For the CaOH molecular beam, the fraction of slow molecules was increased by two orders of magnitude. The YbOH molecule was more difficult to decelerate due to its greater structural complexity. The $\tilde{A}^2\Pi_{1/2}$ excited state in YbOH has an effective g-factor that is more than order of magnitude greater than that of the corresponding state in CaOH, which leads to a nonlinear Zeeman shift for magnetic fields much less than 2.5 T. Additionally, the large Λ-doubling in the YbOH $\tilde{A}^2\Pi_{1/2}$ state causes a near-degeneracy between the $J' = 3/2$ and $J' = 1/2$ rotational levels in the excited state, leading to mixing among the excited rotational levels. Both of these factors lead to inefficiencies in optical pumping and loss of molecules to dark states during deceleration, and these complications apply to many of the heavy polar molecules of interest for precision measurement. Ultimately, only 10-15% of the YbOH molecules could be slowed in this configuration. While efficiencies can be recovered by vibrational repumping, one has to contend with the Zeeman splitting of the relevant transitions along with complex substructure. Nonetheless, Zeeman-Sisyphus deceleration was demonstrated in 100 YbOH molecules per pulse.

4.3 Developing and testing optimized magnet arrays

While superconducting magnets offer a combination of strong, uniform, tunable magnetic fields over large areas, they present some difficulties. The cryogenic requirements for installing several-T superconducting coils are significant, and the engineering of the coil mounts to handle large inter-magnet forces is highly nontrivial. The design, manufacture, and testing of superconducting ZS magnets can require several months and hundreds of thousands of dollars. There is therefore an incentive to explore a regime more like that in the ZS proposal–slowing using an array of permanent magnets.

ZS deceleration with permanent magnet arrays explores a different regime than ZS using superconducting magnets, though the basic principles remain identical. There are a number of factors that limit the maximum attainable fields in permanent magnet arrays, though we explored strategies to engineer large permanent magnet fields. Because of the smaller peak field per stage relative to superconducting coils, more stages are required to achieve an equivalent amount of energy removal. More stages increases the number of opportunities for molecules to be optically pumped incorrectly or for population to be lost. This leads to an increase in variance in the final velocity distribution compared to a slower with fewer stages.

Additionally, it is not possible to turn permanent magnets on and off. The magnetic fields in the slower are always present, and therefore one cannot simply "turn it off" to evaluate the performance of the slower relative to the "on configuration." Furthermore, permanent magnet arrays are assembled out of individual permanent magnets whose forces can make manual assembly challenging and time consuming. Careful glueing of magnets is possible, but outgassing can make glue potentially problematic if the array is installed in a room temperature vacuum chamber. The cryogenic requirements for superconducting solenoids, on the other hand, completely mitigate the issue of beamline pressure. Note that bakeout of permanent magnets, even at low temperatures, is inadvisable, as magnetic field strengths can be significantly reduced for temperatures much lower than the Curie point. Fortunately, in our experiences, commercially available permanent magnets are relatively clean and in practice required only surface-level cleaning with isopropyl alcohol before being anchored to the room-temperature beamline.

A ZS magnet array could be thermally anchored to the cryogenic vacuum chamber, but N52 grade NdFeB magnets behave anomalously at cryogenic temperatures [77]. In particular, at 135 K NdFeB magnets experience spin reorientation which results in a 14% reduction in magnetic flux and a greater susceptibility to demagnetization, although this spin-reorientation is reverses as the temperature increases. Praseodymium can be substituted for neodymium to mitigate this effect above 10 K. Fortunately, if cryogenic operation is required, SmCo magnets produce fields that are more resilient at cryogenic temperatures, and are only marginally weaker than NdFeB magnets.

This discussion highlights the salient point that permanent magnets behave nonlinearly and undergo nontrivial hysteresis and demagnetization. Therefore, careful design of a complex permanent magnet array requires simulation taking into account, saturation, hysteresis, and demagnetization effects.[2] Superconducting coils, on the other hand, can be described with relatively simple analytic expressions.

Strong, rare-earth permanent magnets, however, are far easier to procure cheaply and rapidly tinker with that there is sufficient incentive to study ZS deceleration using them. The permanent magnet array modeled in the original ZS proposal are Halbach arrays,

---

[2] See [78] for an in-depth look into the world of permanent magnets.

which are cylindrical. Each stage is constructed out of permanent magnet wedges with a particular dipole orientation. The Halbach dipole produces a strong, uniform magnetization in the central gap, while the Halbach hexapole produces a magnetic guide field [66]. The array described in this proposal consists of alternating dipole and guiding stages to provide both deceleration and prevent beam divergence. Additionally, the optical pumping lasers in this configuration propagate longitudinally, which means there is optical power at all positions in the beamline at the optical pumping frequencies.

The remaining portion of this section details our efforts to model and design Zeeman-Sisyphus magnet arrays that can in some way improve on the Halbach design, either in field strength, simplicity, or both. The goal of this work was to identify candidate designs for building and testing a prototype slower in our apparatus. The ZS magnet design criteria are those that will maximize deceleration, minimize the slower length, minimize beam divergence. Therefore, each magnet stage should: 1) maximize the field magnitude at the center of the magnet along the propagation axis, 2) produce a uniform field in the transverse plane intersecting this axis with small field gradients, 3) have a sufficiently large bore for molecule propagation, and 4) be compact. Additionally, we especially considered designs that allow for optical pumping light to propagate transverse to the molecule axis. The WFS $\rightarrow$ SFS would propagate through the center of a stage near the field maximum, and the SFS $\rightarrow$ WFS pump would propagate between two adjacent magnet stages. This configuration provides the advantage of controlling exactly where—and at which value of the magnetic field—the pumping occurs, preventing off-resonant or unintentional pumping at undesirable positions along the slower.

The simulations detailed in this section were carried out in COMSOL Multiphysics using the Magnetic Fields, No Currents module (mfnc). Unless otherwise noted, the magnets were modeled as nonlinear, permanent magnets using the B-H curve for magnetic materials. In many cases, the simulations were run with the finest mesh that allowed the simulation to be converge and complete in at most 24 hours. It is important to note that the time-independent framework used in these simulations modeled at least some portion of the nonlinear/saturation effects present, but time-dependent simulations must be used to fully capture these dynamics. In our work, we were unable to make the time-independent simulations converge after significant search of the simulation parameter space, including the mesh parameters. In general, for complex arrays, we do not have quantitative confidence in simulation results to better than 50% accuracy, due to limitations of the time-independent modeling and

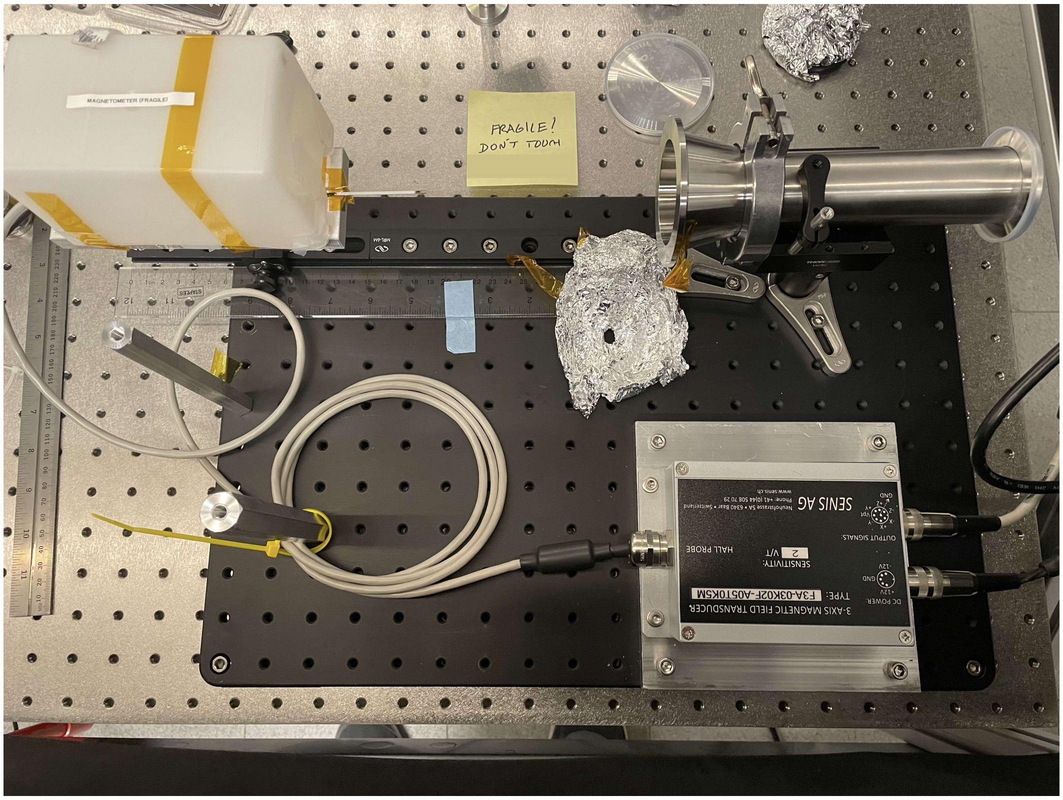

Figure 4.6: Magnetic field measurement setup. The Hall probe sensor is extremely fragile and therefore cannot be rigidly mounted to a hard surface without risk of breaking it. Therefore the probe cable was fastened to an aluminum plate using cable ties and Kapton tape. The plate is mounted on a Thorlabs optical rail mounted against a ruler, used to measure the distance of the probe against some reference value. Due to the way the probe is mounted, there is a slight sag in the position of the sensor relative to the cable. In all field measurements in this thesis, the probe was centered around the air gap by eye.

the need for extensive mesh refinement studies; however, the trends observed here point to promising directions for optimizing magnet design and identify which design features are important.

However, true confidence comes from prototyping and measurement. A few of these magnet designs were built and their on-axis fields were measured using a three-axis Senis Hall Probe (F3A-03K02F-A05T0K5M), which combines a 2 mm thin sensor with a ± 5 T measurement range. The magnetic field measurement setup is described in Fig. 4.6, and relevant measurements are shown in the corresponding subsections below.

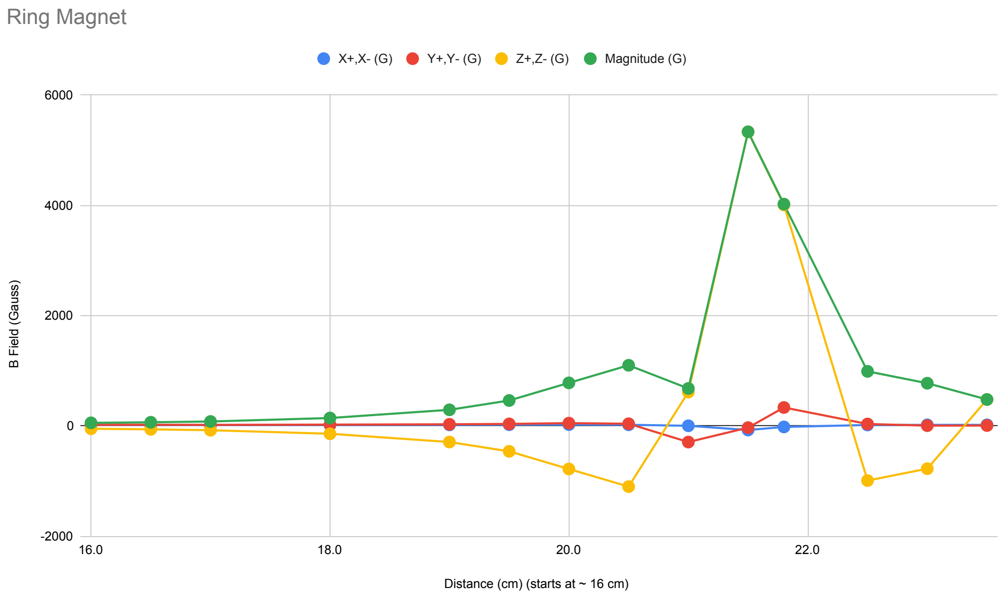

Figure 4.7: Hall probe measurement of magnetic field through the central bore of a ring magnet with magnetization pointing through the bore (K&J Magnetics RX054-N52). The z-axis corresponds to the axis through the bore.

4.3.1 Axially-magnetized ring magnet

A particularly simple magnet for testing a single stage of ZS deceleration is a ring magnet with magnetization through the bore. In this configuration, the molecules would only experience a single stage of slowing, and therefore only a single optical pumping beam is needed, which is sent through the magnet bore. This design was implemented in a K&J Magnetics RX054-N52 NdFeB ring magnet, which was glued to a restrictor ring placed directly in the room-temperature beam line. The peak field achieved in the center of the ring magnet was 0.53 T, which was less than the COMSOL prediction of 0.75 T. The field measured in our setup is shown in Fig. 4.7.

4.3.2 Two-cylinder and Two-cube magnet

Yi Zeng noted that the field in a gap between two sufficiently large rare-earth permanent magnets can easily reach 1 T with little effort, while providing transverse optical access. This configuration is a particularly attractive for a practical test of ZS due to its ease of assembly, modeling, and large optical access. After simulating this simple configuration, the basic design was implemented in two formats.

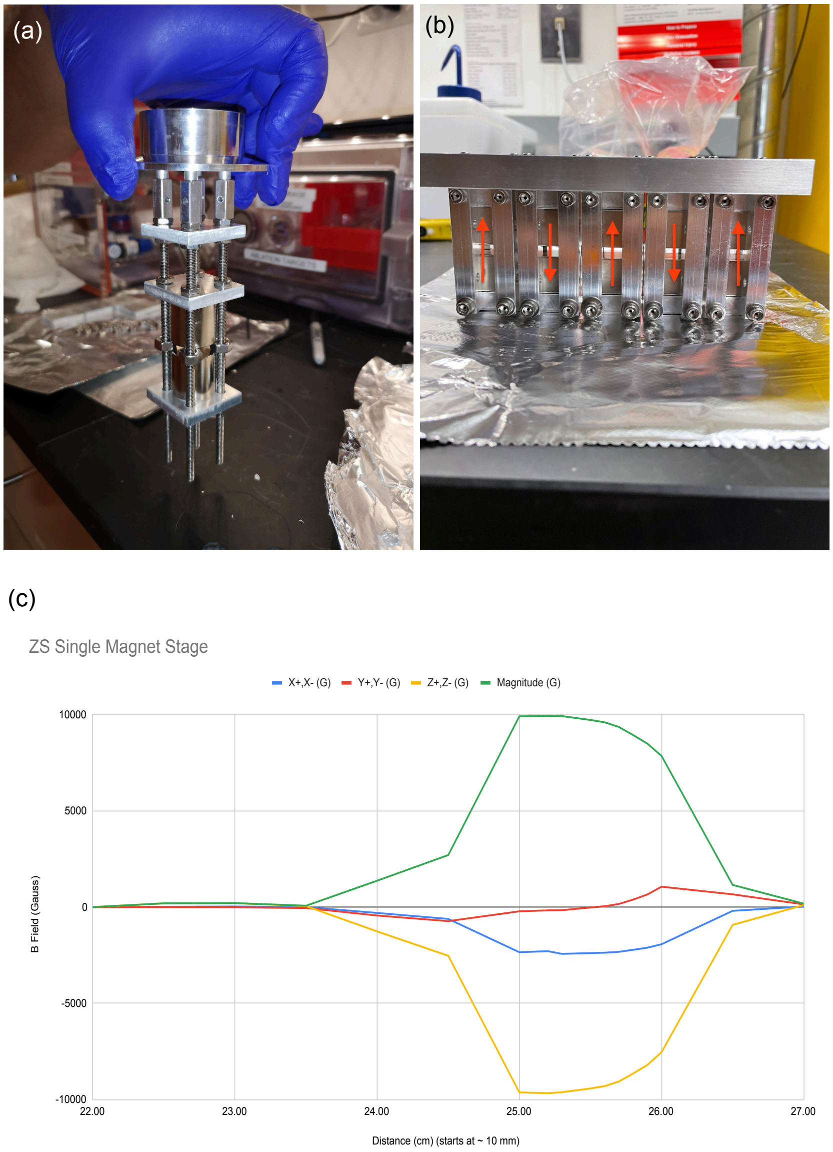

Figure 4.8: Simple ZS magnet stages consisting of two magnets. Arrows indicate the direction of the magnetic field. (a) The "two-cylinder" magnet (0.9874 T in the center) (b) (Side view) Five copies of the "two-cube" magnet, mounted to an adapter plate (0.9938 T, 1.020 T, 0.9978 T, 1.022 T, and 0.9798 T peak, on-axis fields). (c) Hall probe measurement of magnetic field for a single two-cube magnet stage. The axes are inverted compared to other measurements in this thesis because the probe was inserted transverse to the central bore. The z-axis corresponds to the down-up direction in this plot. The relative flatness of the field in the air gap indicates a degree of uniformity in the center of the magnet, as expected from COMSOL simulations.

The first configuration consists of two $1\ \mathrm{in}$ diameter, $1\ \mathrm{in}$ tall cylindrical N52 NdFeB magnets with magnetization through the length of the material. The two cylinders were spaced by roughly $5\ \mathrm{mm}$. The magnets were confined by four 10-32 threaded rods fastened from above to a KF-50 stub, and the spacing was set by four nuts on the rods held between both magnets. The entire assembly was installed in the beamline from the top plate of a $9\ \mathrm{in}$ Ideal Vacuum cube shown in Fig. 3.4. See Chap. 5 for experimental tests of ZS in an atomic beam of $^{23}\mathrm{Na}$ using this single cylindrical stage. The two cylinder design is shown in Fig. 4.8(a).

The second configuration uses $0.75\ \mathrm{in}$ cubic N52 NdFeB magnets, magnetized in the same way as the cylinders, but held in a custom aluminum mounting structure with $3/16\ \mathrm{in}$ "feet" spacing the two magnets. Five of these magnets with alternating magnetic field direction (up-down-up-down-up) were mounted to a custom aluminum adapter plate, which was further mounted by threaded rods to a custom $9\ \mathrm{in}$ plate compatible with the Ideal Vacuum cube (Fig. 4.8(b)). A drawing of the magnet holder and the entire assembly is shown in Fig. 4.9 and COMSOL simulations of the magnetic field achieved in the two-cube design are shown in Fig. 4.10. This diagram indicates that there are both trapping and anti-trapping directions in the center of the magnet, consistent with Maxwell's equations, but both are relatively flat over a $0.5\ \mathrm{cm}$ region about the stage center. The shape of these curves has direct experimental consequences discussed further in Sec. 4.4.1. The original Halbach arrays in the Zeeman-Sisyphus proposal interleaved magnetic guiding stages in between high-field stages to mitigate losses from magnet forces, but we did not consider designs of this kind for the sake of simplicity [66].

A magnetic field profile with the Hall probe transverse to the magnet stage bore is shown in Fig. 4.8 (c), and it indicates the level of uniformity in the peak, on-axis field that one can expect for particles propagating off-axis through the magnet. While simple in construction, there are a number of complications to this design that are experimentally relevant. As indicated in the figure caption, the peak, on-axis fields vary by as much as $\sim 4\%$ between adjacent stages. Note that the second and fourth magnets (which point down) have higher measured peak, on-axis fields than the first, third, and fifth (pointing up). Indeed, during assembly of this array, there is an attractive force between the two magnets in a single stage, as well as between adjacent stages, causing magnets to sit in their mounts in an asymmetric fashion. It is likely that by moving to a design where each stage points in the same direction (up, for example), the asymmetry would be reduced. However, in this configuration all magnet stages would

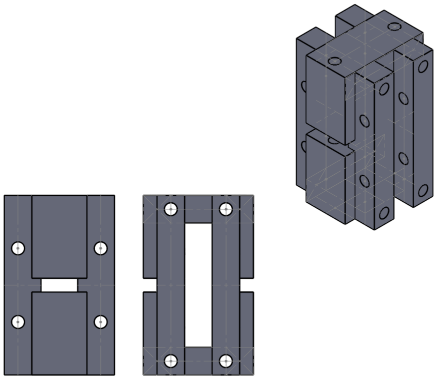

Figure 4.9: The two-cube magnet holder consists of a pair of u-shaped mounts that are held together by four connecting bars and which contain a 3/4 in cube magnet each. The connecting bars have 3/16 in protrusions on which the magnets sit that maintains their spacing. Each of these mounts is connected to an adapter plate that is attached to the top plate of the Ideal Vacuum cube.

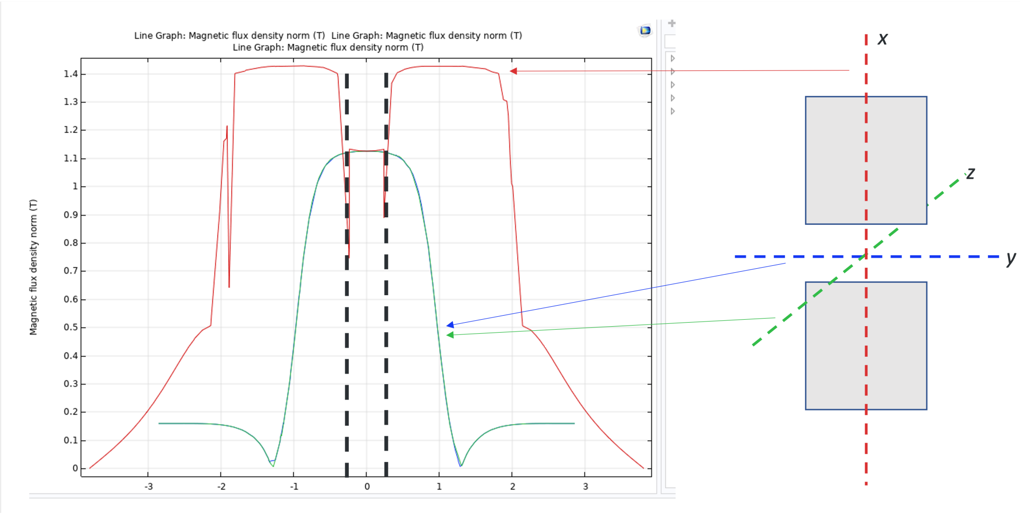

Figure 4.10: Plot of simulated magnetic field magnitude in a two-cube magnet. Each curve shows the magnetic field along a line along the x, y, and z axes and intersect the center of the magnet assembly, placed at the origin. The horizontal axis on the plot is in cm.

repel each other, making assembly-by-hand difficult. Introducing more space between magnet stages would reduce the number of stages that can fit in the Ideal Vacuum Cube from 5 to 3, thereby reducing the increase in field for this experiment compared to the Harvard superconducting implementation. The result of this field asymmetry is that transverse optical pumping beams, which have position-determined frequencies along the beamline, would need to be generated with five independent frequencies per laser to account for the different Zeeman shifts for particles in each stage.

A second complication is that due to attractive forces between the magnet stages, the gaps between adjacent magnets are too small to measure with our Hall probe. Therefore the precise magnetic field behavior between adjacent stages is not exactly known. Adjacent stages are oppositely aligned, which means that the field magnitude likely becomes small due to field superposition between stages. Due to the observed field asymmetries, it is likely that the size of the smallest on-axis field is not so small as to cause non-adiabatic WFS $\rightarrow$ SFS transitions as discussed earlier in Sec. 4.2.2, but the exact behavior is unknown. Furthermore, the tight spacing between adjacent magnet stages greatly limits the optical access for weak-field optical pumping, and the five independent frequencies for this laser would need to be determined empirically without Hall probe measurements for guidance. Once again, having magnet stages aligned in the same direction (with fewer stages and larger inter-stage gaps) would solve this problem, but at the expense of reducing the magnitude of slowing.

Therefore, this magnet array was tested using a simpler configuration with two longitudinally propagating optical pumping beams, though this forwent some of the many advantages of transverse optical pumping and introduced some new challenges in their place. See Chap. 5 for experimental tests of ZS in an atomic beam of ^{39}K using this five-magnet array.

4.3.3 Magnets with pole pieces – Stelter-like

As alluded to in Sec 4.3, permanent magnets can be demagnetized by nearby magnetic fields. The parameter characterizing a material's resistance to changes in magnetization is the *coercivity*, which describes the applied field needed to reduce the material's magnetic field to zero [78]. With magnet arrays constructed out of permanent magnet building blocks, the demagnetization due to adjacent magnets can limit the maximum fields that are achieved. The field maximum can be further optimized by mitigating the demagnetization effect. It has also been empirically observed that permanent magnets are twice as resistant to demagnetization when the demagnetizing field is orthogonal to the magnet orientation [79, 80]. This suggests that it can be beneficial to construct magnet arrays using orthogonally oriented magnets. Note that the adjacent sections of a $K = 2$ Halbach array are not orthogonally oriented.

Furthermore, because the primary objective is to increase the field strength in a particular small region, soft magnetic materials—in particular materials with high permeability and high saturation induction—can be leveraged to divert and focus field lines through particular regions, while reducing field leakage and fringing away from the central bore. Mu-metal is a soft-magnetic nickel-iron alloy commonly used in EDM experiments for magnetic shielding. While mu-metal has a high permeability, the material saturates at around 0.75 T, and therefore not particularly useful in amplifying field flux far over 1 T. A more ideal material is Hiperco 50A, which is a iron-cobalt-vanadium alloy, that saturates at 2.4 T, though its permeability is roughly an order of magnitude lower than mu-metal.

U.S. Patent 5635889A describes an invention by Richard E. Stelter that combines the orthogonality of adjacent magnets and tapered soft magnet pole pieces to achieve 2.2 T fields in a small air gaps [81]. These “Stelter” magnets described in the patent are currently exclusively sold by Dexter Magnetic Technologies with fields as high as 3.0 Tesla, with larger fields in small air gaps and more uniform fields in larger air gaps. While this vendor was not interested in designing a Stelter magnet for our application, we pursued some “Stelter-like” magnets using the basic principles outlined above. Other research groups have demonstrated large magnetic fields using the design principles outlined here [82].

The first such design utilizes rectilinear (as opposed to tapered/trapezoidal) Hiperco 50A pole pieces with exclusively horizontal and vertical magnet polarizations. This design was modeled extensively in COMSOL and experimentally prototyped. The second design, detailed in Sec 4.3.4 is a more significant departure from the Stelter structure but utilizes many of its basic design principles, with the additional benefit of transverse optical axis for optical pumping at particular magnet locations.

The Stelter design was simulated in COMSOL assuming N52 NdFeB magnets and Hiperco 50A pole pieces. Along with the Stelter geometry using trapezoidal pole pieces, two additional simplified designs were investigated that had rectangular pole pieces and no pole pieces, respectively. All three geometries are shown in Fig. 4.11. The first set of simulations fixed the transverse cross-section of the magnet array to be an $80\ \mathrm{mm} \times 80\ \mathrm{mm}$ square, and varied the shape of the pole piece and the size of the air

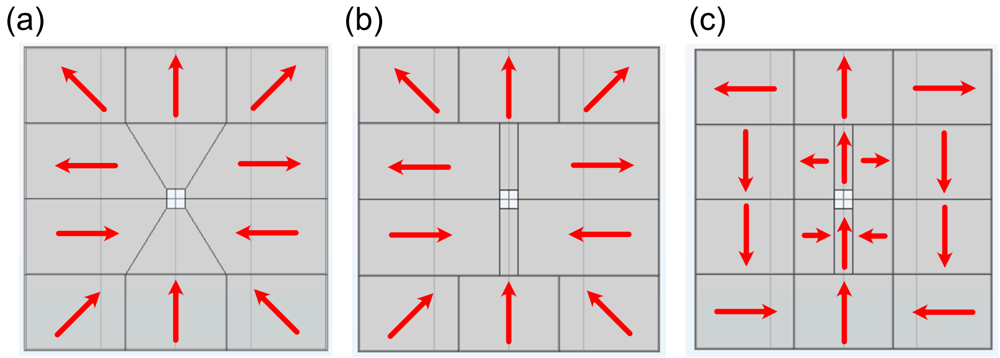

Figure 4.11: Several variations on the Stelter magnet geometry which were simulated in COMSOL. Magnetizations are shown in red. Gray segments without magnetization correspond to Hiperco 50A pole pieces. (a) The original Stelter magnet. (b) A Stelter magnet using rectilinear pole pieces only. (c) A Stelter magnet without pole pieces.

gap (5 mm or 10 mm square). Similarly, the thickness of the magnet stage was varied from $5-30$ mm. Finally, for a 5 mm square air gap, 20 mm thickness, and rectangular pole piece, the dimension of the square cross-section was varied from 30 mm $-$ 100 mm side length. Additional versions of the simulation considered the presence of aluminum or stainless steel mounting structures on the front and back of the magnet assembly (and around the perimeter) as well as a magnet made entirely out of identical cubes with nonzero spacing between each cube reflective of real-world mounting requirements. In each of the dozens of resulting simulations, the field magnitude at the center of the magnet was determined. In order to gauge the field uniformity, the minimum magnetic field in a circular region in a plane transverse to the air gap axis was also determined.

In summary, our simulations found that (1) rectangular pole pieces achieved the largest maximum fields in the air gap with comparable uniformity to trapezoidal pieces, and that these maximum fields increase with (2) decreasing air gap, (3) increasing thickness, and (4) increasing cross-sectional area. This is not particularly surprising given in our construction that the magnet sizes themselves scale with increased thickness and cross-sectional area.

A simple variation of this design was also experimentally studied using 0.5 in thick rectangular N52 NdFeB magnets mounted in an aluminum magnet mount (Fig. 4.12). The magnets were slotted into their corresponding cutouts, and the field was measured with and without two Hiperco 50A pieces inserted in the middle. The Hiperco 50A pieces were cut by a waterjet out of a larger slab purchased from the supplier, Ed Fagan. Magnetic materials such as Hiperco 50A can lose their properties when exposed to

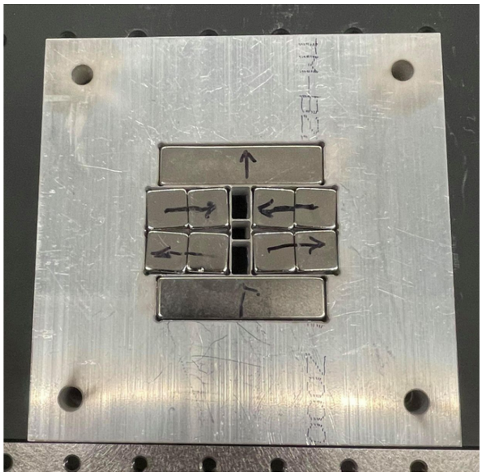

Figure 4.12: Experimental implementation of a simplified Stelter-like ZS magnet with magnetization direction drawn in marker, mounted in an aluminum structure. The slots above and below the central air gap are for pole pieces. The front and back aluminum mounts are not shown. Ultimately, the insertion of pole pieces did increase the peak, on-axis field but not as much as was predicted by COMSOL simulations.

stresses, especially from machining due to the disturbance of existing magnetic domains in the material. Thus, before testing magnetism, the Hiperco pieces were sent to Solar Atmospheres, Inc. to be annealed in a dry hydrogen atmosphere. Pieces of Hiperco were cut both vertically and horizontally out of the slab in order to test for the effect of material grain orientation.

While constructing the array, the magnets experienced forces from other nearby magnets, leading to some deflection of the orientation when they are placed in their corresponding slot. To adjust the orientation of the magnets, small pieces of Kapton tape were used as shims. The field at the center of the magnet was measured with and without the pole piece. In all testing, the horizontally cut and vertically cut pole pieces showed no significant relative difference, and the presence of the pole piece increased the field maximum from 8350 G to 9400 G, while COMSOL simulations predicted an increase from 10198 G to 13060 G.

It is apparent that this the prototype did not demonstrate the predicted increase due to the pole material, and further modeling of the nonlinearity in this system is required to understand the observed field magnitude and guide future designs using pole pieces. Full modeling of the magnet nonlinearity will be required to account for the discrepancy between the measurements and predictions.

4.3.4 Magnets with pole pieces – Cube rod and Cylinder rod

Simulations suggest that there are simple magnet arrays that can combine the high fields of Stelter-like magnets with transverse access and field uniformity. Two of these designs—the "cube rod" and "cylinder rod"—were simulated, but were not built for laboratory testing. Nevertheless, the designs show promise for use in ZS deceleration and are worthy of mentioning here as well as further study.

In the cube rod design, a rectangular slab of Hiperco 50A is surrounded by rectangular magnets with orientation pointing toward the central slab. Underneath is a second slab surrounded by rectangular magnets with orientation pointing away from the slab. The gap between the top and bottom pieces is the region where particles can travel, and the field points from the top piece towards the bottom piece. The cylindrical rod design is an idealization of this design, where the central slab is a cylinder surrounded by a single annular magnetic piece with radial magnetization pointing towards (or away from) the center. This design has a central gap that allows for both transverse optical access and a large, uniform magnetic field on the longitudinal plane in the air gap.

Both designs were modeled in COMSOL, with variation in the dimensions of the pole piece and surrounding magnets, the extent of the pole that protrudes further than the bottom of the magnet ("slideback"), whether the pole pieces is tapered to a smaller face, and whether said taper is "single-sided" or "double-sided" in the case of the cube rod. Additionally, the cube rod simulations studied configurations where individual magnets had diagonal magnetizations as well as strictly rectilinear configurations (while in the cylinder rod case, the magnetization points radially towards or away from the center). Examples of all these geometries are shown in Fig. 4.13. These configurations have practical utility for ZS slowing. For example, nonzero slideback would allow for a less constrained beamline, increasing vacuum integrity in a room temperature beamline and reducing collisional loss from backscatter. Furthermore, magnets without diagonal magnetization are much easier to procure from standard suppliers as stock items.

In each simulation, the peak, on-axis field value was extracted. For the sake of practicality, here we primarily discuss the cube rod design, as the cylinder rod is an extreme generalization and would be difficult to procure in practice. The results of simulations studying slideback on a cube rod design with an untapered pole piece is shown in Fig. 4.14(a), while the results of a single and double-sided taper on a magnet with fixed slideback is shown in Fig. 4.14(b). Slideback predictably decreases the field maximum, while tapering the pole piece can in fact increase the maximum field achieved by a

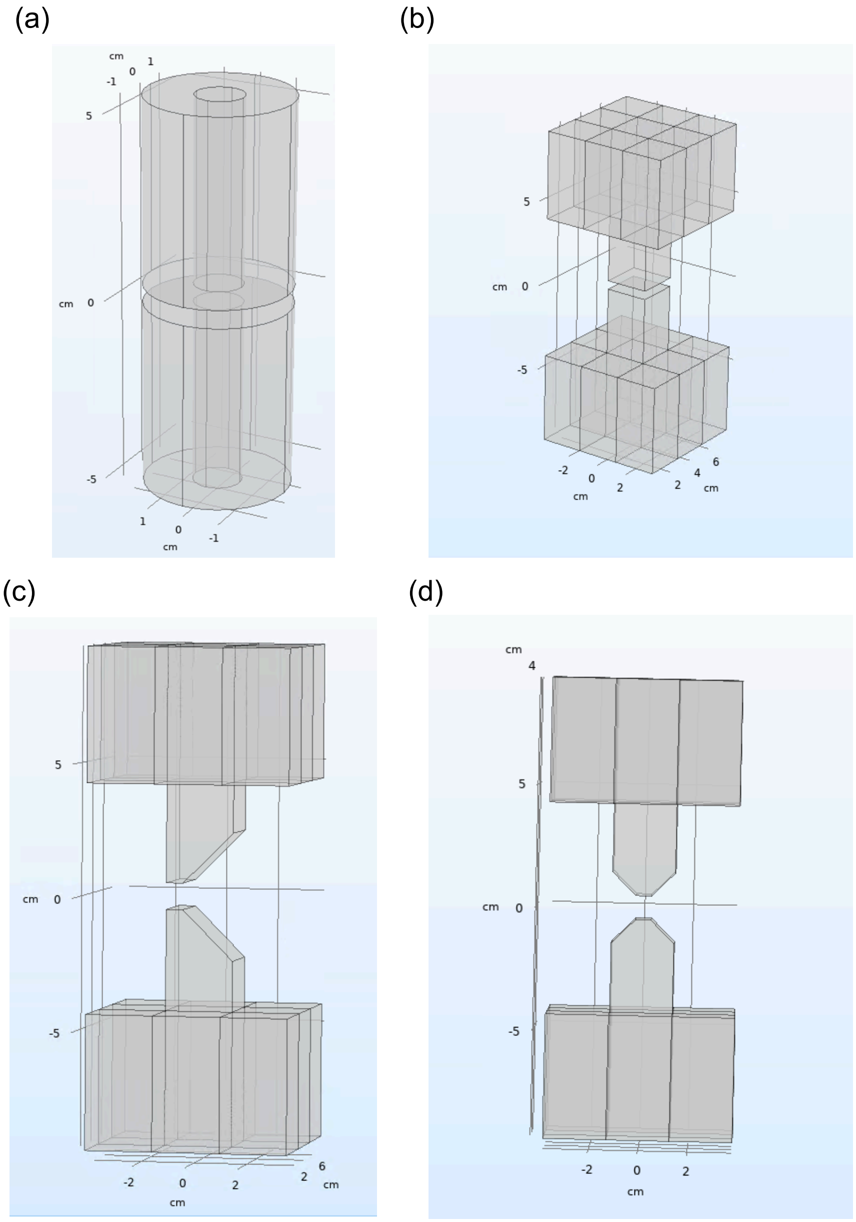

Figure 4.13: Magnet geometries inspired by the Stelter(-like) magnets. (a) Cylinder rod magnet where the top cylinder has magnetization pointing radially inward and the bottom has magnetization pointing radially outward. In the center of both cylindrical magnets are cylindrical Hiperco 50A pole pieces. (b) Cube rod magnet with "slideback" in which central pole piece is exposed beyond edge of top and bottom magnets. Magnetization directions for the cube rod are essentially the same as for the cylinder rod, except that the radial directions is discretized among the rectilinear magnets present (c) Cube rod with slideback and single-sided taper. (d) Cube rod with slideback and double-sided taper.

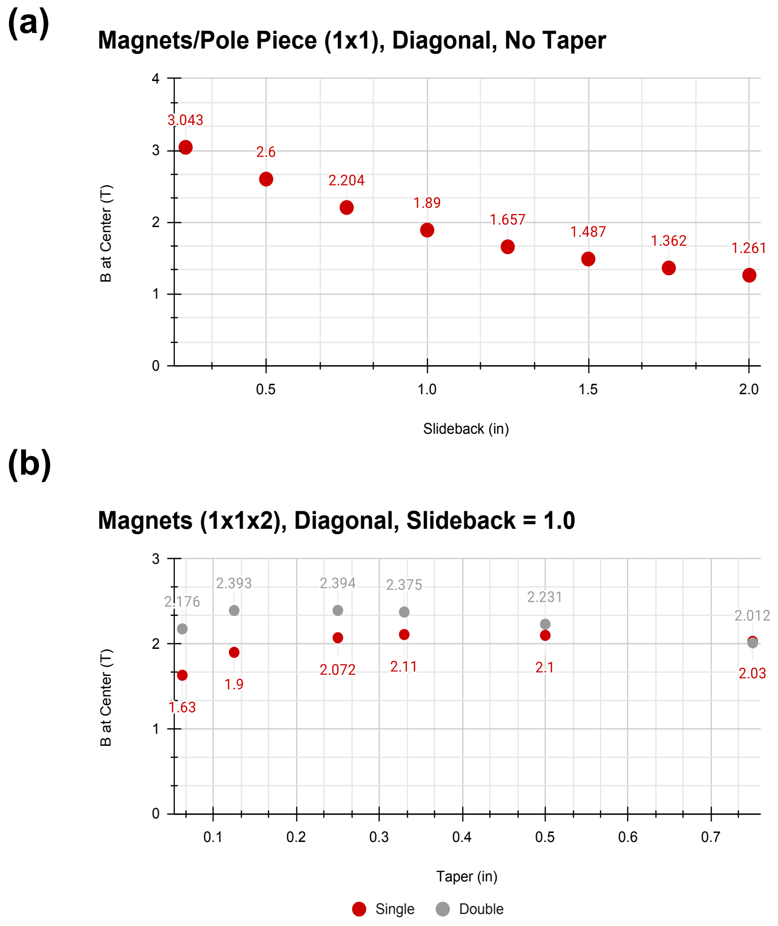

Figure 4.14: Peak, on-axis magnetic field values from COMSOL simulations of the cube rod design. (a) Results for simulations with no taper while varying slideback. (b) Results for simulations with single or double-sided taper of a pole piece with fixed slideback.

non-negligible amount, with a more pronounced increase for a double-sided taper, though this effect is not dramatic. This suggests a design principle in which the field decrease from slideback can be compensated with pole tapering. Furthermore, simulations suggest that while increasing the length and width of the array can increase the field achieved in the center, an increase in the height of the magnets between $2-4$ in has a negligible effect.

A number of promising designs were identified from the simulation results, with fields achieved between $1-2$ T. One design in particular, shown in Fig. 4.15 is a further simplification where where only four rectangular magnets surround a fixed-size pole piece. The air gap is 5 mm, with the pole piece protruding by 1 in with a 0.125 in

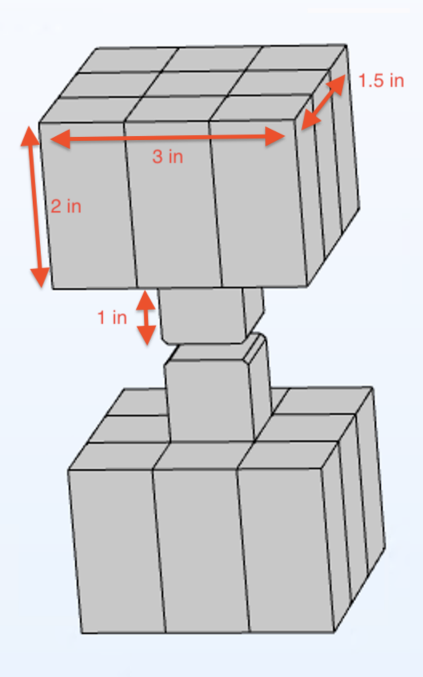

Figure 4.15: A particular practical design for a cube rod magnet. COMSOL predicts a maximum, on-axis field of 1.8 T, with a taper length of 0.125 in.

double-sided taper. COMSOL simulations found that the field achieved here can reach 1.8 T. Going beyond the two-cube and two-cylinder designs we actually used for ZS prototyping will require the use of pole pieces, and tapered pole pieces promise large magnetic field enhancements. Ultimately, further laboratory testing is required to gauge the quantitative accuracy of these simulations.

4.4 Simulation of ZS deceleration

Using both idealized, analytical magnetic fields (e.g., a sinusoidal field in one direction, which does not solve Maxwell's equations) as well as physical solutions from COMSOL simulations, the simulation framework described in Sec. 3.4 were used to study possibilities for Zeeman-Sisyphus deceleration. Simulations were performed in both 1D and 3D, with a variety of laser powers, and with realistic and simplified level structures. For the sake of brevity, only a few simulations are described here. Ultimately, most of the work around ZS was experimental in nature.

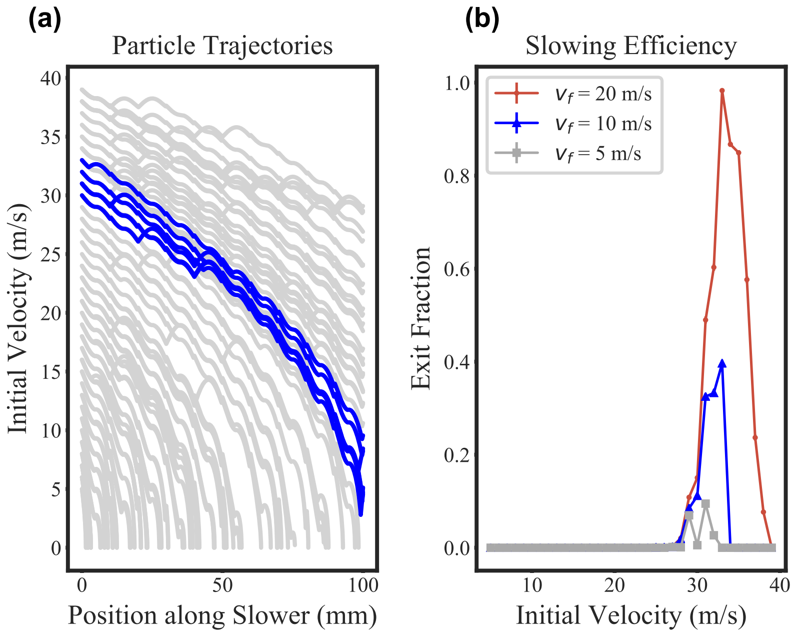

Figure 4.16: Simulations of Zeeman-Sisyphus in YbOH molecules. (a) YbOH trajectories. Trajectories in blue are molecules slowed to final forward velocities $v_f < 10$ m/s. (b) Fraction of particles exiting Zeeman-Sisyphus slower with $v_f < 5, 10,\ 20$ m/s as a function of initial forward velocity.

4.4.1 Simulating loss due to magnet anti-confinement

One particular simulation that provided insight into the challenges of permanent magnet ZS deceleration explores the behavior shown in Fig. 4.10. In particular, this simulation shows that for the two-cube magnet (Sec. 4.3.2), at the magnet center the WFS particles experience forces that push them out the sides of the magnet, as well as a restoring force in the direction parallel to the magnetization. The SFS particles, on the other hand, are pushed towards the magnets, but are confined in the other directions. Importantly, when the SFS particle is more than ~ 0.25 cm away from the center of the magnet, the force pushing it toward the magnets is much stronger due to than the forces pushing on the WFS particles. This asymmetry means that the particular amount of time that WFS and SFS particles spend in the high-field region has a direct impact on the loss through the slower. SFS particles with large transverse velocities that quickly traverse away from the central axis are prone to loss compared to WFS particles.

We conducted Monte Carlo simulations to gain insight into the loss of SFS particles. The simulations was initialized using 100000 ^{39}K atoms and the simulated magnetic field for the five-stage two-cube magnet (Fig. 4.8(b)) as an interpolating function, rescaled to account for the actual measured magnetic fields in the lab. The simulation was run with lasers turned off to study the loss behavior in the absence of optical pumping.

The atoms were initialized to randomly fill a $5 \text{ mm} \times 10 \text{ mm}$ rectangular corresponding to the actual air gap in the magnet. The initial transverse velocity was uniformly distributed from $0 - 5 \text{ m/s}$ and the initial forward velocity was uniformly sampled from $0 - 200 \text{ m/s}$. The particles begin at $z = 0 \text{ mm}$, and the magnets lie in between $z = 10 - 151.3 \text{ mm}$; the magnetic field is zero at $z = 175 \text{ mm}$, and particles are detected at $z = 350 \text{ mm}$, corresponding to the actual distances in the lab.

Some summary plots for the simulations are shown in Fig. 4.17 and Fig. 4.18. As expected, the former figure shows that loss for SFS atoms through this five-stage array is larger than for the WFS atoms. The latter figure shows that while WFS atoms that crash in transit crash into the four walls that surround them, the SFS atoms are more likely to crash into the magnets themselves more than the other two surfaces. This behavior is due to the strong forces that push them into the magnet surfaces. Furthermore, the simulations show that slow particles do not exit the slower due to the longer amount of time they spend in the slower, subject to anti-trapping forces. The consequences of this behavior in a slowing configuration is the subject of further simulation and experimental testing.

4.4.2 Extensions: A toy model for ZS deceleration

While simulations like those above are useful for determining ZS dynamics, an accurate simulation with small-enough time steps and sufficient numbers of particles requires computational time to run. Such full simulations are not as useful for making rapid determinations of what kind of slowing behavior is expected. On the other hand, the simplest possible model, whereby a particle remains on-axis and is optically-pumped with unit probability at exactly the correct positions along the slower amounts to a simple paper-and-pencil calculation (See Fig. 5.1 for an example); but this calculation does not capture the realistic scenario of imperfect optical pumping and its consequences.

We conclude this chapter by describing a toy model for ZS deceleration that was developed to bridge the gap between a full simulation and the simplest possible calculation. This model is 1D, and assumes all particles remain on the central axis, and assumes that there are only two ground states. The optical pumping probabilities for SFS $\rightarrow$ WFS

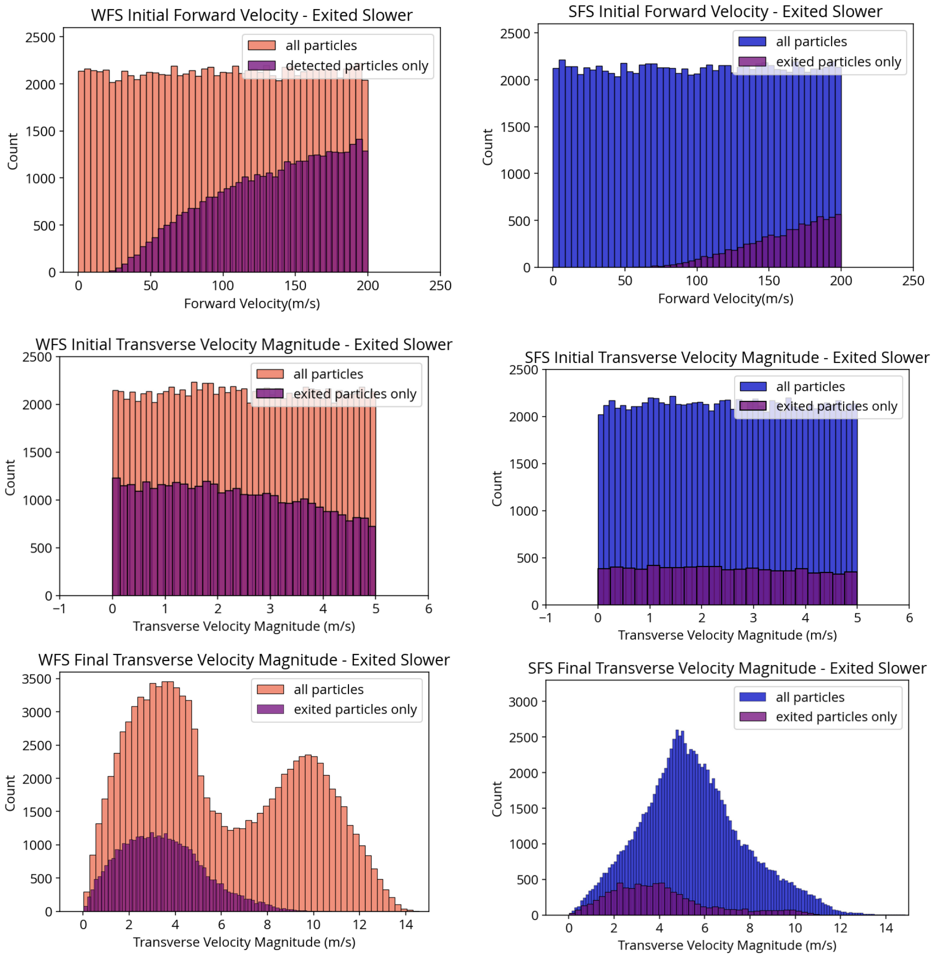

Figure 4.17: Initial forward velocity distribution and initial and final transverse distributions for particles that exit the five stage two-cube magnet. Final forward velocities are not shown because the laser power is set to zero in these simulations, and no deceleration slowing will occur. Results for particles that are detected further downstream but the additional losses there are fully determined by ballistic expansion of the particles as opposed to forces from the magnets.

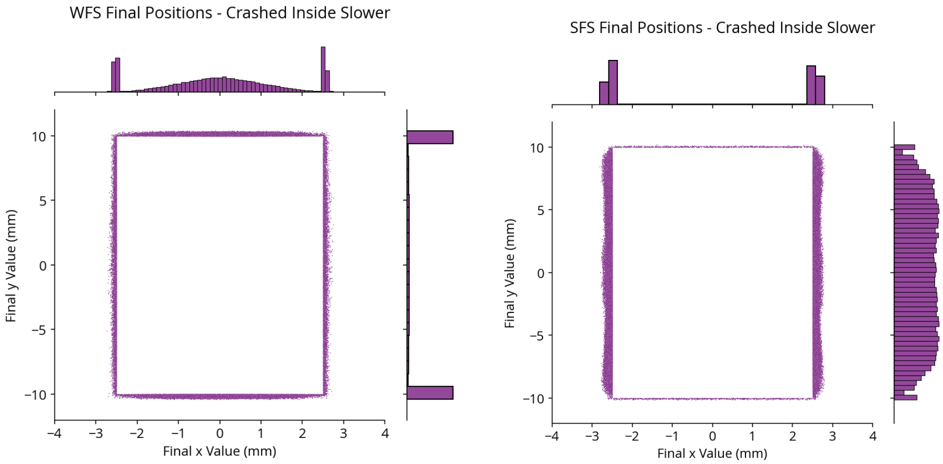

Figure 4.18: Final position in a transverse plane for particles that crashed inside the five stage two-cube magnet array.

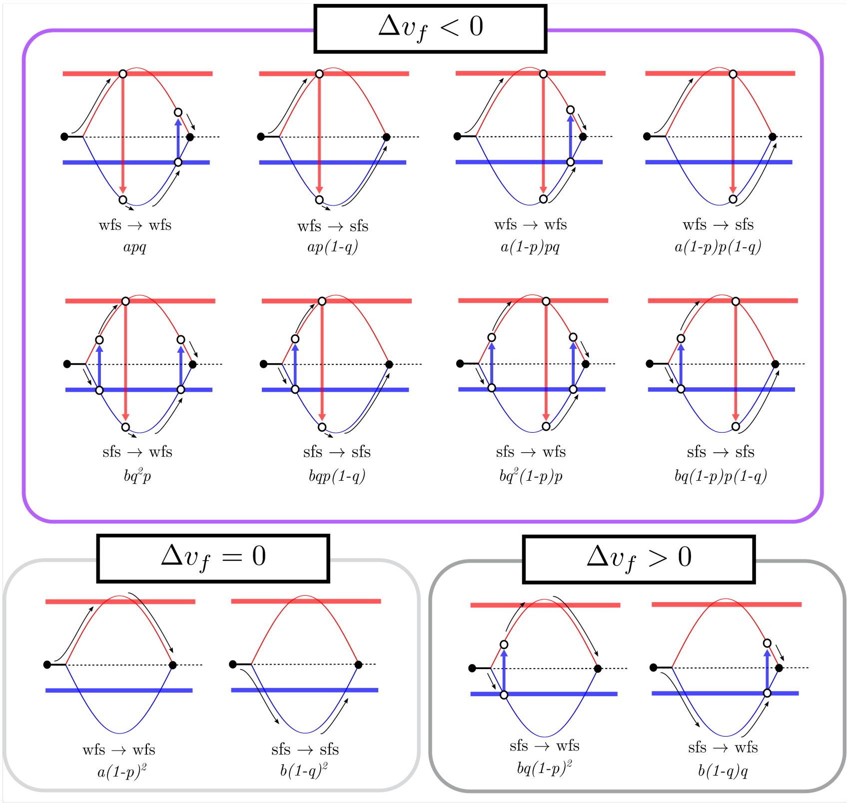

Figure 4.19: Enumeration of possible optical pumping and associated forward velocity change for a 1D, single-stage Zeeman-Sisyphus scheme for a two-level ground state.

and WFS $\rightarrow$ SFS are described by fixed probabilities p and q, respectively. The imperfect optical pumping leads to variance in the final velocity distribution.

For each magnet stage, there are twelve possible outcomes per stage depending on the initial stage of the particle (WFS or SFS) and whether it gets pumped at high field or at low field (Fig. 4.19). The effect of these outcomes is determined by energy conservation and can be calculated exactly. For every input configuration, consisting of the ground state sublevel and initial forward velocity, the probability distribution of output configurations (final forward velocity and ground state sublevel) are calculated. Treating the output configurations and probabilities for one stage as the input for the following stage, the calculation can consider multi-stage ZS slowing. This procedure is repeated for all relevant initial forward velocities for both ground state sublevels. All probability distributions are totaled and normalized to give a calculated final forward velocity distribution, which should give an accurate picture of 1D ZS deceleration when the number of propagating particles is large. While the number of possible outcomes grows exponentially with each additional ZS stage, the calculation terminates nearly instantaneously for the five stage array we consider here.

For a $1\ \mathrm{T}$ magnet, a red-detuning of 0.9 of the magnetic field maximum, and a blue detuning of -0.1 of the magnetic field maximum, we studied the probability of returning to the WFS state after a single ZS stage, as well as the expected velocity change for a ^{39}K atom moving at $100\ \mathrm{m/s}$ (Fig. 4.20). As expected, the velocity change is largest when the optical pumping probabilities p and q are close to 1, and the particle is most likely to return to the WFS state when q is close to 1.

For illustrative purposes, we plotted the results of the model for five ZS stages where $p, q = 1$, and where the input forward velocity distribution is given by a Gaussian with mean $200\ \mathrm{m/s}$ and FWHM of $100\ \mathrm{m/s}$ (Fig. 4.20). We can see that the final velocity of the WFS particles is slower than the input distribution, and due to the perfect pumping, there are no particles left in the SFS state by the end of the slower. As p and q are reduced from 1, variance in the final velocity distribution decreases the deceleration that is observed on-average.

In reality, the p and q parameters are determined by the magnetic field gradient, particle velocity, and laser power. A more-realistic extension of this model would treat p and q as functions of v_z. Simulations in Python using the QuTiP package were developed to determine $p(v_z)$ and $q(v_z)$ by modeling the atom as a two-level ground state with a single excited state using calculated Zeeman shifts from real atomic structure parameters, in a magnetc field environment determined by COMSOL. This system can be described

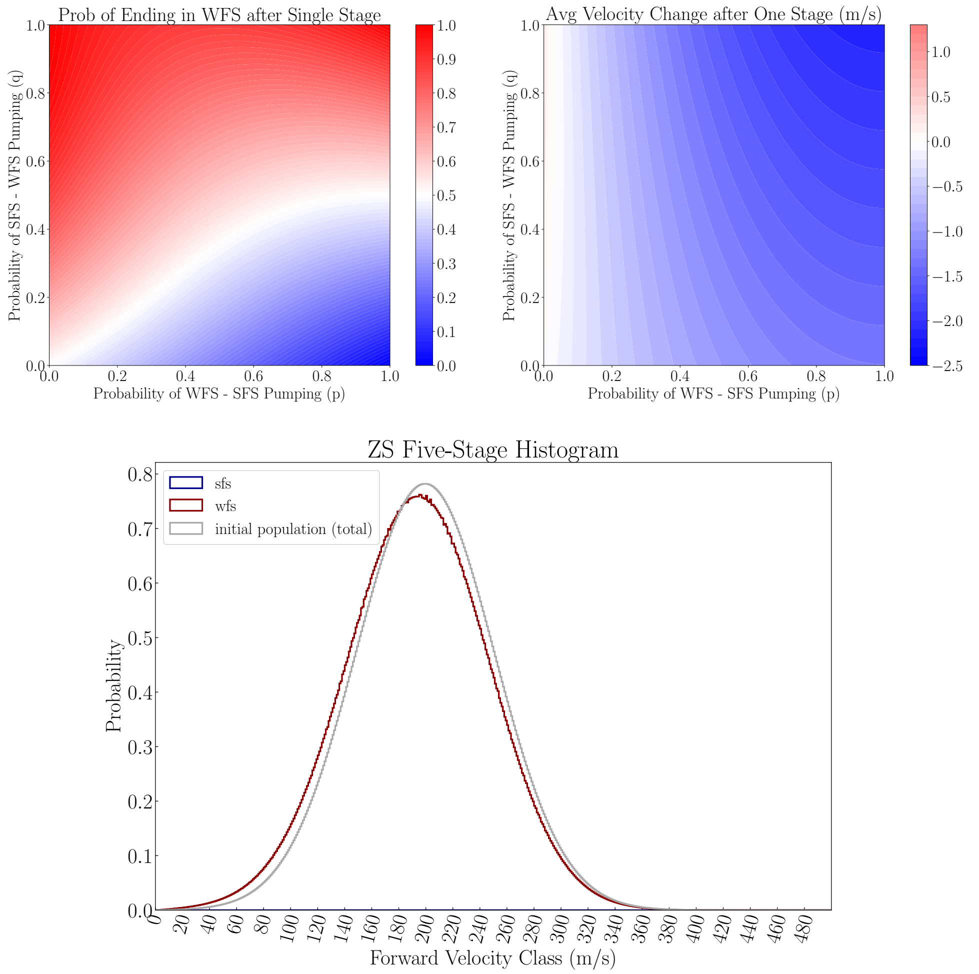

Figure 4.20: Summary of results from the 1D toy model. (Top) Expected probability of returning to the WFS state and forward velocity change after a single ZS stage. (Bottom) Expected final forward velocity distribution for WFS and SFS final states after five ZS stages.

by a three-level Hamiltonian where the laser detuning varies with time as the atom with velocity v_z experiences a Zeeman shift as it moves through the resonance. The time-dependent Hamiltonian with spontaneous emission can be modeled using a Lindblad master equation solver, and the results give the final state amplitudes that can be used to determine p and q for each v_z. Issues with convergence prevented further development of this calculation, but this model is a natural and accurate way to determine the true optical pumping probability in a nontrivial magnetic field environment without resorting to time consuming Monte Carlo simulation.

This approach is in a sense brute force, but underlying it is the simplicity of 1D energy conservation. Ultimately, this toy model fails to take into account the very real phenomenon of beam divergence, but it nonetheless shows that even in a best-case scenario, the changes in velocity at the level of distributions is likely to be modest, foreshadowing the difficulty in experimentally observing ZS deceleration discussed in the next chapter.

Acknowledgments

This work was supported by the Gordon and Betty Moore Foundation and the Alfred P. Sloan Foundation. We thank Ben Augenbraun, Zack Lasner, Amar Vutha, and other collaborators for useful conversations and atomic/molecule structure code.

Chapter 5

Prototyping Zeeman-Sisyphus Deceleration in Atoms

> *"Marco Polo describes a bridge, stone by stone.*
> *'But which is the stone that supports the bridge?'*
> *Kublai Khan asks.*
> *'The bridge is not supported by one stone or another,' Marco answers, 'but by the line of the arch that they form.'*
> *Kublai Khan remains silent, reflecting. Then he adds: 'Why do you speak to me of the stones? It is only the arch that matters to me.'*
> *Polo answers: 'Without stones there is no arch.'"*
>
> Italo Calvino, *Invisible Cities*

In this chapter, we overview the experimental effort to study and prototype Zeeman-Sisyphus deceleration. Because of the much smaller cryogenic, vacuum, and financial overhead, permanent magnet designs were used instead of superconducting solenoids. The main purpose of this work was to demonstrate the effect, and therefore, rather than contend with the vast forest of molecular states and loss channels in molecules like YbOH, we decided to study the deceleration in the much simpler setting of alkali atoms. While the experimental work in this chapter is presented in a simple linear fashion, the work was conducted over a period of three years, interspersed with periods of simulation, calculation, and theory detailed in the previous chapter. Ultimately, the Zeeman-Sisyphus deceleration effect was not conclusive in the systems we studied, but many lessons were learned that should aid the next person who wishes to build a permanent magnet decelerator.

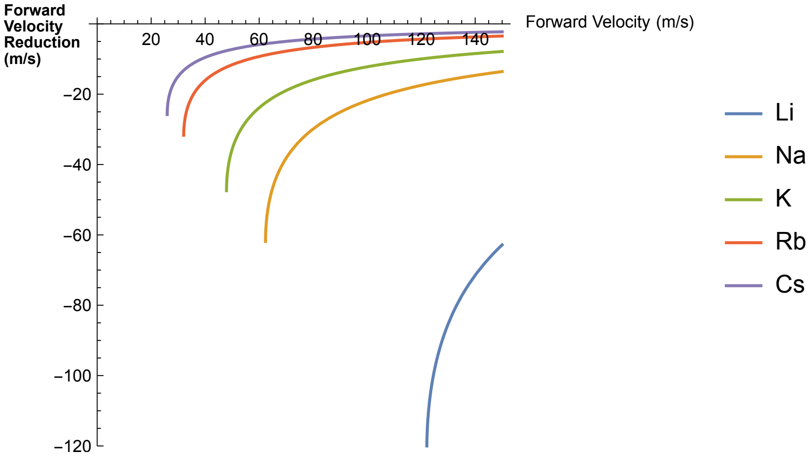

Figure 5.1: Estimated amount of slowing from a five-stage ZS decelerator using 1 T magnetic fields for several alkali atoms for atoms that are optically pumped properly at each stage.

5.1 ZS deceleration in alkali atoms

The alkali atoms have among the simplest structure of all atomic systems, with a single unpaired electron in the ground S state and the excited P state. The ground state is then a ${}^2S_{1/2}$ and the excited states are, taking into account spin-orbit coupling, ${}^2P_{1/2}$ and ${}^2P_{3/2}$. The D1 line commonly refers to the ${}^2S_{1/2} \rightarrow {}^2P_{1/2}$ transition, and the D2 line refers to ${}^2S_{1/2} \rightarrow {}^2P_{3/2}$; we adopt the same convention in this thesis.

The alkali atoms that could conceivably be easily produced in a buffer gas source are Li, Na, K, Rb, Cs. For the sake of comparison, we can determine the ideal behavior of each species in a Zeeman-Sisyphus decelerator as follows. Consider an atom with forward velocity v_z moving through n ZS stages with maximum magnetic field magnitude B_{max}. The alkali atom is idealized to have a two-level ground state with WFS and SFS character, respectively, for the pair of sublevels, with all of the initial population in the WFS state. An atom that is optically pumped to the intended states for ZS each time loses approximately $2\mu_B B_{\text{max}} \times n$ of energy.[1] Conservation of energy can then be used to determine the final forward velocity, and therefore the amount of slowing, as a function of v_z. In Fig. 5.1, we plot the change in velocity for Li, Na, K, Rb, Cs for a set of five, 1 T magnet stages, motivated by the two-cube array described in Sec. 4.3.2.

---

[1] This expression is only approximate because the optical pumping lasers are detuned slightly from the field magnitude maxima and minima for reasons discussed in Sec. 4.2.

This simple calculation omits a some important factors. Most importantly, the real transition dipole moment and branching structure of the multilevel ground state determines the WFS $\leftrightarrow$ SFS optical pumping efficiencies. Furthermore, the transverse forces from the magnetic field are ignored, along with the highly relevant phenomenon of transverse loss. In reality, the final velocity for a particular input velocity becomes smeared into a distribution out due to loss of atoms and inefficient optical pumping. This simple calculation provides an initial assessment of which alkali atoms are most feasible for a test of ZS deceleration. For a more comprehensive toy model see Sec. 4.4.2. Ultimately, both $^{23}\mathrm{Na}$ and $^{39}\mathrm{K}$ were selected as candidate atoms for this work due to their relatively light atomic masses and the availability of the laser resources required to demonstrate the effect.

Both $^{23}\mathrm{Na}$ and $^{39}\mathrm{K}$ have $I = 3/2$ nuclear spins, and therefore their Zeeman structures and optical pumping/branching characteristics are essentially identical. While simple, there are some subtleties that presented difficulties in our ZS tests in these systems that are important to bear in mind. Historically speaking, the following discussion was fully appreciated only when attempting the ZS scheme in $^{39}\mathrm{K}$ as opposed to our earlier single stage attempts with $^{23}\mathrm{Na}$.

The alkali atomic structure was modeled by diagonalizing effective Hamiltonians for the S and P states in the atom with a Matlab program, slightly modified from one graciously provided by Ben Augenbraun. Both atoms have $F'' = 1$ and $F'' = 2$ ground states with 3 and 5 magnetic sublevels, respectively. At modest magnetic fields when the electron spin is decoupled from the nuclear spin, four states are WFS and four are SFS. This means that the $F'' = 1$ and $F'' = 2$ designations at low fields does not exactly correlate with the SFS and WFS designations at high fields. In particular, the lowest energy $F'' = 2$ sublevel in the ground state correlates to an SFS state at high field, along with the other three sublevels in the $F'' = 1$ ground state. This means that when the atom population is probed at zero magnetic field, a portion of the SFS population will be correlated back into the $F'' = 2$ ground state with the four other (slowed) WFS sublevels. Probing the $F'' = 2$ state can be used to determine the slowed velocity distribution of the WFS states, but there is an inevitable dilution of the signal due to the influx of the one (unslowed) SFS sublevel that correlates into $F'' = 2$ at low fields, where populations are measured. The only way to avoid this situation is to initially optically pump into the stretched $F'' = 2$ state and/or use a magnetic guide at some nonzero field to direct only WFS states into the detection region. Neither approach was used in our ZS testing due to the additional laser resources required and engineering complexity, but these are natural directions forward to make the signal extraction and interpretation more unambiguous.

Using the modeling program, we calculated the eigenstate mixtures and transition dipole moment matrix as a function of magnetic field to extract the branching ratios and transition strengths (as a fraction of the reduced dipole moment). Using this one can conclude, for example, that the transition moment matrix is virtually identical at the 1 T field where WFS $\rightarrow$ SFS pumping happens and the $\sim 0.1 - 0.2$ T field where SFS $\rightarrow$ WFS pumping happens, supporting the decision in the particle trajectory software to use a single transition moment matrix that is independent of magnetic field.

There are two optical pumping laser polarizations that are of primary interest (Fig. 5.4). The first, π-polarization, describes a pump beam with polarization parallel to the magnetic field. One relevant and illustrative case is for a ring magnet with magnetization through the bore (discussed in the next section). The lack of transverse optical axis through the magnet means that the pumping beams must propagate longitudinally. Maxwell's equations forbid the laser polarization from lying along the propagation direction vector, and therefore π-polarization is not possible for this magnet.

The second polarization, here referred to colloquially as "mixed sigma," or $\sigma_+ + \sigma_-$, has the pump polarization is perpendicular to both the beam propagation and the magnetic field direction. The D1 line branching ratios and transition moments for both polarization schemes at $B = 1$ T are shown in Fig. 5.2. The transition moments are listed as a fraction of the reduced dipole moment for each species. The states are given in the decoupled ($|m_S = m_J, m_I\rangle$) basis. Additionally, Fig. 5.3 shows workable optical pumping schemes for WFS $\rightarrow$ SFS and SFS $\rightarrow$ WFS for each polarization configuration.

ZS deceleration relies on the particles being optically pumped at the correct magnetic field values and therefore at the correct positions along the beamline. Because the magnetic field direction sets the quantization axis and because the field direction changes throughout the beamline, it is possible for the laser polarization to be a mixture of π and $\sigma_+ + \sigma_-$. The allowed transitions for both polarizations occur at different energies, different magnetic fields, and therefore different positions. In the configuration with longitudinal pump beams, there is laser power at all locations, which creates the possibility of accidental transitions occurring at incorrect locations in the decelerator.

Typically, the WFS $\rightarrow$ SFS pumping occurs at very large detunings that preclude accidental transitions because the allowed transitions for π and $\sigma_+ + \sigma_-$ are extremely

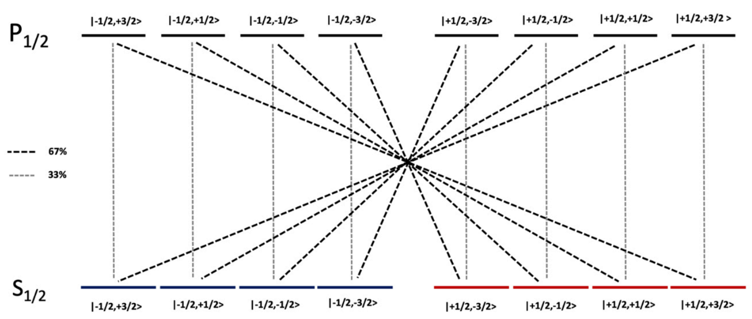

Branching Ratios - $|m_I, m_J\rangle$ basis

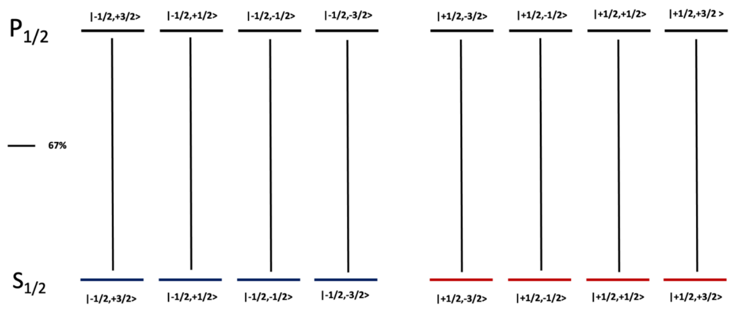

π transitions – $|m_I, m_J\rangle$ basis

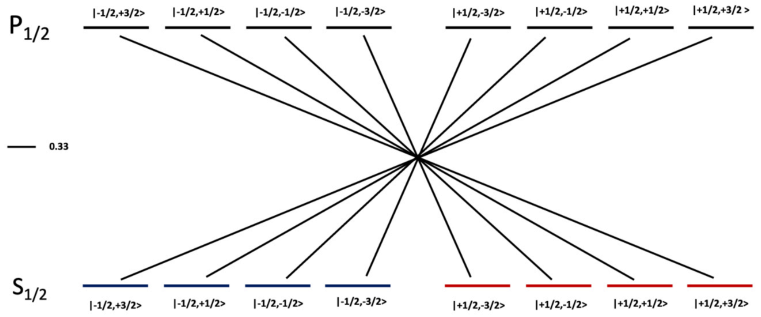

$\sigma^+ + \sigma^-$ transitions - $|m_I, m_J\rangle$ basis

Figure 5.2: Branching ratios and transition moments for the D1 line in ^{23}Na and ^{39}K for both polarization schemes. Transition moments are given as a fraction of the transition dipole moment given in [40, 41]. In a nonzero magnetic field, the allowed π transitions occur at lower energies than the allowed $\sigma_+ + \sigma_-$ transitions.

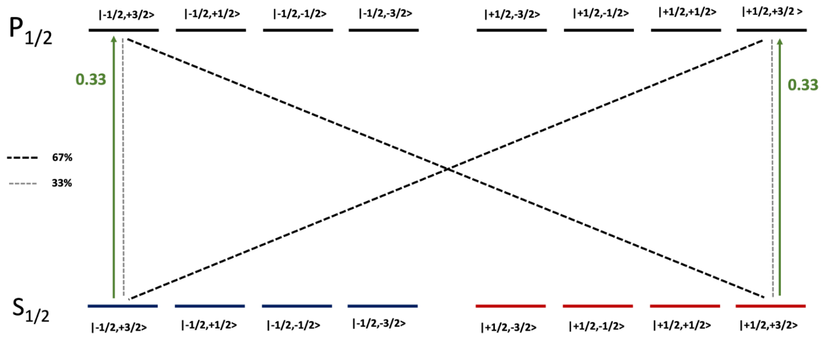

π transition pumping scheme – $|m_I, m_J\rangle$ basis

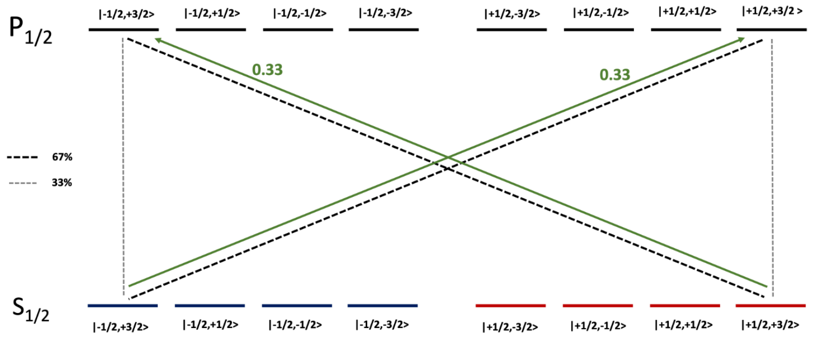

$\sigma^+ + \sigma^-$ transitions pumping scheme – $|m_I, m_J\rangle$ basis

Figure 5.3: Optical pumping scheme for effecting WFS → SFS and SFS → WFS for both polarizations on the D1 line in ^{23}Na and ^{39}K. While the $\sigma_+ + \sigma_-$ transitions are less prone to accidental transitions, the branching ratio to the correct ground state is half of that of the other scheme, meaning that more photons must be scattered for ZS state transfer.

well separated. However, the SFS → WFS pumping occurs with much smaller detunings, and at those correspondingly small values of the magnetic field, the allowed transition energy curves intersect at various magnetic fields. Furthermore, in weak-field regions of the slower, occurring between oppositely oriented magnet stages, the magnetic field direction does not necessarily point strongly in the direction of the magnet orientation, causing polarization mixing and the potential for accidental transitions. Fig. 5.5 shows the allowed transition energies for π and $\sigma_+ + \sigma_-$ in the weak-field regime and over the entire magnetic field range. The possibility of accidental transitions was only fully appreciated during the extensive work with ^{39}K, during which $\sigma_+ + \sigma_-$ polarization was employed with larger detunings due to sufficient separation from

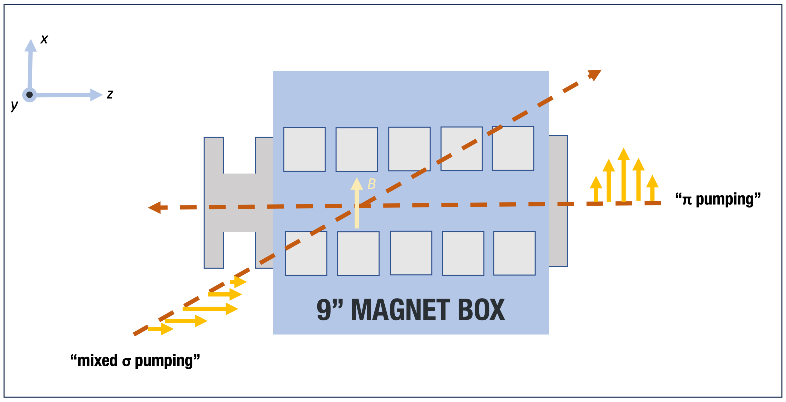

Figure 5.4: A linear polarization for ZS optical pumping can be either be parallel to the magnetic field direction (π), perpendicular ($\sigma_+ + \sigma_-$), or a linear combination of the two. Here the perpendicular orientation is shown with a transverse pump beam, but the same can be true of the longitudinal pump beam as long as the polarization remains orthogonal to the x-axis.

transitions driven by the other polarization. Unfortunately, the difficulty in ascertaining the size and direction of the inter-magnet field meant that we could not rule out the possibility of accidental transitions as a complicating factor.

The work in ^{23}Na was performed in close collaboration with Yi Zeng who recorded the data. This section will describe the ^{23}Na results in much less detail compared to K as the author of this thesis was largely involved in building and testing the magnet assembly, and advising the work. As discussed later in this chapter, the work in ^{23}Na was much more involved, tested the full ZS scheme, and was primarily conducted solely by the thesis author.

5.2 Testing ZS deceleration in ^{23}Na

The sodium atom is the lightest atom for which we tested ZS deceleration, and in an ideal scenario it should require only a few 1 T magnet stages before being slowed to a stop. Unfortunately, we had access to only two independent laser frequencies for this atom, as opposed to the four independent frequencies needed for ZS (two for optical pumping, one for production normalization, and one for velocity-sensitive fluorescence detection). Given the available resources, one laser was used to optically pump the WFS ground states into the SFS states for a single stage, and the other laser was used to probe the fluorescence downstream (using the $F'' = 1$ ground state). The lack of a second optical pumping laser meant that the scheme could only be tested

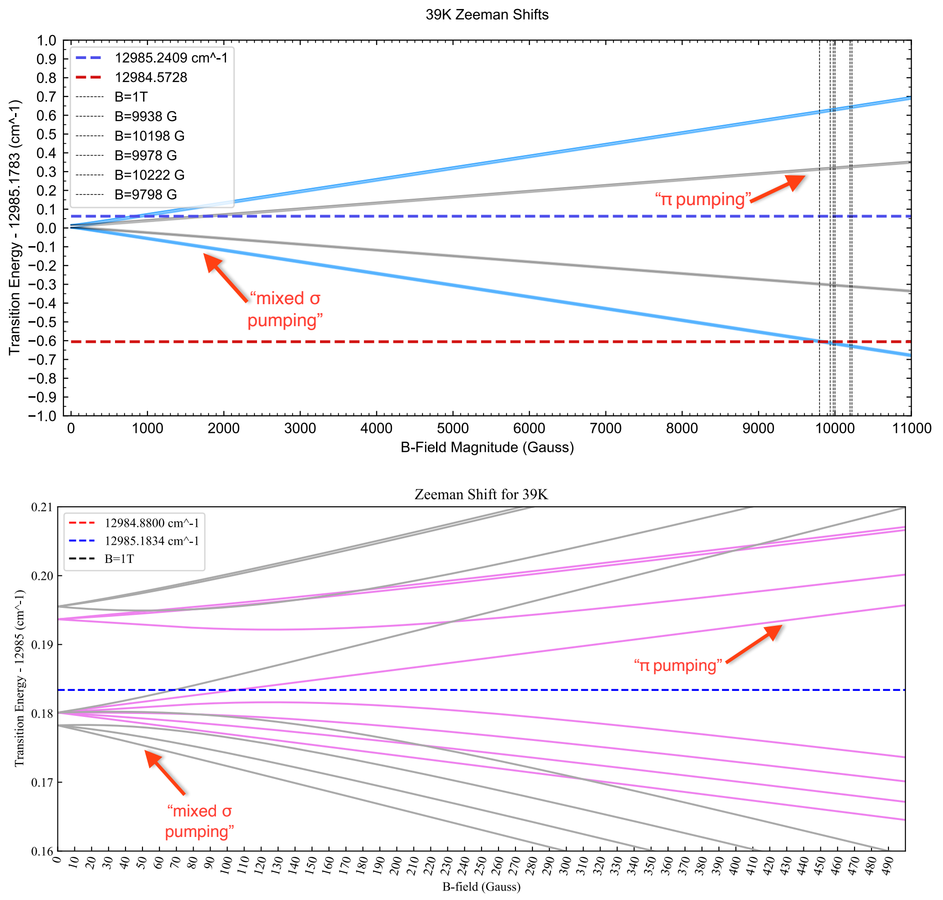

Figure 5.5: Transition energies for allowed D1 transitions for π and $\sigma_+ + \sigma_-$ pumping. Red and blue dotted lines show positions of lasers used for ZS optical pumping. (Top) Allowed transition energies over the complete magnetic field range. Dotted lines show measured on-axis, maximum fields for the five-stage ZS array. (Bottom) Allowed transition energies in the low-field regime, where lines cross and accidental transitions are possible. Note: the use of the color gray is different in the top vs. bottom plots.

in a single stage. Both the optical pumping and detection used the D1 line in ^{23}Na (589 nm), with 100 μW of $F'' = 1$ detection light at 16973.4026 cm^{-1} at 45° to the beamline (scanned to the blue to for a beam velocity measurement) and 8 mW of 16955.566 cm^{-1} light for WFS → SFS pumping. The former was generated through a 1179 nm MogLabs ECDL sent through a SHG oven doubling cavity, and the latter was generated from the MixTrain system. Both the probe and pump are multipassed in order to increase the signal size.

Because the lasers allow for only a single ZS stage, two single-stage magnet designs were tested. The first is the ring magnet with longitudinal magnetization, mounted to an inline KF50 restrictor ring described in Sec. 4.3.1, in conjunction with a longitudinal optical pumping beam. The second is the simple two-cylinder design, mounted to the magnet box, described in Sec. 4.3.2, with a center field of 0.987 T. This second design allowed for transverse optical pump, which helps with rejecting scattered light background from the optical pumping beam in the detection region.

Sodium atoms were produced in the 1K beam source through ablation of commercially-available NaCl pellets at a range of YAG energies. Transverse fluorescence was measured to characterize the brightness of the $^{23}\mathrm{Na}$ atomic beam. A non-resonant intensity build-up cavity was used to increase the amount of fluorescence by a factor of about 25 [64]. The $^{23}\mathrm{Na}$ beam velocity was characterized using diagonal fluorescence. A major issue with a longitudinal optical pumping beam with nearly the same frequency of the detected photons is background scatter, in particular scatter off of the permanent magnets and other shiny surfaces.[2]

In order to try to observe the deceleration effect, the optical pumping beam was shuttered open and closed and the velocity distributions were compared. The ning of the optical pumping beam relative to the high-field atomic resonance was varied, and the average of four measurements was taken for each velocity (shutter open - shutter closed - shutter closed - shutter open). Transverse fluorescence from the transition out of $F'' = 1$ was used to confirm the population transfer was occurring as expected, though the signal was noisy. Ultimately, the red-detuned optical pumping laser led to a downstream $F'' = 1$ diagonal fluorescence signal consistent with very slight slowing, while a blue-detuned laser led to a downstream $F'' = 2$ signal consistent with acceleration. Nevertheless, the signals were not particularly convincing as the effect was quite small.

In order to increase the magnitude of the slowing effect, the ring magnet was swapped out for the two-cylinder magnet. This assembly presents the additional benefit of transverse optical access, which allows for a transverse optical pumping beam, drastically reducing the amount of scattered light background. Unlike the case of longitudinal pumping, where atoms are resonant somewhere along the beamline due to the varying magnetic field, the transverse pump requires tuning of the laser frequency to account for the Zeeman shift at the magnet field value precisely in the region where the laser intersects the atomic beam. This can be determined empirically by measuring the $F'' = 1$ population downstream as a function of the optical pumping frequency.

---

[2] The typical black paint used to mitigate scattered light (Alion MH2200) was not usable for permanent magnets because the curing procedure requires a bakeout that can easily demagnetize these magnets.

An approximate 50% increase in $F'' = 1$ population was observed when the optical pumping detuning was optimized.

Once again, the slowing was perhaps apparent but not entirely convincing. In both of these attempts with Na atoms, the detection laser power was limited and there was not another laser available as an absorption probe for normalizing production. Similarly, the lack of a second optical pumping beam means that this prototype does not truly test the full ZS scheme, which requires sequential, reliable transfer of population from WFS to SFS and back again. Therefore, we pursued another system that would allow for the full scheme to be prototyped. The available laser resources, relatively light particle mass, and available transitions enabled our substantial work in $^{39}\mathrm{K}$.

5.3 Testing ZS deceleration in ^{39}K

The potassium atom is heavier than sodium and therefore experiences a smaller deceleration, but we had access to a full suite of lasers to test slowing with multiple ZS stages. In particular, we tested ZS deceleration in $^{39}\mathrm{K}$ using the five stage, two-cube magnet from Sec. 4.3.2, mounted to a $9\ \mathrm{in}$ cubic vacuum chamber from Ideal Vacuum. The entire beamline is depicted and pictured in Fig. 5.6.

Potassium atoms are produced through laser ablation of a pressed powder target consisting of equal parts KCl and Yb powder by mass, with PEG included as a binder. Initially, we used Zr powder suspended in water to increase the opacity of the resulting target, but found that including Yb powder was easier to work with and yielded more consistent ablation results. The atoms are cooled via collisions with $1.4\ \mathrm{K}$ He buffer gas and forms an cold atomic beam. Upon exiting the cryogenic chamber through a KF-50 gate valve, the atoms propagate through the Ideal Vacuum cube. Measurements of the state populations and atomic beam velocity is performed in the octagonal vacuum chamber attached to the magnet chamber. Fluorescence photons are collected on a PMT (Hamamatsu Photonics H10492-012) via a quartz light pipe mounted above the vacuum chamber.

The optical pumping lasers propagate longitudinally to the beamline axis. The two laser frequencies are detuned from the D1 transition at $12985.1917\ \mathrm{cm}^{-1}$ to drive atomic resonances at high and low field regions in the magnetic field, respectively. We generated up to $80\ \mathrm{mW}$ using two Toptica TA Pro lasers. In principle, the lasers are capable of generating $\sim 1\ \mathrm{W}$ of power, but due to degraded TA performance and losses

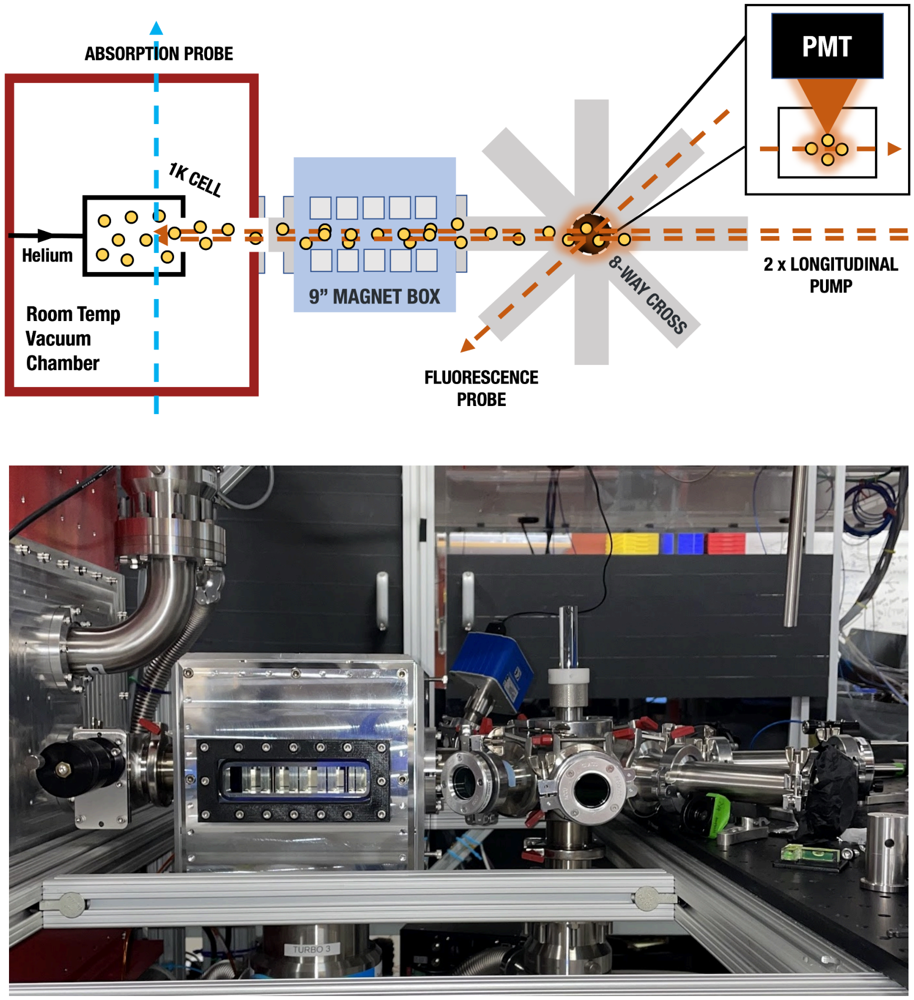

Figure 5.6: Schematic of the experiment to test ZS in ^{39}K using five 1 T magnets. A photo of the apparatus is shown below. See main text for descriptions of each component.

from coupling the two lasers through the same optical fiber, the power to the table was limited, but still sufficient to saturate the optical pumping transition many times.

Aligning the optical pumping beams through the 1 m long beamline proved to be a major challenge, given the large number of small apertures from the magnets and collimators in the system. Whenever the source was open (which unfortunately was somewhat often due to persistent vacuum and cryogenic issues), we aligned the optical pumping beams by trying to observe the laser spot going into the buffer gas cell, indicating a large degree of overlap between the atomic beam and the pumping lasers. The optical pumping light further contributed a large amount of scattered light background to the PMT signal. In addition to decreasing the SNR for fluorescence measurements,

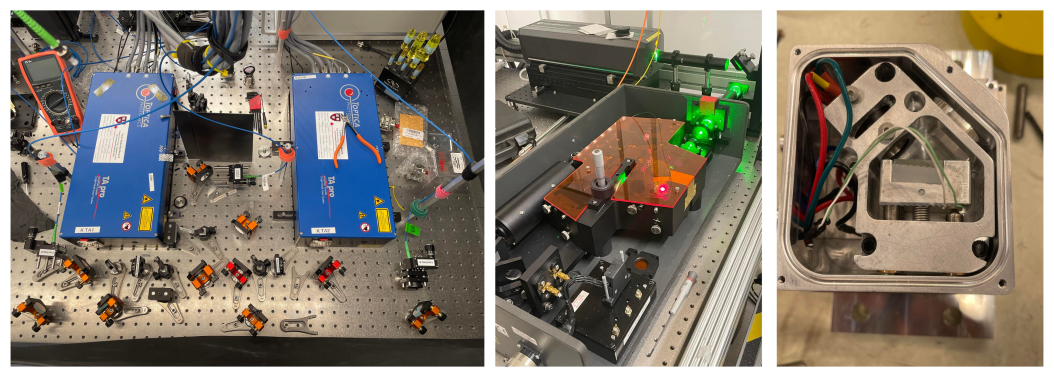

Figure 5.7: Laser systems used to test ZS deceleration in $^{39}\mathrm{K}$. (Left) Two TA Pro lasers used for optical pumping with $770\ \mathrm{nm}$ light co-aligned through one optical fiber. (Middle) Coherent MBR laser system producing $770\ \mathrm{nm}$ light resonant. (Right) Homemade ECDL that generates light resonant with the weaker $4S-5P$ transition at $405\ \mathrm{nm}$.

minimizing the scattered light background was a reliable and repeatable way to ensure proper alignment. We confirmed empirically that transverse pump beams lead to a completely negligible scattered light background, but we could not pursue the transverse pumping scheme without additional difficulty due to the aforementioned small gaps between magnets.

We had access to a third laser frequency at $12985.1917\ \mathrm{cm}^{-1}$ using a Coherent MBR laser. Finally, we generated $405\ \mathrm{nm}$ light resonant with the weaker $4S-5P$ transition in $^{39}\mathrm{K}$ using an ECDL built by the thesis author and Yi Zeng. For the data shown in this thesis, we used these two lasers for in-cell absorption (for signal normalization and a gauge of sufficient production and thermalization) and as beamline fluorescence probes. Each of the two lasers has performed each of the aforementioned roles, and there are advantages and disadvantages discussed in the coming subsections. Each of the lasers were stabilized to a HighFinesse wavemeter. All four laser systems are shown in Fig. 5.7.

The work described in the following subsections was conducted in a very different chronology than what is presented here because low SNR and other issues prompted changes in the experimental protocols. Nevertheless, for the sake of organization, observations and measurements have been rearranged into three categories—spectroscopy, optical pumping, and velocity measurements.

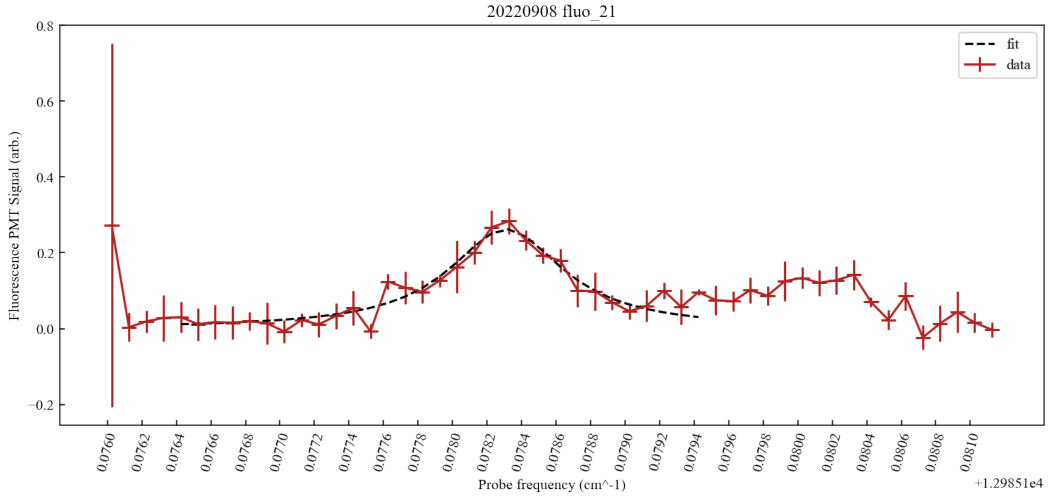

Figure 5.8: Integrated PMT fluorescence vs. transverse fluorescence probe frequency for a transverse probe driving the $4^2S_{1/2}$–$4^2P_{1/2}$ transition in ^{39}K. The $F'' = 2 \rightarrow F' = 1$ transition is clearly visible. The leftmost point is a non-repeatable outlier. Signals were normalized using in-cell absorption of 405 nm light.

5.3.1 ^{39}K Spectroscopy

In order to be confident in our measurements in ^{39}K, we needed to confirm that our beamline measurements correspond to the known atomic level structure. In particular, measurements of the D1 transitions between the ground and excited $F'' = 1$ and $F'' = 2$ states was essential. Furthermore, the $4S - 5P$ transition at 405 nm also needed to be measured with sufficient precision.

We observed transitions at 770 nm corresponding to both the $F'' = 1$ and $F'' = 2$ ground states in ^{39}K in both absorption and fluorescence. The $F'' = 2 \rightarrow F' = 1$ transition at 12985.1783 cm^{-1} was observed to be stronger than the $F'' = 2 \rightarrow F' = 2$ transition at 12985.1802 cm^{-1}. Furthermore, transitions out of the $F'' = 1$ state were difficult to observe in fluorescence, but these transitions were observed in in-cell absorption. It is likely that the weak $F'' = 1$ signals were due to losses from magnet forces near the peak of the magnetic field (see Sec. 4.4.1). The $F'' = 1$ signals were more visible after optical pumping, as discussed in the next subsection. Fig. 5.8 shows our observation of the 12985.1783 cm^{-1} when scanning the transverse fluorescence probe frequency.

The 405 nm transition was first observed through in-cell absorption for normalizing atomic fluorescence. The feature was observed at 24720.1527 cm^{-1} and the signals

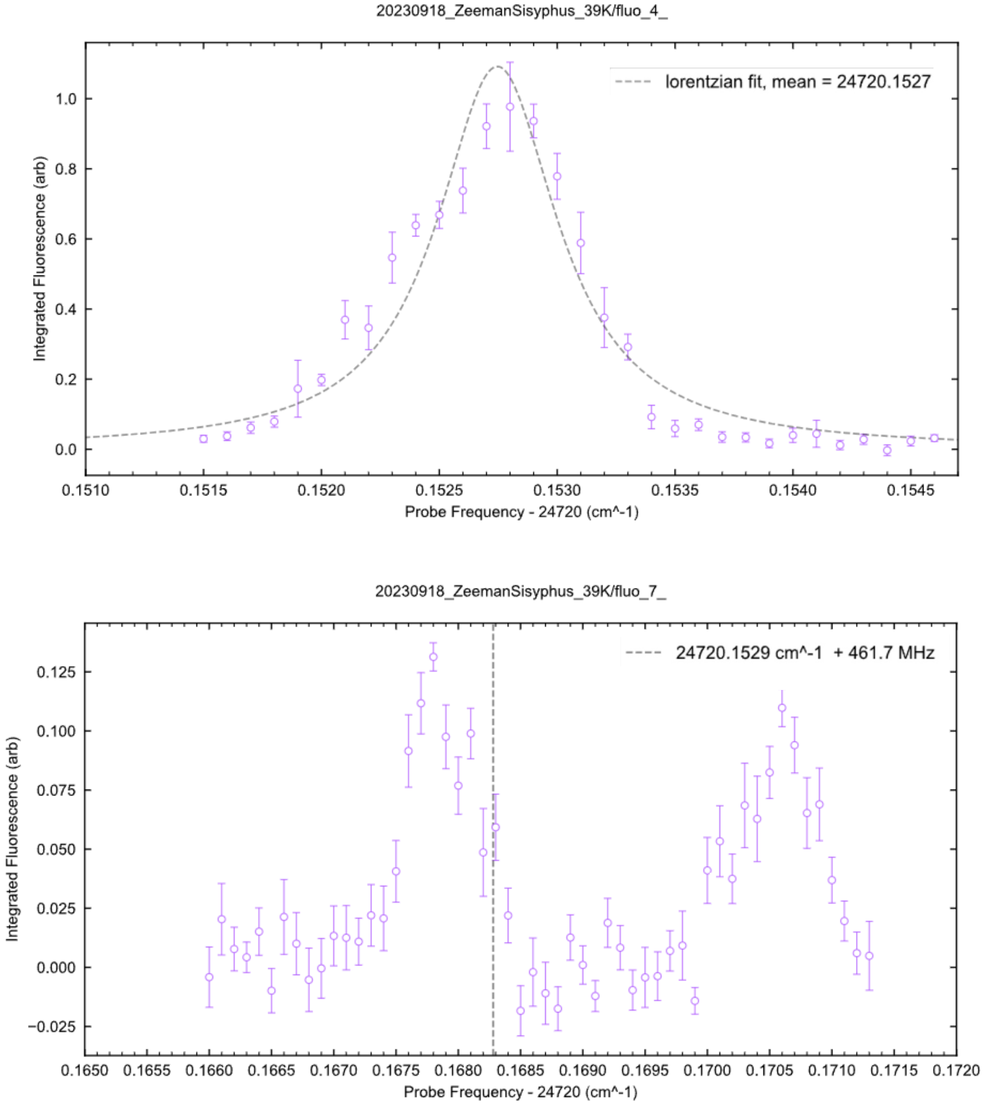

Figure 5.9: Integrated PMT fluorescence for a transverse probe driving the $4^2S_{1/2} - 5^2P_{3/2}$ transition in ^{39}K. The top transition likely corresponds to driving the $F'' = 2$ ground state while the bottom transitions correspond to the $F'' = 1$ ground state. Signals were normalized using in-cell absorption of 770 nm light slightly detuned from resonance to prevent full absorption.

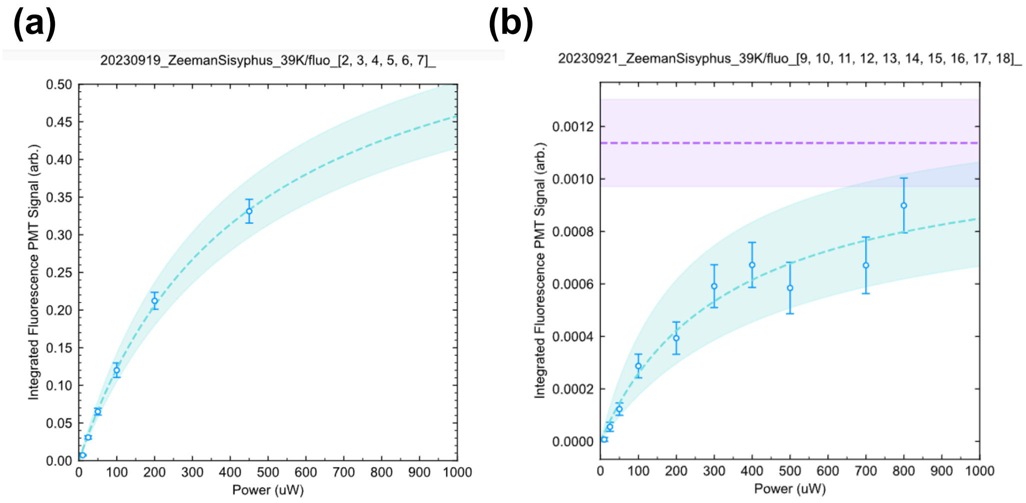

Figure 5.10: Integrated PMT fluorescence vs. $405\ \mathrm{nm}$ laser power for (a) transverse fluorescence and (b) diagonal fluorescence for a $150\ \mathrm{m/s}$ velocity class. Dashed lines are a guide for the eye. Signals were normalized using in-cell absorption of $770\ \mathrm{nm}$ light slightly detuned from resonance to prevent full absorption.

were fairly broad due to Doppler broadening. When we switched to using this frequency for velocity measurements, the transition was mapped out in more detail since the WFS $\leftrightarrow$ SFS pumping structure must be well understood. With the MBR tuned to the D1 transition for in-cell absorption normalization, the $405\ \mathrm{nm}$ was used as a transverse fluorescence probe and the frequency was scanned. As expected, we observed an integrated fluorescence peak at $24720.1527\ \mathrm{cm}^{-1}$ (Fig. 5.9). We observed more peaks when we scanned blue detuned the probe frequency by the ground state hyperfine splitting, which provided strong evidence that the initial transition we observed at $24720.1527\ \mathrm{cm}^{-1}$ corresponds to a transition out of the $F'' = 2$ ground state. Scanning the laser by the same amount to the red, yielded only noise, lending further credence to this hypothesis.

As with the D1 transition probe, we measured the fluorescence as a function of laser power for the $405\ \mathrm{nm}$ laser. With the transverse probe fixed to address the $F'' = 2$ ground state we measured the integrated fluorescence as a function of power. For a diagonal probe, we measured the integrated fluorescence for a $150\ \mathrm{m/s}$ velocity class. Saturation of the transition was observed in both cases, which confirmed that we had sufficient laser power. See Fig. 5.10 for the power saturation curves.

5.3.2 ^{39}K Optical Pumping

The Zeeman-Sisyphus scheme depends strongly on the ability to optically pump at particular magnetic field locations. Using the measured magnetic field values and predicted Zeeman shifts, we observed optical pumping between $F'' = 1 \leftrightarrow F'' = 2$ at expected laser frequencies. In contrast, due to loss out of $F'' = 1$ from magnet forces and our limited knowledge of the low-field magnetic field profile, the $F'' = 2 \rightarrow F'' = 1$ optical pumping behavior was not straightforward to interpret.

In general, optical pumping signals were measured with one of the 770 nm TA Pro pumps propagating longitudinally down the beamline and the other laser blocked, with a range of laser powers. The downstream $F'' = 1$ and $F'' = 2$ signals were measured using a transverse fluorescence probe at 770 nm. The intense optical pumping light led to a tremendous laser scatter off of magnets and other shiny surfaces, leading to noise for optical pumping and beam velocity measurements. Therefore, the detection light was switched to 405 nm, which is well separated from the laser scatter through the use of filters. In this subsection, results from both detection schemes are discussed. These measurements confirm our state assignments, because they show depletion from one state and accumulation into the other, when optical pumping frequencies match low-field or high-field resonances.

Fig. 5.11 shows a pair of plots indicating depletion of the $F'' = 2$ population and the corresponding accumulation into $F'' = 1$. The reverse optical pumping is apparent with the other pumping laser blocked. The data in the figure was taken with a few-mW laser power over a ~ 1 mm spot, but the TA Pro lasers were capable of outputting much more power. In order to confirm that the laser power was sufficient for saturating the optical pumping behavior, we measured the ratio of state populations vs. the optical pumping laser power.

For pumping into $F'' = 1$, we measured the ratio of the signal with pump on divided by the signal with pump off. Likewise, for the other ground state, we measured the same ratio using the other pump laser instead. Both are shown in Fig. 5.12 and exhibit the expected saturation behavior, saturating at about 4 mW. This is consistent with calculations using predicted transition moments. We also studied the loss out of $F'' = 1$ in particular by measuring the opposite population ratio (Fig. 5.13).

Because we had difficulty observing slowing with the configurations we tested above, we measured the population ratio as a function of the optical pumping laser frequency. Scanning the red detuned pump over $12984.4900 - 12984.8200$ cm^{-1}, we probed

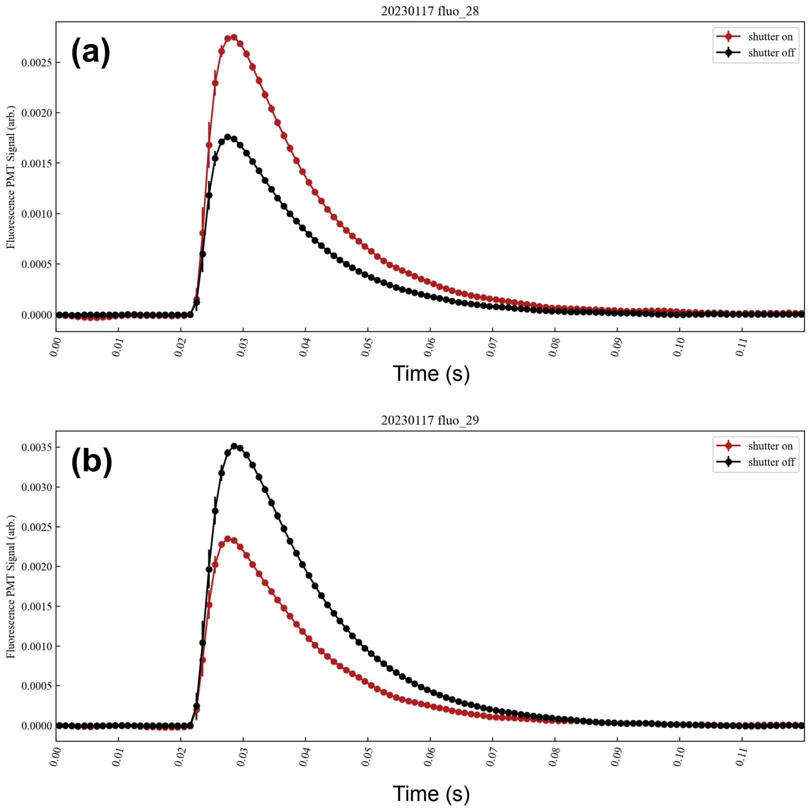

Figure 5.11: Fluorescence vs. time signals when the WFS → SFS laser at 12984.5728 cm^{-1} is shuttered on vs. off. The SFS → WFS pump laser is blocked in both configurations. The pump laser frequency is detuned from the zero-field transition frequency by over 18 GHz to the red. (a) Downstream $F'' = 1$ fluorescence signal showing accumulation of population. (b) Downstream $F'' = 2$ fluorescence signal showing depletion of population.

optical pumping from $\sim 11000 - 6200$ G. Because of an all-too-common laser malfunction with the homemade ECDL, the data was recorded without normalization with a fixed ablation position, but population ratios were taken with adjacent ablation shots prior to averaging in order to account for overall target degradation. This scan confirmed that our original laser frequency was close to optimal, with the maximum occurring when the laser is set to ~ 12984.5600 cm^{-1}.

The same scans were performed using the SFS → WFS probe. When detuned too close to the zero-detuning transition, the signal would be confounded by overall photon scattering in the beamline. At this stage, we also noted that the magnetic field profile for the ZS magnets shown in Fig. 4.10 indicates a "plateau" between $0.1 - 0.2$ T, followed by a decrease in the field to near-zero as the particles traverse along the z-axis. In order

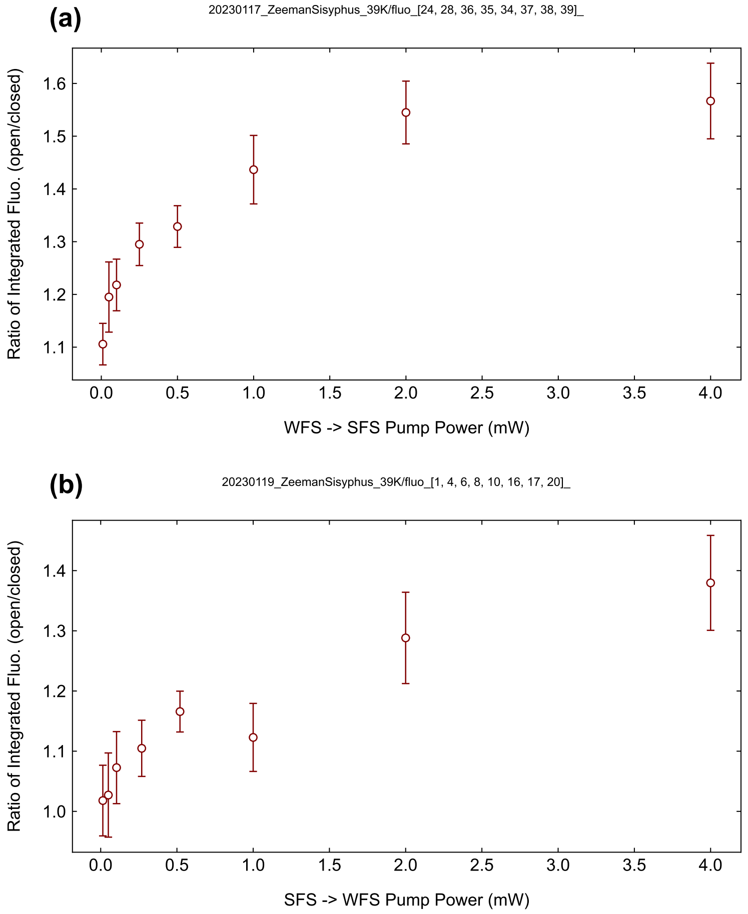

Figure 5.12: Integrated PMT fluorescence ratio vs. pump power for (a) WFS → SFS pumping and (b) SFS → WFS pumping. The pump laser frequencies were $12984.5728\ \mathrm{cm}^{-1}$ and $12984.2409\ \mathrm{cm}^{-1}$, respectively. All data is normalized to in-cell absorption of $405\ \mathrm{nm}$ light.

to ensure that particles are being optically pumped properly in the low-field region, the SFS → WFS was set to operate at a magnetic field well above the plateau region, where we believed all particles likely came into resonance. We observed (optimized) population ratios of ~ 1.5 at $12985.3200\ \mathrm{cm}^{-1}$, which corresponds to a transition where the magnetic field is ~ 2000 G. These frequency scans were repeated when we switched to using a $405\ \mathrm{nm}$ probe and appropriate filtering, with no fundamental change to our initial observations. At various configurations discussed above, we measured the ^{39}K beam velocity.

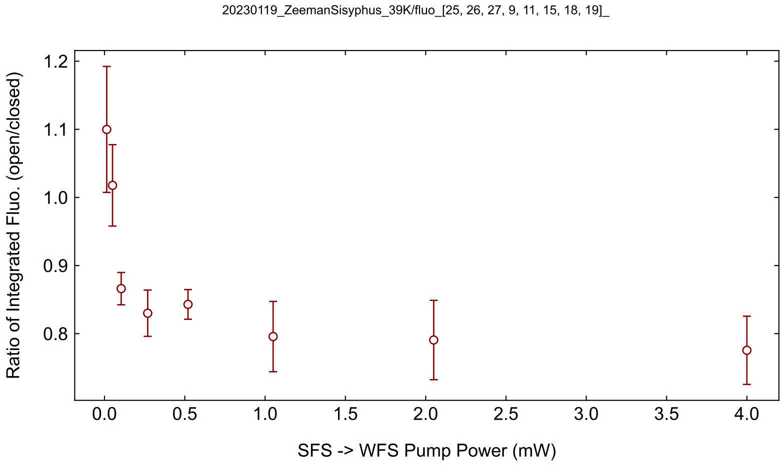

Figure 5.13: Integrated PMT fluorescence ratio vs. pump power for $\mathrm{SFS} \rightarrow \mathrm{WFS}$ pumping, looking at loss of population from the $F'' = 1$ state. The pump laser frequency is $12984.2409\ \mathrm{cm}^{-1}$ and all data is normalized to in-cell absorption of $405\ \mathrm{nm}$ light.

5.3.3 ^{39}K Velocity Measurements

Complications in measuring the beam velocity to probe for ZS deceleration became increasingly understood as the work proceeded. As mentioned several times in this chapter, the $405\ \mathrm{nm}$ laser was ultimately used to measure the beam velocity due to its separation from the optical pumping frequencies. This allows for total background scatter rejection with the optical pumping lasers at maximum power $(60 - 120\ \mathrm{mW})$. An additional advantage with $405\ \mathrm{nm}$ detection is that the transition Doppler shift for a fixed velocity class is larger compared to the redder $770\ \mathrm{nm}$ transition. This means that smaller changes in forward velocity are more easily resolved when using the blue detection scheme. Unfortunately, our $405\ \mathrm{nm}$ light was generated through a homemade ECDL that was often afflicted by frequency instability. This particular ECDL was designed with fixed-frequency, Doppler broadened, in-cell absorption in mind, and not for stability during frequency-scanned beamline fluorescence measurements. Though the MBR laser generating the $770\ \mathrm{nm}$ detection light was far more stable and user-friendly than the ECDL, ultimately off-diagonal detection allowed us to test ZS using the full power available from the TA Pro pumps without scattered light background. Perhaps ironically, the simplicity of the atomic system is missing the widespread off-diagonal detection pathways that are available in numerous molecules with optical transitions.

A second complication comes from the detection scheme itself. Initially, we tried to measure the velocity change by comparing data where both pumps are shuttered off vs. when both pumps are exposed, detecting fluorescence out of $F'' = 2$. When the pump lasers are on, the final pumping step transfers SFS population into the WFS, which largely correlates with $F'' = 2$. Therefore, shuttering the pumping lasers off will not optically pump $F'' = 1$ population into $F'' = 2$, manifesting as an overall decrease in the detected atom signal across all velocity classes, compared to when the pump lasers are on. This enhancement of across all velocities is, of course, not a consequence of slowing.

When we realized this particular issue with the detection scheme, we instead shuttered just the WFS $\rightarrow$ SFS pump on and off, leaving the other pump on. We also took scans where we shuttered the SFS $\rightarrow$ WFS pump, and kept the other on. In the last orientation, we shuttered both pumps individually and added the resulting velocity distributions. This final method is the most robust because it is the least sensitive to velocity-independent population transfer.

In all pump shuttering configurations, a particular velocity class is probed four times with the shutter open, closed, closed, and then open. This sequence of four measurements is repeated some number of times in order for signal averaging. We have both averaged the velocity distributions for open and closed configurations and subtracted them, as well as taken the difference of adjacent open and closed shots prior to averaging. It is simple to see that the difference of averages and the average difference is the same. However, the variance of the two analyses can be different if there are time-dependent correlations. In this particular case, repeated ablation causes target degradation and a reduction in signal independent of optical pumping. Therefore, the scheme with sequential, pairwise subtraction is more robust because it allows one to look for deceleration between data collected as close in time as possible.

Even with pairwise subtraction, a velocity scan with too many velocity classes will provide limited information about the final velocity classes considered due to target decay. The ablation was manually rastered to limit this effect, but target decay was still observed. Practically, this means we considered fewer velocity classes—a few points near the $80 - 100$ m/s range where slowing is expected with a few points at slower and faster velocities. Because we were operating our cryostat at 1.4 K, we were limited in how quickly we could ablate to a mere 0.7 Hz. This relatively slow experimental repetition rate meant that measuring many velocity classes for each data run became impractical, especially when working with an ECDL that was not optimized for scanning.

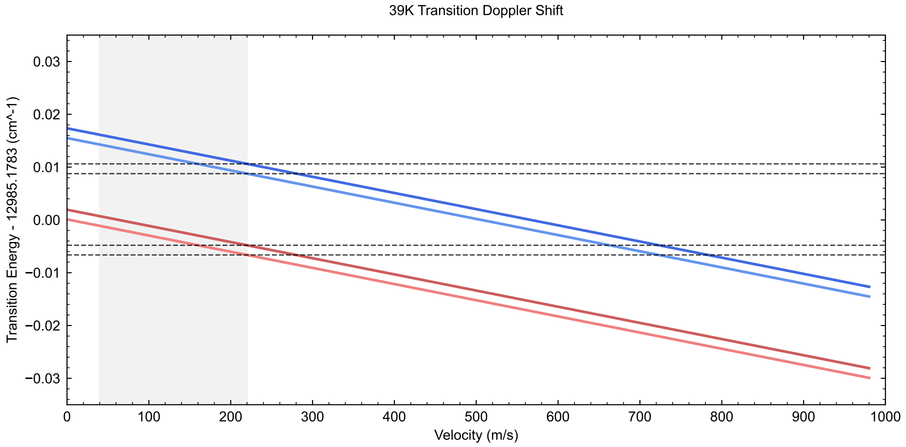

Figure 5.14: Doppler shift of the four transitions in the $4^2S_{1/2} \rightarrow 4^2P_{1/2}$ system. The gray shaded region shows the range over which we measured velocities for our beam. The black dotted lines show examples where the Doppler shifted transition due for velocity class overlaps with a nearby transition for another velocity class.

Finally, because velocity scans are based on transition Doppler shifts, signal leakage from nearby transitions was observed. The detection light probing a particular velocity class was also resonant with the nearby transition for much faster moving atoms. Fig. 5.14 shows the Doppler shifts for the four transitions at $770\ \mathrm{nm}$ and possible sources of spurious velocity data.

After this lengthy discussion of the measurement complications, we now share some of the velocity curves we measured over the course of this experiment, measured in some of the configurations discussed above. The first set of plots (Fig. 5.15) shows velocity curves from a configuration when the $\mathrm{SFS} \rightarrow \mathrm{WFS}$ was shuttered on and off, with the pumps at $12984.5600\ \mathrm{cm}^{-1}$ and $12985.3200\ \mathrm{cm}^{-1}$ with $4\ \mathrm{mW}$ power in each pump. The probe was at $770\ \mathrm{nm}$, so larger pump powers were not possible due to background scatter. Only the $F'' = 2$ states were measured. The averaged velocity distributions did not indicate slowing, so we also looked at the distribution of pairwise differences between shutter open and shutter closed configurations. This pairwise analysis was also not a strong indicator of slowing.

At this point, we switched to $405\ \mathrm{nm}$ detection which enabled much larger pump laser powers. We also switched to measuring both $F'' = 1$ and $F'' = 2$ velocity distributions and summing them together. While this method mixes unslowed particles into the data, it seemed to help account for optical pumping between populations. However, the measurement of two velocity curves and summing them together increases the total

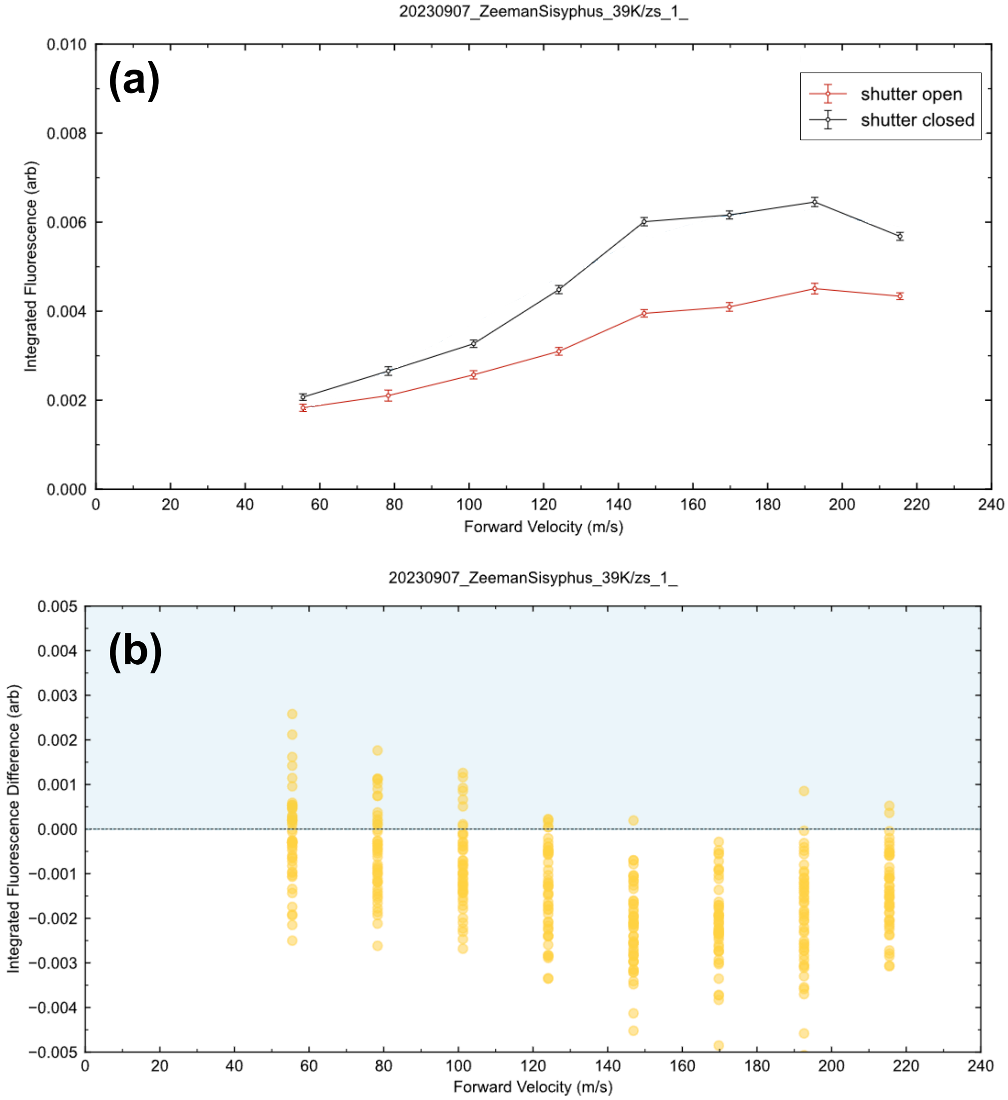

Figure 5.15: Velocity measurements using 770 nm detection with the SFS pump shuttered open and closed and the WFS pump always on. (a) Measured velocity distribution for slowing and non-slowing configurations. (b) Difference in signal for adjacent shutter open and closed data points. The peak velocities may show signs of slowing, but the signal is not conclusive.

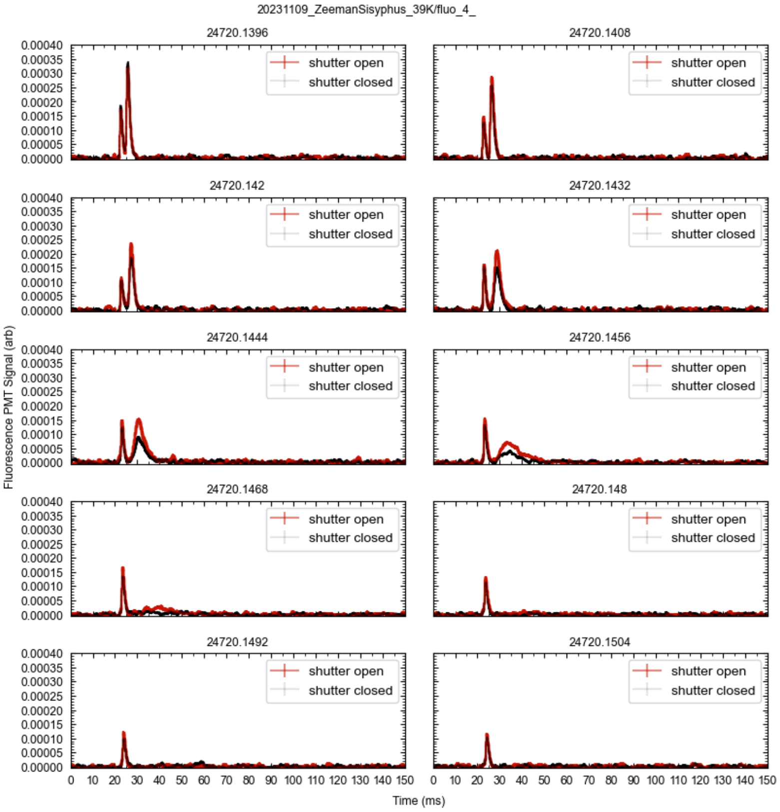

Figure 5.16: 405 nm fluorescence vs. time for $40-225$ m/s velocity classes. Transitions from both ground state hyperfine levels are visible.

noise. In order to improve the number of particles that can be slowed, we expanded the pump beams by a factor of four along the long side of the magnet gap using a telescope. We confirmed that the expanded beams cleared all five magnets by eye and also using the laser scatter as a proxy for alignment. The 405 nm detection scheme meant that the expanded pump beams contributed $< 2\%$ more background scatter when the PMT is set to its maximum gain with the red-detuned and blue-detuned pumps at maximum power (70 mW and 200 mW, respectively).[3]

Fig. 5.16 shows the $F'' = 2$ diagonal fluorescence vs. time curves for velocities between $40 - 225$ m/s. The feature that appears before the main feature corresponds to faster velocity classes resonant with a nearby transition. This fast initial peak is excluded from the integration range when these plots are converted into a 1D velocity curve. The individual and added together $F'' = 1$ and $F'' = 2$ velocity curves is shown in Fig. 5.17. Once again, there is not evidence of deceleration in this velocity profile.

---

[3] The maximum powers for both lasers were different because one tapered amplifier module appeared more degraded than the other.

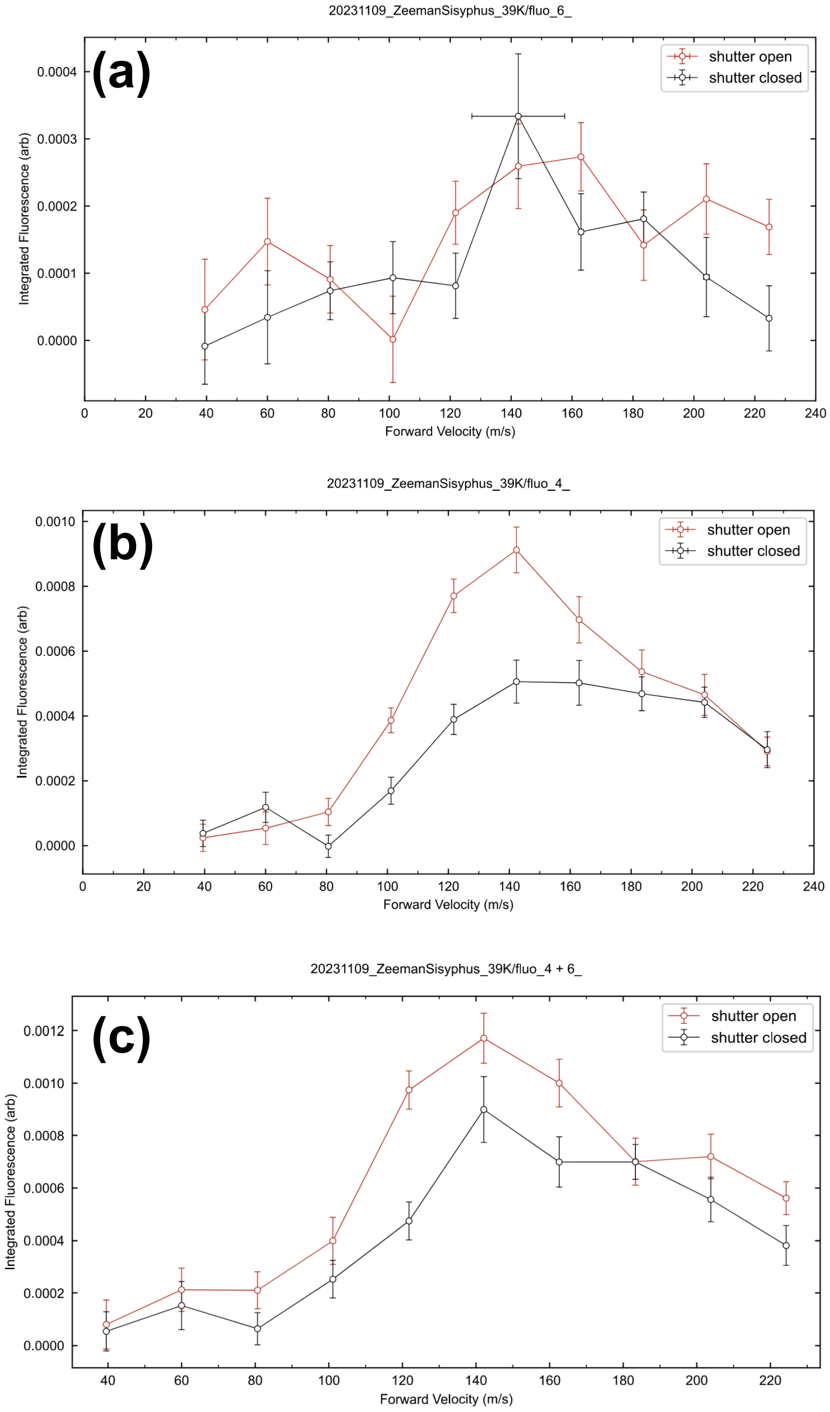

Figure 5.17: ZS velocity profiles when using expanded pump beams and 405 nm detection. (a) Velocity distribution for the $F'' = 1$ state. (b) Velocity distribution for the $F'' = 2$ state. (c) The sum of (a) and (b) with proper Gaussian error propagation.

All velocity scans we measured indicated a peak beam velocity between $160 - 180$ m/s, when we ablated with 27 mJ pulses at 0.7 Hz with 2 SCCM helium flow. The overall beam velocity can be slowed if we used a lower ablation energy and added a slowing stage to our buffer gas cell. This modification would come at the cost of overall atom signal due to reduced cell extraction. In the next section, we discuss pathways to improve the prototype permanent magnet ZS decelerator.

5.4 Outlook

Given our experience with ^{39}K, we have identified a number of possible avenues that are likely to improve one's chances to observe ZS deceleration.

One major improvement can come from inserting a magnetic guide at the end of the slower to cut down on geometric losses from beam divergence. Furthermore, the magnetic guide would allow us to detect only WFS particles, allowing us to measure only slowed atoms. Former undergraduate and post-baccalaureate research assistant Victoria Su, advised by the author of this thesis, developed particle tracing simulations to determine optimal parameters for a magnetic guide (and magnetic lens) for our beam source. Ultimately, we decided to machine mounts to build a version of the magnetic guide shown in Fig. 7.29 of Ben Augenbraun's thesis [76], which has a peak field of ~ 0.5 T.

Magnets would be glued to aluminum plates with cutouts to hold them in place. The cutouts have holes for threaded rods to pass through, secured in place by nuts. The threaded rods would be mounted to a KF-50 restrictor ring that sits in the beamline. A drawing of the proposed magnetic guide that leads from the end of the ZS stage to the detection region is shown in Fig. 5.18. As of the writing of this thesis, the magnetic guide has not been built, but the parts to do so have been procured.

Many of the most significant complications in testing ZS, including the scattered light background, could be mitigated with larger gaps between magnet stages. Removing the second and fourth magnet from the array leaves three magnets with magnetizations in the same direction and large gaps between them. The removal of the intermediate magnets would likely ameliorate the peak magnetic field differences between adjacent stages observed in the five-stage design. If this new arrangement allows for a single optical pumping frequency for each stage, then the pumping beams can be routed through the array transverse to the beam propagation, greatly reducing the scattered light background from longitudinal lasers. Furthermore, increased gaps between the

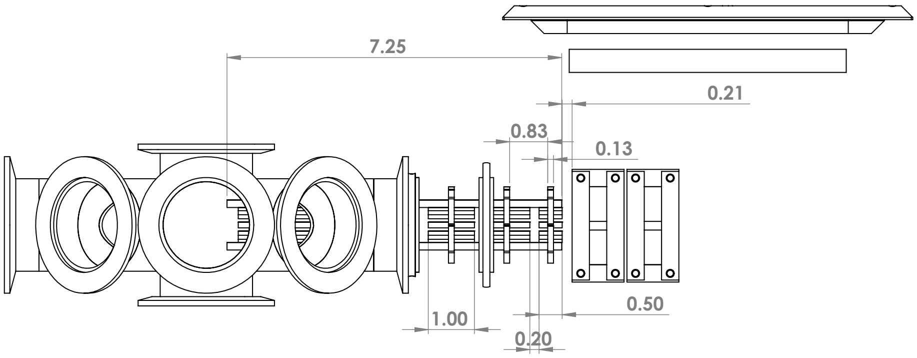

Figure 5.18: Technical drawing of a proposed magnetic guide for the beam extension, connecting the ZS magnets to the detection chamber. All dimensions are in inches. The guide consists of five identical stages along with a single short stage made of permanent magnets.

magnets would allow for a proper measurement of the minimum field experienced between the magnets, a quantity that was not possible to measure in the five-stage configuration. Knowing this quantity would give further confidence in the low-field optical pumping frequency and provide an estimate of losses due to non-adiabatic state changes. Because the downward pointing magnets would be removed, the inter-magnet minimum field is likely to be high enough to avoid these losses and accidental transitions that can occur below 10000 G, potentially allowing us to use π transitions that have a larger branching ratio from WFS $\leftrightarrow$ SFS sublevels. Finally, the increased gap may open up enough space to insert a short guiding stage that can help reduce losses from magnet force induced divergence.

Removing two stages would reduce the total amount of slowing, making the observation of ZS slowing in ^{39}K more challenging. However, we have since acquired a larger supply of tunable lasers that can allow us to work with the lighter ^{23}Na atom in which the slowing effect is much more dominant. While time and funding constraints did not allow us to re-test the system in ^{23}Na, this would be the natural place to restart prototyping ZS slowing in alkali atoms.

Finally, revisiting optimized magnet designs to achieve truly large, several-Tesla magnetic fields remains an important task for permanent magnet ZS slowing. Further simulation and laboratory prototyping of designs employing HIPERCO 50A pole pieces is necessary for this endeavor to succeed. Achieving an design for a high-field, few stage, permanent magnet ZS slower would move this technology from the domain of cryogenic superconducting mechanical engineering to a machine that can be assembled by hand on a laboratory bench.

Acknowledgments

This work was supported by the Gordon and Betty Moore Foundation and the Alfred P. Sloan Foundation. We thank our collaborators in the Doyle Group at Harvard University for loaning us the TA Pro laser systems.

Chapter 6

Molecular Spectroscopy for Quantum Science

> *"There are clues everywhere — all around us. But the puzzle maker is clever. The clues, although surrounding us, are somehow mistaken for something else. And the something else — the wrong interpretation of the clues — we call our world. Our world is a magical smoke screen. How should we interpret the happy song of the meadowlark, or the robust flavor of a wild strawberry?"*
>
> Log Lady, *Twin Peaks* Season 2 Ep. 20

Electric dipole moment searches in molecules require accurate knowledge of the system's quantum states and their properties. These experiments leverage the additional degrees of freedom afforded by molecular structure for enhancements to quantum control or sensitivity to new physics. Likewise, in each system, the molecular states of interest must be isolated and distinguished from the numerous other states that serve as loss channels or degrade coherence.

One must at minimum identify "science states" that are sensitive to EDMs, and measure and fit their rotational spectra at high resolution, in both magnetic and electric fields. The identification and characterization of useful quantum states in molecules inevitably involve high-resolution spectroscopy. Often, additional electronic, vibrational, and rotational states are needed for optical pumping, repumping, quantum state control, and state preparation and readout. In general, accurate knowledge of the rotational, vibrational, centrifugal distortion, spin-rotation, Λ doubling, and hyperfine constants is necessary at a minimum. In many cases, spectroscopy of other weak lines is also required. For example, laser cooling and trapping experiments requires repumping ~ 10 vibrational states, which necessitates characterization of vibrational-rotational structure for these states and measurement of vibrational branching ratios (VBRs) to high precision, including of states with weak transition dipole moments [83, 84]. It is both necessary and time consuming to make VBR measurements little natural population out of buffer gas sources, as many independent laser frequencies must be scanned and optimized to observe successively weaker optical pumping signals into states with successively smaller VBRs.

When selecting a molecule as a platform for quantum science or precision measurement, molecules with some existing spectroscopy are often chosen to minimize the additional amount of spectroscopy that must be performed. Even so, in many cases, existing spectroscopy has insufficient resolution or a higher temperature at which quantum science and precision measurement experiments typically operate, thus excluding low-J states that are critical resources. Many short-lived species have not been produced or studied in the gas phase, where physicists most often work. Therefore, preexisting spectroscopic measurements in "new" molecular systems for precision measurement often have uncertainties that are too large ($>$ MHz) for quantum state control and readout.

Advances in high-resolution spectroscopy, then, enable both rapid development of quantum science and precision measurement systems, as well as better benchmarking of *ab initio* of quantum chemistry calculations, increased sensitivity to trace elements and rare isotopes studied in geology, medicine, and atmospheric science and astronomy, and improved knowledge of molecular structure, dynamics, material properties and reaction kinetics. These advances can take shape broadly as technological improvements in molecule production methods, in light sources, and in detectors. In the first portion of this chapter, we describe a novel (and practical) method for DC absorption spectroscopy of molecules, which can simultaneously measure several bands in a single shot without frequency stabilization, frequency scanning, or complex control schemes, using broadband supercontinuum light in combination with a sub-pm resolution, virtually imaged phased array (VIPA) etalon spectrometer, which was published in [85]. This method combines many of the advantages of existing methods while maintaining simplicity and ease of use, to enable rapid spectroscopic characterization of molecules, with particular applicability to the gas-phase species and short-lived, free radicals that are commonly found in quantum science, precision measurement, astronomy, chemistry, geology, and materials science. The second portion of this chapter describes progress towards spectroscopic characterization of the EDM-sensitive bending mode in the SrOH molecule, using traditional methods.[1]

6.1 Overview of existing spectroscopic methods

Some of the common methods for high-resolution molecular spectroscopy include DC absorption and laser induced fluorescence (LIF), which have both been discussed in Chapter 3.3 due to their ubiquity in molecular beam experiments. Single-frequency DC absorption spectroscopy is not a zero-background measurement, which ultimately limits the achievable SNR. The resolution that is achievable is furthermore limited by the Doppler width of the molecular cloud, though saturated absorption with overlapped counter-propagating probe beams allows for Doppler-free measurement.

Frequency modulation (FM) absorption spectroscopy is another common single-frequency method that uses lock-in detection in combination with AOMs to measure spectral features in the radio frequency (RF) range, suppressing low frequency noise [86, 87]. In our group, FM absorption has been used to measure and assign 38 lines in the $\tilde{A}^2\Pi_{1/2}(1,0,0) - \tilde{X}^2\Sigma^+(3,0,0)$ band of $^{174}\mathrm{YbOH}$, as well as to study the unassigned [17.68] and [17.64] bands in the same molecule [88]. The technique ultimately provided approximately 100-fold increase in SNR over DC absorption, allowing for relatively simple measurement of a higher-order repump transition in YbOH and insight into highly perturbed excited states, which are both critical for laser cooling and quantum control. Nonetheless, FM absorption can be affected by SNR degradation from broadband attenuation of the probe through dust and debris that accumulate in buffer gas cells. This effect can be especially pronounced in closed cryogenic buffer gas cells, which our group is using for spectroscopy of cold, radioactive molecules such as RaOH.

LIF spectroscopy in a molecular beam, in which a transition is driven and fluorescence photons from excited state decay are collected on a PMT or camera, has the advantage over DC absorption that the signal has zero background, and high signal-to-noise ratios (SNR) are achievable if scattered light at the detector is minimized through geometry and appropriate spatial and optical filtering. While the molecule density is smaller in a

---

[1] Let it be known to the reader that work on SrOH preceded our work on new spectroscopic methods, but a very unfortunate, three-month chilled water outage completely shut down all cryogenic experiments until after funding for SrOH spectroscopy ended. The earliest spectroscopic methods work was thus done in atomic titanium in a vacuum chamber filled with *room temperature* helium buffer gas, as discussed later in this chapter. Once cryogenic operation was possible, the integrated spectrometer was tested in more typical conditions.

beam compared to inside a buffer gas cell, collimators installed along the beam path significantly reduce the Doppler broadening of spectral features probed by a transverse laser.

All of the methods discussed so far—DC/FM absorption and LIF spectroscopy—are all single-frequency methods. Recording a molecular band spectrum with sufficient precision to extract molecular constants would require scanning a frequency-stabilized, narrow linewidth laser ($\sim$ MHz) over many 10s of GHz, with multiple measurements in each frequency bin for averaging away noise. As molecules used in quantum science and precision measurement are commonly produced in pulsed beam sources through laser ablation, shot-to-shot fluctuations in molecular production limit experimental confidence in observed line intensities. Without adjusting the position of the ablation laser (rastering) or using a (heated) fill line to introduce reagent species, a typical ablation target will support "good" production for 10-100 shots. Without any compensation for overall target decay, portions of a spectrum recorded later in time will have smaller intensities compared to those recorded earlier. Spectra can be recorded from red to blue, followed by the reverse direction to compensate for these systematic effects, or frequencies can be recorded at random. Even with rastering and heated fill lines, fluctuations in production lead to noise in the relative intensities of spectral features. In order to compensate for this noise, single-transition absorption spectroscopy either inside or directly outside of a buffer gas cell is used to normalize LIF signals measured further downstream. Even so, in-cell absorption on a particular line may not track fluctuations in molecule number perfectly well and requires including a second frequency-stabilized laser in the experiment.

In many cases, knowledge of relative line intensities is important. For this reason, and for the sake of overall measurement efficiency, methods for simultaneous measurement of several spectral features are employed. These include dispersed LIF (DLIF) and an assortment of frequency comb-based methods [89, 90]. In DLIF, molecules are excited to particular excited states, either via single frequency lasers (which must still be scanned) or through pulsed dye lasers, and the resulting decay fluorescence from the excited state(s) is dispersed and imaged on a monochromator. Ultimately, this technique is limited by the calibration and resolution of the monochromator. DLIF has been used extensively to study the vibrational branching ratios of molecules, but existing monochromators generally do not provide the resolution to study the rotational structure of decay channels [91]. As an aside, amplified spontaneous emission of the probe light and contamination of the beamline with other species can cause extraneous features to appear in the spectra, which must be disentangled in analysis. In the case of DC/FM absorption and LIF/DLIF, one must take care to calibrate the spectrum (or x-axis of the monochromator), for example, using the well-studied spectrum of I_2 vapor.

There are also a number of interferometric and Fourier transform-based frequency comb methods to make simultaneous measurements of complex molecular absorption spectra. In this case, the frequency comb itself provides with absolute frequency calibration provided by the frequency comb itself. When sent through a molecular sample, the DC absorption of each comb tooth can be monitored to extract the spectrum [92]. The signal obtained can be enhanced by increasing the optical path length of the light through the sample. This can be achieved with a pair of mirrors in, for example, the Herriott configuration, or through the use of resonant optical cavities [64, 90]. Fourier transform spectroscopy (FTS), using scanning Michelson interferometers with motorized mirrors, is one common way to read out the spectrum with a frequency comb. Here, one must accept long data acquisition times and moving mechanical components inside the scanning interferometer. Dual comb spectroscopy (DCS) uses a second frequency comb with a time delay relative to the first instead of a moving interferometer arm. Over the last 15 years, VIPA etalon spectrometers have been used in conjunction with frequency combs to improve measurement sensitivity and data acquisition times for IR spectroscopy [90, 93].

Frequency comb spectroscopy methods continue to be developed and improved, but in general, they require expensive equipment and sophisticated control systems to maintain phase coherence and manage noise [92]. Using a custom VIPA etalon spectrometer and a commercially available supercontinuum light source with radicals produced in our pulsed, cryogenic molecular beam source, we have recently demonstrated a simple and novel method for rapid, high-resolution, and broadband molecular spectroscopy. Ultimately, we have recorded single-shot spectra with 0.56 pm resolution between $525 - 540$ nm, with shot-noise limited absorption sensitivity of $0.01/\text{shot}$. The following section will provide details about each component of this integrated molecular spectrometer.

6.2 Broadband DC absorption spectroscopy with a VIPA etalon spectrometer

Using existing technologies, rapid spectroscopic characterization of cold molecules is enabled by the integration of three subsystems: a highly broadband, (quasi-) continuous wave laser with sufficient power in each spectral bin, a high-resolution spectrometer which can resolve individual absorption lines, and a cryogenic buffer gas molecular beam source. We now discuss each subsystem in some detail.

6.2.1 HyperFine spectrometer with sub-pm resolution

The spectrometer used in this manuscript is a custom "HyperFine" spectrometer designed and manufactured by LightMachinery Inc. The spectrometer combines a high-efficiency and high-resolution VIPA etalon, which provides large angular dispersion for light of different wavelengths, with an orthogonally aligned diffraction grating (2400 l/mm) that separates out degenerate VIPA mode orders. The resulting 2D pattern of stripes is imaged on an integrated Teledyne Photometrics IRIS 9 sCMOS camera (9 Megapixel sensor, $17.8\ \mathrm{mm}$ field of view, and 16 fps acquisition rate). Included software converts the camera image into a 1D spectrum. The spectrometer is sensitive to sub-pW laser powers per spectral element. The spectrometer takes a single-mode fiber input, which is convenient for imaging intense broadband sources such as the supercontinuum laser. The model we currently have is a prototype with a $0.55\ \mathrm{pm}$ resolution and sensitivity between $525 - 540\ \mathrm{nm}$. The overall detection efficiency is approximately 10% when combining the quantum efficiency of the camera and optical transmission through the spectrometer. We plan to receive a finished model of the spectrometer with sensitivity over the entire visible and near-IR range in the months to come.

6.2.2 Broadband laser source

Supercontinuum lasers generically produce light with large spectral bandwidth through nonlinear optical processes. Commonly, ultrafast pulses are sent through highly non-linear, photonic crystal single-mode fibers in order to generate extremely broadband lasers with high spatial coherence (but low temporal coherence) [94]. Supercontinuum light can be used to drive probe molecular resonances simultaneously as long as there is sufficient intensity in each spectral bin.

In our method, 1 W of light over $415 - 2250$ nm is generated from an NKT SuperK EVO supercontinuum fiber laser (NKT SuperK EVO ERL-04), which is then directly coupled into a NKT SuperK VARIA tunable filter. This filter transmits light in any adjustable $10 - 100$ nm window between 400 nm and 840 nm, which is convenient for limiting the laser spectrum to the range of interest, while dumping the large amount of laser power outside of this range. The SuperK EVO laser has a typical spectral power density of $\sim 0.3\ \mathrm{mW/nm^2}$ in the visible range.

The SuperK VARIA settings are chosen to maximize transmitted power and uniformity over the sensitivity range of the spectrometer and to dump power in unused wavelengths away. For all data shown here, unless otherwise stated, a center frequency of 520 nm with a 100 nm bandwidth was used because it maximizes the flatness of the laser spectrum on the spectrometer.

6.2.3 5 K cryogenic buffer gas molecular source

The cryogenic buffer gas source used for this work is largely the same as described in Chapter 3, with the 1K stage thermally anchored to the 4K stage with copper braids. The copper cell is the same one used for the deceleration work in Chap. 5, but some of its features are not optimized for absorption spectroscopy. In particular, the absorption window is small and located near the cell exit aperture, where the molecule density is lower. In order to increase the molecular density near the exit aperture, a 100-mesh copper sheet was epoxied to the cell aperture, reducing the effective flow of molecules through the exit while helium buffer gas is flowed.

Molecules are produced via laser ablation of targets on the target plate with 50 mJ, 6 ns pulses generated from a 532 nm Nd:YAG laser. The helium buffer gas was introduced at a flow rate of 20 SCCM, which was the maximum afforded by our mass flow controller. With a buffer gas flow and ablation at about 2 Hz, the cell temperature typically rose from 4.2 K to 5.1 K after several initial ablation shots. This beam source was used to produce both atoms and molecules in order to study the performance of this spectroscopic method.

6.2.4 Subsystem integration for pulsed molecular spectroscopy

The integrated spectrometer sends in the supercontinuum light through the pulsed molecular cloud, and then this light is imaged on the spectrometer (Fig 6.1). Pulsed

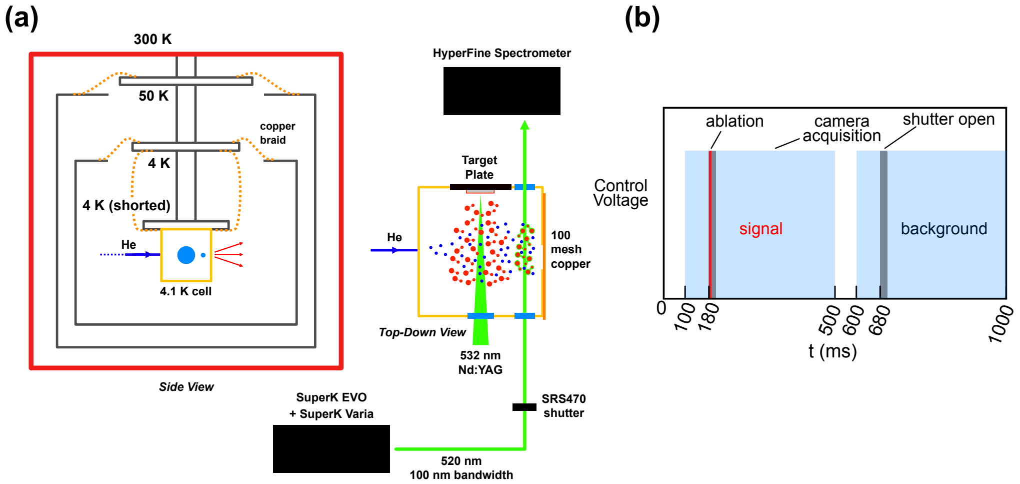

Figure 6.1: Schematic of the integrated spectroscopy apparatus. (a) Molecules are produced in a 5 K helium buffer gas beam through laser ablation of a solid target. A 100-mesh copper sheet is placed in front of the exit aperture to increase in-cell molecule density and fractional absorption of the supercontinuum light. (b) Data acquisition timing sequence for a pair of acquisitions (signal and background). The laser shutter is responsible for exposing the camera to supercontinuum light. The impact of integrating dark counts when molecules are not present is completely negligible.

molecular production which means that the spectrometer must acquire data in sync with the molecular pulse in order to maximize the SNR. A picture of the data acquisition timing sequence is shown in Fig. 6.1.

The camera image acquisition rate is 16 Hz, but processing of the 2D spectrum and saving of the 1D spectrum adds significant temporal overhead. Therefore, each acquisition timing sequence is kept at 500 ms in order to allow for 2 Hz acquisition. During the entire run, helium is flowed at 20 SCCM. At $t = 100$ ms, the camera is triggered to begin acquisition for a duration of 400 ms.[2] A SRS470 laser shutter was used to transmit the supercontinuum light for a 4 ms duration (near-)simultaneously with the ablation pulse occurring at around $t = 180$ ms.[3] Therefore, for the majority of the detection window the camera is receiving no light. In practice, the dark count rate on the camera is so small that this additional exposure does not reduce the sensitivity

---

[2] This duration can likely be shortened, but this time was chosen because it did not lead to any bugs in data saving and was still sufficiently rapid for practical use.

[3] Due to mechanical limitations, the shutter cannot be opened and closed in any less than $4 - 5$ ms. For atoms, the shutter is usually opened a few ms before ablation. Because molecules are formed out of reactions, the molecular pulse is often slightly delayed relative to the atomic pulse. Therefore, for molecular spectroscopy, simultaneous shuttering and ablation led to the largest signals on the spectrometer.

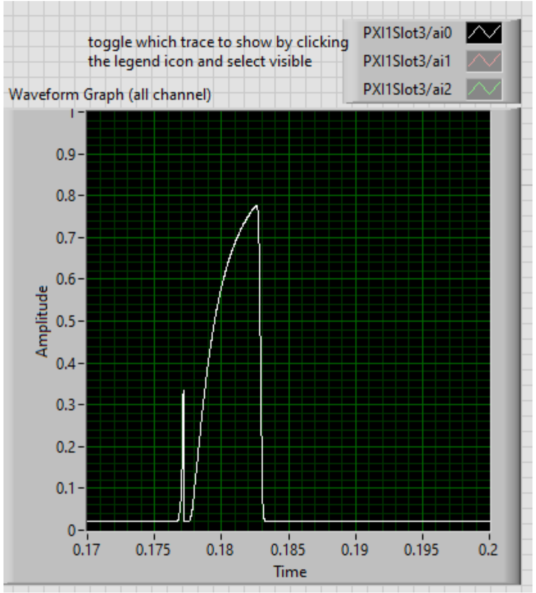

Figure 6.2: Photodiode signal of Ti atom absorption of 25057.087 cm^{-1} laser light after ablation of solid Ti metal with ~ 30 mJ pulses and 20 SCCM helium buffer gas flow. The pulse around the absorption dip shows the action of the SRS shutter, whose open window is well-overlapped with the atom absorption. The Ti absorption laser is co-aligned with the supercontinuum light to ensure approximately optimized shutter timing for the spectrometer data acquisition.

of the final measurement. Large helium flows are useful for increasing the duration of the molecular pulse, and therefore there is interest in exploring higher buffer gas flow regimes and closed buffer gas cells. To confirm sufficient overlap between molecular production and the shutter window, Ti atom absorption of laser light at 25057.087 cm^{-1} generated by a 399 nm MogLabs ECDL was observed on an amplified photodiode with the shutter in place (Fig. 6.2).[4]

Absorption spectra are obtained through sequential differential measurement. In other words, spectra acquired with ablation are subtracted from spectra acquired without ablation, and the difference signal, appropriately processed, gives the absorption spectrum. This method allows us to compensate for slow drifts in the broadband laser spectrum as well as shot-to-shot laser intensity fluctuations. A portion of the broadband probe light is also diverted through a room temperature vapor cell of I_2 , which has well-studied

---

[4] Initial prototyping of this spectrometer was performed in a room temperature buffer gas source at fixed vacuum chamber pressures between 100-1000 mTorr. Ti atomic absorption was studied because there are several lines in the spectrometer's range, though none of them out of ground states. Ultimately, only one of these lines was visible with low SNR and 500-fold averaging, and we quickly moved onto to investigating room temperature I_2 vapor absorption and the cryogenic work described here. Therefore, further details about room temperature buffer gas work are omitted from this thesis.

transitions over a large spectral region [95, 96]; this vapor cell allows for rapid, single-shot calibration of the entire spectrometer frequency range by comparing the hundreds of strong transitions visible on the spectrometer with known line positions tabulated in the IodineSpec5 software. The data analysis is discussed briefly in Sec. 6.3.2 and the I_2 calibration is described in Sec. 6.3.3. It is good practice to run the "Quick Calibrate" command on the spectrometer software each day. Because this cannot be done with triggered data acquisition, the spectrometer is quick-calibrated on the supercontinuum light with no shutter for a continuous exposure of $4\ \mathrm{ms}$, which roughly matches the effective exposure when the shutter is used.

6.3 Molecular absorption spectroscopy data and analysis

6.3.1 Initial measurements of atomic spectra

For initial testing of the spectrometer in a cryogenic apparatus and refinement of the data analysis scheme, four atomic species were investigated with transitions between $525 - 540\ \mathrm{nm}$—Ti, Tm, La, and Dy. The absorption spectra of for each species is shown in Fig. 6.3. For the preliminary data analysis, the signal intensity envelope was rescaled to match that of the background by a smooth interpolation of the background in order to compensate for laser intensity drift during data taking.[5] For these plots, the absorption fraction was computed by subtracting the rescaled signal from the background and then dividing by the background. If one then plots the histogram of spectrometer counts, one would find a Gaussian centered about zero representing noise and a low-incidence tail corresponding to transitions. The Gaussian can be fit to extract a cutoff that can be used in plots to show only signal. This artificial cutoff was used in preliminary data analysis but was ultimately abandoned in favor of a more robust scheme described in the next section.

6.3.2 Data analysis

The entire spectrum extraction protocol was developed by Nick Hutzler and is detailed in [85]. This scheme was used to analyze the spectra shown in Sec. 6.3.4, and is therefore described briefly here. Briefly, adjacent signal and background data are subtracted from each other and then divided by the average of the signal and background. The result is

---

[5] The scaling function was computed using a third-order Savitzky-Golay filter on the ratio of signal and background. See [85] for more details.

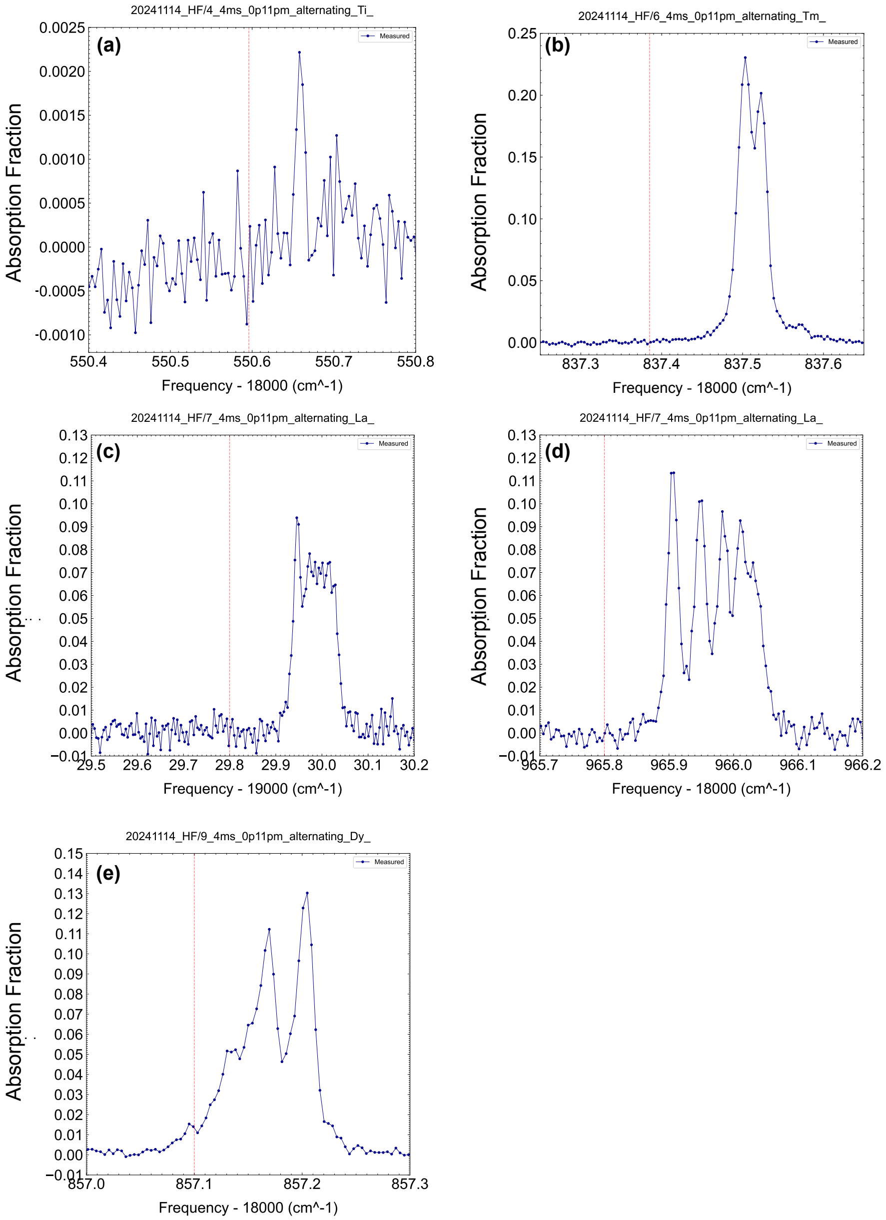

Figure 6.3: Absorption spectra for atomic (a) Ti at 19034.710 cm^{-1} ($[3d^24s^2]\ a^3F_4 - [3d^2(^3F)4s4p(^3P^\circ)]\ z^3F_3{}^\circ$) [97], (b) Tm at 18837.385 cm^{-1} ($[4f^{13}(^2F^\circ)6s^2]\ ^2F^\circ{}_{7/2} - [4f^{12}(^3H_6)5d_{5/2}6s^2]\ (6,5/2)_{9/2}$) [98, 99], (c) La at 18965.8 cm^{-1} ($[5d6s^2]\ ^2D_{5/2} - [5d(^1D)6s6p]^\circ{}_{3/2}$) [99], (c) La at 19029.8 cm^{-1} ($[5d6s^2]\ ^2D_{5/2} - [5d^2(3F)6p]\ ^4F^\circ_{3/2}$) [99], and (e) Dy at 18857.1 cm^{-1} ($[4f^{10}6s^2]\ ^5I^\circ{}_8 - [4f^9(^6F^\circ)5d6s^2]^\circ{}_7$) [99]. Red lines show the NIST Atomic Spectra Database transition wavenumbers, with an offset from the measured feature due to the uncalibrated x-axis [100]. The number of spectra averaged are 250, 100, 5, 5, and 25, respectively. The La$^+$ ion also has transitions in this range, but ion absorption was not observed.

an "uncorrected spectrum" that clearly shows lines. Nevertheless, the supercontinuum light imaged on the spectrometer shows a "slow" frequency-dependent drift on this uncorrected spectrum, oscillating with a $\sim 200\ \mathrm{cm}^{-1}$ period. To remove this slow background, the uncorrected spectrum is fit to a sextic polynomial with robust bisquare weighting (essentially to have the fit ignore sharp spectral features).

The spectrometer itself exhibits slow temperature-dependent drift over several hours, and therefore, prior to averaging multiple datasets, a relative calibration against a strong single shot feature is applied. In other words, an offset is applied to shift spectra so identical features are made to "line up." For the work in CaF, described in Sec. 6.3.4, the unresolved feature consisting of the ${}^{P}Q_{12}(1)$ line at $188832.445\ \mathrm{cm}^{-1}$ and $P_1(1)$ line at $18832.441\ \mathrm{cm}^{-1}$ are used for calibration. The resulting spectrum exhibits both a slow and fast background, which are fit to an eighth order polynomial and robust spline, respectively. With all of these corrections applied, the fractional absorption resolution averages to down to the 7.3×10^{-5} level, consistent with shot noise averaging for 10^4 averages. We call the absorption fraction with all corrections applied the "corrected spectrum." The absolute calibration of the spectrometer is provided by an room temperature molecular iodine reference, described in the following subsection.

6.3.3 Spectroscopy of room temperature I_2 and spectrometer calibration

As mentioned earlier, the forest of I_2 transitions are used for absolute frequency calibration of the spectrometer to around the linewidth of the spectral features. The room temperature vapor cell of molecular iodine is dense enough that there are hundreds of strong absorption features in a single shot. As discussed above, the noise in the spectrum occurs over a much wider frequency range ($1\ \mathrm{cm}^{-1}$) compared to the observed linewidth of $0.018\ \mathrm{cm}^{-1}$. Therefore, the iodine absorption provides an easy and reliable calibration for the entire x-axis with minimal additional processing. When the I_2 vapor cell path is imaged, the spectrometer image shows absorption in numerous pixels across the entire sensitive range that are easily visible by eye, indicating the presence of strong absorption features that can be used to calibrate the entire x-axis (Fig. 6.4).

In order to extract the I_2 spectrum, a pair of 50-50 beamsplitters are used to send supercontinuum light through the vapor cell (signal) and bypassing the vapor cell (background). The two optical paths have different etaloning properties and throughput, and therefore the same smoothing procedure as given in Eq. (4) of [85] is used to compensate in the mismatch between intensity envelopes for the signal and background.

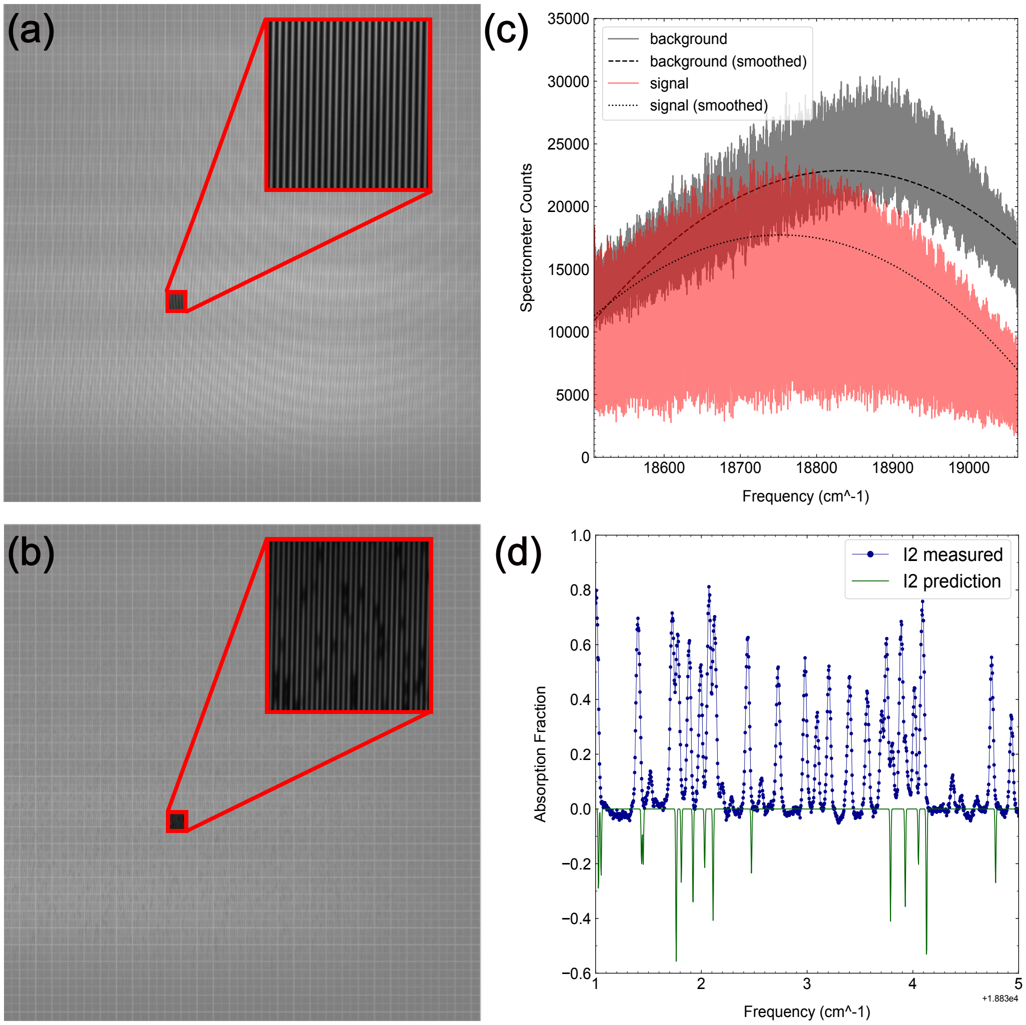

Figure 6.4: Spectrometer 2D camera images and unwrapped 1D spectra for molecular iodine. (a) and (b) show typical 2D images recorded by the spectrometer camera for the supercontinuum laser (background) and absorption in an I_2 vapor cell (signal). The image shown is dimmed with an inset to show a small region of the camera sensor. Each stripe in (a) corresponds to a mode of the VIPA etalon diffracted off of the diffraction grating. The image in (b) has the same set of stripes with dark spots appearing where there is molecular absorption. (c) 1D spectrum for a single background and signal measurement, along with curves indicating the smoothed signal and background used to compute the absorption fraction. (d). Single-shot measurement of the iodine spectrum. There are hundreds of measured lines over the entire spectrometer range that approximately align with predictions from IodineSpec5, which are plotted as a sum of Lorentzians with 420 MHz FWHM (scaled and inverted for clarity of comparison).

The absorption fraction is computed following Eqs. (1) and (2) from [85].

The iodine line predictions are generated in IodineSpec5 and compared to the observed absorption fractions, which show clear agreement across all regions of the frequency axis. A slight linear correction is needed to calibrate the spectrometer. The linear fit can be computed by trying to match features, line by line, but we adopted a more efficient and straightforward method, in which the overlap integral between the prediction and the measurement is numerically optimized over a set of linear corrections.

For recording CaF data, described in the following subsection, a single shot of I_2 calibration data was recorded between each CaF data run. This allowed for observation of the calibration over the ~ 10 hours of spectrometer operation. The linear scaling was found to be extremely consistent at 1.0002 across the entire spectrometer range, while the instrument offset was measured to be stable within $-0.164 \pm 0.001\ \mathrm{cm}^{-1}$. Fluctuations and drifts in the spectrometer temperature are the main driver of this offset, and the manufacturer has quoted that the temperature-dependent frequency shift is about which $0.12\ \mathrm{cm}^{-1}$/°C. As an additional confirmation of our ability to calibrate the spectrometer, we used the known positions of lines in the $(0,0)B^2\Sigma^+ - X^2\Sigma^+$ band of CaF and compared them to our observed line positions post-calibration [101]. In particular, we studied the ${}^PQ_{12}(1)$ line at $18832.445\ \mathrm{cm}^{-1}$ and $P_1(1)$ line at $18832.441\ \mathrm{cm}^{-1}$, which agrees well with our observation of the feature at $18832.44 \pm 0.001\ \mathrm{cm}^{-1}$ over several hours of data acquisition.

Thus we have demonstrated our ability to calibrate the spectrometer to within instrument resolution, a necessary component of analyzing data acquired over several hours.

6.3.4 Spectroscopy of cold, pulsed CaF molecular beam

The polar molecule CaF is a well-studied molecular system with extensive spectroscopic characterization [101, 102], and it is widely used in quantum science experiments, having been laser cooled and trapped in optical tweezers [49]. The $B^2\Sigma^+ - X^2\Sigma^+$ system in CaF at $531\ \mathrm{nm}$ lies near the center of the sensitivity range of the spectrometer and is therefore an ideal species to test the performance of the integrated spectrometer.

Additionally, there are strong motivations from geology ([103]), medicine ([104]), and astronomy ([105]) to understand the relative abundances of Ca isotopes. For example, isotope ratios can be used to study mineral imbalances in astronauts that can be early warning signs of disease [106]. Mass-spectrometry (i.e., multi-collector inductively coupled plasma mass spectrometery or MC-ICP-MS) is often used to measure isotopic abundances but an all-optical technique is also simple and desirable. Direct measurements of the isotope shift in atoms are small ($\sim\ 100 - 1000$ MHz) and can be challenging to measure. However, in molecules like CaF, the isotope shifts in vibronic features are amplified, and in the case of CaF, the isotope shifts are well resolved ($\sim$1000s of MHz) and easily measured in our spectrometer. The relative isotopic abundance of ^{40}Ca and ^{44}Ca was recently measured by comparing the bandhead intensity of the $(1,0)A^2\Pi_{1/2} - X^2\Sigma^+$ band in ^{40}CaF and ^{44}CaF, derived from a human urine sample [107]. Using our spectrometer, we have been able to study and measure the 531 nm $B^2\Sigma^+ - X^2\Sigma^+$ system in CaF, including thirteen overtone bands. Isotope shifts are also apparent in the fundamental and first overtone band.

In previous work, cold CaF molecules were produced through ablation of solid Ca in the presence of SF_6 background gas reagent, which was found to produce cold and bright beams [108, 109]. A simple alternative for testing our spectrometer is to ablate a CaF_2 sputtering target, in line with the other simple solid-state ablation targets we frequently work with.

CaF was produced through laser ablation of a this sputtering target with ~ 50 mJ pulses. In total, 13198 CaF absorption spectra were acquired over approximately 10 hours, which when properly analyzed and averaged allowed us to unambigously observe up to the 16-16 overtone band. The strongest features of the CaF origin band ($R_1(1)$ and $R_2(1)$) were visible in a single shot on the spectrometer and these absorption features were used to monitor and optimize CaF production in real time. Spectra were collected with occasional adjustment of the ablation steering, until target decay caused sufficient signal degradation. In order to account for drift in observed spectral lines over $\sim$ 10 hours of data collection, a single pair of I_2 background and absorption spectra was collected before and after every CaF data set, and the frequency axis was calibrated before fitting.

Fig. 6.5(b) shows the $(0,0)$ band along with a spectrum prediction, while the full absorption spectra is shown in Fig. 6.5(a). Fig. 6.5(c) shows a single observed line with the experimental resolution of 0.018 cm^{-1}, consistent with the quoted spectrometer resolution of 0.5 pm.

Our collaborator, Tim Steimle, performed a full simultaneous fit of the 0-0, 1-1, ..., 14-14 bands to an effective Hamiltonian. In total, 386 spectral features were fit and assigned across these fifteen bands, and spectroscopic constants were extracted. The ground state spin-rotation splitting is smaller than the instrument resolution and therefore the value of this parameter was kept fixed to the known value during the

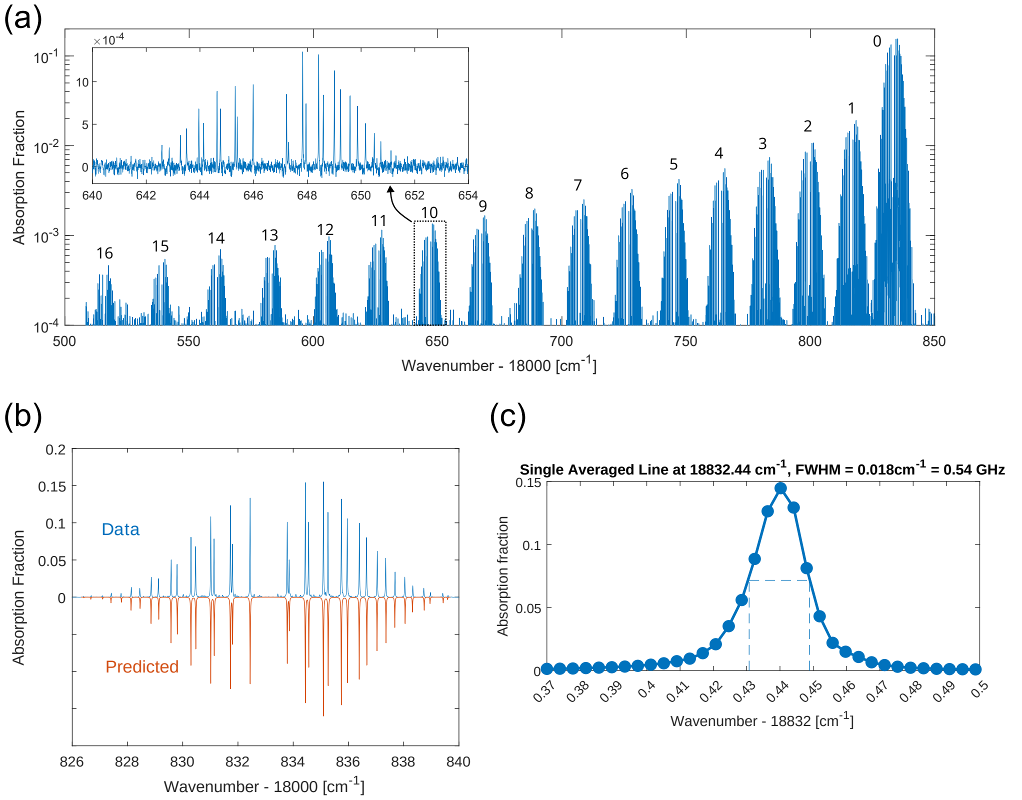

Figure 6.5: Measured CaF spectra. (a) All observed $\Delta v = 0$ bands in the CaF $B^2\Sigma^+ - X^2\Sigma^+$ system, with the observed (10,10) band in the inset. (b) The measured absorption spectrum of the CaF $(0,0)B^2\Sigma^+ - X^2\Sigma^+$ band with effective Hamiltonian line predictions. (c) The observed ${}^PQ_{12}(1)$ and $P_1(1)$ lines in the $(0,0)B^2\Sigma^+ - X^2\Sigma^+$ band in CaF. These lines are overlapped and unresolved within our instrument, which has an apparent resolution of 0.018 cm^{-1}. Plots generated by Nick Hutzler and taken from [85].

fit. In general, the rotational constant, excited state spin-rotation constant, and band origin constants show excellent agreement with previous measurements in other systems. The full results are tabulated in [85]. Additionally, a "stick" diagram of the predicted transitions in ^{40}CaF and ^{44}CaF are shown in the manuscript. A quick comparison with Fig. 6.5(b) shows that several of the transitions in the less abundant ^{44}Ca isotope are visible in the Q-gap of the origin band.

Thus, we have demonstrated the ability to record multiple bands of molecular spectra at high resolution *simultaneously* and at high resolution in a matter of hours of data taking. The simultaneous measurements allow for accurate comparisons of line intensities, compared to single-frequency spectroscopy methods which must contend with fluctuations in production from shot to shot. For example, using this method, we used the the measured intensity of a particular transition in each overtone band to extract the vibrational temperature of $T_{\text{vib}} = 2240$ K by fitting to an exponential function, confirming the fact that the buffer gas does not effectively thermalize molecular vibrational states (Fig. 11 of [85]).

6.3.5 Spectrometer noise properties

For this work, we describe the noise level as the standard deviation of the corrected spectrum, where the spectrum uses only background shots where no molecules are present or regions of the true spectrum where there are no lines. The noise histogram for all 13198 CaF shots is shown in Fig. 6 of the manuscript and demonstrates that this quantity is Gaussian [85]. For a single shot, the noise floor in fractional absorption is 0.009. Because the molecular spectra are obtained through sequential differential measurements across a wide frequency range and spectral features are much narrower than fluctuations due to laser intensity noise or slow spectral drifts, the noise floor is set by the photon shot noise.

6.3.6 Future improvements to supercontinuum spectroscopy and outlook

There are a number of straightforward means to improve the operation of this integrated molecular spectrometer. Building a cryogenic cell optimized for absorption spectroscopy would involve increasing the size of the absorption window and moving the optical path closer to the center of the cell where the molecular density is highest. The larger windows would also enable multipassing the supercontinuum light, linearly increasing the optical path length in the molecular cloud. In order to minimize losses from multiple reflections, various windows in the beam source and cell could be AR coated for visible or near-IR wavelengths.

A number of molecules of interest have transitions in the visible and near-IR, and extending the range of the spectrometer over this range is critical for widespread use of this technology. In order to extend operation across the entire visible and near-IR range, a HyperFine spectrometer with tunable sensitivity is in development. This is accomplished by including a swappable diffraction grating and further optimizing the camera imaging system to correct for chromatic aberrations across this range. Upgrades to the camera, e.g., hardware pixel binning, would improve data acquisition rate and reduce the time required to record and average 10^5 spectra in order to measure weak features.

In order to straightforwardly improve the resolution of the spectrometer, filter cavities can be employed to convert the supercontinuum light into a series of peaks in the frequency domain, spaced by the free spectral range of the cavity. The cavity length can be scanned to shift these peaks across molecular resonances and imaged on the spectrometer in order to resolve features smaller than the maximum spectrometer resolution, enabling measurement of MHz-scale spin-rotation and hyperfine splittings, and rotational structure in complex molecules with small rotational constants, such as $\mathrm{SrOC_6H_5}$ (SrOPh) [110]. Nonetheless, the Doppler broadening of molecules inside a buffer gas cell would ultimately limit the resolution of this method.

The broadband absorption methods discussed thus far are helpful for characterizing and unambiguous assignment of the ground and excited state energies, but spectra collected in this manner do not give information about the transition dipole moments between these states. The transition dipole moments directly relate to important properties for laser cooling such as lifetimes and vibrational branching ratios. Transition dipole moments can be highly sensitive to higher-order perturbations and therefore difficult to model and predict accurately, compared to energy levels. Even "simple" polyatomic molecules like ^{173}YbOH has a very complex rotational structure that must be tamed in order to do state preparation, photon cycling, and quantum control operations. Large asymmetric top molecules, such as calcium(I) phenoxide or strontium(I) phenoxide, that have lower symmetry than linear molecules and less stringent selection rules, have complex vibrational-rotational branching that must be measured precisely to use these species for quantum science applications [110, 111].

As mentioned earlier in this chapter, DLIF detected on a monochromator has been used to study decays from particular excited states, and in principle the HyperFine spectrometer could be used to do the same with much greater resolution in order to resolve rotational structure. One could, for example, optically pump into particular excited states and study decay channels into all symmetry-allowed ground states simultaneously, in order to extract branching ratios and lifetimes. The intensity of fluorescence from a dilute molecular gas is small in the absence of photon cycling, so the coupling efficiency into a single-mode fiber must be modeled. Towards this end, we are building ray tracing simulations of front-of-cell fluorescence collection schemes in the LightTools software. A combination of broadband supercontinuum absorption and state-specific fluoresence collection using the methods discussed here will provide a tremendous boost to spectroscopy efforts that are necessary for quantum science using cold molecules.

6.4 An electron electric dipole moment search in trapped SrOH

As described in Chapter 1, much of the work described in this thesis was done as part of the PolyEDM collaboration, which is building an electron EDM search in trapped, polyatomic molecules. The very first molecule proposed in this collaboration was $^{174}\mathrm{YbOH}$, which was extensively studied by members of our collaboration, including in the theses of former Hutzler Lab members Nickolas Pilgram, Arian Jadbabaie, and Yi Zeng. In 2022, spectroscopy and *ab initio* structure calculations for the YbF EDM experiment at Imperial College, London, revealed complications arising from the Yb electronic structure that would make laser cooling impossible without significant additional spectroscopy [32, 33].

To summarize, the Yb electronic configuration is $[\mathrm{Xe}]4f^{14}6s^2$, and in molecules like YbF, there are molecular excited states that correspond to electronic excitations out of the inner $4f^{14}$ (leaving $4f^{13}$), which are often referred to as "$4f$ hole states." These hole states both perturb the $^2\Pi_{1/2}$ excited state and low-lying hole states mix with the $^2\Sigma_{1/2}$ ground state, causing 10^{-4} level leakage out of the photon cycling scheme. In YbF, only 2000 photons can be scattered without repumping these $4f$ hole states, which is not enough for trapping in a MOT [32]. These states are expected cause major issues in laser cooling YbOH. At the time of the writing of this thesis and after several years of effort, the low-lying $^{174}\mathrm{YbF}$ hole states have been characterized spectroscopically at Imperial College, but repumping has not been demonstrated [34]. Therefore, laser cooling and trapping YbOH would require a significant spectroscopic effort.

Therefore, a decision was made in the collaboration to consider which alkaline-earth(-like) hydroxide molecule would be best suited for a proof-of-principle demonstration of an EDM measurement in trapped, polyatomic molecules that could nonetheless set competitive limits with conceivable upgrades. Fortunately, every step toward performing an EDM experiment–production, slowing, trapping in a MOT, trapping in an ODT, and spin precession and readout–has been demonstrated in the CaOH molecule, with extended coherence times using field-insensitive states that generically arise in polyatomic molecules. Due to the light mass of Ca and the corresponding smaller effective electric field, however, a measurement competitive with the current limit set by the JILA II experiment would require 500000 CaOH molecules trapped in an ODT, which is a factor of 25 more than the number currently trapped in a MOT [50]. Some of the heavier species also pose problems. BaOH contains low-lying, metastable states that complicate laser cooling, just like in BaF [112], and RaOH while predicted to be extremely laser coolable has very limited spectroscopy and presents a severe radiation safety overhead while working with even a very limited quantity. HgOH is not laser coolable [113], and YbOH faces the severe spectroscopic challenges for the same reasons as YbF.

We are then left with SrOH as a particularly promising candidate. When the molecule was first proposed in our collaboration, there was extensive spectroscopy and a demonstration of 1D Sisyphus cooling, with the 3D laser cooling scheme well-understood [47]. By the time of the writing of this thesis, $\sim$ 2000 SrOH molecules have been trapped in a MOT [35]. Approximately 10000 molecules are needed in an ODT to be competitive with the JILA II limit, but these factors are significantly more attainable in the near-term than a 25-fold improvement in CaOH or a years-long spectroscopy effort in YbOH. Importantly, radiative laser slowing methods have been employed successfully in SrOH, and trapping was not dependent on non-radiative schemes like ZS deceleration, which are still in development.

The laser slowing, cooling, and trapping of SrOH was done by our collaborators at Harvard University. At Caltech, our objective was to characterize the EDM science state in SrOH, which is the ground state bending mode $\tilde{X}^2\Sigma^+(010)$, in particular its Stark and Zeeman tuning properties, as was done earlier in YbOH [114]. The remainder of this chapter describes the progress made towards characterizing the EDM science state in SrOH.

6.5 Towards science state spectroscopy in cold SrOH

6.5.1 Possible measurement schemes

The basic level structure of the ground and first two electronic excited states in SrOH are shown in Figure 6.5.1. There are a number of bands that could be used to study the $\tilde{X}^2\Sigma^+(010)$ state in a pump probe scheme. Transitions between the ground state bending mode to the fundamental bending mode in either excited state ($\tilde{A}^2\Pi_{1/2}(010)$ at 687 nm or $\tilde{B}^2\Sigma^+(010)$ at 609 nm) are relatively easy to drive due to the strong Franck-Condon factor between the states, with a correspondingly fast decay rate back to the ground state bending mode. Bandpass filters can be used to detect weak, off-diagonal decays to other ground states, such as $\tilde{X}^2\Sigma^+(000)$, which has the advantage of filtering out scattered probe light from the detector. Alternatively, with a laser with sufficient power, the off-diagonal transition between $\tilde{X}^2\Sigma^+(010)$ and $\tilde{A}^2\Pi_{1/2}(000)$

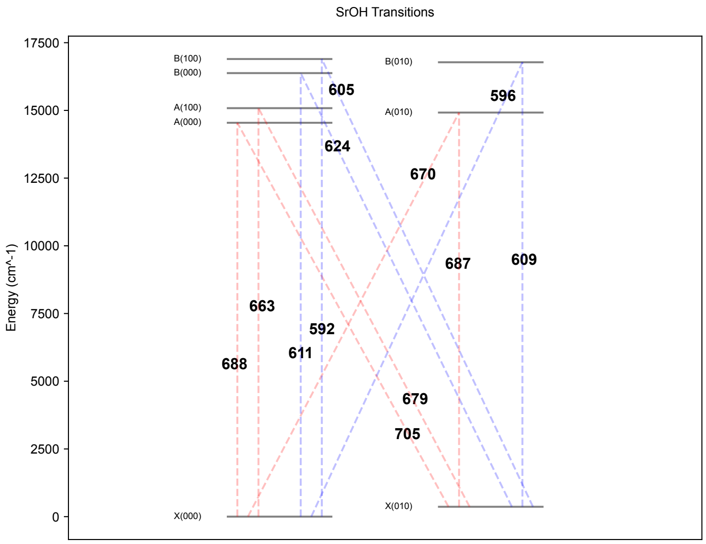

at 705 nm or $\tilde{B}^2\Sigma^+(000)$ at 624 nm while the strong decay photons at 688 nm or 611 nm photons, respectively, can be collected with appropriate filters.

Given the laser resources available, we opted to attempt to drive the $\tilde{B}^2\Sigma^+(000) - \tilde{X}^2\Sigma^+(010)$ transition at 624 nm and use filters easily available at Thorlabs to collect the 611 nm fluorescence from decay back to $\tilde{X}^2\Sigma^+(000)$.[6]. Our collaborators at Harvard university had recently measured this transition and had confidence in their internal assignment, making this a natural starting place for us at Caltech. The $\tilde{X}^2\Sigma^+(000) - \tilde{A}^2\Pi_{1/2}(000)$ transition at 688 nm would be used to monitor for production of SrOH inside the buffer gas cell. Initially, there were plans to optically enhance SrOH-forming chemistry by driving Sr atoms into the metastable $^3P_1$ state, as has been previously demonstrated in YbOH, but a high power laser at 689 nm unavailable at Caltech. Therefore, we also explored increasing SNR through increasing the ground state bending mode population through optical pumping. Specifically, the off-diagonal $\tilde{X}^2\Sigma^+(000) - \tilde{B}^2\Sigma^+(010)$ transition at 596 nm can be driven to build up population in $\tilde{X}^2\Sigma^+(010)$ state. This frequency is well-separated from others present in the detection scheme and easily filtered. The proposed experimental apparatus and scheme are shown in Fig. 6.6.

---

[6] FBH610-10 and FEL0600

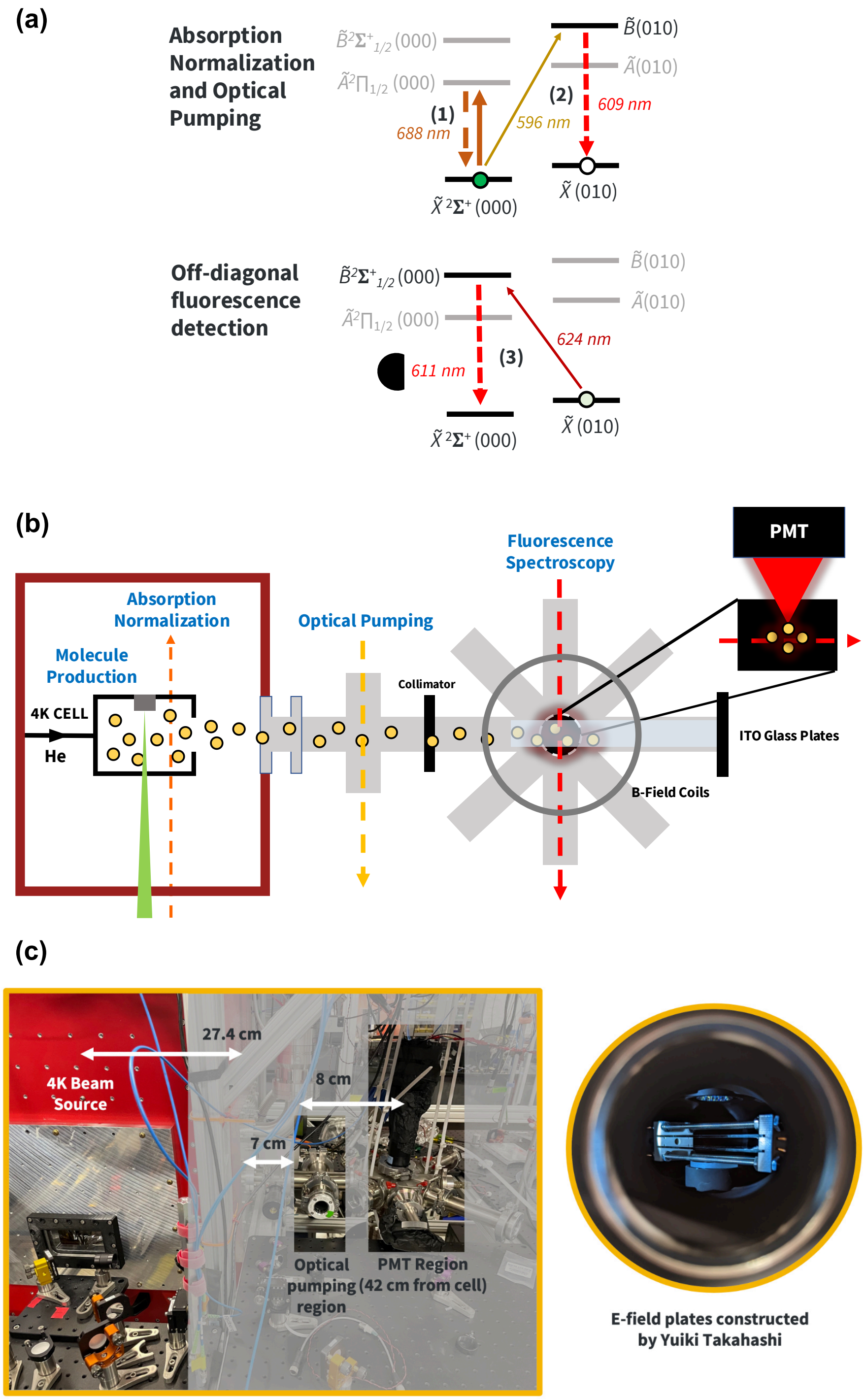

Figure 6.6: SrOH measurement scheme and apparatus. (a) Proposed measurement scheme for SrOH bending mode spectroscopy. Off-diagonal detection can be used to probe the bending mode with high SNR. (b) Schematic of the apparatus for SrOH bending mode spectroscopy. (c) Side view of the SrOH spectroscopy beamline, installed electric field plates, and retroreflector.

Figure 6.7: Flexible copper braids are used to short the 1K and 4K stages in the cryostat, and helium liquefaction is not used when operating in this configuration. The cell temperature equilibrates around 5.1 K under normal ablation conditions. In order to increase the robustness of this thermal short and bring the cell temperature closer to 4 K, additional braids can be added to other sides of the 1K cold head, though these orientations are inaccessible without considerable effort.

6.5.2 Apparatus

Prior to this work, our molecular beam source was more optimized for studying ZS deceleration with an eye towards laser cooling and trapping. To produce the slowest molecular beams possible, the source was operated at 1.4 K in a manner described in Chapter 3. At typical ablation energies, our cryogenic source could not maintain 1.4 K operation when ablating at repetition rates faster than ~ 1 Hz, limiting the amount of data that could be collected. In order to increase the allowable repetition rate and pulse energies used in spectroscopy, the 1K cold head was thermally shorted to the 4K cold head using flexible copper braids (Fig. 6.1), without using the liquid helium pot. As long as the ultimate cell temperature under a heat load leaves sufficient rotational population in the bands of interest, moving to a higher cell temperature can be advantageous for collecting molecular spectra.

Four copper braids were connected between the 1K and 4K cold heads using thin clamps designed by Yi Zeng, pictured in Figure 6.7. Due to peculiarities in our cryostat described in Chapter 3, there was not enough space to attach more thermal braids without working on the opposite, inconvenient-to-access side of the vacuum chamber.

Nonetheless, the cell temperature remained around $4.1 - 4.2$ K upon cooling down and rose to 5.1 K under typical ablation heat loads. This temperature is more than sufficient to perform spectroscopy on the lowest three rotational states in SrOH.

Given previous experience in the Hutzler Lab measuring the Stark and Zeeman spectra in the EDM science state of YbOH, we implemented several changes to the beamline to streamline the process. After removing irrelevant sections of the beamline (e.g., magnet cube used to test Zeeman-Sisyphus deceleration), a KF-50 four-way cross was introduced to allow for optical pumping into the bending mode. Additionally, the electric field plates and magnetic field coils used for YbOH were installed in the SrOH apparatus. Finally, a pair of windows glued to KF nipples cut at Brewster's angle were installed in the probe beam path to further reduced noise due to scattered light.

The detection optics were almost identical to the configuration used for Zeeman-Sisyphus slowing, as described in Chapter 5, consisting of a light pipe surrounded by a 2 in blackened lens tube leading up to a PMT (Hamamatsu Photonics H10492-012). In order to approximately double the amount of fluorescence collected, a 9 mm focal length concave retroreflector was inserted below the center of the octagon, after removing the lens tube shroud that was previously there.[7]

The 688 nm light driving the $A - X$ origin band for monitoring in-cell absorption was generated by a home-made ECDL (see Chap. 3.2). The 624 nm light was produced using a Coherent 699 Dye Laser using Rhodamine 640 perchlorate dye and a 5 W, 532 nm pump generated by a V5 Verdi. We attempted to generate the necessary light for optical pumping at 596 nm through temperature tuning of a 595.4 nm Raman Fiber Amplifier laser from MPB (VRFA-P-4000-595.4-SF-Plus) which frequency doubled 1191 nm light generated by a MOGLabs ECDL. Despite our efforts, the low conversion efficiency at 596 nm within the allowable temperature settings precluded the use of this laser for optical pumping. While no further testing with optical pumping was performed during this period of time, the Sirah MixTrain laser could be used to generate light at this frequency.

6.5.3 Characterizing SrOH production

In principle, a simple way to produce SrOH is to ablate Sr metal in the presence of water vapor. There are two complications that arise from this approach. Sr metal is highly reactive and has to be installed in an inert environment, minimizing its exposure

---

[7] The reflector used was the identical one used for Stark and Zeeman spectroscopy of YbOH.

to air. The oxide that forms in the presence of air has a chalky consistency and makes for an extremely poor ablation target. Furthermore, a heated fill line would be required to introduce water vapor in a cryogenic environment. While Yi Zeng constructed the necessary hardware for a heated fill line in our cryogenic beam source, the components have not been installed or tested. In our group, we have ample experience with producing molecules through ablation of solid pressed, powder targets. What these targets lack in shot-to-shot consistency, they compensate for in ease of prototyping.

Mixture	$Sr(OH)_2$	$SrTiO_3$	Yb	PEG	Density (g/cm^3)
1	×		×	×	2.94
2	×	×		×	2.42
3	×	×	×	×	3.01

Table 6.1: Various SrOH pressed powder target compositions and their densities. Each target was composed of equal parts by mass non-PEG ingredients with an additional 4% PEG by mass.

A number of pressed powder targets were made and tested in order to compare target performance. In our apparatus, SrOH has been previously produced through ablation of a pressed $Sr(OH)_2$ + Yb + PEG mixture, which we refer to as mixture 1. The hydroxide does not react with air and is simple to press into a powder, with the Yb metal powder increasing the density of the final product. Other groups have used $SrTiO_3$ for producing Sr^+ ions, so a $Sr(OH)_2$ + $SrTiO_3$ + PEG target (mixture 2) was also tried, using powdered $SrTiO_3$. Finally, a mixture including Yb metal powder—$Sr(OH)_2$ + $SrTiO_3$ + Yb + PEG—was also tested (mixture 3). In each case, all non-PEG ingredients were mixed with a 200-mesh grain size and added in equal amounts by mass, with an additional 4% PEG added (also by mass). The targets were pressed in a hydraulic press at 10 MPa for 15 minutes in an 8 mm die. The final densities for each mixture are shown in Table 6.1.

In order to confirm production of SrOH and test each target, 40 μW of 688 nm light was sent through the cell absorption window while ablating the targets with 860 V on the YAG flash-lamp and 4 SCCM He flow. The cell was at 5.2 K and the $P_{11}(J'' = 3/2)$ transition was observed at the expected position. Multiple ablation shots were taken for each target. The integrated optical depth for each target vs. ablation shot number is plotted in Fig. 6.8. Generally, mixture 1 and 3, both of which contain Yb metal powder produced SrOH more consistently and with slightly higher yield than mixture 2. All following work with SrOH, then, used the composition in mixture 3

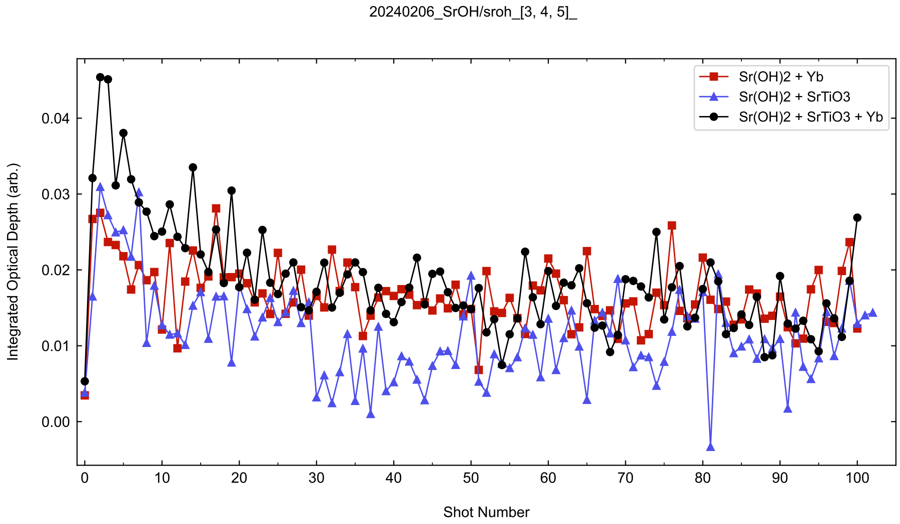

Figure 6.8: Integrated optical depth for each SrOH target mixture vs. ablation shot number. The targets were ablated with approximately 27 mJ pulses and the ablation position was not changed.

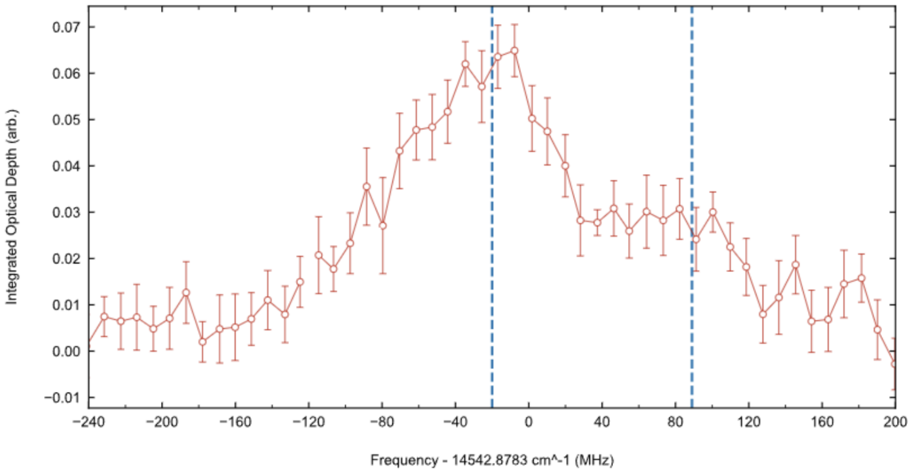

Figure 6.9: Integrated optical depth for SrOH molecules as a function of 688 nm absorption probe frequency. The probe was scanned over the expected positions of the $Q_{11}(J''=3/2)$ and $R_{12}(J''=1/2)$ lines, with 10 absorption measurements per point. The observed line positions match previous work within normal wavemeter offsets, and the relative line intensities are as expected [115].

as that target had the largest density with reasonable stability and yield. In order to confirm that what was observed was in fact SrOH , the light was scanned over the $Q_{11}(J'' = 3/2)$ and $R_{12}(J'' = 1/2)$ transitions and the absorption spectrum was recorded (Fig. 6.9). The line positions and relative intensities matched the expected behavior for SrOH, and the correct ground state spin-rotation splitting and excited state Λ doubling was observed between the transitions discussed in this paragraph. (see Fig. 3.2.1 in [115]). Thus we were able to confirm our ability to produce cold SrOH molecules in the buffer gas cell.

6.5.4 Beamline fluorescence and SNR improvements

Attempts were made to collect both 688 nm on-diagonal $\tilde{A} - \tilde{X}$ fluorescence in the beamline as well as the off-diagonal fluorescence out of the bending mode. In both cases, fluorescence signals were observed but not reproducible during the subsequent days of data taking. Both apparent fluorescence signals are shown in Fig. 6.10.

In order to increase the likelihood of observing SrOH beamline signals, the entire beamline region was greatly simplified. The electric field plates were removed to increase geometric acceptance of molecules in the detection region. The collimating apertures in the beam extension removed for the same reason. Lacking a suitable optical pumping laser, we also removed the optical pumping region, which allowing the beamline to move about 5 in closer to the source. Finally, the light pipe position was adjusted to lie closer to the center of the detection region. Because the SrOH targets were doped with Yb, the Yb atoms produced in ablation were used as a proxy atom in order to optimize beamline signals, using a 399 nm MogLabs ECDL as a fluorescence probe.

First, the polarization of the probe beam was rotated from vertical, where we were operating, to horizontal, where the signal size was increased by a factor of ~ 2. This meant that the Brewster windows ultimately had to be rotated to match this new polarization and π-transitions were no longer planned for the spectroscopic work with SrOH. For the rest of the diagnostic work with Yb atoms, horizontal polarization was used.

Second, the gas flow rate was varied from negligible flow to maximum flow at 20 SCCM and the beamline fluorescence was compared (Fig. 6.11). Atom thermalization set in with flows of 1 SCCM, but the fluorescence peaked at 4 SCCM. At higher flow rates, the signal size degraded. The previous work with SrOH was being done with 6 SCCM flows, so this diagnostic indicated that 4 SCCM was a more optimal choice.

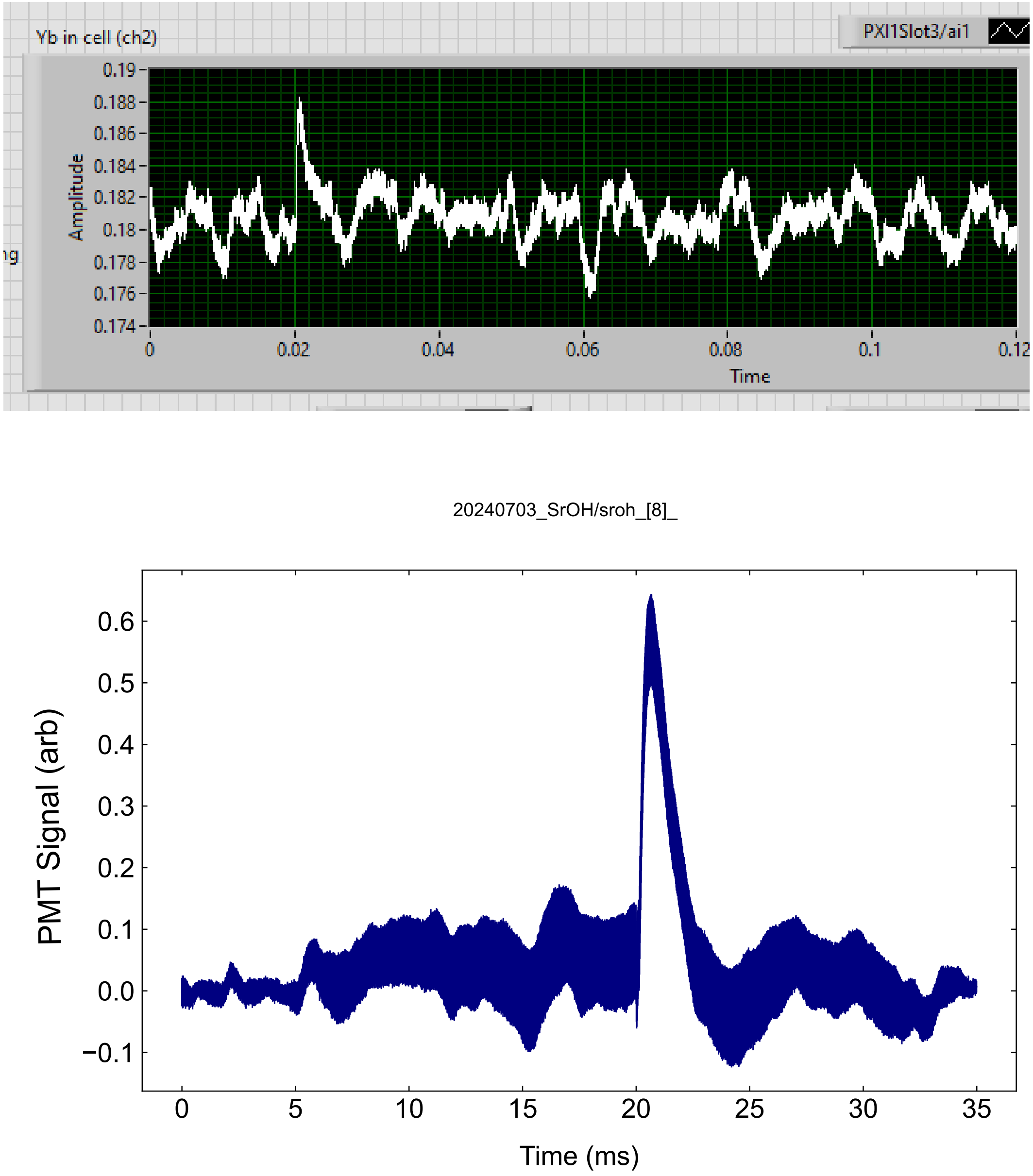

Figure 6.10: Beamline fluorescence as measured on the PMT. These signals were observed multiple times each on a single day but were not able to be recovered in subsequent data runs. (Top) Possible $\tilde{A}^2\Sigma^+(000) - \tilde{X}^2\Sigma^+(000)$ PMT fluorescence at 688 nm. (Bottom) $\tilde{B}^2\Sigma^+(000) - \tilde{X}^2\Sigma^+(000)$ off-diagonal fluorescence at 611 nm, with a 624 nm bend to non-bend pump (135 averages).

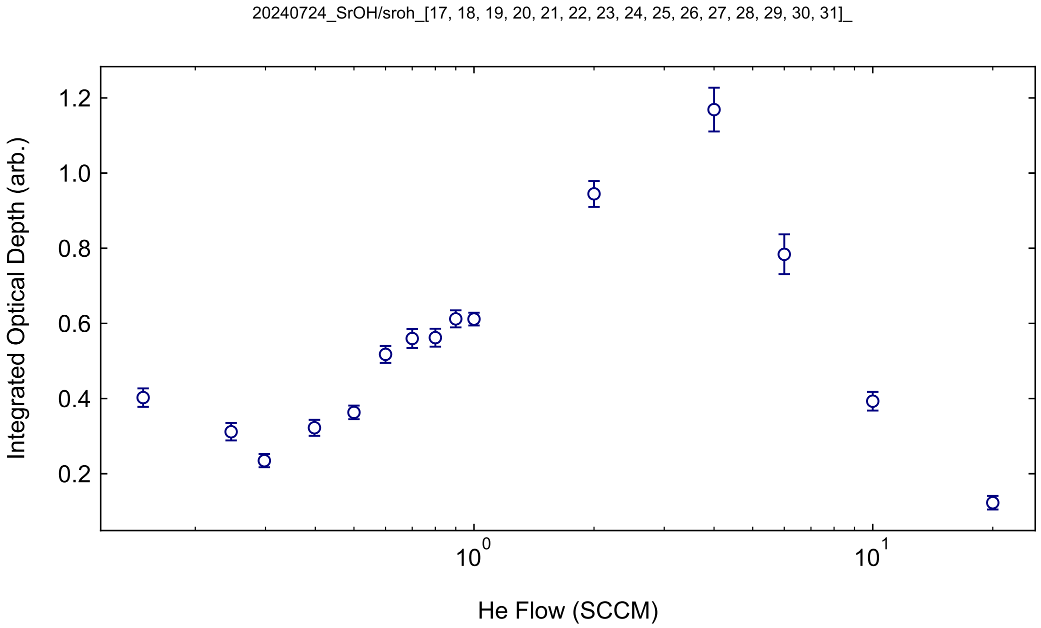

Figure 6.11: Yb beamline integrated fluorescence vs. helium buffer gas flow (∼ 20 averaged shots per point, no normalization applied within each shot).

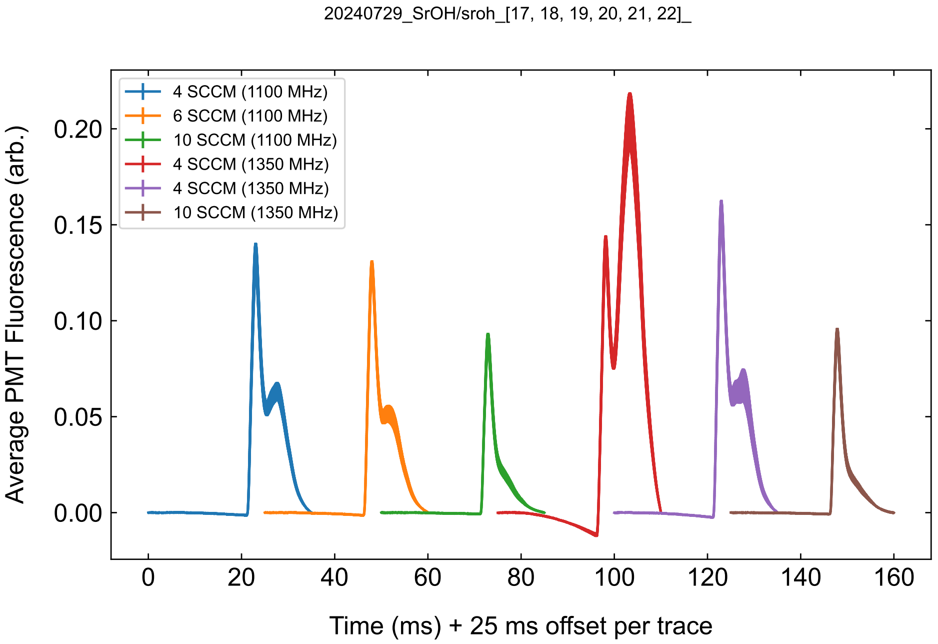

Figure 6.12: Yb beamline fluorescence vs. turbo pump speed for various helium flow rates. A fixed temporal offset is added between plots for ease of comparison (∼ 20 averaged shots per point, no normalization applied within each shot).

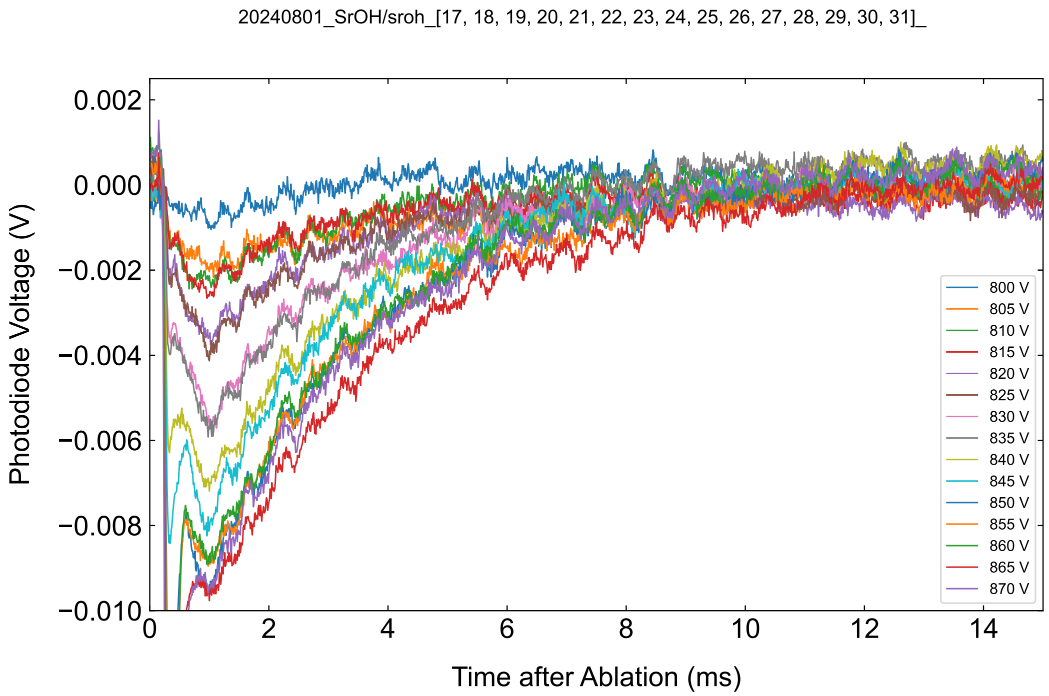

Figure 6.13: SrOH $\tilde{A}(000) - \tilde{X}(000)$ absorption on the $Q_{11}(3/2)$ line vs. ablation energy, given by the YAG voltage. For YAG voltages higher than 840 V ($\sim$ 19 mJ per pulse), the athermal population dominates without significant increase in the thermalized population (10 averaged shots per curve).

The fluorescence signal was insensitive to probe beam steering. With the beamline changes and re-optimized gas flow rate and polarization orientation, the Yb atom fluorescence SNR was improved by an overall factor of approximately 70. As a final test of the effect of background gas collisions, the effect of intentionally reducing the turbo pump speed was measured as a function of a few gas flow rates (Fig. 6.12). The 4 SCCM configuration with the high-speed turbo pump was indeed optimal compared to 6 or 10 SCCM with either pumping configuration.

Even with these changes, neither the $\tilde{A}(000) - \tilde{X}(000)$ or $\tilde{A}(000) - \tilde{X}(100)$ decays were visible in fluorescence in the beamline. The YAG energy was next optimized using in-cell absorption. With the probe laser at 14542.8776 cm^{-1} to drive the $Q_{11}(3/2)$ transition, the YAG voltage was varied from 800 V - 870 V in order to find the minimal value where the thermalized molecule population was the largest (Fig 6.13), using a 4 SCCM helium flow rate. Indeed, the previously used ablation voltage of 860 V produced larger integrated absorption signals, but these signals were dominated by a large unthermalized population. Lower ablation voltages of 840-850 V were more suitable then for producing thermalized molecules.

Unfortunately, even with these SNR improvements, the SrOH fluorescence signals were unable to be measured. In order to make progress on the spectroscopy, we made preparations to measure the zero-field bending mode spectrum inside the buffer gas cell, where we have observed SrOH reliably. FM absorption was successfully used to study the $\tilde{X}(300)$ state in YbOH [88], and therefore it is likely this method will be successful in studying the SrOH bending mode. With a zero-field bending mode spectrum on hand, calibrated with an I_2 reference, one of our supersonic sources could likely be used to measure the Stark and Zeeman effect in the SrOH bending mode. This supersonic source has been used recently to perform Stark and Zeeman measurements on $SrNH_2$.

Unfortunately,"the best-laid plans of mice and men often go awry." In this case, nearby campus construction for a new research building damaged the campus central chilled water plumbing that is essential for cryostat operation. This led to a several-month shut down of our cryogenic beam sources during which our funding to study SrOH in detail lapsed. Nevertheless, FM spectroscopy of the SrOH bending mode inside a buffer gas cell should be eminently possible in our apparatus.

Acknowledgments

The spectrometer work was supported by the De Logi Science and Technology Grant. The SrOH work was supported by the Gordon and Betty Moore Foundation and the Alfred P. Sloan Foundation. We thank our collaborator Tim Steimle for useful conversations and for fitting of the molecular spectra shown in this chapter.

Chapter 7

Outlook and Conclusions

> *"I think here I will leave you. It has come to seem there is no perfect ending. Indeed, there are infinite endings. Or perhaps, once one begins, there are only endings."*
>
> *Louise Glück, Faithful and Virtuous Night*

At the beginning of this thesis work in 2018, the mission for the PolyEDM team at Caltech was to develop and test new technologies for the laser cooling and trapping of YbOH for an EDM experiment. The corner of the lab where this experiment at Caltech was to take place was empty. Over the weeks, months, and years to come, it was filled up with cryogenic, vacuum, and optical systems. As a number of unfortunate disasters occurred in the background—manufacturing flaws in our commercial cryostat, the COVID-19 pandemic, a three to four month campus chilled water outage, and nearby urban fires that displaced this thesis author for six weeks—our project at Caltech nevertheless continued.

The cryostat was made functional during the pandemic lockdown, during which the collaboration decided to make the challenging but necessary switch to SrOH. We continued working to prototype Zeeman-Sisyphus deceleration during this time. Though our attempt did not ultimately yield a conclusive demonstration in alkali atoms, there are promising directions to continue pursuing this technology—including, for example, the inclusion of a magnetic guide and construction of optimized magnet arrays. The development of an inexpensive permanent magnet Zeeman-Sisyphus slower will be a great boon for heavy molecule deceleration without a significant additional cryogenic engineering overhead requirement.

Our cryogenic beam source has over the years become a setting for testing of new technologies for molecular control and measurement, in particular tackling challenges of deceleration and spectroscopy. One proposal from our group suggests that it is possible to slow and cool molecules through sympathetic cooling via collisions with laser cooled and slowed Rydberg atoms [116]. The large enhancement of the atomic-molecular cross section for atomic Rydberg states enables this collisional cooling, and the losses from collisions with Rydberg atoms are predicted to be low and manageable. The production of Yb Rydberg atoms was tested in our beam source by Yi Zeng and Chi Zhang (Sec. 3.6 of [56]), and efforts are underway to prototype beam deflection from Rydberg atoms in our cryogenic source. This novel deceleration method could enable the slowing and cooling of molecules that do not traditionally permit laser cooling, in particular diatomic molecules with ground state parity doublets.

Our novel spectroscopic method also shows tremendous promise in finally bridging a major rate-limiting step of studying EDM sensitive molecules. It was only after several years of spectroscopic work with YbOH that it is not laser coolable without repumping $4f$ hole states. The ability to flag issues much earlier in the life cycle of an experiment is a practical requirement, and rapid spectroscopy increases the rate at which we can prototype different candidate molecules for precision measurement and quantum science. More broadly, the new technology will enhance our spectroscopic knowledge of the molecular structure of free radicals across the chemical landscape.

Science and technology progress hand in hand. New methods lay the foundation for the experiments of tomorrow. May we all live to observe a violation of the Standard Model in the years to come.

Bibliography

[1] S. Koppes, “Michelson helped build Chicago’s physics program while pursuing exactitude in his lab experiments,” The University of Chicago Chronicle **27** (2007).

[2] X. Fan, T. G. Myers, B. A. D. Sukra, and G. Gabrielse, “Measurement of the electron magnetic moment,” Physical Review Letters **130**, 071801 (2023) `10.1103/PhysRevLett.130.071801`.

[3] Planck Collaboration, N. Aghanim, Y. Akrami, M. Ashdown, J. Aumont, C. Baccigalupi, M. Ballardini, A. J. Banday, R. B. Barreiro, N. Bartolo, S. Basak, R. Battye, K. Benabed, J.-P. Bernard, M. Bersanelli, P. Bielewicz, J. J. Bock, J. R. Bond, J. Borrill, F. R. Bouchet, F. Boulanger, M. Bucher, C. Burigana, R. C. Butler, E. Calabrese, J.-F. Cardoso, J. Carron, A. Challinor, H. C. Chiang, J. Chluba, L. P. L. Colombo, C. Combet, D. Contreras, B. P. Crill, F. Cuttaia, P. De Bernardis, G. De Zotti, J. Delabrouille, J.-M. Delouis, E. Di Valentino, J. M. Diego, O. Doré, M. Douspis, A. Ducout, X. Dupac, S. Dusini, G. Efstathiou, F. Elsner, T. A. Enßlin, H. K. Eriksen, Y. Fantaye, M. Farhang, J. Fergusson, R. Fernandez-Cobos, F. Finelli, F. Forastieri, M. Frailis, A. A. Fraisse, E. Franceschi, A. Frolov, S. Galeotta, S. Galli, K. Ganga, R. T. Génova-Santos, M. Gerbino, T. Ghosh, J. González-Nuevo, K. M. Górski, S. Gratton, A. Gruppuso, J. E. Gudmundsson, J. Hamann, W. Handley, F. K. Hansen, D. Herranz, S. R. Hildebrandt, E. Hivon, Z. Huang, A. H. Jaffe, W. C. Jones, A. Karakci, E. Keihänen, R. Keskitalo, K. Kiiveri, J. Kim, T. S. Kisner, L. Knox, N. Krachmalnicoff, M. Kunz, H. Kurki-Suonio, G. Lagache, J.-M. Lamarre, A. Lasenby, M. Lattanzi, C. R. Lawrence, M. Le Jeune, P. Lemos, J. Lesgourgues, F. Levrier, A. Lewis, M. Liguori, P. B. Lilje, M. Lilley, V. Lindholm, M. López-Caniego, P. M. Lubin, Y.-Z. Ma, J. F. Macías-Pérez, G. Maggio, D. Maino, N. Mandolesi, A. Mangilli, A. Marcos-Caballero, M. Maris, P. G. Martin, M. Martinelli, E. Martínez-González, S. Matarrese, N. Mauri, J. D. McEwen, P. R. Meinhold, A. Melchiorri, A. Mennella, M. Migliaccio, M. Millea, S. Mitra, M.-A. Miville-Deschênes, D. Molinari, L. Montier, G. Morgante, A. Moss, P. Natoli, H. U. Nørgaard-Nielsen, L. Pagano, D. Paoletti, B. Partridge, G. Patanchon, H. V. Peiris, F. Perrotta, V. Pettorino, F. Piacentini, L. Polastri, G. Polenta, J.-L. Puget, J. P. Rachen, M. Reinecke, M. Remazeilles, A. Renzi, G. Rocha, C. Rosset, G. Roudier, J. A. Rubiño-Martín, B. Ruiz-Granados, L. Salvati, M. Sandri, M. Savelainen, D. Scott, E. P. S. Shellard,

C. Sirignano, G. Sirri, L. D. Spencer, R. Sunyaev, A.-S. Suur-Uski, J. A. Tauber, D. Tavagnacco, M. Tenti, L. Toffolatti, M. Tomasi, T. Trombetti, L. Valenziano, J. Valiviita, B. Van Tent, L. Vibert, P. Vielva, F. Villa, N. Vittorio, B. D. Wandelt, I. K. Wehus, M. White, S. D. M. White, A. Zacchei, and A. Zonca, "*Planck* 2018 results: VI. Cosmological parameters," Astronomy & Astrophysics **641**, A6 (2020) `10.1051/0004-6361/201833910`.

[4] J. M. Munoz, S. M. Udrescu, and R. F. Garcia Ruiz, "Discovering nuclear models from symbolic machine learning," Communications Physics **8**, 101 (2025) `10.1038/s42005-025-02023-2`.

[5] J. Brown and A. Carrington, *Rotational spectroscopy of diatomic molecules* (Cambridge University Press, 2003).

[6] C. S. Wu, E. Ambler, R. W. Hayward, D. D. Hoppes, and R. P. Hudson, "Experimental test of parity conservation in beta decay," Physical Review **105**, 1413–1415 (1957) `10.1103/PhysRev.105.1413`.

[7] R. L. Garwin, L. M. Lederman, and M. Weinrich, "Observations of the failure of conservation of parity and charge conjugation in meson decays: The magnetic moment of the free muon," Physical Review **105**, 1415–1417 (1957) `10.1103/PhysRev.105.1415`.

[8] C. D. Froggatt and H. B. Nielsen, *Origin of symmetries* (WORLD SCIENTIFIC, Aug. 1991), `10.1142/0090`.

[9] D. Colladay and V. A. Kostelecký, "CPT violation and the standard model," Physical Review D **55**, 6760–6774 (1997) `10.1103/PhysRevD.55.6760`.

[10] A. G. Cohen, A. De Rújula, and S. L. Glashow, "A matter-antimatter universe?" The Astrophysical Journal **495**, 539–549 (1998) `10.1086/305328`.

[11] A. Coc, J.-P. Uzan, and E. Vangioni, "Standard big bang nucleosynthesis and primordial CNO abundances after Planck," Journal of Cosmology and Astroparticle Physics **2014**, 050–050 (2014) `10.1088/1475-7516/2014/10/050`.

[12] Planck Collaboration, P. A. R. Ade, N. Aghanim, M. Arnaud, M. Ashdown, J. Aumont, C. Baccigalupi, A. J. Banday, R. B. Barreiro, J. G. Bartlett, N. Bartolo, E. Battaner, R. Battye, K. Benabed, A. Benoît, A. Benoit-Lévy, J.-P. Bernard, M. Bersanelli, P. Bielewicz, J. J. Bock, A. Bonaldi, L. Bonavera, J. R. Bond, J. Borrill, F. R. Bouchet, F. Boulanger, M. Bucher, C. Burigana, R. C. Butler, E. Calabrese, J.-F. Cardoso, A. Catalano, A. Challinor, A. Chamballu, R.-R. Chary, H. C. Chiang, J. Chluba, P. R. Christensen, S. Church, D. L. Clements, S. Colombi, L. P. L. Colombo, C. Combet, A. Coulais, B. P. Crill, A. Curto, F. Cuttaia, L. Danese, R. D. Davies, R. J. Davis, P. De Bernardis, A. De Rosa, G. De Zotti, J. Delabrouille, F.-X. Désert, E. Di Valentino, C. Dickinson, J. M. Diego, K. Dolag, H. Dole, S. Donzelli, O. Doré, M. Douspis, A. Ducout, J. Dunkley, X. Dupac, G. Efstathiou, F. Elsner, T. A. Enßlin, H. K. Eriksen, M. Farhang, J. Fergusson, F. Finelli, O. Forni, M. Frailis, A. A. Fraisse, E. Franceschi, A. Frejsel, S. Galeotta, S. Galli, K. Ganga, C. Gauthier, M. Gerbino, T. Ghosh, M. Giard, Y. Giraud-Héraud, E.

Giusarma, E. Gjerløw, J. González-Nuevo, K. M. Górski, S. Gratton, A. Gregorio, A. Gruppuso, J. E. Gudmundsson, J. Hamann, F. K. Hansen, D. Hanson, D. L. Harrison, G. Helou, S. Henrot-Versillé, C. Hernández-Monteagudo, D. Herranz, S. R. Hildebrandt, E. Hivon, M. Hobson, W. A. Holmes, A. Hornstrup, W. Hovest, Z. Huang, K. M. Huffenberger, G. Hurier, A. H. Jaffe, T. R. Jaffe, W. C. Jones, M. Juvela, E. Keihänen, R. Keskitalo, T. S. Kisner, R. Kneissl, J. Knoche, L. Knox, M. Kunz, H. Kurki-Suonio, G. Lagache, A. Lähteenmäki, J.-M. Lamarre, A. Lasenby, M. Lattanzi, C. R. Lawrence, J. P. Leahy, R. Leonardi, J. Lesgourgues, F. Levrier, A. Lewis, M. Liguori, P. B. Lilje, M. Linden-Vørnle, M. López-Caniego, P. M. Lubin, J. F. Macías-Pérez, G. Maggio, D. Maino, N. Mandolesi, A. Mangilli, A. Marchini, M. Maris, P. G. Martin, M. Martinelli, E. Martínez-González, S. Masi, S. Matarrese, P. McGehee, P. R. Meinhold, A. Melchiorri, J.-B. Melin, L. Mendes, A. Mennella, M. Migliaccio, M. Millea, S. Mitra, M.-A. Miville-Deschênes, A. Moneti, L. Montier, G. Morgante, D. Mortlock, A. Moss, D. Munshi, J. A. Murphy, P. Naselsky, F. Nati, P. Natoli, C. B. Netterfield, H. U. Nørgaard-Nielsen, F. Noviello, D. Novikov, I. Novikov, C. A. Oxborrow, F. Paci, L. Pagano, F. Pajot, R. Paladini, D. Paoletti, B. Partridge, F. Pasian, G. Patanchon, T. J. Pearson, O. Perdereau, L. Perotto, F. Perrotta, V. Pettorino, F. Piacentini, M. Piat, E. Pierpaoli, D. Pietrobon, S. Plaszczynski, E. Pointecouteau, G. Polenta, L. Popa, G. W. Pratt, G. Prézeau, S. Prunet, J.-L. Puget, J. P. Rachen, W. T. Reach, R. Rebolo, M. Reinecke, M. Remazeilles, C. Renault, A. Renzi, I. Ristorcelli, G. Rocha, C. Rosset, M. Rossetti, G. Roudier, B. Rouillé d'Orfeuil, M. Rowan-Robinson, J. A. Rubiño-Martín, B. Rusholme, N. Said, V. Salvatelli, L. Salvati, M. Sandri, D. Santos, M. Savelainen, G. Savini, D. Scott, M. D. Seiffert, P. Serra, E. P. S. Shellard, L. D. Spencer, M. Spinelli, V. Stolyarov, R. Stompor, R. Sudiwala, R. Sunyaev, D. Sutton, A.-S. Suur-Uski, J.-F. Sygnet, J. A. Tauber, L. Terenzi, L. Toffolatti, M. Tomasi, M. Tristram, T. Trombetti, M. Tucci, J. Tuovinen, M. Türler, G. Umana, L. Valenziano, J. Valiviita, F. Van Tent, P. Vielva, F. Villa, L. A. Wade, B. D. Wandelt, I. K. Wehus, M. White, S. D. M. White, A. Wilkinson, D. Yvon, A. Zacchei, and A. Zonca, "*Planck* 2015 results: XIII. Cosmological parameters," Astronomy & Astrophysics **594**, A13 (2016) `10.1051/0004-6361/201525830`.

[13] A. D. Sakharov, "Violation of *CP* invariance, *C* asymmetry, and baryon asymmetry of the universe," Soviet Physics Uspekhi **34**, 392–393 (1991) `10.1070/PU1991v034n05ABEH002497`.

[14] D. Bödeker and W. Buchmüller, "Baryogenesis from the weak scale to the grand unification scale," Reviews of Modern Physics **93**, 035004 (2021) `10.1103/RevModPhys.93.035004`.

[15] S. J. Huber, K. Mimasu, and J. M. No, "Baryogenesis from transitional CP violation in the early universe," Physical Review D **107**, 075042 (2023) `10.1103/PhysRevD.107.075042`.

[16] C. Cesarotti, Q. Lu, Y. Nakai, A. Parikh, and M. Reece, "Interpreting the electron EDM constraint," Journal of High Energy Physics **2019**, 59 (2019) `10.1007/JHEP05(2019)059`.

[17]T. Chupp, P. Fierlinger, M. J. Ramsey-Musolf, and J. Singh, "Electric dipole moments of atoms, molecules, nuclei, and particles," Reviews of Modern Physics **91**, 015001 (2019) `10.1103/RevModPhys.91.015001`.

[18]Y. Ema, T. Gao, and M. Pospelov, "Standard model prediction for paramagnetic electric dipole moments," Physical Review Letters **129**, 231801 (2022) `10.1103/PhysRevLett.129.231801`.

[19]E. D. Commins, J. D. Jackson, and D. P. DeMille, "The electric dipole moment of the electron: An intuitive explanation for the evasion of Schiff's theorem," American Journal of Physics **75**, 532–536 (2007) `10.1119/1.2710486`.

[20]G. Edvinsson and A. Lagerqvist, "Rotational analysis of some violet and green bands in the ThO spectrum," Journal of Molecular Spectroscopy **122**, 428–439 (1987) `10.1016/0022-2852(87)90017-8`.

[21]N. R. Hutzler, "A new limit on the electron electric dipole moment: Beam production, data interpretation, and systematics," PhD thesis (Harvard University, 2014).

[22]ACME Collaboration, "Improved limit on the electric dipole moment of the electron," Nature **562**, 355–360 (2018) `10.1038/s41586-018-0599-8`.

[23]J. J. Hudson, D. M. Kara, I. J. Smallman, B. E. Sauer, M. R. Tarbutt, and E. A. Hinds, "Improved measurement of the shape of the electron," Nature **473**, 493–496 (2011) `10.1038/nature10104`.

[24]T. S. Roussy, L. Caldwell, T. Wright, W. B. Cairncross, Y. Shagam, K. B. Ng, N. Schlossberger, S. Y. Park, S. Wang, J. Ye, and E. A. Cornell, "An improved bound on the electron's electric dipole moment," Science **381**, 46–50 (2023) `0.1126/science.adg4084`.

[25]W. B. Cairncross, "Searching for time-reversal symmetry violation with molecular ions: Quantum state control and photofragment imaging," PhD thesis (University of Colorado, 2019).

[26]W. C. Griffith, M. D. Swallows, T. H. Loftus, M. V. Romalis, B. R. Heckel, and E. N. Fortson, "Improved limit on the permanent electric dipole moment of ^{199}Hg," Physical Review Letters **102**, 101601 (2009) `10.1103/PhysRevLett.102.101601`.

[27]J. Lim, J. R. Almond, M. A. Trigatzis, J. A. Devlin, N. J. Fitch, B. E. Sauer, M. R. Tarbutt, and E. A. Hinds, "Laser cooled YbF molecules for measuring the electron's electric dipole moment," Physical Review Letters **120**, 123201 (2018) `10.1103/PhysRevLett.120.123201`.

[28]I. Kozyryev and N. R. Hutzler, "Precision measurement of time-reversal symmetry violation with laser-cooled polyatomic molecules," Physical Review Letters **119**, 133002 (2017) `10.1103/PhysRevLett.119.133002`.

[29]D. G. Ang, C. Meisenhelder, C. D. Panda, X. Wu, D. DeMille, J. M. Doyle, and G. Gabrielse, "Measurement of the $H^3\Delta_1$ radiative lifetime in ThO," Physical Review A **106**, 022808 (2022) `10.1103/PhysRevA.106.022808`.

[30] L. Anderegg, N. B. Vilas, C. Hallas, P. Robichaud, A. Jadbabaie, J. M. Doyle, and N. R. Hutzler, “Quantum control of trapped polyatomic molecules for eEDM searches,” Science **382**, 665–668 (2023) `10.1126/science.adg8155`.

[31] Y. Takahashi, C. Zhang, A. Jadbabaie, and N. R. Hutzler, “Engineering field-insensitive molecular clock transitions for symmetry violation searches,” Physical Review Letters **131**, 183003 (2023) `10.1103/PhysRevLett.131.183003`.

[32] C. Zhang, C. Zhang, L. Cheng, T. C. Steimle, and M. R. Tarbutt, “Inner-shell excitation in the YbF molecule and its impact on laser cooling,” Journal of Molecular Spectroscopy **386**, 111625 (2022) `10.1016/j.jms.2022.111625`.

[33] T. D. Persinger, J. Han, A. T. Le, T. C. Steimle, and M. C. Heaven, “Direct observation of the states and accurate determination of the YbF ionization energy,” Physical Review A **106**, 062804 (2022) `10.1103/PhysRevA.106.062804`.

[34] S. Popa, S. Schaller, A. Fielicke, J. Lim, B. Sartakov, M. Tarbutt, and G. Meijer, “Understanding inner-shell excitations in molecules through spectroscopy of the $4f$ hole states of YbF,” Physical Review X **14**, 021035 (2024) `10.1103/PhysRevX.14.021035`.

[35] Z. D. Lasner, A. Frenett, H. Sawaoka, L. Anderegg, B. Augenbraun, H. Lampson, M. Li, A. Lunstad, J. Mango, A. Nasir, T. Ono, T. Sakamoto, and J. M. Doyle, “Magneto-optical trapping of a heavy polyatomic molecule for precision measurement,” Physical Review Letters **134**, 083401 (2025) `10.1103/PhysRevLett.134.083401`.

[36] A. Jadbabaie, “Measuring fundamental symmetry violation in polyatomic molecules,” PhD thesis (California Institute of Technology, 2023), `10.7907/2jry-1s28`.

[37] N. H. Pilgram, “Production and characterization of ytterbium monohydroxide (YbOH) for next-generation parity and time-reversal violating physics searches,” PhD thesis (California Institute of Technology, 2023), `10.7907/05m0-4g74`.

[38] G. Herzberg, *The spectra and structures of simple free radicals: an introduction to molecular spectroscopy* (Dover Publications, New York, 1988), 226 pp.

[39] W. Demtröder, *Molecular physics: Theoretical principles and experimental methods*, 1st ed. (Wiley, Sept. 26, 2005), `10.1002/9783527618095`.

[40] D. A. Steck, *Sodium D Line Data*, revision 2.3.3, (May 28, 2024) `http://steck.us/alkalidata`.

[41] T. G. Tiecke, *Properties of Potassium*, v1.03, (June 2024) `http://steck.us/alkalidata`.

[42] M. J. Dick, “Spectroscopy of selected calcium and strontium containing polyatomic molecules,” PhD thesis (University of Waterloo, 2007), `10.7907/05m0-4g74`.

[43] T. C. Melville and J. A. Coxon, “The visible laser excitation spectrum of YbOH: the $\tilde{A}2\Pi - \tilde{X}2\Sigma^+$ transition,” The Journal of Chemical Physics **115**, 6974–6978 (2001) `10.1063/1.1404145`.

[44] G. Fischer, *Vibronic coupling: the interaction between the electronic and nuclear motions*, Theoretical chemistry v. 9 (Academic Press, London ; Orlando, Fla, 1984), 222 pp.

[45] A. C. Vutha, "A search for the electric dipole moment of the electron using thorium monoxide," PhD thesis (Yale University, 2011).

[46] H. J. Williams, S. Truppe, M. Hambach, L. Caldwell, N. J. Fitch, E. A. Hinds, B. E. Sauer, and M. R. Tarbutt, "Characteristics of a magneto-optical trap of molecules," New Journal of Physics **19**, 113035 (2017) `10.1088/1367-2630/aa8e52`.

[47] Z. Lasner, A. Lunstad, C. Zhang, L. Cheng, and J. M. Doyle, "Vibronic branching ratios for nearly closed rapid photon cycling of SrOH," Physical Review A **106**, L020801 (2022) `10.1103/PhysRevA.106.L020801`.

[48] B. K. Stuhl, B. C. Sawyer, D. Wang, and J. Ye, "Magneto-optical trap for polar molecules," Physical Review Letters **101**, 243002 (2008) `10.1103/PhysRevLett.101.243002`.

[49] L. W. Cheuk, L. Anderegg, Y. Bao, S. Burchesky, S. S. Yu, W. Ketterle, K.-K. Ni, and J. M. Doyle, "Observation of collisions between two ultracold ground-state CaF molecules," Physical Review Letters **125**, 043401 (2020) `10.1103/PhysRevLett.125.043401`.

[50] C. Hallas, G. K. Li, N. B. Vilas, P. Robichaud, L. Anderegg, and J. M. Doyle, *High compression blue-detuned magneto-optical trap of polyatomic molecules*, (Apr. 4, 2024) `10.48550/arXiv.2404.03636`, `http://arxiv.org/abs/2404.03636`.

[51] C. Hallas, N. B. Vilas, L. Anderegg, P. Robichaud, A. Winnicki, C. Zhang, L. Cheng, and J. M. Doyle, "Optical trapping of a polyatomic molecule in an ℓ-type parity doublet state," Physical Review Letters **130**, 153202 (2023) `10.1103/PhysRevLett.130.153202`.

[52] N. B. Vilas, P. Robichaud, C. Hallas, G. K. Li, L. Anderegg, and J. M. Doyle, "An optical tweezer array of ultracold polyatomic molecules," Nature **628**, 282–286 (2024) `10.1038/s41586-024-07199-1`.

[53] H. Sawaoka, A. Frenett, A. Nasir, T. Ono, B. L. Augenbraun, T. C. Steimle, and J. M. Doyle, "Zeeman-Sisyphus deceleration for heavy molecules with perturbed excited-state structure," Physical Review A **107**, 022810 (2023) `10.1103/PhysRevA.107.022810`.

[54] B. L. Augenbraun, Z. D. Lasner, A. Frenett, H. Sawaoka, C. Miller, T. C. Steimle, and J. M. Doyle, "Laser-cooled polyatomic molecules for improved electron electric dipole moment searches," New Journal of Physics **22**, 022003 (2020) `10.1088/1367-2630/ab687b`.

[55] A. Marc, M. Hubert, and T. Fleig, "Candidate molecules for next-generation searches of hadronic charge-parity violation," Physical Review A **108**, 062815 (2023) `10.1103/PhysRevA.108.062815`.

[56] Y. Zeng, "Progress toward precision measurements using polyatomic molecules," PhD thesis (California Institute of Technology, 2024), `10.7907/39gs-s382`.

[57]J. M. D. N. R. Hutzler H. -I. Lu, "The buffer gas beam: An intense, cold, and slow source for atoms and molecules," Chemical Reviews **112**, 4803–4827 (2012) `10.1021/cr200362u`.

[58]D. Xiao, D. M. Lancaster, C. H. Allen, M. J. Taylor, T. A. Lancaster, G. Shaw, N. R. Hutzler, and J. D. Weinstein, "Shaped nozzles for cryogenic buffer-gas beam sources," Physical Review A **99**, 013603 (2019) `10.1103/PhysRevA.99.013603`.

[59]Y. Takahashi, D. Shlivko, G. Woolls, and N. R. Hutzler, "Simulation of cryogenic buffer gas beams," Physical Review Research **3**, 023018 (2021) `10.1103/PhysRevResearch.3.023018`.

[60]L. Baum, "Laser cooling and 1d magneto-optical trapping of calcium monohydroxide," PhD thesis (Harvard University, May 4, 2020).

[61]N. R. Hutzler, *Charcoal as a helium cryopump: version 1.0*, (Oct. 28, 2008) `https://drive.google.com/file/d/1zm_Zl1MWvTldaE2Talg0daLFGmR7sS8h/view?usp=sharing`.

[62]A. Jadbabaie, N. H. Pilgram, J. Kłos, S. Kotochigova, and N. R. Hutzler, "Enhanced molecular yield from a cryogenic buffer gas beam source via excited state chemistry," New Journal of Physics **22**, 022002 (2020) `10.1088/1367-2630/ab6eae`.

[63]Y. Zeng, A. Jadbabaie, A. N. Patel, P. Yu, T. C. Steimle, and N. R. Hutzler, "Optical cycling in polyatomic molecules with complex hyperfine structure," Physical Review A **108**, 012813 (2023) `10.1103/PhysRevA.108.012813`,

[64]Y. Zeng and N. R. Hutzler, "Nonresonant cavity for multipass laser intensity buildup," Applied Optics **62**, 3574–3580 (2023) `10.1364/AO.487531`.

[65]I. D. Boyd and T. E. Schwartzentruber, *Nonequilibrium gas dynamics and molecular simulation* (Cambridge University Press, Cambridge, 2017), `10.1017/9781139683494`.

[66]N. J. Fitch and M. R. Tarbutt, "Principles and design of a Zeeman-Sisyphus decelerator for molecular beams," ChemPhysChem **17**, 3609–3623 (2016) `10.1002/cphc.201600656`.

[67]T. A. Isaev and R. Berger, "Polyatomic candidates for cooling of molecules with lasers from simple theoretical concepts," Physical Review Letters **116**, 063006 (2016) `10.1103/PhysRevLett.116.063006`.

[68]J. F. Barry, "Laser cooling and slowing of a diatomic molecule," PhD thesis (Yale University, 2013).

[69]N. Fitch and M. Tarbutt, "Laser-cooled molecules," in *Advances in atomic, molecular, and optical physics*, Vol. 70 (Elsevier, 2021), pp. 157–262, `10.1016/bs.aamop.2021.04.003`.

[70]T. K. Langin and D. DeMille, "Toward improved loading, cooling, and trapping of molecules in magneto-optical traps," New Journal of Physics **25**, 043005 (2023) `10.1088/1367-2630/acc34d`.

[71] E. Narevicius, A. Libson, C. G. Parthey, I. Chavez, J. Narevicius, U. Even, and M. G. Raizen, "Stopping supersonic beams with a series of pulsed electromagnetic coils: An atomic coilgun," Physical Review Letters **100**, 093003 (2008) `10.1103/PhysRevLett.100.093003`.

[72] R. Fulton, A. I. Bishop, and P. F. Barker, "Optical Stark decelerator for molecules," Physical Review Letters **93**, 243004 (2004) `10.1103/PhysRevLett.93.243004`.

[73] S. Y. Van De Meerakker, N. Vanhaecke, and G. Meijer, "Stark deceleration and trapping of OH radicals," Annual Review of Physical Chemistry **57**, 159–190 (2006) `10.1146/annurev.physchem.55.091602.094337`.

[74] B. L. Augenbraun, A. Frenett, H. Sawaoka, C. Hallas, N. B. Vilas, A. Nasir, Z. D. Lasner, and J. M. Doyle, "Zeeman-Sisyphus deceleration of molecular beams," Physical Review Letters **127**, 263002 (2021) `10.1103/PhysRevLett.127.263002`.

[75] H.-I. Lu, J. Rasmussen, M. J. Wright, D. Patterson, and J. M. Doyle, "A cold and slow molecular beam," Physical Chemistry Chemical Physics **13**, 18986 (2011) `10.1039/c1cp21206k`.

[76] B. L. Augenbraun, "Methods for direct laser cooling of polyatomic molecules," PhD thesis (Harvard University, 2021).

[77] *Using permanent magnets at low temperature*, TN 0302, TECHNotes, Arnold Magnetic Technologies (2015).

[78] R. M. Bozorth, *Ferromagnetism*, in collab. with IEEE Xplore (Online service) and IEEE Magnetics Society (IEEE Press, John Wiley& Sons, Inc, Piscataway, New Jersey, 2003), 1 p., `10.1109/9780470544624`.

[79] M. Katter, "Angular dependence of the demagnetization stability of sintered Nd-Fe-B magnets," IEEE Transactions on Magnetics **41**, 3853–3855 (2005).

[80] C. Li and M. Devine, "Strong permanent magnet dipole with reduced demagnetizing effect," IEEE Transactions on Magnetics **45**, 4380–4383 (2009) `10.1109/TMAG.2009.2024541`.

[81] R. E. Stelter, "Dipole permanent magnet structure," U.S. Patent 5 635 889 (June 3, 1997).

[82] M. Kumada, E. Antokhin, Y. Iwashita, M. Aoki, and E. Sugiyama, "Super strong permanent dipole magnet," IEEE Transactions on Applied Superconductivity **14**, 1287–1289 (2004) `10.1109/TASC.2004.830555`.

[83] N. J. Fitch and M. R. Tarbutt, "Laser-cooled molecules," Advances in Atomic, Molecular and Optical Physics **70**, 157–262 (2021) `10.1016/bs.aamop.2021.04.003`.

[84] B. L. Augenbraun, L. Anderegg, C. Hallas, Z. D. Lasner, N. B. Vilas, and J. M. Doyle, "Direct laser cooling of polyatomic molecules," Advances in Atomic, Molecular and Optical Physics **72**, 89–182 (2023) `10.1016/bs.aamop.2023.04.005`.

[85] A. N. Patel, M. I. Howard, T. C. Steimle, and N. R. Hutzler, *Rapid, broadband, optical spectroscopy of cold radicals*, (May 6, 2025) 10.48550/arXiv.2505.03650, http://arxiv.org/abs/2505.03650,

[86] G. C. Bjorklund, "Frequency-modulation spectroscopy: a new method for measuring weak absorptions and dispersions," Optics Letters **5**, 15 (1980) 10.1364/OL.5.000015.

[87] G. C. Bjorklund and E. A. Whittaker, "High sensitivity frequency modulation spectroscopy and the path to single molecule detection," The Journal of Physical Chemistry A **125**, 8519–8528 (2021) 10.1021/acs.jpca.1c05752.

[88] N. H. Pilgram, A. Jadbabaie, C. J. Conn, and N. R. Hutzler, "Direct measurement of high-lying vibrational repumping transitions for molecular laser cooling," Physical Review A **107**, 062805 (2023) 10.1103/PhysRevA.107.062805.

[89] D.-T. Nguyen, T. C. Steimle, I. Kozyryev, M. Huang, and A. B. McCoy, "Fluorescence branching ratios and magnetic tuning of the visible spectrum of SrOH," Journal of Molecular Spectroscopy **347**, 7–18 (2018) 10.1016/j.jms.2018.02.007.

[90] P. B. Changala, "High resolution infrared spectroscopy of complex polyatomic molecules," PhD thesis (University of Colorado, 2019).

[91] C. Zhang, B. L. Augenbraun, Z. D. Lasner, N. B. Vilas, J. M. Doyle, and L. Cheng, "Accurate prediction and measurement of vibronic branching ratios for laser cooling linear polyatomic molecules," The Journal of Chemical Physics **155**, 091101 (2021) 10.1063/5.0063611.

[92] N. Picqué and T. W. Hänsch, "Frequency comb spectroscopy," Nature Photonics **13**, 146–157 (2019) 10.1038/s41566-018-0347-5.

[93] F. Adler, M. J. Thorpe, K. C. Cossel, and J. Ye, "Cavity-enhanced direct frequency comb spectroscopy: Technology and applications," Annual Review of Analytical Chemistry **3**, 175–205 (2010) 10.1146/annurev-anchem-060908-155248.

[94] A. Dubietis, A. Couairon, and G. Genty, "Supercontinuum generation: introduction," Journal of the Optical Society of America B **36**, SG1 (2019) 10.1364/JOSAB.36.000SG1.

[95] E. J. Salumbides, K. S. Eikema, W. Ubachs, U. Hollenstein, H. Knöckel, and E. Tiemann, "$^{129}I_2$ and $^{127}I^{129}I$ in the $B^3\Pi_{0_u^+} - X^1\Sigma_g^+$ band system," The European Physical Journal D **47**, 171–179 (2008) 10.1140/epjd/e2008-00045-y.

[96] C.-C. Liao, K.-Y. Wu, Y.-H. Lien, H. Knöckel, H.-C. Chui, E. Tiemann, and J.-T. Shy, "Precise frequency measurements of $^{127}I_2$ lines in the wavelength region $750 - 780$ nm," Journal of the Optical Society of America B **27**, 1208 (2010) 10.1364/JOSAB.27.001208.

[97] P. Forsberg, "The spectrum and term system of neutral titanium, Ti I," Physica Scripta **44**, 446 (1991) 10.1088/0031-8949/44/5/008.

[98] J. Sugar, W. Meggers, and P. Camus, "Spectrum and energy levels of neutral thulium," Journal of Research of the National Bureau of Standards Section A: Physics and Chemistry **77A**, 1 (1973) `10.6028/jres.077A.001`.

[99] W. F. Meggers, C. H. Corliss, and B. F. Scribner, *Tables of spectral-line intensities: part 1 - arranged by elements*, NBS MONO 145p1 (National Bureau of Standards, Gaithersburg, MD, 1975), `10.6028/NBS.MONO.145p1`.

[100] A. Kramida, Y. Ralchenko, J. Reader, and NIST ASD Team, NIST Atomic Spectra Database (ver. 5.12), [Online]. Available: `https://physics.nist.gov/asd` [2025, April 3]. National Institute of Standards and Technology, Gaithersburg, MD. 2024.

[101] J. Devlin, M. Tarbutt, D. Kokkin, and T. Steimle, "Measurements of the Zeeman effect in the $A^2\Pi$ and $B^2\Sigma^+$ states of calcium fluoride," Journal of Molecular Spectroscopy **317**, 1–9 (2015) `10.1016/j.jms.2015.07.009`.

[102] L. Lavy, P. F. Bernath, and A. Pastorek, "Line list for the $A^2\Pi - X^2\Sigma^+$ and the $B^2\Sigma^+ - X^2\Sigma^+$ systems of CaF," The Astrophysical Journal **979**, 19 (2025) `10.3847/1538-4357/ad9c7a`.

[103] M. A. Antonelli, J. Kendrick, C. Yakymchuk, M. Guitreau, T. Mittal, and F. Moynier, "Calcium isotope evidence for early archaean carbonates and subduction of oceanic crust," Nature Communications **12**, 2534 (2021) `10.1038/s41467-021-22748-2`.

[104] M. B. Channon, G. W. Gordon, J. L. Morgan, J. L. Skulan, S. M. Smith, and A. D. Anbar, "Using natural, stable calcium isotopes of human blood to detect and monitor changes in bone mineral balance," Bone **77**, 69–74 (2015) `10.1016/j.bone.2015.04.023`.

[105] M. C. Valdes, K. R. Bermingham, S. Huang, and J. I. Simon, "Calcium isotope cosmochemistry," Chemical Geology **581**, 120396 (2021) `https://doi.org/10.1016/j.chemgeo.2021.120396`.

[106] M. Costas-Rodríguez, J. Delanghe, and F. Vanhaecke, "High-precision isotopic analysis of essential mineral elements in biomedicine: natural isotope ratio variations as potential diagnostic and/or prognostic markers," TrAC Trends in Analytical Chemistry **76**, 182–193 (2016) `10.1016/j.trac.2015.10.008`.

[107] M. B. T. Zanatta, F. V. Nakadi, M. Resano, and M. A. M. S. da Veiga, "Calcium isotope determination in urine samples via the monitoring of ^{44}CaF and ^{40}CaF molecules by high-resolution continuum source graphite furnace molecular absorption spectrometry," Journal of Analytical Atomic Spectrometry **34**, 2280–2287 (2019) `10.1039/C9JA00233B`.

[108] S. Truppe, H. J. Williams, N. J. Fitch, M. Hambach, T. E. Wall, E. A. Hinds, B. E. Sauer, and M. R. Tarbutt, "An intense, cold, velocity-controlled molecular beam by frequency-chirped laser slowing," New Journal of Physics **19**, 022001 (2017) `10.1088/1367-2630/aa5ca2`.

[109] L. Anderegg, B. L. Augenbraun, E. Chae, B. Hemmerling, N. R. Hutzler, A. Ravi, A. Collopy, J. Ye, W. Ketterle, and J. M. Doyle, "Radio frequency magneto-optical trapping of CaF with high density," Physical Review Letters **119**, 103201 (2017) `10.1103/PhysRevLett.119.103201`.

[110] G. Lao, G.-Z. Zhu, C. E. Dickerson, B. L. Augenbraun, A. N. Alexandrova, J. R. Caram, E. R. Hudson, and W. C. Campbell, "Laser spectroscopy of aromatic molecules with optical cycling centers: Strontium(i) phenoxides," The Journal of Physical Chemistry Letters **13**, 11029–11035 (2022) `10.1021/acs.jpclett.2c03040`.

[111] B. L. Augenbraun, J. M. Doyle, T. Zelevinsky, and I. Kozyryev, "Molecular asymmetry and optical cycling: Laser cooling asymmetric top molecules," Physical Review X **10**, 031022 (2020) `10.1103/PhysRevX.10.031022`.

[112] R. Albrecht, M. Scharwaechter, T. Sixt, L. Hofer, and T. Langen, "Buffer-gas cooling, high-resolution spectroscopy, and optical cycling of barium monofluoride molecules," Physical Review A **101**, 013413 (2020) `10.1103/PhysRevA.101.013413`.

[113] R. Mitra, V. S. Prasannaa, B. K. Sahoo, N. R. Hutzler, M. Abe, and B. P. Das, "Study of HgOH to assess its suitability for electron electric dipole moment searches," Atoms **9**, 7 (2021) `10.3390/atoms9010007`.

[114] A. Jadbabaie, Y. Takahashi, N. H. Pilgram, C. J. Conn, Y. Zeng, C. Zhang, and N. R. Hutzler, "Characterizing the fundamental bending vibration of a linear polyatomic molecule for symmetry violation searches," New Journal of Physics **25**, 073014 (2023) `10.1088/1367-2630/ace471`.

[115] I. Kozyryev, "Laser cooling and inelastic collisions of the polyatomic radical SrOH," PhD thesis (Harvard University, May 2017).

[116] C. Zhang, S. T. Rittenhouse, T. V. Tscherbul, H. R. Sadeghpour, and N. R. Hutzler, "Sympathetic cooling and slowing of molecules with rydberg atoms," Physical Review Letters **132**, 033001 (2024) `10.1103/PhysRevLett.132.033001`.